UNIVERSITÀ DEGLI STUDI DI TRIESTE

Convenzione tra

UNIVERSITÀ DEGLI STUDI DI TRIESTE

e

UNIVERSITÀ CA' FOSCARI DI VENEZIA

XXXVI CICLO DEL DOTTORATO DI RICERCA IN CHIMICA

Metal oxide photocatalysts: the role of surface and nanostructure

Settore scientifico-disciplinare: **CHIM/03**

DOTTORANDO / A
LETIZIA LICCARDO

COORDINATORE
PROF. ENZO ALESSIO

SUPERVISORE DI TESI
PROF. ELISA MORETTI

ANNO ACCADEMICO 2022/2023

Abstract

Human activities are causing severe environmental impacts, above all global warming and water insecurity. The widespread presence of contaminants of emerging concerns (CECs) in water effluents is causing deleterious effects on living beings. Photo-driven advanced oxidation processes (AOPs), including heterogeneous photocatalysis, have been demonstrated to be highly efficient for wastewater treatment. Additionally, addressing energy demand and its sustainable production is urgently needed to mitigate the deleterious effects of global warming. In this frame, hydrogen (H_2) has been considered one of the most promising renewable energy carriers, thus extensive efforts have been made to achieve low-emission H_2 production and develop new technologies for large-scale production. Specifically, scientific interest has been focused on finding new photocatalysts for both CECs photodegradation and H_2 production driven by solar light irradiation. In line with Goals 6 and 7 of the 17 Sustainable Development Goals (SDGs) Agenda 2030, the present doctoral thesis explores the design and development of novel metal oxide-based nanostructured materials as efficient photocatalysts for dyes and drugs photodegradation and H_2 production through photoelectrochemical water splitting (PEC WS) and photoreforming. In detail, focusing on titanium dioxide (TiO_2), considered the benchmark photocatalyst, several strategies have been investigated to tailor and improve its optical and electronic properties, using smart and cost-effective synthetic routes to boost both the overall photoresponse and catalytic activity. A direct correlation among morphological, structural, optical, and electronic properties and the photoactivity of the synthesized nanomaterials has been established by critically discussing the experimental results obtained by using advanced experimental techniques. Overall, the research findings provided by the nanostructured systems designed and investigated in this thesis aim to significantly contribute to the development of new and sustainable solar-driven technologies for future large-scale applications in the field of heterogeneous photocatalysis.

List of acronyms

AFM	Atomic Force Microscopy
ALD	Atomic Layer Deposition
AOPs	Advanced Oxidation Processes
API	Active Pharmaceutical Ingredients
AQY	Apparent Quantum Yield
BET	Brunauer, Emmett, Teller
BJH	Barrett, Joyner, Halenda
CB	Conduction Band
CECs	Contaminants of Emerging Concerns
CIP	Ciprofloxacin
CVD	Chemical Vapor Deposition
DFT	Density Functional Theory
DOS	Density Of States
DRUV-Vis-NIR	Diffuse Reflectance UV-Vis-NIR
EDX	Energy Dispersive X-ray
Eg	Energy bandgap
EIS	Electrochemical Impedance Spectroscopy
EPA	Environmental Protection Agency
FE	Field Emission
FTO	Fluorine-doped Tin Oxide
FWHM	Full Width at Half Maximum
GDP	Gross Domestic Product
GHG	Greenhouse Gas
GSDR	Global Sustainable Development Report
HAADF	High-Angle Annular Dark Field
HER	Hydrogen Evolution Reaction

HOMO	Highest Occupied Molecular Orbital
HR	High Resolution
IPCC	Intergovernmental Panel on Climate Change
IR	Infrared
IUPAC	International Union of Pure and Applied Chemistry
JCPDS	Joint Committee on Powder Diffraction Standards
LSV	Linear Sweep Voltammetry
LUMO	Lowest Unoccupied Molecular Orbital
MB	Methylene Blue
MDZ	Metronidazole
Mw	Microwave
NOh	Nano-octahedra
NP	Nanoparticle
NR	Nanorod
NW	Nanowire
NZE	Net Zero Emission
OCP	Open Circuit Potential
OER	Oxygen Evolution Reaction
Ov	Oxygen vacancies
PDF	Powder Diffraction File
PEC	Photoelectrochemical
PL	Photoluminescence
PMMA	Poly(methyl methacrilate)
PVD	Physical Vapor Deposition
PZC	Point of Zero Charge
RBS	Rutherford Backscattering
RF	Radiofrequency
RhB	Rhodamine B

ROS	Reactive Oxygen Species
SAED	Selected Area Electron Diffraction
SDGs	Sustainable Development Goals
SEM	Scanning Electron Microscopy
SSA	Specific Surface Area
SSL	Simulated Solar Light
STEM	Scanning Electron Microscopy
TEM	Transmission Electron Microscopy
UN	United Nations
UNFCCC	United Nations Framework Convention on Climate Change
UV	Ultraviolet
VB	Valence Band
Vis	Visible
WHO	World Health Organization
WS	Water Splitting
XPS	X-ray Photoemission Spectroscopy
XRD	X-ray Diffraction

Table of contents

Chapter 1 – *Introduction*

This Chapter opens the research thesis by addressing the pressing issues of energy and environmental crisis, emphasizing the critical need for sustainable solutions. In detail, the issue of water contamination is highlighted and Advanced Oxidation Processes (AOPs) are explored as potential remedies. Additionally, it delves into the role of hydrogen (H_2) as green fuel, setting the stage for the aim of this thesis that investigates innovative approaches for addressing environmental challenges. An outline of the thesis is provided at the end of this chapter, offering a roadmap for the comprehensive exploration of these topics.

1.1 Energy and environmental crisis

In the past two decades, the global population has exponentially grown along with the related economic activities, such as mass production and consumption, and unrestrained use of natural resources, clearly producing severe repercussions on the environment. Consequently, human-caused environmental issues, above all global warming and water insecurity, have been jeopardizing our existence.

In detail, in 2022 the world's total energy annual consumption per capita, which refers to primary energy before being transformed into forms of energy for end-use such as electricity or oil for transportation, reached 21,039 kWh. [1] During the same year, the world gross electricity production rose by 2.4% (nearly 700 TWh), and over 60% of the total global electricity generation was given by fossil fuels. [2] Global greenhouse gas (GHG) emissions, dominated by carbon dioxide and methane, have been strongly increasing due to the unsustainable energy use caused by human activities.[2,3] The energy crisis is not only limited to GHG emissions, but includes also the tremendous gap between rich and poor countries with respect to energy access. Gross Domestic Product (GDP) - the total value of goods and

services produced by a country in a year – is indeed very high for rich countries, which means high CO_2 emissions, while low emissions are mostly detected in poor countries. [3–5] The lack of access to modern electricity and clean energy technologies reveals an energy poverty scenario. Prices and economic pressure are the main causes for the rising number of people without access to modern electricity, which forces them to go backward to the use of traditional biomass. In this frame, oil and coal must be seen as a short-term option [5]. In addition, GHG emissions and subsequent climate change are very expensive in terms of impacts on both human and natural systems causing the environmental crisis. For the impact on ecosystems, it is enough to think about extreme events such as heatwaves with related droughts, floods, changes in the seasonal timing or species migration, and sometimes their extinction.

In our society, there is often the tendency to think that humans are not affected at all. On the contrary, climate change is causing severe effects on food security and water availability, which are related to the physical and mental health of human beings.[6] It is worth pointing out that water availability is a concept concerning the access to groundwater, water quality, and demand.[5] Almost half of the global population is experiencing water scarcity due to the combination and the synergistic effect of climatic factors (i.e., the increasing of weather extreme events), and non-climatic factors (i.e., mass production).[7] Furthermore, in our modern society, the increase of health diseases related to environmental pollution has led to an increase in drugs consumption. Thus, according to the World Health Organization (WHO), finding higher concentrations of hazardous compounds in surface- or ground- water is getting more and more common with deleterious effects. At this point, it is clear that extreme and slow-onset events correlated to the energy and environmental crisis are undermining, not only natural systems, but also human well-being. As a result, thanks to the rising of knowledge and awareness about this topic, efforts to tackle climate change at various government levels have been accelerated. Emerging international climate agreements and policies are positive signs of a transition toward a more sustainable world. In the last decade, mitigation

policies such as the Kyoto protocol or the Paris Agreement, adopted under the United Nations Framework Convention on Climate Change (UNFCCC), have not only led to a reduction of GHG emissions in some countries, but also improved the transparency of climate action and the support for the implementation of such policies. In addition, it is worth mentioning the 2030 Agenda for Sustainable Development, adopted in 2015 by the member states of the United Nations (UN). 17 Sustainable Development Goals (SDGs, **Figure 1.1**) were defined with the aim of ending the extreme poverty, protecting the planet by overcoming energy and environmental crisis, and promoting more diplomatic, wealthy, and inclusive societies all over the world. According to the SDGs agenda, safeguarding global commons is the key for long-term human development and social economic well-being. An annual SDG progress report, presented by the UN Secretary General, and a Global Sustainable Development Report (GSDR), produced every four years by an Independent Group of Scientists hired by the Secretary General, are essential documents to account for the developments on the agenda.[8] Unfortunately, according to GSDR 2023, we are terribly late on this roadmap scheduled for 2030. The late shocking events like the COVID-19 pandemic and the conflicts in many regions including the war in Ukraine, are deteriorating the already accomplished progresses and those that need to be achieved. The race towards SDGs must be urgently accelerated and actions must be taken to weaken, break down and stop unsustainable practices. For this purpose, science driven transformations are extremely needed.

Figure 1.1 Sustainable Development Goals to achieve by 2030 with a view towards ending all forms of poverty, fighting inequalities, and tackling climate change.

1.2 Water contamination and AOPs

It is well-established that high levels of industrialization mean high levels of environmental pollution. To meet the needs of mass production, big and small companies are indeed overusing resources such as fossil fuels to produce energy, making them the main responsible for air pollution. Additionally, it is well known that water is extensively used in industrial processes, which results in highly polluted wastewater.[9] Industries that are considered accountable for water contamination usually work in petroleum refining, dye manufacturing, polymeric, chemical, coking coal, leather, textile, pharmaceutical and paper sectors.[10] In general, water contamination or pollution, especially due to human activities, is considered one of the most urgent ecological issues worldwide. In fact, wastewater treatment plants, urban and agricultural discharges are the major sources of organic contaminants in water.[11] According to the US Environmental Protection Agency (EPA), organic contaminants are complex organic molecules, including surfactants, dyes, pesticides, pharmaceuticals, and other low-degradable complex substances. All of these have been defined as Contaminants of Emerging Concern (CECs) since they are ubiquitously present in freshwater bodies causing adverse impacts on both ecosystems and human health.[12] CECs have been detected in effluent sewers and surface waters with a concentration ranging from ng L^{-1} to µg L^{-1}. [13–15] The reason for the toxicity of these compounds is the presence of amino, nitro (-NO_2) and carbon-carbon double bond (C=C) groups that are hardly degradable.[16] Examples of their chemical structure are shown in **Figure 1.2**.

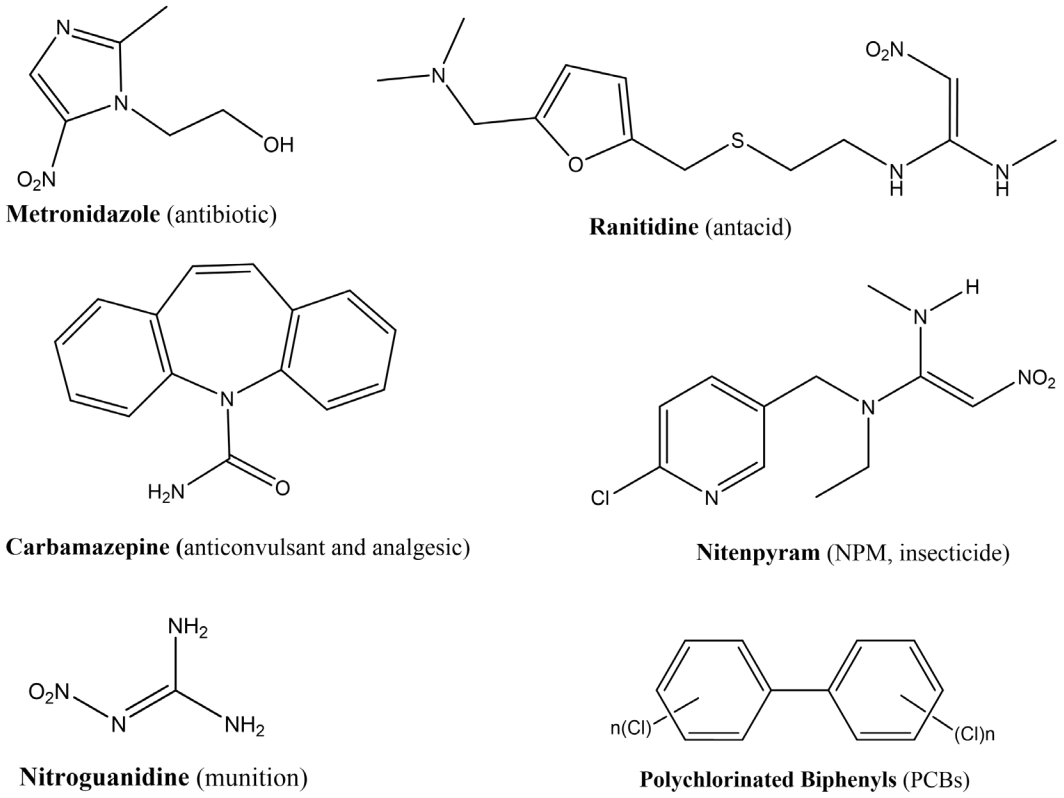

Figure 1.2 Examples of the chemical structures of the most common CECs.

In the last decade, among all CECs, pharmaceuticals have been the objects of increasing concern. Pharmaceuticals can be synthetic or natural chemicals, found in prescription medicines, counter and veterinary drugs, which contain active principles with pharmacological effects. A wide array of pharmaceutical compounds is continually released into the environment because they are ubiquitously used in human and veterinary medical practices, aquaculture, and agricultural sectors.[17–19] Additionally, as highlighted above, the increasing of health diseases related to environmental pollution has led to an increase in drugs consumption. Thus, pharmaceuticals in water may derive from different sources such as personal care products discharge, pharmaceutical industry and hospital waste or therapeutic drugs present in urban run-off, landfill leachate and biosolids.[20] **Figure 1.3** illustrates some of pharmaceuticals' entry routes in the environment.

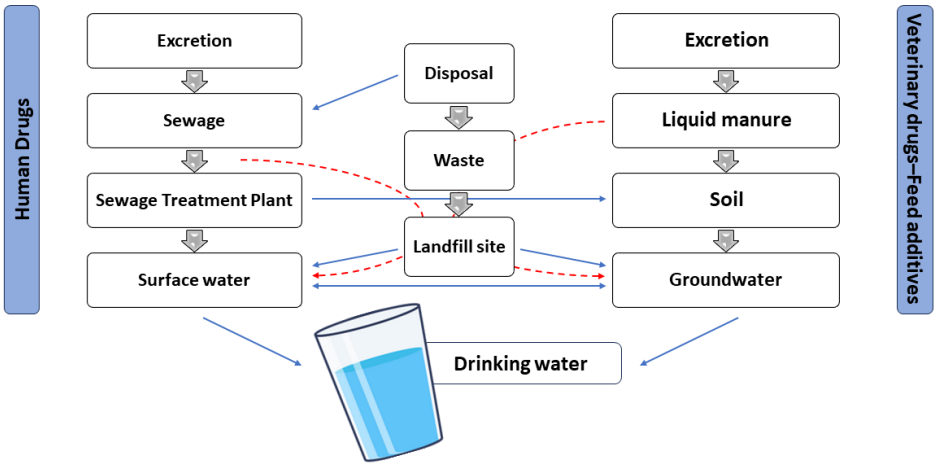

Figure 1.3 Fate of pharmaceuticals in the environment.

It is worth noticing that such compounds are gaining attention for their intrinsic peculiarities like (i) the complex chemical structure, which can be formed by several molecules; (ii) the specific design to be persistent against biological degradation to reach the desired therapeutic effect; (iii) the polarity and degree of ionization that depend on the medium's pH; (iv) the lipophilicity and solubility in water; (v) the ability to undergo metabolic reactions. [21,22] Furthermore, traces of these compounds in drinking water can potentially cause chronic health effects associated with their long-term ingestion. [23,24] Major concerns include endocrine disrupting compounds, such as estrogen steroids from human contraceptive pills and antibiotics that can contribute to bacterial antimicrobial resistance. [25] The most common therapeutic groups found in water are reported in Table 1.1.

Finding high concentrations of these hazardous compounds in surface- or groundwater is getting more and more common. These have several deleterious consequences such as mutagenic, genotoxic, eco-toxicological and carcinogenic effects on living beings. [23] To highlight this issue, it is worth mentioning the global-scale research, carried out by Wilkinson and his team, [26] on the pollution by active pharmaceuticals ingredients (APIs).

Table 1.1 Most common therapeutic groups found in water. Data reproduced from ref. 20-24.

Therapeutic groups	Active principles
Anti-inflammatories and analgesics	Paracetamol, acetylsalicylic acid, ibuprofen, and diclofenac
Antidepressants	Benzodiazepines
Antiepileptics	Carbamazepine
Lipid-lowering drugs	Fibrates
β-blockers	atenolol, propanolol, and metoprolol
Antiulcer drugs and antihistamines	ranitidine and famotidine
Antibiotics	tetracyclines, macrolides, β-lactams, penicillins, quinolones, sulfonamides, fluoroquinolones, chloramphenicol, and imidazole derivatives
other substances	cocaine, barbiturates, methadone, amphetamines, opiates, heroin, and other narcotics

Samples were obtained from 1052 locations in 104 countries, representing all the continents. Among all the contaminants, the most frequently detected in high concentrations were paracetamol, caffeine, metformin, fexofenadine, sulfamethoxazole (antimicrobial), metronidazole (antimicrobial) and gabapentin. The study showed that in 25.7% of sampling sites the concentrations of at least one API were higher than those considered safe for aquatic life or for antimicrobial resistance. Furthermore, the most contaminated sites were from low- to middle-income countries and attributed to poor wastewater and waste management treatment plants. Consequently, it is of great relevance to put effort into finding effective and sustainable removal technologies.

Wastewater treatments include physical, chemical and biological processes, which consist of four removal steps depending on the material of interest.

(1) Preliminary treatments used to remove coarse solids and coarse materials, such as oils, grease, sand and dust, which are done mechanically by filtration.
(2) Primary treatments carried out to separate the organic or colloidal solid suspensions, which are also necessary to perform the subsequent treatments.
(3) Secondary treatments useful to substantially degrade the organic content of wastewater and usually performed using biological or physicochemical methods.
(4) Tertiary treatments in which advanced treatment processes are applied when wastewater contains contaminants hardly degradable with secondary treatments. [27] Conventional wastewater treatment plants typically use secondary treatments based on biological degradation, like activated sludge processes or biofilms, [28] whereas advanced facilities are using tertiary treatments, such as reverse osmosis, ozonation and chemical methods. [29,30] As already stated above, pharmaceuticals are complex molecules with different physical and chemical properties, thus when designing an efficient removal technology, their reactivity towards different treatment processes and parameters (*i.e.*, temperature, retention time and pH of the medium) should be considered. For instance, most pharmaceuticals are relatively hydrophobic, thus physicochemical, and biological methods may be insufficient for their complete removal. [31] In other words, secondary or conventional treatments may not be suitable, thus pharmaceutical compounds may be discharged in the environment causing adverse effects due to their ability to interact with living beings. [32,33] Therefore, greater efforts to search for new sophisticated wastewater treatment plants and the introduction of advanced wastewater treatment processes are needed.
In the last decades, among several chemical methods, advanced oxidation processes (AOPs) have been widely investigated since they are promising powerful and environmentally friendly methods for the complete removal and mineralization of persistent organic pollutants present in wastewater. AOPs are based on the in-situ production and in media reaction of reactive oxygen species (ROS), such as hydroxyl radicals (HO·) or other strong oxidant species (*e.g.*, $\cdot O_2^-$, HOO·, ROO·), that are produced in enough quantities to oxidize persistent organic contaminants. The

starting point for an advanced oxidation process is precisely the ROS production. In fact, ROS are free radicals with high standard reduction potential, meaning that they are strong oxidizing agents. For instance, HO· with his high standard reduction potential (E^0=2.7 V) can react with a wide range of organic contaminants leading to their high or complete mineralization into small molecules and harmless by-products such as H_2O or CO_2.[34]

Under appropriate conditions, AOPs can be an efficient wastewater treatment technology thanks to high mineralization efficiency, rapid oxidation reaction rate and non-secondary pollutants production. Several types of processes are included under the broad definition of AOPs, namely: sonolysis, ozonation, photolysis, photocatalysis, electrochemical oxidation, gamma ray/electron beam radiation, and a number of others electric and electrochemical methods. Hence, it is worth pointing out that in most individual AOPs their oxidation capacity and degradation efficiency are strictly limited by ROS production, which is related to some key operating parameters, like mass transfer resistance and nature of wastewater matrix.[35] A single AOP is basically not enough for effective wastewater treatment, thus process integration is needed to overcome the limits associated with each individual process.[36,37] In addition, the combination of AOPs can widen the range of operating parameters. [38] Therefore, the research in this field is focused on the improvement of single AOPs or the combination of individual AOPs in order to increase the applicability of these techniques for practical applications. In this frame, photo driven-AOPs such as heterogeneous photocatalysis have been proven to be highly efficient for wastewater treatment but their practical use is still limited by the high operating costs. As a result, scientific interest has been focused on finding new photocatalysts driven by solar light irradiation, being the renewable energy source *par excellence*. Consequently, the possibility of broadening the ability of photocatalysts to work under solar light irradiation will be widely discussed in the following chapters of this thesis.

1.3 H_2 as green fuel

As already mentioned in section 1.1, world energy demand and consumption are increasing enormously due to the rapid growth of human beings and industrialization. Furthermore, most of the energy is still produced by fossil fuels, which are the primary sources of CO_2 emissions. In 2022, CO_2 emissions from energy combustion and industrial processes increased by an unprecedented 0.9% to a new high of 36.8 Gt, following two years of exceptional oscillations in energy-related emissions due to the COVID-19 pandemic.[39] However, emissions rebounded past pre-pandemic levels in 2021 growing more than 6% as a result of economic recovery and people mobility.[40] Moreover, according to worldwide data, power electricity and heat sectors emissions reached an all-time high of 14.6 Gt in 2022, increasing by 1.8% with respect to 2021, as depicted in **Figure 1.4**.[40]

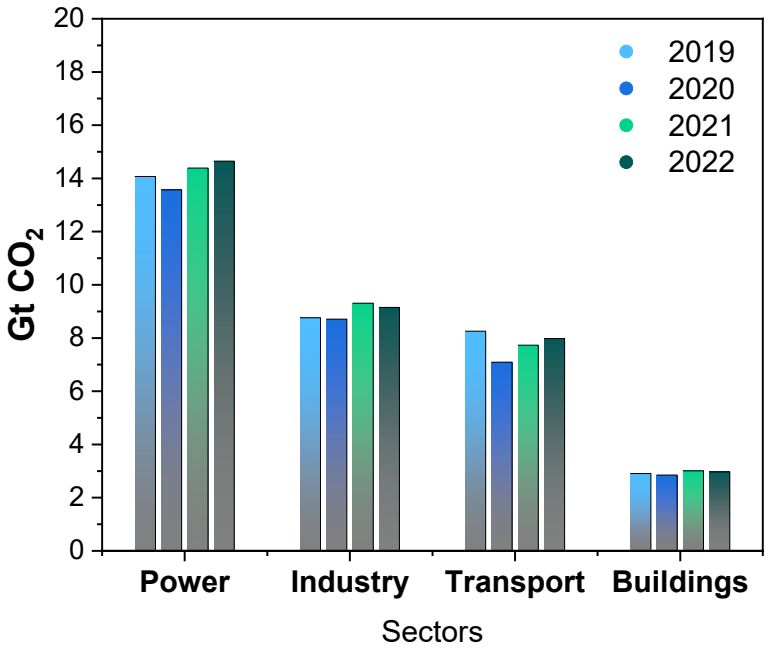

Figure 1.4 Worldwide distribution of CO_2 emissions per sector. Values are reported in Gt. Data reproduced from reference [40].

Although global GHG emissions have not reached their maximum yet, the global average surface temperature is already 1.2 °C higher than pre-industrial levels. Thus, tracking progress by estimating the amount of carbon that can still be emitted to constrain anthropogenic warming offers useful insights into what strategies should be followed. According to the Intergovernmental Panel on Climate Change (IPCC) report 2023, there is indeed a fixed carbon "budget" (*i.e.*, the amount of CO_2 in Gt that can be emitted in the future) that cannot be exceeded in order to limit global warming. This implies that CO_2 emissions should be controlled along with a strong reduction in other GHG emissions. In detail, the current 2023 carbon budget to limit global warming to 1.5°C is 250 CO_2 Gt to have a 50% chance, equivalent to six years (i.e., until ~2029) of current CO_2 emissions.[3,5] Therefore, within the framework of the Net Zero Emission (NZE) scenario, new strategies are urgently needed to limit global warming to 1.5 ºC and achieve international climate goals. To face the energy demand and its production in a sustainable way, it is essential to shift our energy systems away from fossil fuels. A good strategy may be the search for clean and renewable energy resources and the transition to a CO_2-neutral energy carrier, especially in sectors with higher emissions such as power and transportation. Among several alternatives, hydrogen (H_2) has been considered the most promising one, thanks to its excellent properties such as very low density (lower than air) and high energy density-to-mass ratio (120-142 $MJ \cdot kg^{-1}$) with potentially no CO_2 emissions. These features make hydrogen around three times more energetic than gasoline.[41] Hence, in the last decades hydrogen fuel production has been one of the main research areas in the field of energy production. H_2 is considered the ultimate clean energy carrier and can be an energy resource with many advantages. It can be produced from a variety of feedstocks, including both fossil resources, such as natural gas and coal, and renewable resources such as biomass and water. In this frame, in 2022 H_2 production increased by 3% with respect to 2021, reaching 95 Mt. However, it is mainly produced from CO and CH_4 derived from fossil fuels by steam reforming reaction coupled with water gas shift and purification reaction.[42] Thus, given the scarcity of fossil fuels and the CO_2-

emission-related environmental issues, H_2 produced in this way cannot longer be seen as a valid alternative for a clean energy transition process.[43] Thus, only the H_2 production from renewable resources by using renewable energy sources should be considered. Luckily, another great advantage of H_2 is its production reactions versatility (**Figure 1.5**) and the possibility to use several environment-friendly technologies including chemical, biological, electrolytic, photolytic, and thermo-chemical, each in its stage of development and with its benefits and challenges.

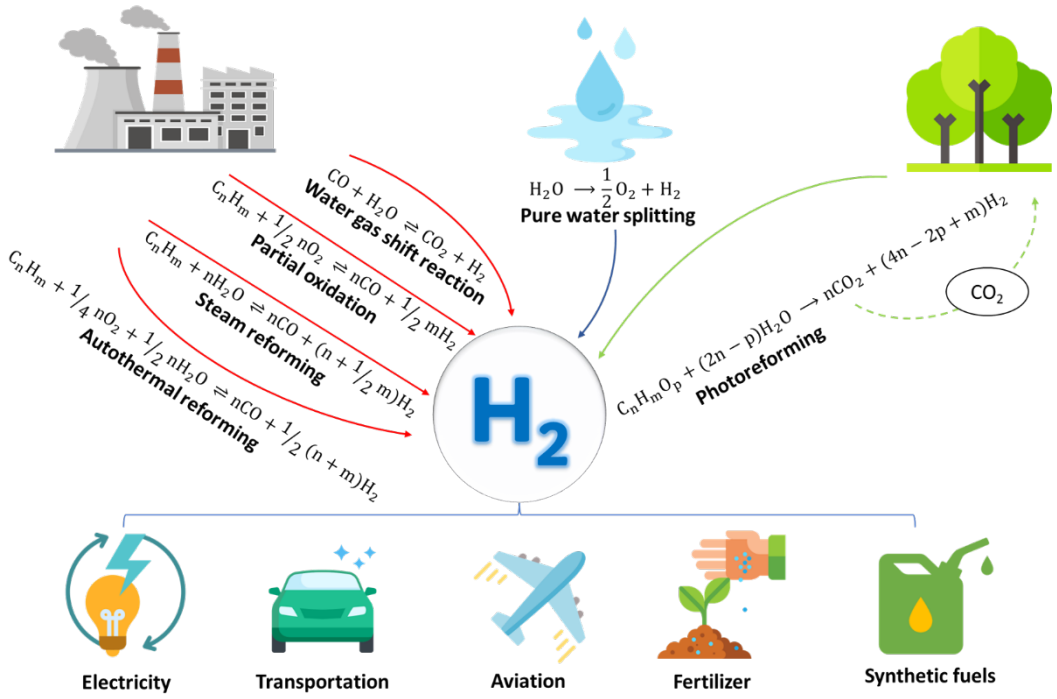

Figure 1.5 Different routes for H_2 production.

The basic issue related to the use of renewable energy resources is the low hydrogen production efficiency and rates that are still far from supplying the energy demand, thus being far from a practical use. However, some efforts have been made to reach low-emission H_2 production and design new technologies for large-scale production. In this frame, the research is mainly focused on the development of new methods able to exploit solar energy. Solar light is considered the best renewable energy source thanks to its limited anthropogenic impact. Each year, it is

estimated that Earth is continuously irradiated by about $1.2 \cdot 10^5$ TW equal to 6000 times the current energy consumption.[43] However, due to its diffuse nature, there is the need for a cost-effective and highly efficient way for its low environmental impact harvesting.[44] At present, a good possibility is the storage of sunlight energy in the form of chemical fuel like H_2. Thus, solar photochemical water splitting (WS) for the H_2 production using technologies such as photoelectrochemical (PEC) WS and photoreforming, have gained attention.

Water splitting (WS) into hydrogen and oxygen has always been considered an ideal approach for the production of hydrogen under mild conditions.[45,46] The overall WS reaction (equation 1.3) occurs in an electrolytic cell made up of a anode, a cathode and an aqueous electrolyte, and it is given by two half-reactions, hydrogen evolution reaction (HER, equation 1.1) at the cathode, and oxygen evolution reaction (OER, equation 1.2) at the anode. [47]

$$\mathrm{HER: } 2\mathrm{H}^+ + 2\mathrm{e}^- \rightarrow \mathrm{H}_2 \quad (1.1)$$

$$\mathrm{OER: } \mathrm{H}_2\mathrm{O} \rightarrow \frac{1}{2}\mathrm{O}_2 + 2\mathrm{H}^+ + 2\mathrm{e}^- \quad (1.2)$$

$$\mathrm{WS: } \mathrm{H}_2\mathrm{O} \rightarrow \mathrm{H}_2 + \frac{1}{2}\mathrm{O}_2 \quad (1.3)$$

From a thermodynamic point of view, the WS reaction is energetically disfavored. An overpotential (potential higher than the theoretical thermodynamic potential of 1.23 eV at 25 °C and 1 atm) is required and the needed energy to overcome the potential barrier is given by a Gibbs free energy variation of 237 kJ mol^{-1}. For this reason, the exploitation of solar light irradiation and a photoinduced catalytic process may be the keys to easily get the WS reaction in a sustainable way.

For PEC WS, the electrolytic cell usually requires a photoanode and a cathode, which are semiconductor materials, and an electrolyte-containing aqueous environment. Semiconductor materials are able to interact with light and play an important role in converting photons into chemical energy. At the same time, photons with energy higher or equal to the semiconductors energy bandgap (E_g),

provide the energy needed to overcome the potential barrier. To reach an effective PEC WS, both the reduction and oxidation potentials of water should lie within the band gap of the semiconductor material. In fact, the range of applicability of a semiconductor material is strongly limited by its valence band (VB) and conduction band (CB) position. To select the right material, there are some important conditions to take into account: (i) the VB potential should be more positive than the O_2/H_2O redox potential to allow water oxidation, while the CB should be more negative than H^+/H_2 redox potential to allow water reduction; (ii) the E_g should be between 1.23 and 3.26 eV; (iii) the semiconductor material should be electrochemically and photochemically stable. Generally, H_2 production by water electrolysis accounts for just 0.1% of today's global production, but more and more projects on WS have been lately announced.[42]

However, despite many efforts have been made, PEC WS is still far from a large-scale application due not only to the extremely low H_2 production efficiency, but also because of the high production costs of efficient photoelectrodes. [48] In fact, pure WS can lead to the formation of intermediates such as H_2O_2, making the backward reaction (*i.e.*, the recombination of H_2 and O_2) more feasible and slowing down the overall H_2 production rates.[48,49] Moreover, the backward reaction can be controlled by using sulfides, metal oxides, noble metal, or non-metal catalysts but their drawbacks such as high costs or low availability, low stability and high charge carriers recombination rates make them still unsuitable.[47] For this reason, to boost the H_2 production, several strategies like the use of water vapor or electron donors have been investigated.[50] The use of electron donors such as organic compounds as sacrificial hole scavengers is beneficial to enhance the HER by timely consuming photogenerated holes or active radicals thus inhibiting OER.[51–54] When a sacrificial agent and light are simultaneously used to boost HER, the process is known as light-induced reforming or photoreforming. However, the addition of sacrificial agents could lead to several drawbacks, *e.g.*, increase in production costs and environmental issues related to the chemical nature of the selected sacrificial agent. On the contrary, if renewable compounds are considered as sacrificial target

molecules and the photocatalyst employed in the process is finely designed, photoreforming can be particularly attractive thanks to the simultaneous production of H_2, the reduction of potential organic pollutants or the creation of new value-added chemicals.[55,56] On this basis and from a thermodynamic point of view, photoreforming is considered more feasible than steam reforming and WS. In fact, the Gibbs free energy variation (ΔG°) for photoreforming reactions of many common natural waste polymers or biomass-derived compounds is highly lower than that of WS or steam reforming of carbon, ethanol, methane, and ethane that shows large positive ΔG° values. For instance, photoreforming of biomass-derived glycerol shows a ΔG° equal to 5.1 kJ mol^{-1} against a ΔG° equal to 237 kJ mol^{-1} for WS and 130.7 kJ mol^{-1} for methane steam reforming, respectively.[57] Photoreforming involves two different half-reactions: HER, and a sacrificial organic compound oxidation reaction that consists in complex multistep reactions. Briefly, in the photoreforming process, the semiconductor material is excited by a light source, which induces the formation of electron-hole (e^-—h^+) pairs. Afterwards, the reduction reaction of water to H_2 occurs thanks to the generated electrons (e^-) in the CB, while simultaneously the photogenerated holes (h^+) in the VB lead the oxidation reaction of the sacrificial organic substrate. The photogenerated holes in the photocatalyst VB can directly or indirectly oxidize the organic substrate through the formation of oxidative radicals.[58] Therefore, photoreforming can be seen as a hybrid process between photocatalytic WS and photo-oxidation of organic compounds, where the solvent (usually water) is reduced by electrons donated by the sacrificial agent oxidation in the presence of a suitable photocatalyst (**Figure 1.6**). Summarizing, photoreforming shows unique benefits such as the applicability to off-grid systems, the possibility to use renewable sources, and the great potential to produce pure, fuel-cell-grade H_2.[59] Nevertheless, despite the emerging number of papers concerning the H_2 production by photoreforming, the efficiency of the overall reaction is still low. There are, indeed, competing processes such as high rates of recombination of photogenerated charge carriers that strongly decrease efficiency. In addition, the high variety of operational conditions (*e.g.*, reactor

type, gas carrier flows, light source, substrate concentration and photocatalyst type) make the comparison and consequently the improvement among different systems very challenging.

The following chapters will therefore describe the challenges in the H_2 production by both PEC WS and photoreforming, with a particular focus on the design of good photocatalysts.

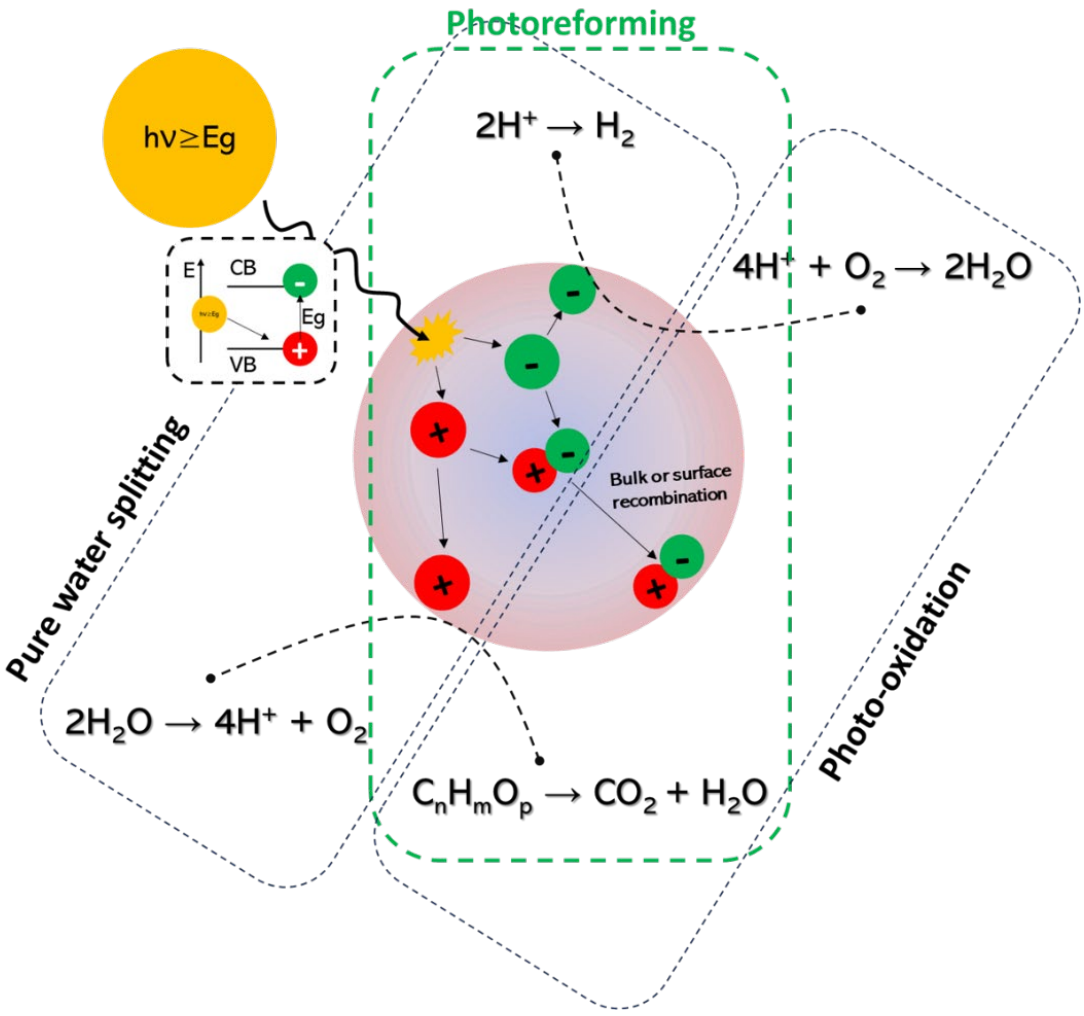

Figure 1.6 Photoreforming as a hybrid process between pure water splitting reaction and organic compounds photo-oxidation reaction.

1.4 Aim & Outlines of the thesis

Human activity is causing severe environmental issues, above all global warming and water insecurity. It has also become very common to find high concentrations of Contaminants of Emerging Concerns (CECs), such as pharmaceuticals, in surface water or groundwater, which are causing deleterious effects on living beings. Photo driven-AOPs like heterogeneous photocatalysis have been proven to be highly efficient for wastewater treatment, but their practical use is still limited.

In order to limit global warming, it is essential to face the energy demand and its production in a sustainable way far from the use of fossil fuels. Among several renewable energy resources, hydrogen (H_2) has been considered the most promising one, thanks to its excellent properties. In the last decade, many efforts have been made to reach low-emission H_2 production and design new technologies for large-scale production.

In this context, scientific interest has been focused on finding new photocatalysts for both CECs photodegradation and H_2 production driven by solar light irradiation.

As a result, the present doctoral thesis perfectly fits in two of the 17 Sustainable Development Goals (SDGs), specifically goal 6 regarding availability and sustainable management of clean water, and goal 7 related to the access to affordable and clean energy for all.

In detail, this thesis focuses on the design and development of new metal oxide (MOx)-based nanostructured materials as efficient photocatalysts for CECs photodegradation and H_2 production through photoelectrochemical water splitting (PEC WS) and photoreforming. Several strategies to tune the optical and electronical properties of the photocatalysts, based on different smart and low-cost synthetic routes, were investigated. A tight correlation between the catalysts properties and photocatalytic activity was directly established by using several advanced experimental techniques.

In this chapter (**Chapter 1**) a general introduction on the most important aspects of the global energy and environmental crisis is reported, and particular attention is given to both water insecurity and energy demand. Some possible strategies and key features of different photocatalytic processes in the field of heterogenous photocatalysis are also described by highlighting three different applications: CECs photodegradation process for water remediation, and PEC WS and photoreforming for hydrogen production.

In **Chapter 2** an overview on the fundamentals of photocatalysis and semiconductor materials in the field of heterogeneous photocatalysis is presented. Further details are then given in **Chapter 3**, where titanium dioxide (TiO_2) is described as the benchmark photocatalyst.

From chapter 4 to 6, several strategies to tune the optical and electronical properties of semiconductor materials, such as pure TiO_2, are investigated.

Specifically, **Chapter 4** concerns the use of surface engineering, *i.e.*, the possibility to create surface defects, and the synergistic effects of the morphology to enhance the overall photoactivity toward visible light in two different applications (drug photodegradation and methanol photoreforming). In **Chapter 5,** the possibility to build homo- and hetero-junctions between different metal oxides is proposed to enhance the photoactivity for both dye degradation and PEC WS. Finally, in **Chapter 6**, doping strategies are also considered.

The general conclusions on the obtained results and future perspectives are presented in the final chapter (**Chapter 7**).

1.5 References

[1] Energy Institute, *Statistical Review of World Energy 2023*, **2023**.

[2] International Energy Agency, *International Energy Agency (IEA) World Energy Outlook 2022*, **2022**.

[3] P. Friedlingstein, M. O'Sullivan, M. W. Jones, R. M. Andrew, L. Gregor, J. Hauck, C. Le Quéré, I. T. Luijkx, A. Olsen, G. P. Peters, W. Peters, J. Pongratz, C. Schwingshackl, S. Sitch, J. G. Canadell, P. Ciais, R. B. Jackson, S. R. Alin, R. Alkama, A. Arneth, V. K. Arora, N. R. Bates, M. Becker, N. Bellouin, H. C. Bittig, L. Bopp, F. Chevallier, L. P. Chini, M. Cronin, W. Evans, S. Falk, R. A. Feely, T. Gasser, M. Gehlen, T. Gkritzalis, L. Gloege, G. Grassi, N. Gruber, Ö. Gürses, I. Harris, M. Hefner, R. A. Houghton, G. C. Hurtt, Y. Iida, T. Ilyina, A. K. Jain, A. Jersild, K. Kadono, E. Kato, D. Kennedy, K. Klein Goldewijk, J. Knauer, J. I. Korsbakken, P. Landschützer, N. Lefèvre, K. Lindsay, J. Liu, Z. Liu, G. Marland, N. Mayot, M. J. McGrath, N. Metzl, N. M. Monacci, D. R. Munro, S.-I. Nakaoka, Y. Niwa, K. O'Brien, T. Ono, P. I. Palmer, N. Pan, D. Pierrot, K. Pocock, B. Poulter, L. Resplandy, E. Robertson, C. Rödenbeck, C. Rodriguez, T. M. Rosan, J. Schwinger, R. Séférian, J. D. Shutler, I. Skjelvan, T. Steinhoff, Q. Sun, A. J. Sutton, C. Sweeney, S. Takao, T. Tanhua, P. P. Tans, X. Tian, H. Tian, B. Tilbrook, H. Tsujino, F. Tubiello, G. R. van der Werf, A. P. Walker, R. Wanninkhof, C. Whitehead, A. Willstrand Wranne, R. Wright, W. Yuan, C. Yue, X. Yue, S. Zaehle, J. Zeng, B. Zheng, *Earth Syst. Sci. Data* **2022**, *14*, 4811.

[4] A. Goldthau, S. Tagliapietra, *Nature* **2022**, *612*, 627.

[5] H. L. and J. R. (eds.). Contribution of Working Groups I, II and III to the Sixth Assessment Report of the Intergovernmental Panel on Climate Change Core Writing Team, Geneva , Switzerland, pp. 35–115.

[6] Y. Yamada, X. Zhang, M. E. T. Henderson, H. Sagayama, H. Pontzer, D. Watanabe, T. Yoshida, M. Kimura, P. N. Ainslie, L. F. Andersen, L. J. Anderson, L. Arab, I. Baddou, K. Bedu-Addo, E. E. Blaak, S. Blanc, A. G. Bonomi, C. V. C. Bouten, P. Bovet, M. S. Buchowski, N. F. Butte, S. G. Camps, G. L. Close, J. A. Cooper, R. Cooper, S. K. Das, L. R. Dugas, S. Eaton, U. Ekelund, S. Entringer, T. Forrester, B. W. Fudge, A. H. Goris, M. Gurven, L. G. Halsey, C. Hambly, A. El Hamdouchi, M. B. Hoos, S. Hu, N. Joonas, A. M. Joosen, P. Katzmarzyk, K. P. Kempen, W. E. Kraus, W. Kriengsinyos, R. F. Kushner, E. V. Lambert, W. R. Leonard, N. Lessan, C. K. Martin, A. C. Medin, E. P. Meijer, J. C. Morehen, J. P. Morton, M. L. Neuhouser, T. A. Nicklas, R. M. Ojiambo, K. H. Pietiläinen, Y. P. Pitsiladis, J. Plange-Rhule, G. Plasqui, R. L. Prentice, R. A. Rabinovich, S. B. Racette, D. A. Raichlen, E. Ravussin, L. M. Redman, J. J. Reilly, R. M. Reynolds, S. B. Roberts, A. J. Schuit, L. B. Sardinha, A. M. Silva, A. M. Sjödin, E. Stice, S. S. Urlacher, G. Valenti, L. M. Van Etten, E. A. Van Mil, J. C. K. Wells, G. Wilson, B. M. Wood, J. A. Yanovski, A. J. Murphy-Alford, C. U. Loechl, A. H. Luke, J. Rood, K. R. Westerterp, W. W. Wong, M. Miyachi, D. A. Schoeller, J. R. Speakman, *Science* **2022**, *378*, 909.

[7] W. B. WHO, UNICEF, *State of the world's drinking water: an urgent call to action to accelerate progress on ensuring safe drinking water for all.*, Geneva: World Health

Organization, **2022**.

[8] Independent Group of Scientists appointed by the Secretary-General, *Global Sustainable Development Report 2023: Times of crisis, time of change: Science for accelerating transformations to sustainable development*, United Nations, New York, **2023**.

[9] A. Sonune, R. Ghate, *Desalination* **2004**, *167*, 55.

[10] T. Rasheed, M. Bilal, F. Nabeel, M. Adeel, H. M. N. Iqbal, *Environmentally-related contaminants of high concern: Potential sources and analytical modalities for detection, quantification, and treatment*, Vol. 122, Pergamon, **2019**, pp. 52–66.

[11] Y. Yang, Y. S. Ok, K.-H. Kim, E. E. Kwon, Y. F. Tsang, *Sci. Total Environ.* **2017**, *596–597*, 303.

[12] D. Yadav, S. Rangabhashiyam, P. Verma, P. Singh, P. Devi, P. Kumar, C. M. Hussain, G. K. Gaurav, K. S. Kumar, *Chemosphere* **2021**, *272*, 129492.

[13] E. E. Mitsika, C. Christophoridis, N. Kouinoglou, N. Lazaridis, C. K. Zacharis, K. Fytianos, *J. Hazard. Mater.* **2021**, *403*, 123819.

[14] S. Wu, Y. H. Hu, *Chem. Eng. J.* **2021**, *409*, 127739.

[15] C. Alberoni, I. Barroso-Martín, A. Infantes-Molina, E. Rodríguez-Castellón, A. Talon, H. Zhao, S. You, A. Vomiero, E. Moretti, *Mater. Chem. Front.* **2021**, *5*, 4138.

[16] B. Mathon, M. Ferreol, M. Coquery, J. M. Choubert, J. M. Chovelon, C. Miège, *J. Hazard. Mater.* **2021**, *407*, 124801.

[17] P. Kay, S. R. Hughes, J. R. Ault, A. E. Ashcroft, L. E. Brown, *Environ. Pollut.* **2017**, *220*, 1447.

[18] B. Kasprzyk-Hordern, R. M. Dinsdale, A. J. Guwy, *Water Res.* **2008**, *42*, 3498.

[19] L. Charuaud, E. Jarde, A. Jaffrezic, M. F. Thomas, B. Le Bot, *Veterinary pharmaceutical residues from natural water to tap water: Sales, occurrence and fate*, Vol. 361, Elsevier, **2019**, pp. 169–186.

[20] H. B. Quesada, A. T. A. Baptista, L. F. Cusioli, D. Seibert, C. de Oliveira Bezerra, R. Bergamasco, *Chemosphere* **2019**, *222*, 766.

[21] J. E. Drewes, *Compr. Anal. Chem.* **2007**, *50*, 427.

[22] L. Feng, E. D. van Hullebusch, M. A. Rodrigo, G. Esposito, M. A. Oturan, *Chem. Eng. J.* **2013**, *228*, 944.

[23] M. I. Vasquez, A. Lambrianides, M. Schneider, K. Kümmerer, D. Fatta-Kassinos, *Environmental side effects of pharmaceutical cocktails: What we know and what we should know*, Vol. 279, Elsevier, **2014**, pp. 169–189.

[24] J. Rivera-Utrilla, M. Sánchez-Polo, M. Á. Ferro-García, G. Prados-Joya, R. Ocampo-Pérez, *Chemosphere* **2013**, *93*, 1268.

[25] World Health Organization (WHO), In *WHO* (Ed.: Rickert, Bettina; Chorus, Ingrid;

Schmoll, O.), World Health Organization, **2016**, p. 196.

[26] J. L. Wilkinson, A. B. A. Boxall, D. W. Kolpin, K. M. Y. Leung, R. W. S. Lai, D. Wong, R. Ntchantcho, J. Pizarro, J. Mart, S. Echeverr, J. Garric, A. Chaumot, P. Gibba, I. Kunchulia, S. Seidensticker, G. Lyberatos, J. M. Morales-salda, H. Kang, *PNAS* **2022**, *119*, 1.

[27] L. Feng, E. D. van Hullebusch, M. A. Rodrigo, G. Esposito, M. A. Oturan, *Chem. Eng. J.* **2013**, *228*, 944.

[28] M. Sgroi, S. A. Snyder, P. Roccaro, *Chemosphere* **2021**, *273*, 128527.

[29] S. G. Zimmermann, M. Wittenwiler, J. Hollender, M. Krauss, C. Ort, H. Siegrist, U. von Gunten, *Water Res.* **2011**, *45*, 605.

[30] J. S. George, A. Ramos, H. J. Shipley, *J. Environ. Chem. Eng.* **2015**, *3*, 969.

[31] I. Michael, Z. Frontistis, D. Fatta-Kassinos, In *Comprehensive Analytical Chemistry*, Elsevier B.V., **2013**, pp. 345–407.

[32] A. Ziylan, N. H. Ince, *J. Hazard. Mater.* **2011**, *187*, 24.

[33] I. Michael, Z. Frontistis, D. Fatta-Kassinos, *Compr. Anal. Chem.* **2013**, *62*, 345.

[34] J. Wang, S. Wang, *Reactive species in advanced oxidation processes: Formation, identification and reaction mechanism*, Vol. 401, Elsevier, **2020**, p. 126158.

[35] D. Ma, H. Yi, C. Lai, X. Liu, X. Huo, Z. An, L. Li, Y. Fu, B. Li, M. Zhang, L. Qin, S. Liu, L. Yang, *Chemosphere* **2021**, *275*, 130104.

[36] A. Abdelhaleem, W. Chu, *Chem. Eng. J.* **2020**, *382*, 122930.

[37] W. Fang, M. Xing, J. Zhang, *J. Photochem. Photobiol. C Photochem. Rev.* **2017**, *32*, 21.

[38] A. Tufail, W. E. Price, F. I. Hai, *Chemosphere* **2020**, *260*, 127460.

[39] Z. Liu, Z. Deng, S. Davis, P. Ciais, *Nat. Rev. Earth Environ.* **2023**, *4*, 205.

[40] IEA, *IEA (2023), CO2 Emissions in 2022*, IEA, Paris, **2022**.

[41] P. Parthasarathy, K. S. Narayanan, *Renew. Energy* **2014**, *66*, 570.

[42] IEA, *Global Hydrogen Review 2022*, OECD, **2022**.

[43] M. Bailera, N. Kezibri, L. M. Romeo, S. Espatolero, P. Lisbona, C. Bouallou, *Int. J. Hydrogen Energy* **2017**, *42*, 13625.

[44] D. G. Nocera, *Acc. Chem. Res.* **2017**, *50*, 616.

[45] S. Anantharaj, S. Noda, *Small* **2020**, *16*.

[46] L. Li, P. Wang, Q. Shao, X. Huang, *Chem. Soc. Rev.* **2020**, *49*, 3072.

[47] L. Liccardo, E. Lushaj, L. Dal Compare, E. Moretti, A. Vomiero, *Small Sci.* **2022**, *2*, 2100104.

[48] G. Colón, *Appl. Catal. A Gen.* **2016**, *518*, 48.

[49] G. A. Artioli, A. Mancini, V. R. Barbieri, M. C. Quattrini, E. Quartarone, M. C. Mozzati, G. Drera, L. Sangaletti, V. Gombac, P. Fornasiero, L. Malavasi, *Langmuir* **2016**, *32*, 1510.

[50] P. Nikolaidis, A. Poullikkas, *A comparative overview of hydrogen production processes*, Vol. 67, Pergamon, **2017**, pp. 597–611.

[51] M. Yasuda, T. Matsumoto, T. Yamashita, *Renew. Sustain. Energy Rev.* **2018**, *81*, 1627.

[52] A. S. Hainer, J. S. Hodgins, V. Sandre, M. Vallieres, A. E. Lanterna, J. C. Scaiano, *ACS Energy Lett.* **2018**, *3*, 542.

[53] J. Schneider, D. W. Bahnemann, *J. Phys. Chem. Lett.* **2013**, *4*, 3479.

[54] F. Costantino, P. V. Kamat, *ACS Energy Lett.* **2022**, *7*, 242.

[55] M. Ashraf, N. Ullah, I. Khan, W. Tremel, S. Ahmad, M. N. Tahir, *Chem. Rev.* **2023**, *123*, 4443.

[56] H. Zhao, J. Liu, N. Zhong, S. Larter, Y. Li, M. G. Kibria, B. L. Su, Z. Chen, J. Hu, *Adv. Energy Mater.* **2023**, *13*.

[57] D. Banerjee, N. Kushwaha, N. P. Shetti, T. M. Aminabhavi, E. Ahmad, *Renew. Sustain. Energy Rev.* **2022**, *167*, 112827.

[58] H. Xu, Y. Jia, Z. Sun, J. Su, Q. S. Liu, Q. Zhou, G. Jiang, *Eco-Environment Heal.* **2022**, *1*, 31.

[59] T. Uekert, F. Dorchies, C. M. Pichler, E. Reisner, *Green Chem.* **2020**, *22*, 3262.

[60] J. M. Coronado, M. D. Hernández-Alonso, *The keys of success: TiO2 as a benchmark photocatalyst*, Vol. 71, **2013**.

[61] N. Serpone, A. V. Emeline, S. Horikoshi, V. N. Kuznetsov, V. K. Ryabchuk, *Photochem. Photobiol. Sci.* **2012**, *11*, 1121.

Chapter 2 – *Fundamentals*

Chapter 2 delves into the fundamentals underlying this research thesis, starting with an exploration of photocatalysis and a detailed examination of the distinctions between homogeneous and heterogeneous photocatalysis. The challenges associated with heterogeneous photocatalysis are further investigated. In the second section, semiconductor materials are comprehensively discussed, with a focus on semiconductor-based photocatalysts, and some key considerations for designing effective photocatalysts are outlined. This chapter sets the stage for the following Chapter 3, providing a solid understanding of the principles guiding the research.

2.1 Principle of photocatalysis

There are many theories on the origin of photocatalysis. What is known is the first use of this term, back in 1910, [1,2] and its genesis, connected to the birth of a more sustainable chemistry. Giacomo Ciamician, *The Father of Photochemistry*, highlighted the emerging energy and environmental problems related to the *modern life and civilization* in his famous lecture "The Photochemistry of the Future" at the VIII International Congress of Applied Chemistry in 1912.[3] Briefly, he highlighted the need to deeply understand photochemical reactions to harness solar energy effectively, anticipating the use of suitable catalysts to convert water and carbon dioxide into oxygen and methane and foreseeing present-day photocatalytic applications.

Photocatalysis as a research field began in the 1970s, as a result of the oil crisis and the emerging concern on water pollution by chemicals. Thus, photocatalysis was proposed as a sustainable way to use and produce new energy sources and to overcome environmental pollution. Later, the same photocatalysts were utilized for a third application in the field of organic syntheses. [2,4–6] This is to further highlight that each photocatalytic application perfectly fits in the field of green and

sustainable chemistry, following the “12 principles of Green-Chemistry” proposed by Paul Anastas and John Warner back in 1990s.

As a general term, photocatalysis refers to any reaction that requires the presence of a catalyst activated by light, except for some reactions such as chain reactions *via* a photogenerated intermediate or photoinitiated thermal reactions and sensitized photochemical reactions.[7] Photocatalytic reactions that involve electron or atom transfer occur only on the lowest potential energy surface at any configuration and in the presence of a catalyst activated by light. In general, catalysts are able to lower the activation barrier of the reaction by creating a more favorable reaction pathway.

Thus, in the presence of a photocatalyst, as shown in **Figure 2.1a**, a new path on the ground state becomes accessible to convert the reagents (R) to the products (P).

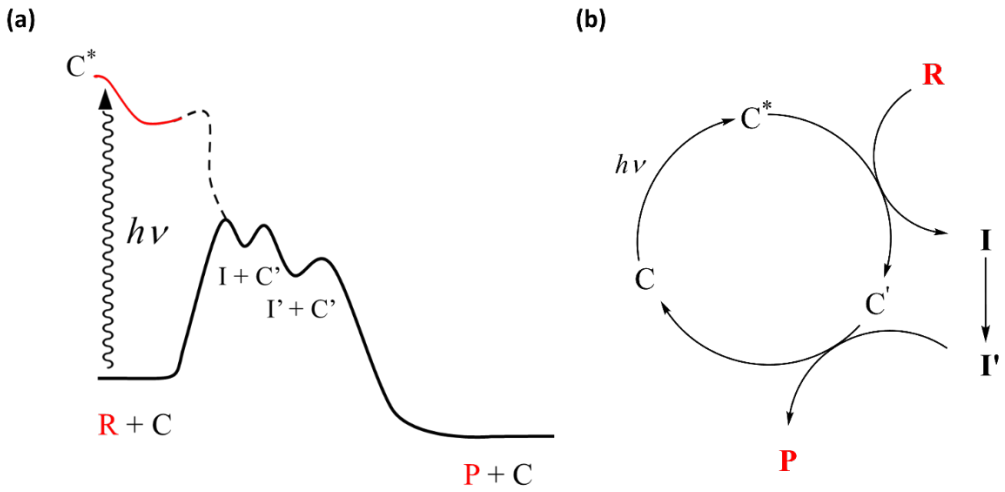

Figure 2.1 (a) Photocatalytic reaction pathway on the ground state after the excitation of the catalyst, **C**, by light and **(b)** scheme of the photocatalyst way of action that leads to the products formation. **I** indicates the intermediate species.

The catalyst (C) absorbs light (hν) and gets excited (C*). While in the excited state, it interacts with the reagents leading to the chemical reaction and the formation of C’. In this step, an intermediate (I), in the form of a radical or radical ion, can be/is simultaneously formed. Finally, C is restored together with the products

formation (**Figure 2.1b**). The overall reaction, as expressed in equation 2.1, is the conversion of R to P after the absorption of light in the presence of C.

$$R \xrightarrow[\text{Catalyst (C)}]{h\nu} P \qquad (2.1)$$

This reaction can be performed using either solid semiconductors, in the heterogeneous photocatalysis, or dissolved molecules or ions, in the homogeneous photocatalysis. In the next two paragraphs, homogeneous and heterogeneous photocatalysis will be compared with a particular focus on the latter and the current challenges in this field.

2.1.1 Homogeneous vs Heterogeneous photocatalysis

As mentioned above, the term photocatalysis derives from the combination of photochemistry and catalysis, thus all the photocatalytic processes depend on the use of a catalyst that can be activated by light. Photocatalysts can be either in homogeneous or heterogeneous phase.

In the homogeneous phase, molecules or ions that are strong reductants (electron donors with vacant orbitals) or strong oxidants (electron acceptors in the Highest Occupied Molecular Orbital, HOMO) can be used as photocatalysts in their excited states, and can be easily involved in electron transfer reactions that promote photoredox reactions (**Figure 2.2a**).[7] A typical example is the use of ruthenium polypyridine complexes, such as the commercial $Ru[(bpy)_3]Cl_2$, for organic synthesis application.[8] Homogeneous photocatalysis can be also based on other mechanisms, for instance atom transfer or ligand dissociation. The most common example is given by the excited state of ketones or soluble inorganic salts, like polyoxometalate salts (e.g., polyoxotungstate $W_{10}O_{32}^{4-}$), where the oxygen atoms can easily become radicals and the extraction of hydrogen from an organic derivative is allowed (**Figure 2.2b)**.[9] Homogeneous catalysts are widely employed in numerous applications, like the wastewater treatment, and particularly the photodegradation of organic pollutants. A typical example is the photo-Fenton process based on

the use of hydrogen peroxide (H_2O_2) and iron(II or III) ions in aqueous media. Briefly, the traditional Fenton process consists in the activation of an iron(II) salt by H_2O_2 and the creation of hydroxyl radicals (HO·) from H_2O_2 decomposition. In the photo-Fenton process, light interacts with the iron complexes, and is the key to accelerate the formation of HO· species, the main responsible for the oxidative capacity of the Fenton reaction. According to the literature, there are several parameters to consider when dealing with the photo-Fenton reaction. [10–13] For instance, the choice of the iron precursor is crucial, even though the photodegradation efficiency is independent of the use of ferric or ferrous ions.[10,11] Additionally, the overall pollutant mineralization is highly influenced by water pH, temperature of the system, and the presence of other inorganic anions (*i.e.*, Cl^- and SO_4^{2-}) in the water medium. The photo-Fenton process is effective only at low pH (⌣3) and requires high operating costs (*e.g.*, catalyst synthesis and UV source). [13] When dealing with homogeneous catalysts, other aspects to take into account are the separation and recovery of the catalysts from the slurry system. These steps are usually very hard and lower the interest of these processes for large-scale application. [14]
To overcome the main issues of traditional photo-Fenton reaction, including the low working pH, the generation of iron sludge and high operating costs, heterogeneous Fenton-like processes have been widely investigated. Particularly, the main goal in this field is the development of visible light-driven heterogeneous photocatalysts that are easy to synthesize and able to give the cycling oxidation/reduction of iron ions (Fe^{2+}/Fe^{3+}) to enable the overall photocatalytic reaction. [15–17]
A way to solve the described issues is to move toward the use of heterogeneous catalysts that are structurally much more complex than their homogeneous counterparts, which are usually composed by a metal center and its ligand sphere. Heterogeneous catalysts are solid compounds with 3D structures and several surface structural properties, such as high surface-to-volume ratios and a significant number of catalytic active sites.[18] Semiconductor materials are generally used as photocatalysts. Their interaction with light can produce the formation of electron-hole pairs (e^- - h^+), also known as excitons (*i.e.*, an electron–hole pair held together by

Coulomb interactions). Excitons can reach the surface of the photocatalysts that can initiate the redox reactions with substrates adsorbed on the catalyst surface (**Figure 2.2c**).

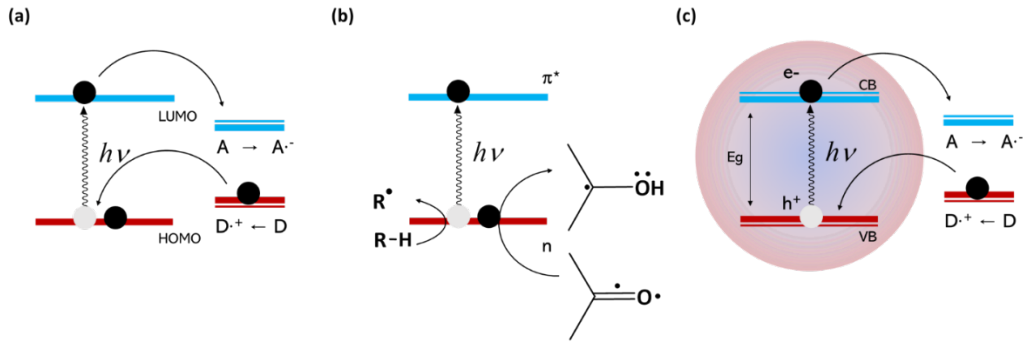

Figure 2.2 **(a)** Homogeneous photocatalyst activated by light and its interaction with donor (D) and acceptor (A) species by electron transfer; **(b)** Example of atom transfer (in this case H abstraction) in the homogeneous phase; **(c)** Heterogeneous photocatalyst activated by light and its interaction with donor and acceptor species by electron transfer.

However, there are some limitations concerning this short-living phenomena[7] and the efficiency of redox processes, which strongly depends on the properties of the catalyst itself. Moreover, even for heterogeneous photocatalysis, the overall photocatalytic process can be influenced by numerous operating parameters; the most important are the catalyst loading, the solution pH, the irradiation source intensity, and the exposure time. [18] Another feature to consider concerns the recovery and the reusability of the photocatalysts, which is extremely important for a future sustainable large-scale application. For what it concerns heterogeneous photocatalysis, there are many promising strategies that can be followed. For instance, the recovery of heterogeneous catalysts can be easily achieved either by immobilizing them on a support (*i.e.*, creating thin films) or by using membrane filtration integrated processes. [19–22] Even in this case, there are advantages and drawbacks affecting the overall efficiency of the photocatalytic application. When dealing with membranes, properties such as pore size or membrane regeneration should

indeed be considered. On the other hand, when the catalyst is immobilized on a support, the mass transfer limits, and additional technical and operating costs should be evaluated.

Since the aim of this thesis was the design of heterogeneous photocatalysts, further details on this topic will be given in the following section.

2.1.2 Heterogeneous photocatalysis and related challenges

As widely stated before (see sections above and Chapter 1), heterogeneous photocatalysis is a wide field comprising several catalytic reactions for different applications, including AOPs for water remediation and organic molecules photoreforming reaction for hydrogen production.

In general, the mechanism of action of a typical heterogeneous photocatalyst (from now on referred to as photocatalyst) involves photoredox reactions on the surface of a semiconductor material in aqueous media and it does not usually require any additional reagents.[23] As shown in **Figure 2.3a**, each photocatalytic reaction is initiated by the interaction of a semiconductor catalyst with light. As will be discussed in *Section 2.2*, the peculiarity of a semiconductor material lies in its bandgap, a small energy gap between the valence and conduction bands, allowing it to exhibit electrical conductivity by applying external stimuli. Thus, if the photon energy is equal to or higher than the bandgap energy (Eg) of the photocatalyst, it leads to charge carrier separation and specifically to e^- - h^+ pairs generation in the bulk phase.[18] The creation and migration of excitons from the bulk phase to the surface are crucial steps. In general, the higher the production of excitons is, the higher the photocatalytic activity is, and any fast charge carriers recombination process should be avoided or delayed.[24] In fact, excited electrons are strong reductants, while holes are powerful oxidants. Hence, photogenerated e^- - h^+ pairs can drive redox reactions with available reactants in the surface proximity, and the overall photocatalytic efficiency depends on the redox potentials and band edge of the target substrate in relationship with those of semiconductor

photocatalysts.[25] In detail, the substrate redox potential should be located in between the valence band (VB) and conduction band (CB) potentials of the photocatalyst.

Besides the photocatalyst activation by light, the whole mechanism of heterogeneous photocatalysis also relies on the efficient electron transfer between the photocatalyst and the reactant, and its transport through the bulk solution. Thus, the overall process can be explained by the following steps (**Figure 2.3b,c**): (1) transport of the reactants through the bulk solution to the boundary layer (*i.e.*, in proximity of the catalyst surface); (2) diffusion of the reactants through the boundary layer; (3) diffusion and (photo)adsorption of reactants on the active catalytic site; (4) surface photocatalytic reactions; (5) desorption of the products by diffusion through the boundary layer and back transport to the solution.[18,26]

It is worth recalling that step 1 and back transport in step 5 are physical steps, and they may be easily influenced and tuned by changing the fluid dynamics. On the contrary, step 3 and desorption of the products in step 5 exclusively depend on textural and surface properties of the photocatalyst. In fact, active sites on the catalyst surface have a key role in directing the reaction toward the products formation following the desired pathway. Hence, surface electronic and structural properties, as well as morphology, are extremely important when designing an efficient photocatalyst (see paragraph 2.2.2).

In the heterogeneous photocatalysis, there are some differences between adsorption and photoadsorption.[26] Generally, adsorption is classified as physical and chemical adsorption. Physical adsorption, also known as physisorption, occurs when molecules bind to the adsorbent surface through weak interactions like electrostatic interactions or Van Der Waals forces. It is a fast process where activation energy is not required. On the contrary, when dealing with chemical adsorption or chemisorption, strong chemical bonds between molecules and the adsorbent surface, such as covalent bonds, are formed. Furthermore, it is a slow process where high activation energy is required.[27–30] The high activation energy can decrease by using light, thus giving rise to photoadsorption. Photoadsorption can be typically

defined as chemisorption initiated by ultraviolet (UV), visible (Vis) or infrared (IR) light irradiation absorbed either by molecules adsorbed on the surface of the photocatalyst or the photocatalyst itself. Thus, surface active sites on a photocatalyst can also be considered as photoadsorption centers, along with defective sites activated after the photoexcitation step.[26]

Photoadsorption can also be seen as the first chemical step in a heterogeneous photocatalytic reaction, crucial for the overall photocatalytic process. Thermodynamically unfavorable reactions can then occur thanks to the extra energy supplied in the form of photons, and photocatalysis kinetics simultaneously sped up. [18,31]

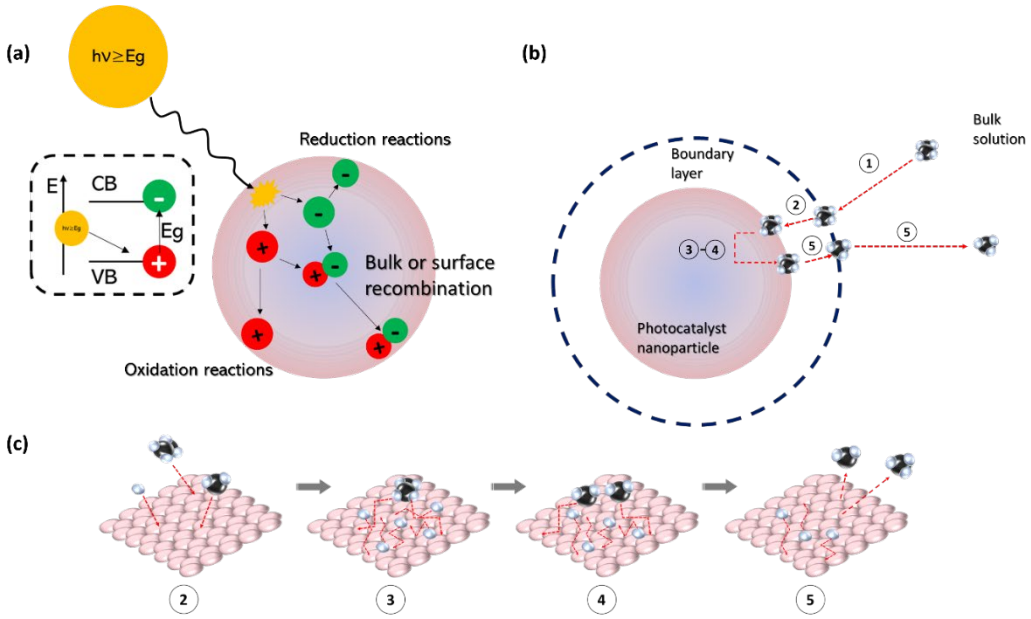

Figure 2.3 (a) Interaction with light and schematic representation of charge carriers creation and migration; **(b)** Schematic representation of a hypothetical catalytic process taking place on a photocatalyst nanoparticle; **(c)** Steps 2-5 of the hypothetical catalytic process shown in figure 2.3b.

The activation of the photocatalyst by light and the adsorption/desorption of substrates on the catalyst surface are only a few factors affecting the overall photocatalytic reaction. As stated in the previous paragraph, there are several important operating parameters to consider when dealing with heterogeneous photocatalysis.[18,26] The most relevant are listed below.

- Photocatalyst loading

The amount of photocatalyst for a given photocatalytic reaction is extremely important. An increase in the amount of photocatalyst does not always lead to improvement in photocatalytic activity, thus the optimum photocatalyst concentration needs to be accurately determined. When dealing with powder photocatalysts, if the amount exceeds the saturation level, light photon absorption coefficient usually decreases radially.[32] Furthermore, light scattering negatively affects photon utilization, which reduces the surface area of the photocatalysts being irradiated and the overall photocatalytic efficiency.[33] This is not the case of systems with immobilized photocatalysts on a support, where the light scattering phenomena is less important.[34] However, even in this case, the catalyst amount or better the total surface of the immobilized catalyst exposed to the light irradiation should be considered. In general, for a given conversion, a larger irradiated surface area is required due to lower surface-to-volume ratio.[35]

- Irradiation source wavelength, intensity, and time

  The reaction rate varies as a function of the incident light wavelength, and it depends on the absorption capability of the photocatalyst, and hence on its bandgap energy structure.[36,37] For instance, the most widely studied photocatalyst, pure titania (TiO_2), shows a wide bandgap (3.0-3.2 eV) and it can be activated only under UV light, thus high photon energy is required.[38] The apparent rate constant of a given photocatalytic reaction also depends on the incident light intensity,[39] which influences charge carriers generation and separation. In fact, at moderately high intensity (≥ 20mW·cm^{-2}), a larger number of photons can reach the photocatalyst surface, thus a larger number of active sites is created and the charge carriers separation competes with their recombination (*i.e.*, higher number of e^- - h^+ pairs generation).[40] However, reaction rate and light intensity do not always follow a linear trend, and optical losses or the presence of fully saturated active sites that limit the mass transport for both adsorption and

desorption should be considered.[36] Another important parameter is the irradiation source time. A typical example is the photocatalytic pollutant removal reaction, directly proportional to the irradiation time, where the degradation efficiency ends beyond a certain time.[41]

- System pH

  The pH of the system highly affects some important properties of the photocatalyst, including charge surface, size of the aggregates (for powder photocatalysts) and position of both VB and CB.[42] For instance, considering the point of zero charge (PZC) of a photocatalyst, *i.e.*, the point at which for a given pH the surface charge is zero and the electrostatic interactions are almost zero, if the operating pH is lower than PZC, the surface will be positively charged. Thereby, electrostatic attraction toward negatively charged compounds, unlike positively charged compounds, will increase, consequently affecting the overall adsorption process onto the photocatalyst surface. [43]

- Temperature of the system

  In general, an increase in the reaction temperature may decrease the activation energy barrier leading to increased photocatalytic activity.[44,45] However, this is a crucial parameter to control because it may influence both the photocatalyst and the reactant properties.[46,47] Too high temperatures may indeed lead to fast charge carriers recombination processes or a decrease in the adsorption of reactants onto the photocatalyst surface.[48] Moreover, from the green chemistry point of view and towards sustainable solutions, the optimal and most environmentally friendly condition is to conduct the photocatalytic reaction at room temperature. Consequently, the optimal reaction temperature should be accurately selected.

- Dissolved oxygen

Dissolved oxygen plays a role as active species during the photocatalytic reaction. It is indeed an efficient scavenger able to trap CB electrons from the photocatalyst surface. Thus, the photooxidation reactions are favored compared to photoreduction ones.[49] Based on the reaction type, dissolved oxygen can enhance or not the overall photocatalytic efficiency. For example, in the organic pollutants photodegradation, dissolved oxygen may accelerate the overall photooxidation reaction acting not only as electrons scavenger but also being involved in other reactive oxygen species (ROS) formation, radical intermediates stabilization and finally favoring the overall pollutants mineralization.[50] On the contrary, in photocatalytic reactions involving photoreduction reactions, such as H_2 production in photoreforming , higher dissolved oxygen concentrations may lower the overall hydrogen production rate.

Therefore, for large-scale applications, some challenges still need to be addressed and the research in this field has been mainly focused on two branches: the design of efficient solar-light-driven and easily recoverable photocatalysts, and the engineering of photoreactors that should ideally be energy-efficient, cost-effective and able to handle large volumes.[33] Briefly, the scaling-up of photoreactors has been limited by two main issues regarding the photocatalyst loading and coating, and the light distribution inside the reactor.[51] The immobilization of the photocatalyst on a support is indeed important to eliminate post-treatment processes, enabling the photocatalyst recovery. However, the overall photocatalytic process efficiency is negatively affected by the reduction of the surface-to-volume ratio (*i.e.*, reducing active sites), light reflections and enlargement of mass transfer limitation.[51–53] Consequently, new active photocatalysts, photocatalytic surfaces and technologies should be investigated.

2.2 Semiconductor materials

Since semiconductor-based photocatalysts have been considered the most promising materials thanks to their efficiency and potential in photocatalytic applications, heterogeneous photocatalysis generally refers to the use of semiconductor materials or nanomaterials in aqueous solution.

As already stated in the previous paragraph, it is essential to design efficient photocatalysts able to exploit solar light by simultaneously considering their activity, stability, selectivity, and recoverability. In this frame, the optical, electronic, and structural properties of the material, as well as other related features such as morphology and surface properties, have to be carefully investigated.

Starting from the basic principles of semiconductor materials, it is extremely useful to provide a deep understanding of photocatalysis and to predict novel materials with superior performances. Thus, the aim of this paragraph is to give a general overview on semiconductor materials applied in heterogeneous photocatalysis, highlighting the fundamentals, and discussing recent advances.

2.2.1 Semiconductor-based photocatalysts

In general, solid materials can be classified as non-conducting (or insulating), semiconducting, and conducting materials. Semiconductors are the class in-between insulating and conducting materials, thus being optically active and conductive with tunable electrical and optical properties.
In terms of energy, a crystal is formed by energy bands, which can either overlap or be separated by energy gaps. According to the band theory, VB is generated by HOMOs while CB by LUMOs (**Figure 2.4a**).

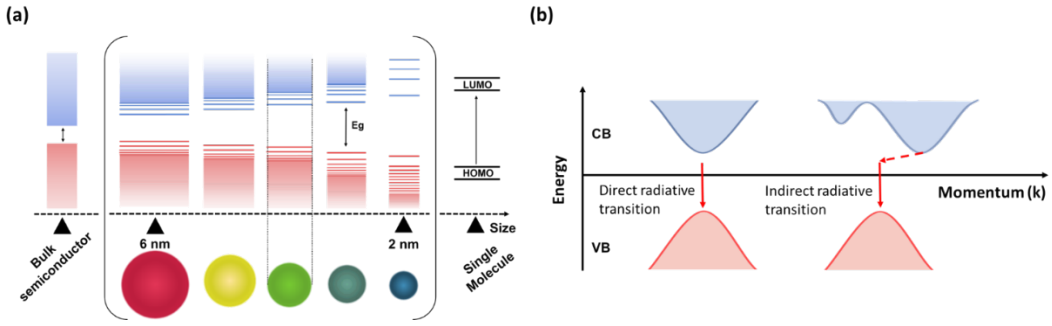

Figure 2.4 (a) Schematic representation of bandgaps' energy of semiconductor materials in comparison with single molecules' HOMO and LUMO. Focus on the size and creation of discrete energy levels at band-edges. **(b)** Inter-band transition of direct and indirect semiconductors.

While conducting materials do not show a gap between VB and CB (*i.e.,* energy bandgap is 0 eV), the only difference between insulators and semiconductors lies precisely in their bandgap values. Unlike non-conducting materials with energy bandgap values higher than 5 eV, the peculiarity of semiconductors is to possess an energy bandgap (Eg) between VB and CB in the range 1-4 eV.[54] Consequently, an electron can be excited to upper levels, gaining an energy equal to or higher than the Eg. In this process, known as electrical conductivity, when an electron absorbs the appropriate energy, for example, in the form of photons, it is promoted from the VB to the CB, leaving a hole in the VB. At this point, an exciton is formed. In a simplistic view as in the case of molecules, photon absorption is dictated by selection rules where only transitions with no change in momentum are allowed. Thus, for semiconductors, the radiative process should conserve the electron momentum described by the quantum number, *k*. Briefly, the band structures of semiconductor materials are defined by a wavefunction called Bloch function, where the energy is expressed as a function of *k*. Based on the values of the electron momentum, *k*, semiconductor materials can be defined as direct or indirect.[55] When the minimum of the CB and the maximum of the VB show the same k values, the semiconductors are referred to as direct, while if they are characterized by different k values, the semiconductors are indirect (**Figure 2.4b**). This is important when dealing with radiative processes probabilities, which are high for direct

semiconductors, while much lower for indirect semiconductors. This usually makes the latter good photocatalysts.

As described in the previous section, the generation and transfer of e^-—h^+ pairs provide the basis for heterogeneous photocatalysis, as long as the charge carriers transfer occurs in a continuous and exothermic way, without impacting on the semiconductor structure. After their creation, photogenerated e^-—h^+ pairs can undergo different pathways. They can migrate onto the semiconductor surface or recombine in the bulk phase. If they reach the surface of the material, they can be both transferred and de-excited by surface recombination processes. The back transfer process from adsorbed species to the photocatalyst surface can also take place. [54–56] Hence, it is evident that improved charge carriers separation efficiency and inhibition of any kind of charge carriers recombination processes (both radiative and non-radiative) are essential to boost the photocatalytic activity of semiconductor materials.

Several strategies, like the optimization of particle size to enhance the surface-to-volume ratio (*i.e.*, nanostructured systems), surface engineering and coupling semiconductors with different electronic energy levels, have been widely investigated in literature.[57–60] Further details on this topic will be given in the following section.

2.2.2 Design of a good photocatalyst

Photocatalytic water splitting for H_2 production and organic pollutants photodegradation are considered as promising approaches to overcome some of the most critical energy and environmental issues. However, some challenges in the field of heterogeneous photocatalysis still need to be addressed. [57,59,60] Working on the design of a good semiconductor photocatalyst means that some features need to be fulfilled, and they can be summarized as follows:

(i) The bandgap energy should be lower than ∼3 eV to exploit a wider portion of solar light energy.

(ii) The recombination rates of photogenerated charge carriers should be delayed, thus their separation efficiency should be optimized by working on the mobility and number of surface-active sites.

(iii) The alignment of both VB and CB referred to water reduction and oxidation potentials should be appropriately selected when dealing with WS or organic molecules photoreforming.

(iv) Photostability, availability and non-toxicity should finally be considered.

TiO_2 is considered an ideal semiconductor photocatalyst thanks to its excellent properties such as non-toxicity, highly negative reduction potentials, high stability, sustainability, relatively ease of synthesis and low cost. Thus, after being employed as photocatalyst for the first time in the PEC WS by Fujishima and Honda in 1972,[5] several research on the use of metal oxides, oxynitride, sulfides and other species have been reported.[60] The most commonly used and studied photoactive materials are reported with the corresponding Eg in **Figure 2.5**.

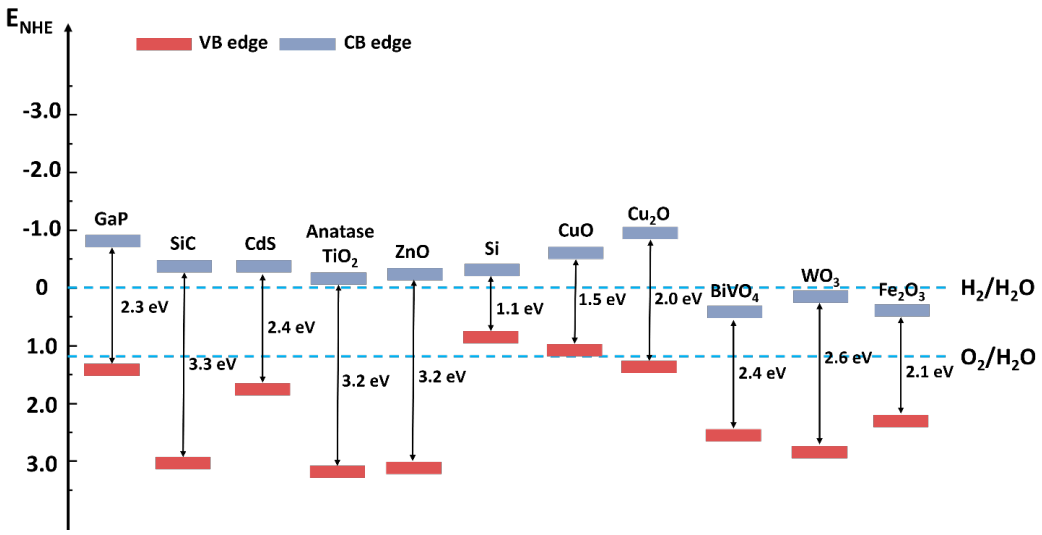

Figure 2.5 Energy bandgaps of commonly used semiconductors at pH zero with reference to water redox potential of 1.23 eV *vs* normal hydrogen electrode (NHE).

Due to the high number of features to be fulfilled, the search for new efficient photocatalysts with solar light-driven performance is still ongoing. As a result,

several strategies including doping, surface engineering and semiconductor composite systems, have been developed. These aspects will be deeply discussed from chapter 4 to 6 by focusing not only on the fundamentals of each approach, but also on the experimental results shown in this thesis.

2.3 References

[1] J. M. Coronado, M. D. Hernández-Alonso, *The keys of success: TiO_2 as a benchmark photocatalyst*, Vol. 71, **2013**.

[2] N. Serpone, A. V. Emeline, S. Horikoshi, V. N. Kuznetsov, V. K. Ryabchuk, *Photochem. Photobiol. Sci.* **2012**, *11*, 1121.

[3] G. Ciamician, *Science* **1912**, *XXXVI*, 926.

[4] J. A. Turner, *Science* **2004**, *305*, 972.

[5] A. Fujishima, K. Honda, *Nature* **1972**, *238*, 37.

[6] M. Fagnoni, D. Dondi, D. Ravelli, A. Albini, *Chem. Rev.* **2007**, *107*, 2725.

[7] D. Ravelli, D. Dondi, M. Fagnoni, A. Albini, *Chem. Soc. Rev.* **2009**, *38*, 1999.

[8] N. Hoffmann, *ChemSusChem* **2012**, *5*, 352.

[9] S. S. Wang, G. Y. Yang, *Chem. Rev.* **2015**, *115*, 4893.

[10] M. I. Polo-López, S. Nahim-Granados, P. Fernández-Ibáñez, in *Applications of Advanced Oxidation Processes (AOPs) in Drinking Water Treatment. The Handbook of Environmental Chemistry.* (Eds.: A. Gil, L. Galeano, M. Vicente), Springer, **2018**, pp. 155–177.

[11] P. Villegas- Guzman, S. Giannakis, S. Rtimi, D. Grandjean, M. Bensimon, L. F. de Alencastro, R. Torres-Palma, C. Pulgarin, *Appl. Catal. B Environ.* **2017**, *219*, 538.

[12] L. Ioannou-Ttofa, S. Raj, H. Prakash, D. Fatta-Kassinos, *Chem. Eng. J.* **2019**, *355*, 91.

[13] A. V. Vorontsov, *J. Hazard. Mater.* **2019**, *372*, 103.

[14] B. Jain, A. K. Singh, H. Kim, E. Lichtfouse, V. K. Sharma, *Environ. Chem. Lett.* **2018**, *16*, 947.

[15] Q. Wang, P. Wang, P. Xu, Y. Li, J. Duan, G. Zhang, L. Hu, X. Wang, W. Zhang, *Appl. Catal. B Environ.* **2020**, *266*, 118653.

[16] A. E. Paiva, J. Paul Guin, J. F. B. Vasquez, K. R. Thampi, J. A. Sullivan, F. G. L. M. Borsagli, M. A. Morris, *Chem. Eng. J.* **2023**, *466*, 142925.

[17] T. Mohapatra, M. Agrawal, P. Ghosh, *Chem. Eng. J.* **2023**, *477*, 146941.

[18] M. J. Muñoz-Batista, R. Luque, *ChemEngineering* **2021**, *5*, 26.

[19] J. Gómez-Pastora, S. Dominguez, E. Bringas, M. J. Rivero, I. Ortiz, D. D. Dionysiou, *Chem. Eng. J.* **2017**, *310*, 407.

[20] M. A. Mohd Adnan, B. L. PHOON, N. Muhd Julkapli, *J. Clean. Prod.* **2020**, *261*, 121190.

[21] A. Balakrishnan, M. Chinthala, *Chemosphere* **2022**, *297*, 134190.

[22] Y. Xue, M. Kamali, X. Zhang, N. Askari, C. De Preter, L. Appels, R. Dewil, *Environ.*

Pollut. **2023**, *316*, 120549.

[23] J. W. Verhoeven, *Pure Appl. Chem.* **1996**, *68*, 2223.

[24] H. Zhang, G. Chen, D. W. Bahnemann, *J. Mater. Chem.* **2009**, *19*, 5089.

[25] X. Li, J. Yu, M. Jaroniec, *Hierarchical photocatalysts*, Vol. 45, The Royal Society of Chemistry, **2016**, pp. 2603–2636.

[26] V. Augugliaro, G. Palmisano, L. Palmisano, J. Soria, In *Heterogeneous Photocatalysis*, Elsevier, **2019**, pp. 1–24.

[27] B. S. Rathi, P. S. Kumar, *Environ. Pollut.* **2021**, *280*, 116995.

[28] D. Han, J. E, Y. Deng, J. Chen, E. Leng, G. Liao, X. Zhao, C. Feng, F. Zhang, *Renew. Sustain. Energy Rev.* **2021**, *135*, 110079.

[29] N. V Tran, A. K. Tieu, H. Zhu, H. T. T. Ta, T. D. Ta, H. M. Le, *J. Phys. Chem. C* **2018**, *122*, 20827.

[30] A. Dąbrowski, *Adv. Colloid Interface Sci.* **2001**, *93*, 135.

[31] J. Zhang, B. Tian, L. Wang, M. Xing, J. Lei, **2018**, pp. 1–15.

[32] B. Bajorowicz, M. P. Kobylański, A. Malankowska, P. Mazierski, J. Nadolna, A. Pieczyńska, A. Zaleska-Medynska, *Application of metal oxide-based photocatalysis*, **2018**.

[33] C. McCullagh, N. Skillen, M. Adams, P. K. J. Robertson, *J. Chem. Technol. Biotechnol.* **2011**, *86*, 1002.

[34] I. Dundar, A. Mere, V. Mikli, M. Krunks, I. O. Acik, *Catalysts* **2020**, *10*, 1.

[35] R. Saravanan, F. Gracia, A. Stephen, In *Nanocomposites for Visible Light-induced Photocatalysis* (Eds.: Khan Mohammad Mansoob; and Pradhan, D.; Youngku, and S.), Springer International Publishing, Cham, **2017**, pp. 19–40.

[36] A. Visan, J. R. van Ommen, M. T. Kreutzer, R. G. H. Lammertink, *Ind. Eng. Chem. Res.* **2019**, *58*, 5349.

[37] K. Takanabe, *ACS Catal.* **2017**, *7*, 8006.

[38] Q. Guo, C. Zhou, Z. Ma, X. Yang, *Adv. Mater.* **2019**, *31,* 1901997.

[39] O. Sacco, V. Vaiano, D. Sannino, *J. Chem. Technol. Biotechnol.* **2020**, *95*, 2608.

[40] R. Yanagi, T. Zhao, D. Solanki, Z. Pan, S. Hu, *ACS Energy Lett.* **2022**, *7*, 432.

[41] I. Khan, K. Saeed, N. Ali, I. Khan, B. Zhang, M. Sadiq, *J. Environ. Chem. Eng.* **2020**, *8*, 104364.

[42] S.-L. Chiam, S.-Y. Pung, F.-Y. Yeoh, *Environ. Sci. Pollut. Res.* **2020**, *27*, 5759.

[43] F. Perreault, A. de Faria, M. Elimelech, *Chem. Soc. Rev.* **2015**, *44*, 5861.

[44] U. Caudillo-Flores, G. Agostini, C. Marini, A. Kubacka, M. Fernández-García, *Appl. Catal. B Environ.* **2019**, *256*, 117790.

[45] F. Platero, A. Caballero, G. Colón, *Appl. Catal. A Gen.* **2022**, *643*, 118804.

[46] V. Nair, M. J. Muñoz-Batista, M. Fernández-García, R. Luque, J. C. Colmenares, *ChemSusChem* **2019**, *12*, 2098.

[47] F. Platero, A. López-Martín, A. Caballero, G. Colón, *ChemCatChem* **2021**, *13*, 3878.

[48] Z. Wang, Z. Yang, R. Fang, Y. Yan, J. Ran, L. Zhang, *Chem. Eng. J.* **2022**, *429*, 132322.

[49] T. Hirakawa, C. Koga, N. Negishi, K. Takeuchi, S. Matsuzawa, *Appl. Catal. B Environ.* **2009**, *87*, 46.

[50] I. García-Fernández, I. Fernández-Calderero, M. Inmaculada Polo-López, P. Fernández-Ibáñez, *Catal. Today* **2015**, *240*, 30.

[51] O. Sacco, V. Vaiano, D. Sannino, *J. Chem. Technol. Biotechnol.* **2020**, *95*, 2608.

[52] R. Molinari, C. Lavorato, P. Argurio, K. Szymański, D. Darowna, S. Mozia, *Catalysts* **2019**, *9*, 239.

[53] O. M. Alfano, D. Bahnemann, A. E. Cassano, R. Dillert, R. Goslich, *Catal. Today* **2000**, *58*, 199.

[54] V. Balzani, P. Ceroni, A. Juris, *Angew. Chemie Int. Ed.* **2014**, *53*, 8817.

[55] J. M. Coronado, F. Fresno, M. D. Hernández-Alonso, R. Portela, *Design of Advanced Photocatalytic Materials for Energy and Environmental Applications*, Springer London, **2013**.

[56] F. X. Xiao, J. Miao, H. B. Tao, S. F. Hung, H. Y. Wang, H. Bin Yang, J. Chen, R. Chen, B. Liu, *Small* **2015**, *11*, 2115.

[57] C. Xu, P. Ravi Anusuyadevi, C. Aymonier, R. Luque, S. Marre, *Chem. Soc. Rev.* **2019**, *48*, 3868.

[58] O. Savateev, *Adv. Energy Mater.* **2022**, *12*, 2200352.

[59] F. F. Wang, Q. Li, D. S. Xu, *Adv. Energy Mater.* **2017**, *7*, 1.

[60] F. Opoku, K. K. Govender, C. G. C. E. van Sittert, P. P. Govender, *Adv. Sustain. Syst.* **2017**, *1*, 1.

Chapter 3 – *Titanium dioxide*

This chapter focuses on titanium dioxide (TiO_2) as ideal photocatalyst, starting with an introduction to its significance in the field. The properties of TiO_2 are meticulously explored, delving into the morphology, crystalline structure, optical and electronic properties, as well as the charge dynamics and photocatalytic activity. Additionally, the limitations of TiO_2 are addressed, paving the way for a critical examination of strategies to extend its capabilities and overcome inherent constraints.

3.1 Introduction on TiO_2

Titanium dioxide (TiO_2), known as titania, is a widely studied and used semiconductor[1] with applications spanning from heterojunction solar cells,[2–4] electrochromic devices,[5,6] or chemo-resistive gas sensors.[7] Since the pioneering work by Fujishima and Honda[8] or Schrauzer and Guth,[9] TiO_2 has emerged in the field of photocatalysis as a promising photoactive material for energy and environmental remediation applications.[10] As anticipated in **Chapter 2**, many efforts have been made to design a good photocatalyst, and several semiconductor materials, such as WO_3, CdS, $SrTiO_3$, $AgPO_4$, C_3N_4, Metal Organic Frameworks (MOFs) and MXenes, have been investigated. However, TiO_2-based photocatalysts remain the best candidate in this field thanks to their exceptional properties, including high photocatalytic activity, excellent structural stability, low cost, low toxicity, and versatile applications.[10] **Figure 3.1** shows the exponential growth in the number of published articles concerning TiO_2 used as photocatalyst for environmental- and energy-related applications since 1972. This highlights the constant importance of TiO_2 materials in the field of photocatalysis.

This chapter aims to elucidate the distinctive and intrinsic properties of TiO_2 that, despite its well-known drawbacks, make it the currently benchmark and ideal

candidate for many photocatalytic processes. Furthermore, strategies to overcome TiO_2 limits, including its wide bandgap and rapid charge carriers recombination, will be explored. In detail, doping with transition metals, surface modification and homo- and hetero-junctions creation will be further discussed in this chapter.

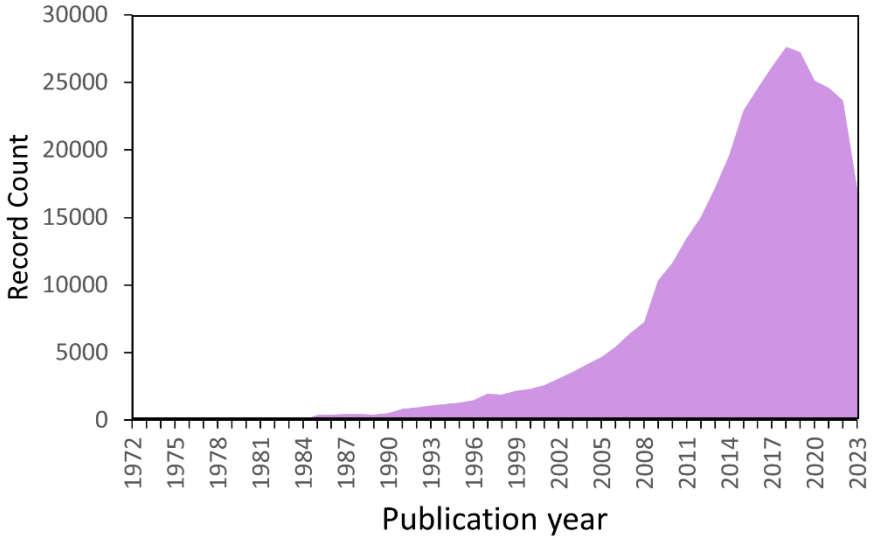

Figure 3.1 Trends in the number of publications in research areas concerning environmental and energy applications of TiO_2 since 1972. Data reproduced from Web of Science (key words: TiO_2, environmental applications, energy applications, life sciences).

3.2 Properties of TiO_2 as an ideal photocatalysts

Thanks to its unique physicochemical properties, TiO_2 has gained attention in the field of heterogeneous photocatalysis. Since bandgap, crystal structure, surface properties and charge carriers dynamics play a pivotal role in the photocatalytic activity of a semiconductor material. The goal of section 3.1 is thus to provide an in-depth analysis of the fundamental properties that make TiO_2 a highly efficient photocatalyst for environmental and energy-related applications.

3.2.1 Morphology and crystal structure

TiO_2 can be found in nature in 3 different polymorphs or crystalline phases, namely anatase, rutile and brookite. All these phases are generally composed of TiO_6

octahedra (*i.e.*, Ti^{4+} coordinated to six O^{2-}) containing Ti-O bonds in different arrangements.[1,10,11] In detail, the anatase phase consists of octahedra where each vertex is shared, shaping a tetragonal structure (**Figure 3.2a**). The tetragonal structure is also present in the rutile phase but, in this case, it involves octahedra sharing edges at (001) planes (**Figure 3.2b**). Whereas, in the brookite phase, both edges and vertices are shared, leading to the formation of an orthorhombic structure (**Figure 3.2c**).

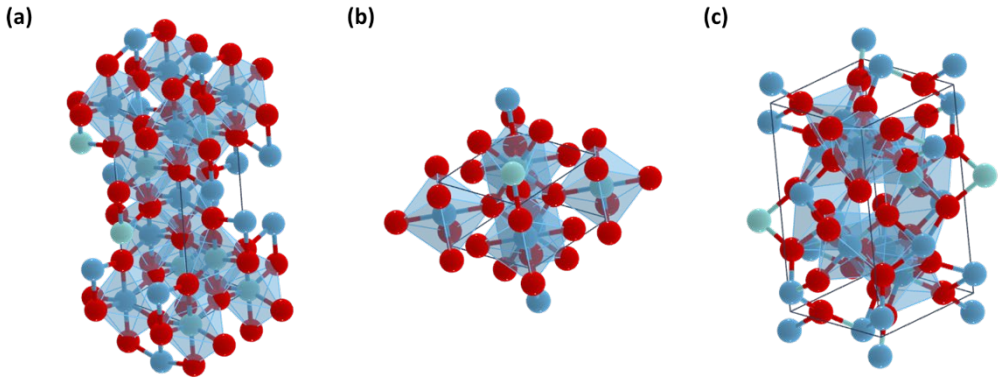

Figure 3.2 Crystal structures of TiO_2 in **(a)** anatase; **(b)** rutile and **(c)** brookite phase. Ti^{4+} is represented in blue and O^{2-} in red.

Since the characteristics of Ti-O bonds play a key role in determining the structural, optical, and electronic properties of each TiO_2 structural phase, the main crystalline and physical parameters are summarized in **Table 3.1**.[11,12]

Among all the 3 phases, rutile is the most thermodynamically stable, while both anatase and brookite are metastable, thus when increasing the temperature above 600°C there is an irreversible transition into rutile phase.[13] However, when dealing with crystals in the range of 8-10 nm brookite and anatase get more stable.

Thanks to their peculiar properties, rutile, anatase and brookite have been widely investigated for different fields of application. Particularly, in the research area of heterogeneous photocatalysis for solar energy applications (i.e., photocatalytic WS, pollutants degradation and biomass conversion), rutile and anatase were found to be the most promising.[14–18] Anatase phase is known for its higher photo-

reactivity[19] compared to the rutile phase due to its larger surface area thanks to smaller grain size, which results in a higher number of active sites attributed to its exposed (001) planes and a higher surface adsorption capacity for H_2O, O_2 and OH groups.[1]

Table 3.1 Crystal structure parameters of TiO_2. Data reproduced from ref. 11,12.

	Anatase	**Rutile**	**Brookite**
Crystal structure	Tetragonal	Tetragonal	Orthorombic
Lattice constant (Å)	a = 3.784 c = 9.515	a = 4.593 c = 2.958	a = 9.184 b = 5.447 c = 5.154
Space group	$I4_1/amd$	$P4_2/mnm$	Pbca
Symmetry	D_{4h}^{19}	D_{4h}^{14}	D_{2h}^{15}
Molecule/Cell	4	2	8
Volume/Molecule (Å^3)	34.061	31.216	31.172
Density (g·cm^{-3})	3.79	4.13	3.99

Furthermore, the presence of a higher concentration of oxygen vacancies (*i.e.,* oxygen vacant sites in the crystal lattice) leads to an enhanced charge-carriers separation efficiency.[15,20,21] In addition, nanocrystalline anatase phase particles are more stable. [1,19] Decreasing the particle size below ~15 nm typically induces a phase transformation from rutile to anatase phase, which becomes thermodynamically stable.[1,11,22] So far, the research has been focused on mixed-phase titania nanomaterials. Mixed-phase structures, combining both anatase and rutile with a proper composition ratio, often show synergistic effects, exploiting the advantages of both phases to boost the overall photocatalytic activity.[20,23,24] A typical example is given by the commercial TiO_2 P25, containing a mixed phase in a ratio of 3:1 between anatase and rutile. This is widely used as standard material in the field of photocatalytic reactions for its high photocatalytic activity.[25] Several studies have been conducted to fully explain these effects, and numerous efforts have been

made to investigate the interface between the two phases.[26] As stated above, anatase and rutile phases show different structure and distances due to different arrangements of Ti and O atoms. When the two phases are coupled together, the expansion of their lattice leads to a variation in the atoms' arrangement, affecting the overall Ti—O bond length.[23] Thus, in the mixed-phase (or heterophase) junction interface, the creation of defects, such as oxygen vacancies, may result in changes of electronic and structural properties.[20,24,26] The overall photocatalytic activity could be improved by bending the band at the interface, which results in a better photogenerated charge-carriers separation efficiency and a reduced electron-hole recombination rate.[1,20]

Summarizing, the specific crystalline structure, surface area, exposed facets and heterophase junctions within TiO_2 play pivotal roles in dictating its photocatalytic efficiency. Other important factors to be considered are porosity and morphology, which correlate both the structural dimensionality and the particle size. Nanostructured TiO_2 showing different morphologies, including spherical shape nanoparticles, nanoflowers, nanotubes, nanorods and nanofibers, have been proved to show improved photocatalytic activity compared to the bulk counterpart.[4] The better performances can be attributed to several effects related to the dimensionality, such as the increase in the surface-to-volume ratio and the decrease in charge-carriers recombination rate.[27–29] Thus, considering these properties is extremely important when designing photocatalysts for applications concerning solar energy conversion. Particularly, in the synthesis of TiO_2-based photocatalysts, the mixed phase ratio, the morphology and surface properties can be controlled by tuning and optimizing the experimental conditions (*i.e.,* temperature, pressure, concentration and type of reagents).[13] Many synthetic strategies, including sol-gel technique, microemulsion techniques, precipitations, hydrothermal and solvothermal methods, have been developed and applied, and each method is directly related to the final properties of the TiO_2-based material.[12] Further details on the synthetic strategies will be given in the following chapters.

3.2.2 Optical and electronic properties

TiO_2 is a widely studied and versatile semiconductor material also known for its peculiar optical and electronic properties. In general, the key optical properties lie in the E_g structure, and the understanding of the electronic structures of TiO_2 is based on both theoretical (Density of States, DOS and Density Functional Theory, DFT calculations) and experimental results coming from several spectroscopic techniques (*i.e.,* UV-Vis Spectroscopy, Synchrotron light-based photoemission spectroscopy, photoluminescence and UV-photoelectron spectroscopy). In this frame, all the aforementioned TiO_2 phases show CB and VB edges mainly consisting of Ti 3d and O 2p states (**Figure 3.3**), which form a wide bandgap ranging from ~3.0 to ~3.2 eV, according to the considered polymorph and corresponding to excitation wavelengths from ~413 nm to ~387 nm in the UV region.[30]

The TiO_2 bandgap structure does not only depend on the crystal structure but it is also strongly influenced by the morphology and the presence of intrinsic defects, including oxygen vacancies (O_v), interstitial titanium ions (*i.e.,* Ti^{3+}) or impurities in the host lattice substituting both anions and cations.[1,30] When dealing with n-type TiO_2, the presence of defects inside the crystal lattice may significantly affect the overall photocatalytic properties, influencing both the mass transport and the conductivity of the material.[1] Furthermore, new electronic states, the so-called defects states, can be formed within the bandgap and their position is strongly affected by both the crystalline phase and the surface structure.[1,31,32] Photoemission spectroscopy is a very suitable technique to investigate the band structures of TiO_2 and it has been useful to prove the band bending in O_v-rich n-type TiO_2 materials.[1,10,30] In detail, O_v surface defects can be assimilated with unpaired electrons, initially located in O 2p orbitals and then, as a result of the oxygen vacancy, transferred to the CB formed by Ti 3d orbitals.[10] From a comprehensive analysis of this electronic situation by theoretical calculations, it has been concluded that in absence of excitation, the unpaired electrons in the vacancies act as donor-like states,

thus creating an accumulation layer close to the surface that results in the downward band bending.[33]

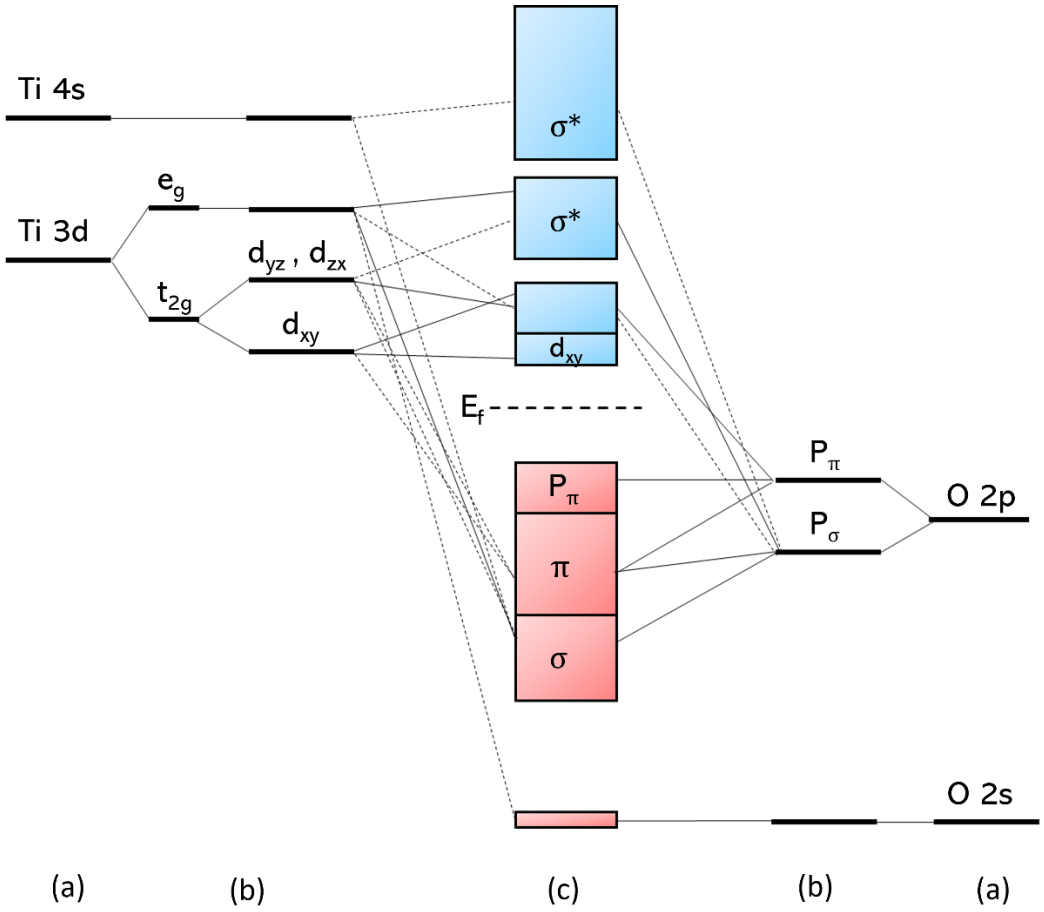

Figure 3.3 Anatase TiO_2 molecular orbitals structure with **(a)** atomic levels, **(b)** crystal field effect and**(c)** final interaction states. Thin solid and dashed lines show large and minor contributions, respectively.

It is important to highlight that the accumulation of electrons and the band bending effect strongly depend on the surface composition and reveal the surface chemistry of TiO_2 material.[10] Most of the photocatalytic applications are performed at atmospheric pressure and in aqueous solution containing molecules to be adsorbed onto the photocatalyst surface. The surface processes are driven toward the equilibrium between the Fermi level (*i.e.,* the highest energy level with a non-zero probability of being occupied by an electron at 0 K) potential and the chemical potential of adsorbed species, meaning that the interactions strongly

depend on the oxidation state of the surface.[1] Thus, according to the electronegativity of the adsorbed molecules and the charge transfer events, both the band bending (downward or upward) and the bands flattening effect may occur.[1,10,34] For instance, it has been theoretically proven that, under dark conditions, the adsorption of water molecules on TiO_2 surface leads to an upward band bending due to the creation of negatively charged species, which decreases the charge carrier density at the surface.[35]On the contrary, when n-type TiO_2 is subjected to prolonged excitation, the band flattening occurs and it can be explained by either surface band shifting or bulk band shifting (**Figure 3.4**).[10,34] This results in a more negative Fermi level in the bulk, while surface states energy remains typically constant.

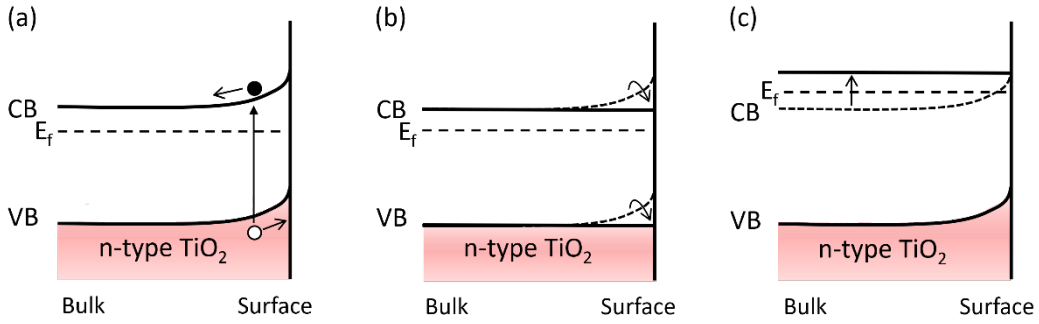

Figure 3.4 Photoinduced band flattening of TiO_2 diagram scheme. **(a)** Photoexcitation and creation of e^-—h^+ pairs in the space charge layer; **(b)** band flattening due to h^+ accumulation and consequent band shifting at the surface; **(c)** band flattening due to e^- accumulation and consequent band shifting in the bulk.

The possibility to engineer the bandgap of pure titania highlights the relevance of this metal oxide semiconductor in photocatalytic applications. The tunability of the optical properties, by altering the bandgap structure, can be achieved following several common strategies including i) the introduction of atoms or other elements inside the TiO_2 lattice (*i.e.,* element-doping); ii) the coupling with other semiconductors (*i.e.,* heterojunctions formation); iii) the surface sensitization by organic molecules, metal complexes or metal nanostructures; and iv) the selection of a proper morphology.[30] Further research into tuning optical and electronic properties through material engineering and surface modifications holds great potential in enhancing TiO_2 performances and expanding its utility under solar light irradiation.

3.2.3 Charge dynamics and photocatalytic activity

Thanks to its properties, titania is the ideal candidate for harnessing solar energy and trigger various photocatalytic reactions. However, as widely stated in the previous sections, TiO_2 particle size and morphology, crystal structure, porosity and surface properties strongly affect the overall photocatalytic efficiency. In addition, the E_g structure needs to be considered. The E_g value, hence the band edges position of VB and CB, determine the absorption ability and the redox capability of TiO_2-based photocatalysts, respectively. In fact, the higher the interaction with light, the higher the number of e^-—h^+ pairs, which are essential to drive photoredox reactions with available reactants close to the photocatalyst surface. The overall photocatalytic efficiency strongly depends on the redox potentials and band edge of the target substrate in relationship with those of TiO_2. Accordingly, the substrate redox potential should be located in between the VB and CB potentials of the photocatalyst.[36] After the photoexcitation of TiO_2, with an energy equal to or higher than its E_g and the creation of e^-—h^+ pairs according to equation 3.1, photoredox reactions can only occur by charge carriers that successfully migrate onto the photocatalyst surface.

$$\mathrm{TiO_2} \xrightarrow{h\nu} \mathrm{TiO_2^*}\ (e_{CB}^- - h_{VB}^+) \qquad (3.1)$$

Upon light excitation, the generation and separation of charge-carriers occur rapidly, but less than ~10% of the created electrons or holes effectively contribute to the redox reactions.[1,37] This is due to the recombination processes, both radiative and non-radiative, occurring in the bulk and surface of TiO_2. After their creation, charges undergo thermalization followed by trapping and recombination or transport and migration before driving the reactions. In terms of time scale, these processes are very fast. For instance, Yoshiaki Tamaki and co-workers used femtosecond transient absorption spectroscopy to investigate the dynamics of electrons and holes, including thermalization and trapping in TiO_2 nanoparticles after

excitation at 266 nm and 355 nm.[38] At 355 nm excitation wavelength, photogenerated e^-—h^+ pairs are trapped ultra-rapidly within 100 fs. Conversely, at higher energy (*i.e.,* 266 nm) the trapping time is slowed to ~200 fs, due to the excess energy of free electrons. Surface-trapped and bulk electrons showed a decay time of 500 ps, relaxing into deep bulk trapping sites.[38] Furthermore, deeply trapped electrons or holes show higher lifetimes compared to the shallowly trapped counterparts.[10,37] In the frame of trapping sites, there are still controversial results on their localization and products formation.[1] From electron spin resonance (ESR) measurements, it is assumed that electrons trapping occurs in the proximity of Ti^{3+} sites at the surface, while holes trapping happens either at a bridging O^{2-} or surface-bound OH^- anions giving the formation of $O^{\cdot -}$ or $OH^{\cdot}$, respectively.[10,33] However, from theoretical calculations it has been predicted that holes and electrons are trapped in the near-surface and subsurface sites, respectively.[1,10] The uncertainty on the localization of charge trapping and on thermalization is due to the ultrafast rate of these processes, which require advanced spectroscopy techniques and sophisticated theoretical investigations. Furthermore, the particle size effect should also be taken into account, since the upward band bending decreases with particle size, thus both electrons and holes are available at the surface.[10] It has indeed been proven that electron-trapping is more efficient by decreasing the TiO_2 particle size below ~15 nm thanks to a larger surface area.[39] As previously said, charge-carriers recombination, following thermalization and trapping, involves both radiative and non-radiative processes. If a radiative recombination process is involved, there is photons emission with an energy smaller than the absorbed light energy (*i.e.,* emission occurs at lower energies than the TiO_2 E_g). Conversely, in a non-radiative process, energy is usually released as heat. Recombination processes usually take place at defect sites or grain boundaries.[37,40] According to what is reported in literature, rutile TiO_2 shows faster recombination rate than anatase TiO_2.[1,19,37,40–42] For both phases, the holes decay in the ns timescale, while electrons have different lifetimes. More precisely, electrons in the anatase TiO_2 CB exist for more than a few µs, while they only live a few tens of ns (~24 ns) in rutile TiO_2

CB.[1,19,37,40–42] The longer lifetime of the electrons is related to the higher photocatalytic activity of anatase with respect to rutile. Furthermore, it may be ascribed to the presence of surface trapping sites, such as oxygen vacancies, in higher density.[10] Thus, the presence of an optimal concentration of surface defects may be beneficial to boost the photocatalytic activity.[28] After the charge-carriers separation, if the recombination is hindered or delayed, the VB holes and CB electrons can drive the redox reaction. It is highly difficult for a semiconductor photocatalyst, like TiO_2, to show good photocatalytic activity for both oxidation and reduction reactions. In fact, the photogenerated electrons migrate between the surface and shallow bulk trapping sites in equilibrium. At this point, the shallowly trapped electrons relax into deeper sites by hopping processes involving energetically distributed trapping sites, since they are not directly available to initiate the surface reduction reactions.[10] Thus, TiO_2 can be activated for reduction reactions, including H_2 production, only if it undergoes proper surface modifications (*i.e.,* metal co-catalyst loading) or a sacrificial agent is used during the photocatalytic reaction.

3.3 Going beyond TiO_2 limits

TiO_2-based photocatalysts have gained attention in the field of heterogeneous photocatalysis thanks to their high stability, versatility and availability. However, TiO_2-based materials show some limitations, and several challenges still need to be addressed. Disadvantages and challenges of TiO_2 may be summarized as follows:

- *Poor absorption of solar light*. The major TiO_2 drawback is its wide bandgap, which hinders the absorption of Vis and NIR light. Thus, a small fraction of the solar spectrum, the UV light which accounts for only 4-5% of the total, can be used to activate photocatalytic reactions.[43] Thus, optical and electronic properties need to be tuned in order to obtain narrower bandgaps.[10]

- *Low quantum efficiency*. Despite the high efficiency in generating electron-hole pairs upon photoexcitation, TiO_2 suffers from fast charge-carriers recombination, leading to low quantum efficiency and consequently to reduced photocatalytic activity.[36,44] Thus, recombination processes should be avoided or delayed.
- *Selectivity*. One of the most important features when dealing with photocatalytic reactions is to have a catalyst that shows selective photoactivity. Unfortunately, TiO_2 exhibits limited selectivity toward certain reactions, leading to undesired byproducts formation or incomplete conversion of target compounds.[45]
- *Crystallinity, surface area and reactivity*. As discussed in section 3.1.1, TiO_2 photocatalytic activity is closely related to its surface area and crystal structure. Achieving a high surface-to-volume ratio while having the desired crystal structure to reach the optimal reactivity may be quite challenging.
- *Synthesis and cost*. The rational design of the size and shape of TiO_2 materials based on the selected synthetic strategy is extremely important to obtain an efficient photocatalyst.[46] When thinking about future large-scale applications, the design of a good photocatalyst should include the ease and cost of its synthesis. However, depending on the selected synthetic method, the development of efficient TiO_2-based photocatalysts with functional properties may be complex and costly, thus not suitable for scaling-up the production. Thus, choosing a suitable synthetic strategy for a future scaling-up while maintaining quality and efficiency poses great challenges.

Going beyond conventional TiO_2 limits is one of the main goals of the nowadays research in the field of heterogeneous photocatalysis. There are many strategies and approaches to go through to overcome these challenges and they can also be combined in order to further boost the overall photocatalytic activity and expand TiO_2 functionality. Some of the most promising ones are listed below.

Morphology engineering

As already mentioned, photoactivity is largely related to the number of active sites provided by the specific surface area of the employed photocatalyst. The higher the surface-to-volume ratio, the higher the abundance of active sites that drive the photoredox reactions. Moreover, the smaller the particle size, the shorter the pathway of the photogenerated charge-carriers towards the catalyst surface. Hence, morphology engineering is extremely important to increase the overall photocatalyst performance in terms of decreasing the charge-carriers recombination rate (i.*e.,* enhancing the quantum efficiency) and increasing the number of active sites.[47,48] Furthermore, as widely discussed in **Chapter 2**, surface properties, influenced by both crystal phase and surface area, highly affect the reactivity with regard to physical adsorption and chemical selectivity.[49] Additionally, it is of extreme importance to properly select the morphological structure, which can be essential to improve the overall photocatalytic activity. For instance, flower-like structures can provide not only a larger specific surface area, which is good for both the reactants physical adsorption and the abundance of active sites, but also higher absorbance ability thanks to the multiple refraction or reflection events.[50] Another interesting morphology is the hollow structure, which can enhance the light absorption toward the visible region thanks to the multiple scattering events, and by modulating the transfer behavior of photogenerated e^-—h^+ pairs. The larger surface area, in combination with enhanced electrical and optical properties provided by the cavity, makes the hollow structure morphology suitable to enhance photocatalytic performance. [28,45] Thus, further details about TiO_2 hollow spheres will be given in **Chapter 4**.

In summary, morphology engineering is a good approach to improve the overall photocatalytic performance of TiO_2-based catalysts by effectively enhancing light absorption, the contact area between the adsorbed reactants and the photocatalysts surface, and finally shortening the diffusion length of e^-—h^+ pairs by simultaneously decreasing their recombination probability.[13]

Surface and Defect engineering

Surface modification and defect engineering are very important and promising methods that can be used to improve TiO_2-based photocatalysts performance. In general, crystal defects, which alter the periodic arrangement of atoms in crystalline materials, usually appear in all crystalline semiconductors influencing their photocatalytic properties.[40] The introduction of defects, such as Ti^{3+} sites or oxygen vacancies, in the surface lattice of TiO_2-based photocatalysts can improve the light absorption capability to the Vis and even NIR regions, thanks to the creation of mid-gap states that lower the overall E_g.[51] Furthermore, the presence of mid-gap states plays a key role in photocatalytic reactions. As stated before, the presence of defects, thus trapping sites, may increase the charge-carriers separation, but also generate recombination centers if the defects are not at their optimum concentration.[28] Moreover, the local electric field distribution and the charge dynamics behavior may be tuned by improving the overall photoactivity. Among all the defects, inducing oxygen vacancies in TiO_2 material is quite easy thanks to their relatively low formation energy. Thus, the introduction of oxygen vacancies can be an easy and effective strategy to enhance photoactivity. In fact, the creation of these kinds of defects leads to the formation of both electron trapping centers, inhibiting e^-—h^+ pairs recombination, to the formation of new defective levels below the TiO_2 CB, which favor electron transport and transfer. [32,52–54] As can be realized, defects engineering steers the modulation of the electronic structure. The controlled introduction of surface defects may not only increase the overall optical and electronic properties but can also enhance the presence of active sites for adsorbed molecules to promote photoredox reactions.

Doping engineering

Doping TiO_2 is a good strategy to expand and improve photocatalytic performance. It can be defined as the incorporation of other atoms or ions, called dopant species, into the crystal lattice. Doping leads to the creation of new charges, defects, and lattice distortions. Similar to defect engineering, doping can generate new

active sites thanks to the reconfiguration of local fields in the original material.[40] Furthermore, TiO_2 doping by using both metal (cation dopants like Cr, Fe, V, Mn, Cu and Ni) and non-metal dopants (anion dopants like N, S and C),[55,56] may boost the overall photocatalytic efficiency by improving charge transport processes, suppressing e^-—h^+ pairs recombination, narrowing the E_g and broadening the light absorption range.[57] Thus, doping engineering by altering both the crystalline and the electronic band structures may bring several improvements. Among them, surface modifications are known to enhance the reactant adsorption and the enrichment of photoexcited e^-—h^+ pairs. Doping engineering can be achieved by using both physical and chemical methods,[56] and dopant agents can occupy substitutional or interstitial sites into the crystal lattice. Based on the selected synthetic process, dopant species can be located at different sites, controlling the final electronic and optical properties of TiO_2.[58–60] However, it has to be pointed out that adjusting the concentration of doping agents is pivotal during the synthesis design. High concentration of dopants could adversely impact the overall photocatalytic process by competitively trapping oxidizing species or by increasing the e^-—h^+ pairs recombination rate. Altering the TiO_2 structure through the incorporation of metal ions (cations) causes a downward shift in the TiO_2 CB or the creation of new gap states. Conversely, the doping with non-metal ions (anions) causes an upward shift in the TiO_2 VB.[56] Both of these approaches result in lowering the bandgap energy, enhancing TiO_2 light absorption capability toward longer wavelengths. In addition, as mentioned before, the introduction of ions into the crystal lattice may induce oxygen vacancies, which leads to the formation of localized energy levels below the CB, shifting the overall absorption edge toward lower energies. Introducing new impurity energy levels between the TiO_2 CB and VB, using suitable metal or non-metal doping elements, is an effective way to reasonably tune and optimize bare TiO_2 band structure, as well as improve the overall photocatalytic performance.

Homo- & hetero-junctions formation

The formation of homojunctions and heterojunctions is often seen as a good approach to extend the boundaries of TiO_2-based photocatalysts. Briefly, homojunction and heterojunction are terms used when talking about different types of junctions formed by the contact between two semiconductor materials that create a peculiar interface region. Homojunctions involve the connection between the same semiconductor material, but with different band structures (*i.e.,* due to the presence of dopant species or defects), while heterojunctions involve the junction between two diverse semiconductor materials.[61] Both types of junctions play crucial roles in the design and functionality of semiconductor photocatalysts. In fact, when dealing with homo- and hetero-junctions, the band structures coupling may be beneficial for the charge transfer processes, separation and migration of photogenerated e^-—h^+ pairs. Furthermore, the construction of junctions is an effective strategy to reduce the bandgap and enhance the light absorption toward visible light. There are two types of heterojunctions that are usually considered to be beneficial for photocatalytic performance: Type-II heterojunctions and direct Z-scheme (**Figure 3.5**).[36]

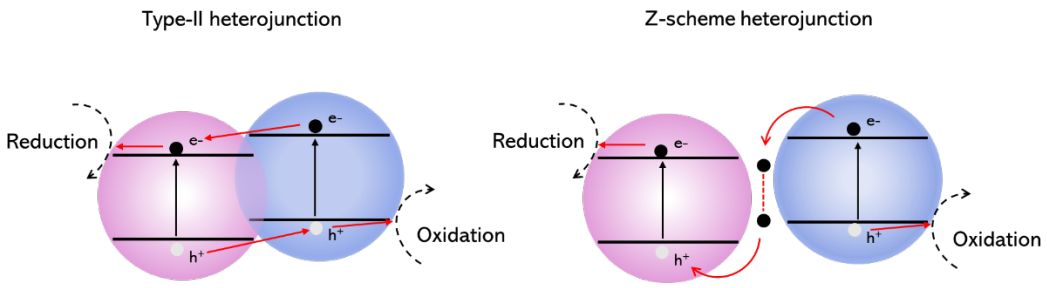

Figure 3.5 Schematic illustration of Type-II (left) and Z-scheme heterojunctions (right).

In Type-II heterojunctions, the alignment of energy bands differs significantly between the two semiconductor materials (namely S-I and S-II), thus the CB minimum of one semiconductor is higher, while the VB maximum of the other is lower. Consequently, in a Type-II heterojunction, electrons and holes are confined to opposite sides of the junction, leading to enhanced charge carriers separation. This

spatial separation prevents immediate recombination, resulting in an extended lifetime for the charge carriers within the junction.[62] However, since photogenerated charge-carriers migrate to more electronegative VB and electropositive CB potentials, the redox ability of the photocatalytic system is weakened.[63] In fact, within the Type-II junction, the charges migration results in a reduction of the required thermodynamic energy, which helps overcome the overpotential barrier for redox reactions occurring on the surfaces of each semiconductor.[36] This issue is solved when dealing with direct Z-scheme heterojunctions, where the letter "Z" resembles the energy band diagram. In this setup, each semiconductor shows band positions able to facilitate different half-photoredox reactions.[62,64] In detail, given a target redox reaction, S-I shows more electronegative VB and CB potentials, whereas S-II is characterized by more electropositive VB and CB potentials (**Figure 3.5**).[36,62] When the direct Z-scheme heterojunction is excited by light, S-I is photoexcited and leads to the formation of e^-—h^+ pairs, which can then migrate to the respective energy levels of S-II to give photoredox reactions. In this setup, S-I and S-II only have enough energy to proceed with reduction and oxidation reactions.[36]

In detail, oxidation and reduction reactions occur in the most electropositive VB and electronegative CB potential of the photosystem, respectively. Simultaneously, the counter photogenerated charges that do not participate in the reactions are recombined at the junction. Thus, the immediate e^-—h^+ pairs recombination is prevented without compromising the redox ability of the photosystem.[65] In general, it is widely accepted that the energy offset between the CB and VB edges within the junction is an effective strategy to enhance the photocatalytic activity. However, achieving the lattice matching by constructing a homojunction may be another feasible way to easily lower the E_g and increase the separation efficiency of photogenerated charge-carriers.[66] In fact, lattice matching in homojunction could also facilitate the photogenerated e^-—h^+ pairs transfer. In addition, homojunction formation provides a better control of the synthesis. The difference in the band edge positions between two sides of the same material amplify e^-—h^+ pairs separation efficiency, thereby boosting the photoactivity. A typical TiO_2-based

homojunction can be obtained by the connection between pure or white TiO_2 and the so-called sub-stoichiometric or colored-TiO_2 (TiO_{2-x}).[67] The deficiency of one or more oxygens within TiO_{2-x} leads to a remarkable enhancement of light absorption of longer wavelengths.[52,53] However, as already mentioned in the previous section, the rapid charge-carriers recombination may be enhanced by the presence of a too high number of defects. Therefore, matching the pure TiO_2 and TiO_{2-x} may be a good strategy to overcome the limits of each semiconductor material. In terms of band positions, the TiO_2 CB is higher than that of TiO_{2-x}, while the VB is more positive than that of TiO_2. Consequently, this kind of homojunction may supply continuity to the band bending and enhance charge-carriers separation efficiency leading to an overall increase in the photocatalytic efficiency of the system.[66,67]

3.3 References

[1] Q. Guo, C. Zhou, Z. Ma, X. Yang, *Advanced Materials* **2019**, *31*, 1901997.

[2] K. Kardarian, D. Nunes, P. Maria Sberna, A. Ginsburg, D. A. Keller, J. Vaz Pinto, J. Deuermeier, A. Y. Anderson, A. Zaban, R. Martins, E. Fortunato*, Solar Energy Materials and Solar Cells* **2016**, *147*, 27.

[3] I. Concina, A. Vomiero, *Small* **2015**, *11*, 1744.

[4] I. Concina, Z. H. Ibupoto, A. Vomiero, Adv Energy Mater **2017**, *7*, 1700706.

[5] M. Barawi, L. De Trizio, R. Giannuzzi, G. Veramonti, L. Manna, M. Manca, *ACS Nano* **2017**, *11*, 3576.

[6] P. J. Wojcik, A. S. Cruz, L. Santos, L. Pereira, R. Martins, E. Fortunato, *J Mater Chem* **2012**, *22*, 13268.

[7] D. Nunes, A. Pimentel, A. Gonçalves, S. Pereira, R. Branquinho, P. Barquinha, E. Fortunato, R. Martins, *Semicond Sci Technol* **2019**, *34*, 043001.

[8] A. Fujishima, K. Honda, *Nature* **1972***, 238*, 37.

[9] G. N. Schrauzer, T. D. Guth, *J Am Chem Soc* **1977**, *99*, 7189.

[10] J. Schneider, M. Matsuoka, M. Takeuchi, J. Zhang, Y. Horiuchi, M. Anpo, D. W. Bahnemann, *Chem Rev* **2014***, 114*, 9919.

[11] Z. Li, Z. Li, C. Zuo, X. Fang, *Advanced Materials* **2022**, *34*, 1.

[12] T. Peng, J. A. Lalman, in *ACS Symposium Series*, **2019**, pp. 135–165.

[13] K. Lee, A. Mazare, P. Schmuki, *Chem Rev* **2014**, *114*, 9385.

[14] X. Li, C. Wang, J. Tang, *Nat Rev Mater* **2022**, *7*, 617.

[15] Y. Chen, L. Soler, C. Cazorla, J. Oliveras, N. G. Bastús, V. F. Puntes, J. Llorca, *Nat Commun* **2023**, *14*, 6165.

[16] T. Zhu, W. Li Ong, L. Zhu, G. Wei Ho, *Sci Rep* **2015**, *5*, 10601.

[17] J. Wu, X. Cao, Y. Ji, F. Zhang, X. Huang, G. F. Ouyang, J. Yu, *Adv Funct Mater* **2023**, *34*, 2309825.

[18] C. Wang, Q. Yao, M. Wang, C. Zheng, N. Wang, Z. Bai, J. Yang, S. Dou, H. Liu, *Adv Funct Mater* **2023**, 2301996.

[19] F. De Angelis, C. Di Valentin, S. Fantacci, A. Vittadini, A. Selloni, *Chem Rev* **2014**, *114*, 9708.

[20] M. G. Ju, G. Sun, J. Wang, Q. Meng, W. Liang, *ACS Appl Mater Interfaces* **2014**, *6*, 12885.

[21] R. Katal, S. Masudy-Panah, M. Tanhaei, M. H. D. A. Farahani, H. Jiangyong, *Chemical Engineering Journal* **2020**, *384*, 123384.

[22] N. Satoh, T. Nakashima, K. Kamikura, K. Yamamoto, *Nat Nanotechnol* **2008**, *3*, 106.

[23] P. Bamola, B. Singh, A. Bhoumik, M. Sharma, C. Dwivedi, M. Singh, G. K. Dalapati, H. Sharma, *ACS Appl Nano Mater* **2020**, *3*, 10591.

[24] X. Lin, M. Sun, B. Gao, W. Ding, Z. Zhang, S. Anandan, A. Umar, *J Alloys Compd* **2021**, *850*, 156653.

[25] D. C. Hurum, A. G. Agrios, K. A. Gray, T. Rajh, M. C. Thurnauer, *J Phys Chem B* **2003**, *107*, 4545.

[26] H. Hussain, G. Tocci, T. Woolcot, X. Torrelles, C. L. Pang, D. S. Humphrey, C. M. Yim, D. C. Grinter, G. Cabailh, O. Bikondoa, R. Lindsay, J. Zegenhagen, A. Michaelides, G. Thornton, Nat Mater 2017, 16, 461.

[27] L. Liccardo, E. Lushaj, L. Dal Compare, E. Moretti, A. Vomiero, *Small Science* **2022**, *2*, 2100104.

[28] L. Liccardo, M. Bordin, P. M. Sheverdyaeva, M. Belli, P. Moras, A. Vomiero, E. Moretti, *Adv Funct Mater* **2023**, *33*, 2212486.

[29] N. Spigariol, L. Liccardo, E. Lushaj, E. Rodríguez-Castellón, I. Barroso Martin, F. Polo, A. Vomiero, E. Cattaruzza, E. Moretti, *Catal Today* **2023**, *419*, 114134.

[30] M. Kapilashrami, Y. Zhang, Y. S. Liu, A. Hagfeldt, J. Guo, *Chem Rev* **2014**, *114*, 9662.

[31] T. Wu, H. Zhao, X. Zhu, Z. Xing, Q. Liu, T. Liu, S. Gao, S. Lu, G. Chen, A. M. Asiri, Y. Zhang, X. Sun, *Advanced Materials* **2020**, *32*, 2000299.

[32] T. S. Rajaraman, S. P. Parikh, V. G. Gandhi, *Chemical Engineering Journal* **2020**, *389*, 123918.

[33] U. Diebold, *Surf Sci Rep* **2003**, *48*, 53.

[34] Z. Zhang, J. T. Yates, *Chem Rev* **2012**, *112*, 5520.

[35] Y. He, O. Dulub, H. Cheng, A. Selloni, U. Diebold, *Phys Rev Lett* **2009**, *102*, 106105.

[36] J. P. Jeon, D. H. Kweon, B. J. Jang, M. J. Ju, J. B. Baek, *Adv Sustain Syst* **2020**, *4*, 1.

[37] R. Qian, H. Zong, J. Schneider, G. Zhou, T. Zhao, Y. Li, J. Yang, D. W. Bahnemann, J. H. Pan, *Catal Today* **2019**, *335*, 78.

[38] Y. Tamaki, K. Hara, R. Katoh, M. Tachiya, A. Furube, *The Journal of Physical Chemistry C* **2009**, *113*, 11741.

[39] Y. Murakami, J. Nishino, T. Mesaki, Y. Nosaka, *Spectroscopy Letters* **2011**, *44*, 88.

[40] D. Wrana, T. Gensch, B. R. Jany, K. Cieślik, C. Rodenbücher, G. Cempura, A. Kruk, F. Krok, *Appl Surf Sci* **2021**, *569*, 150909.

[41] Y. Zhang, D. T. Payne, C. L. Pang, C. Cacho, R. T. Chapman, E. Springate, H. H. Fielding, G. Thornton, *Journal of Physical Chemistry Letters* **2019**, *10*, 5265.

[42] O. E. Dagdeviren, D. Glass, R. Sapienza, E. Cortés, S. A. Maier, I. P. Parkin, P. Grütter, R. Quesada-Cabrera, *Nano Lett* **2021**, *21*, 8348.

[43] Q. Wang, K. Domen, *Chem Rev* **2020***, 120*, 919.

[44] H. He, C. Liu, K. D. Dubois, T. Jin, M. E. Louis, G. Li, *Ind Eng Chem Res* **2012**, *51*, 11841.

[45] S. Liu, J. Yu, M. Jaroniec, *J Am Chem Soc* **2010**, *132*, 11914.

[46] W. Zhang, Y. Tian, H. He, L. Xu, W. Li, D. Zhao, *Natl Sci Rev* **2020**, *7*, 1702.

[47] A. H. Mamaghani, F. Haghighat, C.-S. Lee, *Appl Catal B* **2020**, *269*, 118735.

[48] A. Alshehri, K. Narasimharao, *J Mater Res Technol* **2020**, *9*, 14907.

[49] X. Li, W. Zheng, G. He, R. Zhao, D. Liu, *ACS Sustain Chem Eng* **2014**, *2*, 288.

[50] G. Tian, Y. Chen, W. Zhou, K. Pan, C. Tian, X. Huang, H. Fu, *Cryst Eng Comm* **2011**, *13*, 2994.

[51] X. Mao, X. Lang, Z. Wang, Q. Hao, B. Wen, Z. Ren, D. Dai, C. Zhou, L.-M. Liu, X. Yang, *J Phys Chem Lett* **2013**, *4*, 3839.

[52] S. G. Ullattil, S. B. Narendranath, S. C. Pillai, P. Periyat, *Chemical Engineering Journal* **2018**, *343*, 708.

[53] L. Liao, M. Wang, Z. Li, X. Wang, W. Zhou, *Nanomaterials* **2023**, *13*, 468.

[54] X. Liu, G. Zhu, X. Wang, X. Yuan, T. Lin, F. Huang, *Adv Energy Mater* **2016**, *6*, 1600452.

[55] B. Roose, S. Pathak, U. Steiner*, Chem Soc Rev* **2015**, *44*, 8326.

[56] S. Yadav, G. Jaiswar, *J Chin Chem Soc* **2017**, *64*, 103.

[57] C. Alberoni, I. Barroso-Martin, A. Infantes-Molina, E. Rodriguez-Castellon, A. Talon, H. Zhao, S. You, A. Vomiero, E. Moretti, *Mater Chem Front* **2021**, *5*, 4138.

[58] J. Lynch, C. Giannini, J. K. Cooper, A. Loiudice, I. D. Sharp, R. Buonsanti, *J Phys Chem C* **2015**, *119*, 7443.

[59] T. Wu, P. Niu, Y. Yang, L. Yin, J. Tan, H. Zhu, J. T. S. Irvine, L. Wang, G. Liu, H. Cheng, *Adv Funct Mater* **2019**, *29*, 1901943.

[60] G. Barolo, S. Livraghi, M. Chiesa, M. C. Paganini, E. Giamello, *J Phys Chem C* **2012**, *116*, 20887.

[61] A. Rockett, in The Materials Science of Semiconductors (Ed.: A. Rockett), Springer US, Boston, MA, **2008**, pp. 73–139.

[62] Y. Zhao, Y. Shu, X. Linghu, W. Liu, M. Di, C. Zhang, D. Shan, R. Yi, B. Wang, *Chemosphere* **2024**, *346*, 140595.

[63] L. Zhang, J. Zhang, H. Yu, J. Yu, *Adv Mater* **2022**, *34*, 2107668.

[64] J. Yu, S. Wang, J. Low, W. Xiao, *Phys Chem Chem Phys* **2013**, *15*, 16883.

[65] Y. Zhao, X. Linghu, Y. Shu, J. Zhang, Z. Chen, Y. Wu, D. Shan, B. Wang, *J Environ Chem Eng* **2022**, *10*, 108077.

[66] X. Lü, A. Chen, Y. Luo, P. Lu, Y. Dai, E. Enriquez, P. Dowden, H. Xu, P. G. Kotula, A. K. Azad, D. A. Yarotski, R. P. Prasankumar, A. J. Taylor, J. D. Thompson, Q. Jia, *Nano Lett* **2016**, *16*, 5751.

[67] Z. Miao, G. Wang, L. Li, C. Wang, X. Zhang, *J Mater Sci* **2019**, *54*, 14320.

Chapter 4 – *Surface engineering*

The combination of morphology and surface engineering is presented as a good strategy to enhance TiO_2 photocatalytic activity in the field of environmental remediation and energy applications. The main body of this chapter is based on the appended papers, Paper-I and Paper-II, provided at the end of the dissertation and available under license by Wiley-VCH GmbH.

In detail, the first section based on Paper-I is focused on colored- TiO_2 hollow spheres as promising photocatalysts for photo-oxidation reactions, such as water purification from contaminants of emerging concerns. It demonstrates how the combination of surface-defects engineering, and the design of hollow morphology enhance the overall photocatalytic performances of bare TiO_2 systems. The second section, based on Paper-II, is focused on surface engineered nano-Cu/TiO_2 photocatalysts as promising candidates for energy applications such as hydrogen production from methanol reforming under UV light. The use of Cu co-catalyst combined with the introduction of surface defects on commercial P25 titania, *via* a cost-effective microwave-assisted hydrothermal synthesis, is reported as a good way to easily enhance the overall photoactivity.

Paper-I

L. Liccardo, M. Bordin, P. M. Sheverdyaeva, M. Belli, P. Moras, A. Vomiero, E. Moretti, Surface Defect Engineering in Colored TiO_2 Hollow Spheres Toward Efficient Photocatalysis. *Adv. Funct. Mater.* 2023, 33, 2212486. https://doi.org/10.1002/adfm.202212486

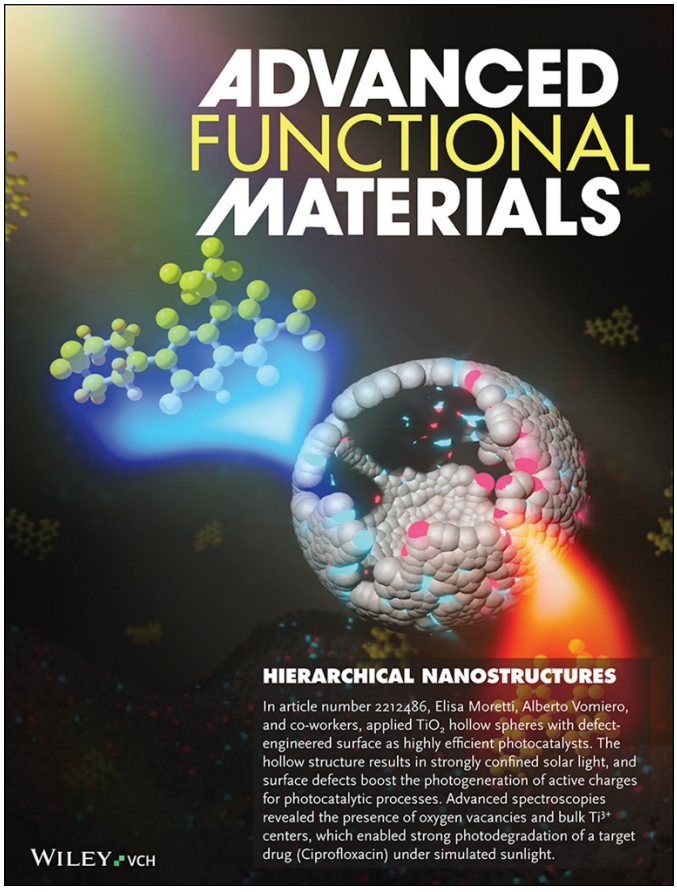

4.1 Defects in colored-TiO_2 Hollow Spheres

As already stated in **Chapter 1**, addressing water contamination stands as a pressing challenge that requires urgent attention. Complex organic compounds including pharmaceuticals, above all antibiotics and antibacterials, have garnered increased concern due to their overuse and poor degradability.[1,2] Specifically, antibiotics have been consistently identified in rivers and water bodies, with concentrations ranging from $ng \cdot L^{-1}$ to $\mu g \cdot L^{-1}$. Consequently, their discharge from wastewater facilities poses significant hazards to both the environment and human health.[3–5] Among all antibiotics, Ciprofloxacin (CIP), a broad-spectrum second-generation fluoroquinolone antibiotic, holds a prominent place as one of the most extensively used and prescribed. Furthermore, studies have confirmed not only the widespread presence of CIP in various water effluents worldwide but also its detection in concentrations higher than the safe concentration limit for antimicrobial resistance.[6] Photocatalytic advanced oxidation processes, AOPs, involving heterogeneous photocatalysis, have been proven to enable the acceleration of oxidation and degradation of a wide range of organic pollutants, including dyes and drugs, in wastewater. Semiconductors find frequent application in AOPs due to their ability to interact with light, generating e^-–h^+ pairs, which lead to the creation of radicals. These species have the great potential to degrade and fully mineralize organic pollutant molecules. Hence, enhancing the creation of photogenerated e^-–h^+ and slowing their charge recombination are necessary to ensure high photocatalytic activity.[7] In this context, summarizing what previously reported in **Chapter 3**, TiO_2 is one of the most attractive photoactive semiconductors for this kind of reactions. However, the fast charge carriers recombination and the wide bandgap (in the range of 3.0-3.2 eV) limit its efficiency and the exploitation of solar light as a source of energy for photocatalytic applications.[8,9] In addition, small titania nanoparticles, whether suspended in a solution or structured into mesoporous layers, lack the ability to scatter the incoming light and channel it within a confined space to boost the absorption probability. The creation of systems with low energy gaps

simultaneously capable of confining and absorbing light remains an ongoing challenge. As noted previously, the functionality of a material can be strongly affected by its surface composition, size and shape. Thus, the optimal combination between surface chemical composition and structure can enhance the overall photochemical performance of a nanostructured system.[10,11]

Accordingly, hydrogenated titania, known as sub-stoichiometric titanium dioxide or colored titania (TiO_{2-x}) due to its varied colors (blue, gray, black), stands out as an excellent sunlight harvester, covering a wide range of wavelengths from UV to IR region. Notably, oxygen-vacancy-rich black TiO_2 exhibits amplified photoactivity in various oxidation reactions under visible light compared to its white (stoichiometric) counterpart (**Box 4.1**). [12,13]

A fascinating structural design involves hierarchical arrangements where small building blocks are combined to form complex morphologies. In this context, TiO_2 hollow spheres (THSs), obtained from self-assembled nanoparticles, have proven to be effective photocatalysts thanks to their high surface area and intense light scattering ability. The hollow cavity, providing the light scattering ability, enables the light confinement within a reduced volume, thereby increasing the absorption probability. [14,15] Nevertheless, pure THSs showing TiO_2 intrinsic wide bandgap, struggle to absorb light significantly.

This section delves into the synthesis, characterizations and applications of colored-THSs composed of hierarchically assembled nanoparticles. An easy way of synthesis, involving a hard template-based method followed by chemical reduction under controlled conditions is proposed. In order to directly access the presence and the properties of defect-induced states within TiO_2 bandgap, synchrotron-based X-ray photoemission spectroscopy (XPS, VUV-Photoemission beamline) and electron paramagnetic resonance (EPR) were synergically used. Photocatalytic activity was evaluated in function of the degradation of CIP, as a target molecule, at room temperature, atmospheric pressure and under simulated solar light irradiation. The main goal is to demonstrate how the hydrogenation content, related to

the presence of defects (i.e., oxygen vacancies), enhance both the optical absorption capability (up to NIR region) and the overall photocatalytic efficiency of the catalysts for the investigated photo-oxidation process.

Box 4.1: Colored-TiO_2

One of the main challenges that our society is facing to meet the energy demand, is the use of the entire range of wavelengths in the solar spectrum focusing on visible (Vis) and infrared (IR) regions, that account for ~43% and ~52% of the total, respectively. Among all the solar light harvester nanomaterials, the most promising is TiO_2. However, pure TiO_2 is a colorless white crystalline material that, according to its wide bandgap (3.0-3.2 eV), exclusively absorbs in the UV region. Extensive efforts have been made to extend the light absorption of pure TiO_2, leading to the discovery and development of the so-called black-TiO_2. Before the synthesis proposed by Chen and co-workers in 2011,[16] which coined the term "black- TiO_2", research on the effects of intrinsic or self-doping on titania, was not as attractive as today. In fact, the introduction of defects, namely oxygen vacancies (Ov) or Ti^{3+} centers, in the TiO_2 crystal lattice, together with the advent of new sophisticated techniques, is now considered a hot topic in the field of energy- and environmentally-related applications. The presence of surface disordered, Ti^{3+} centers, Ov, surface -OH groups, Ti-H bonds are responsible for the color changes in black-TiO_2, as well as the superior electronic, optical, and photocatalytic properties. Several synthetic strategies have been proposed to obtain black-TiO_2,[13] however most of them are based on partial reduction approaches, in which extreme conditions such as high-temperatures in various reducing atmospheres are usually used (*e.g.,* ~500°C , ~20 bar, Ar (g), H_2/Ar (g) or pure H_2 (g) atmosphere).[17] Owing to these synthetic treatments, the crystal and electronic structure of bare TiO_2 can be tuned, obtaining shades of gray, blue, brown or black TiO_2, and giving rise to the so-called colored-TiO_2,

hydrogenated-TiO_2 or substoichiometric TiO_{2-x}. Specifically, the most marked effect of the variation in the number of defects is the resulting color. Generally, an increased degree of reduction results in a higher concentration of defects, leading to TiO_2 materials with darker colors.[17] The study of the electronic band structure is fundamental to deeply understand what the influences of the induced defects on the overall TiO_2 properties are. Examining the differences in the density of states (DOS) between pure or White-TiO_2 and black-TiO_2 helps in comprehending the alterations in the bandgap (**Figure B1**). The position of the VB maximum and the CB minimum of bare TiO_2, that are mainly derived from O *2p* and Ti *3d* orbitals, are shifted by the introduction of the chemical and structural modifications induced by defects. The overall effect is the bandgap reduction (up to ~1.5eV) with the increasing in the optical absorption properties (i.e., light absorption extended up to near-IR region), due to the introduction of new mid-gap or shallow dopant states leading to significant VB and CB tail.[13,17]

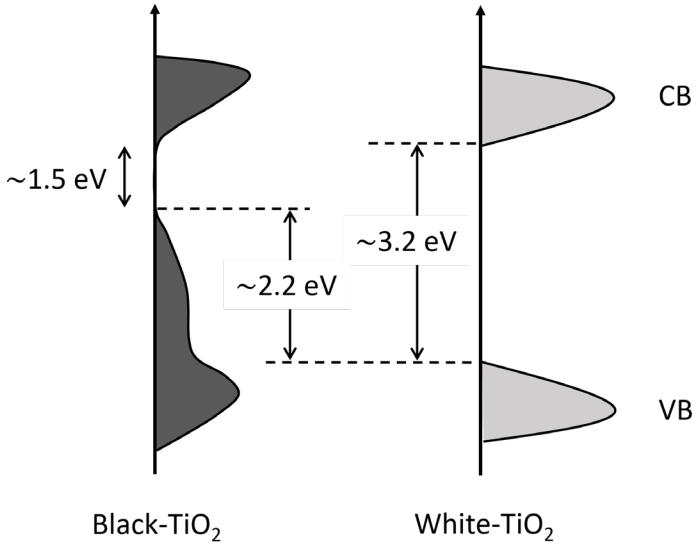

Figure B1 Schematic illustration of Density of States (DOS) for Black- and White-TiO_2.

In general, according to reaction parameters like pressure, time, and temperature, crystal structure of colored titania is characterized by surface disorder, wherein the well-crystallized lattice core of the material is surrounded by a

lattice-disordered shell.[13,18] This disordered surface on hydrogenated-TiO_2 allows for the creation of numerous Ti-H or Ti-OH bonds, leading to mid-gap states creation.[13,18] Additionally, the disordered structure may provide trapping sites for photogenerated carriers, facilitating electron transfer and preventing charge-carriers recombination.[19] The presence of Ti-H or Ti-OH bonds seems to stabilize the surface disorder but, unlike Ov or Ti^{3+} centers, having a minor role in the engineering of the electronic structure of pure TiO_2.[13] In detail, electrons within the Ov states create a donor level below the CB, affecting the overall electronic configuration, changings both physical and chemical properties of titania, significantly influencing the overall photocatalytic activity.[20] Additionally, the incorporation of Ti^{3+} expands the photoresponse of bare TiO_2 from the UV to the Vis light region.

Considering the overall effects due to the presence of defects, such as improved optical properties and favorable electronic structure, including good electron transport and a lower bandgap, black or colored-TiO_2 is expected to exhibit significantly higher photocatalytic activity than white TiO_2, laying the groundwork for further research in this field.

4.1.1 Morphology and crystal structure

As mentioned before, a hard template-based approach combined with the sol-gel process is proposed to obtain white THSs (W_THS), thus in **Figure 4.1a** the synthesis procedure is summarized. A sacrificial core of polymethylmethacrylate (PMMA) spheres (**Figure 4.2b**) were coated with a shell of amorphous TiO_2 nanoparticles (**Figure 4.1a**, step 1 and 2). After the removal of the PMMA cores by calcination in air at 500 °C, W_THS with uniform size, perfectly spherical with a diameter of about 350 nm and composed of pure TiO_2 anatase phase were formed (**Figure 4.1a**, step 3 and **Figure 4.2c**). Finally, to obtain increasingly darker gray THSs, the hard templating method was followed by hydrogenation (i.e., chemical reduction) under controlled temperature and Ar atmosphere, using chemical vapor deposition

(CVD) technique (**Figure 4.1a**, step 4 and **Figure 4.2d, e**). The samples were referred to as X_THSn, where X is the color of the samples (W: white; G: gray; DG: dark gray) and n is the CVD-annealing time when it differs from 60 min. The morphology, the crystal structure and phase-identification were studied by combining the use of Field-emission scanning electron microscopy (FESEM), X-ray diffraction analysis and high-resolution transmission electron microscopy (HRTEM). THSs were successfully synthesized with uniform size, rough surface and a shell thickness of $\sim$ 50 nm. The hollow structure was confirmed and the chemical reduction treatment under annealing of W_THS did not significantly influence the morphology nor the crystal structure.

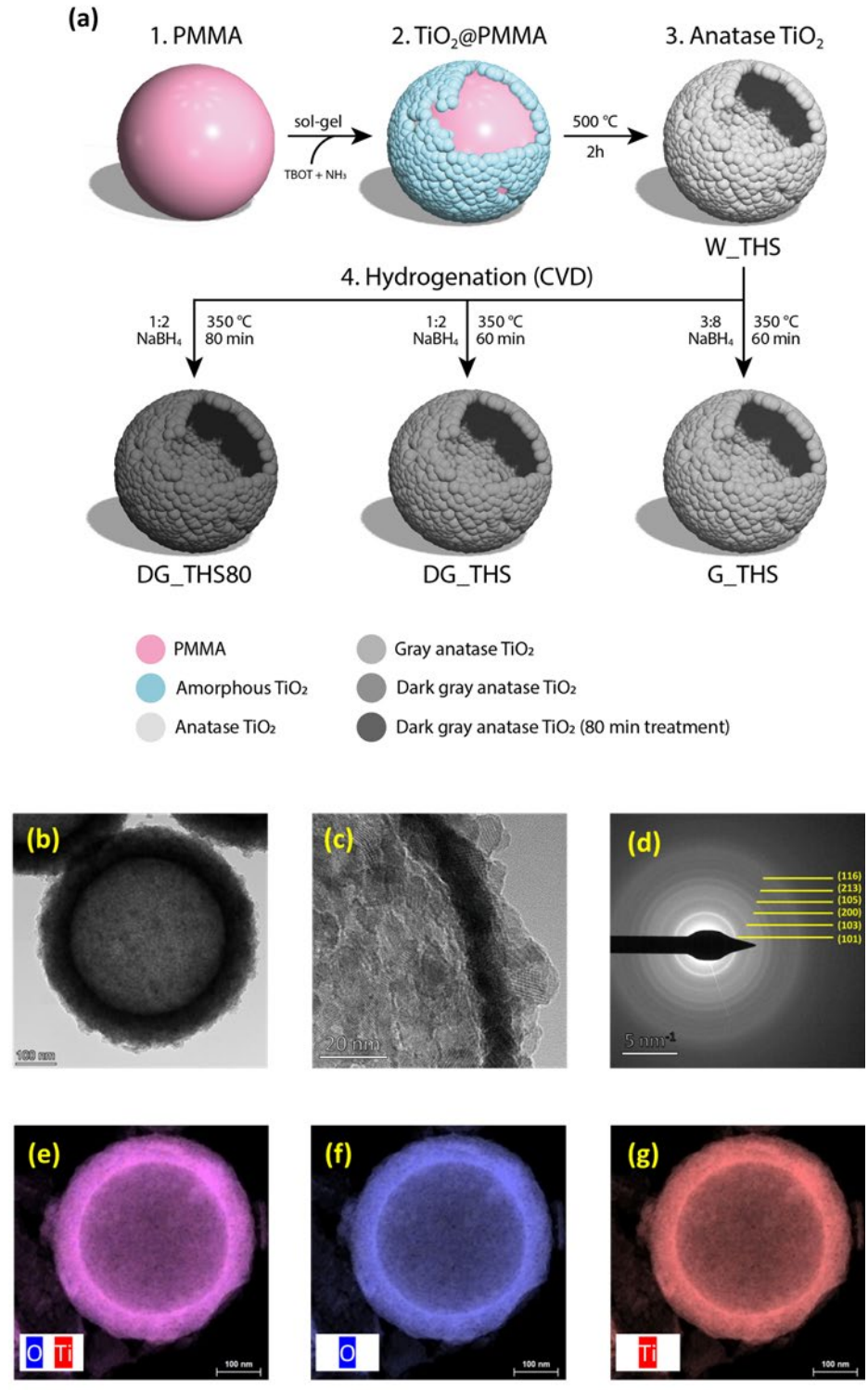

Figure 4.1 (a) Synthesis scheme and **(b-g)** HRTEM analysis of W_THS sample. **(b, c)** HRTEM images at different magnifications. **(d)** SAED pattern with Miller indexes. **(e-g)** EDS images showing the presence of Ti and O only.

All the THSs samples showed the characteristic diffraction peaks of anatase phase at 2θ values 25.3°, 36.9°, 37.8°, 38.6°, 48.1°, 53.9°, 55.1° and 62.7° in agreement with the JCPDS (Joint Committee on Powder Diffraction Standards) card number 21-1272 (**Figure 4.2a**).

As confirmed by both XRD (**Figure 4.2a**) and HR-TEM analysis (**Figure 4.1b-d**), the anatase crystalline structure was preserved during the hydrogenation treatment for all the colored THSs. Samples showed a polycrystalline structure as confirmed by the clearly visible lattice fringes in **Figure 4.1c** and the presence of concentric circles from the selected area electron diffraction (SAED) pattern (**Figure 4.1d**). In addition, the lattice spacing, and the crystal phase revealed by the SAED analysis agreed with XRD results. A preliminary elemental analysis was performed for selected W-THS through energy dispersive X-ray spectroscopy (EDX), revealing the presence of Ti and O species only (**Figure 4.1e-g**).

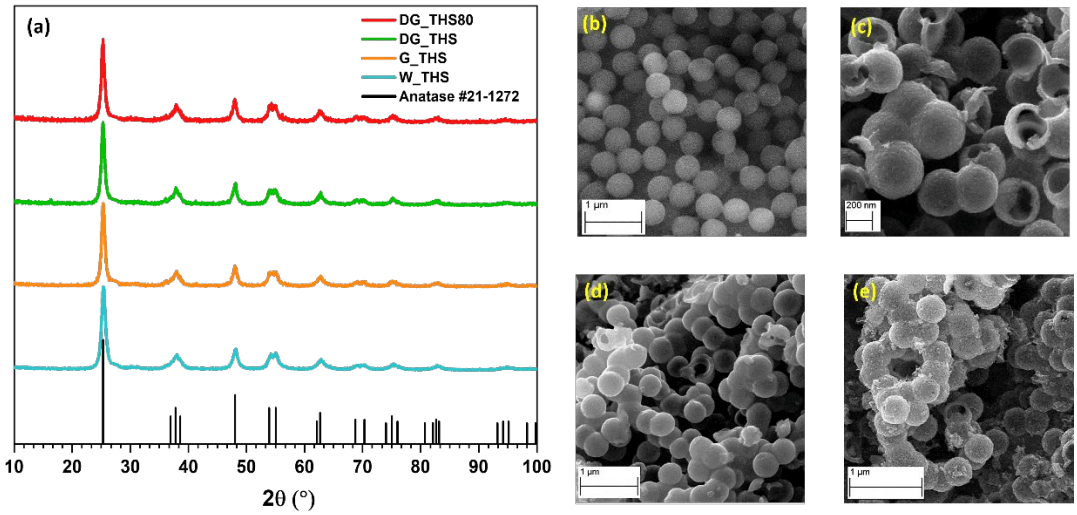

Figure 4.2 (a) X-ray diffraction patterns of THSs samples with TiO_2 anatase pdf #21-1272 as reference. FE-SEM images of **(b)** PMMA spheres **(c)** W_THS, **(d)** G_THS and **(e)** DG_THS80 at different magnifications.

4.1.2 Detection of defects

Optical characterization is of extreme importance not only to understand the optical behavior of the materials but also to investigate the electronic structure and the presence of defects. The diffuse reflectance UV-visible-near infrared (DRUV-Vis-NIR) spectra for all THS samples are showing the main absorption feature associated with the optical bandgap (**Figure 4.3a**), which is responsible for the creation of a strong absorption edge at approximately 390 nm (equivalent to ⌣3.1 eV). Specifically, the spectrum of W_THS highlights the efficacy of the hollow structure,[14] resulting in a flat reflectivity below 75% across the entire range from 390 to 1200 nm. Upon hydrogenation, an additional wide absorption band emerges starting from 500 nm and extending to (at least) 1200 nm. This band is absent in the W_THS sample while its intensity increases by increasing the wavelengths and the hydrogenation degree. The enhancement of light absorption within the visible to near-infrared (vis-NIR) range is attributed to disordered surface layer and the existence of surface defects (such as oxygen vacancies) generated by the hydrogenation process.[14,16,21] It has to be pointed out that the interplay between a well-suited morphology and the hydrogenation treatment resulted in an enhancement of light absorption in a broader spectral range. Furthermore, the onset of the absorption feature in the lower-energy spectral region (higher than 500 nm) can be elucidated by the existence of localized states below the TiO_2 conduction band (CB) minimum, introduced by defects such as oxygen vacancies (Ov) and Ti^{3+} centers.[22]

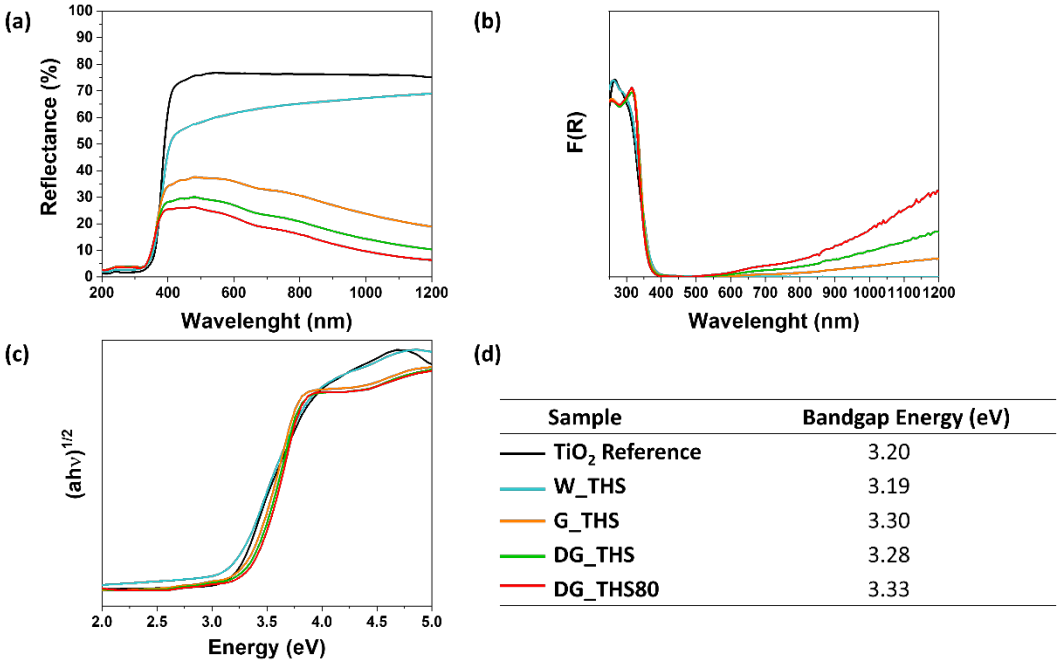

Figure 4.3 (a) DRUV-Vis-NIR spectra; **(b)** F(R) spectra calculated through Kubelka-Munk functions; **(c)** Tauc Plots and **(d)** bandgap energies comparison for all the samples, including the TiO_2 Reference.

The combination of synchrotron-based X-ray photoemission spectroscopy (XPS, VUV-Photoemission beamline) and electron paramagnetic resonance (EPR) allowed for a comprehensive examination of these localized states. The XPS data offers insights into the near-surface region of THS catalysts (**Figure 4.4a**). Across all the samples, the O^{2-}/Ti^{4+} stoichiometric ratio (**Figure 4.4a**, P1/D1), normalized to the respective photoemission cross sections at 750 eV (0.24 for O*1s* and 0.7 for Ti*2p*)[23,24] is approximately 2. Variations observed in the high binding energy region of O*1s* spectra (**Figure 4.4a**, P2-P4) are attributed to the presence of adsorbed species like OH, C-O, C-OH, and H_2O.[25,26] The increased signal of H_2O (**Figure 4.4a**, P4/P1) in darker gray THSs is particularly noticeable, indicating a higher surface density of Ov that tend to attract and bind an increasing number of water molecules. The amount of Ti^{3+} was evident and constant in Ti*2p* core levels for all THSs (**Figure 4.4a**, D2).

Complementing the XPS results, EPR data (**Figure 4.4b**) provide a deeper understanding of the bulk electronic structure of THSs.

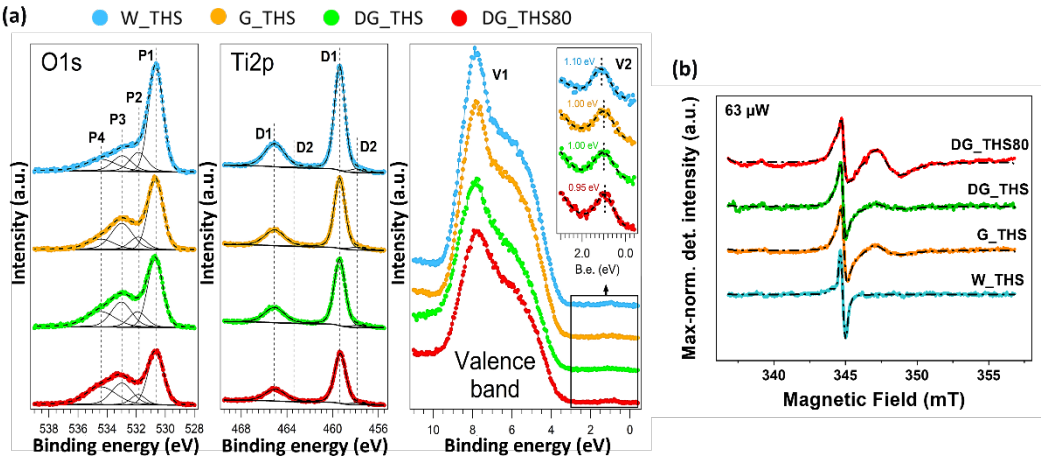

Figure 4.4 (a) O*1s*, Ti*2p* (photon energy 750 eV) and valence band (photon energy 469 eV) XPS spectra of THSs. **(b)** Stacked EPR spectra of the THSs.

The sharp peak at approximately 345 mT was associated with bulk Ov,[27,28] formed during the thermal treatment at 500 °C and persisting through the subsequent CVD hydrogenation treatment process at lower temperatures (**Figure 4.1a**, step 4). Conversely, the broader peak at higher magnetic field emerges only after the hydrogenation treatment, thus indicating the presence of bulk Ti^{3+} defects (color centers)[27,28] and revealing the optical characteristics of colored-THSs.

The XPS valence band analysis (**Figure 4.4a**, valence band) conducted under resonant conditions (photon energy 469 eV) offers higher sensitivity to probe defect states within the bandgap of TiO_2. Notably, strong O*2p*-related states between ~ 3 and 10 eV (V1) and low-intensity defect states at ~ 1 eV (**Figure 4.4a** V2, depicted in the inset) are detected in all THSs. The V2/V1 ratio can be used to estimate the defect concentrations in the near-surface region of the samples. The increasing of surface Ov concentration, resulting from the CVD treatments, is evident. Specifically, the ratio V2/V1 shows an increase in darker gray THSs, while the presence of Ti^{3+} remains consistent at the surface. This correlation highlights the pivotal role of

surface Ov in strongly improving the optical absorption and as described in the following paragraph, the overall photocatalytic activity observed for colored THSs.

4.1.3 Photodegradation of Ciprofloxacin

The photocatalytic activity was evaluated under simulated solar light irradiation in an aqueous solution of the target molecule (CIP) and at room temperature (**Figure 4.5a**). For all the samples, including TiO_2 Reference (Anatase, Merck $\geq$ 99.5%), the CIP main absorbance peak located at 273 nm was monitored for 360 min. The persistency of CIP in water under sunlight irradiation was confirmed by the slight decrease in its C/C_0 curve ($\sim$13%). As widely stated in **Chapter 2**, the efficiency of photocatalytic processes, such as photodegradation, is strongly influenced by the type of adsorption phenomena which are affected by several factors including the pH of the solution. The charge of both TiO_2 surface and CIP molecules thus, their interaction, are significantly influenced by the solution pH and their charges. As reported in literature, CIP molecules can assume different charges according to the pH of the solution. In detail, CIP will be in its anionic form in presence of alkali solutions, cationic form in acidic conditions and zwitterionic form at neutral pH. Additionally, the zero-point charge (pH_{zpc}), known as the pH at which the catalyst surface is free of charge, is strongly affected by the hydrogenation content. Since the pH_{zpc} of hydrogenated TiO_2 particles in water is below the neutral pH, it can be assumed that colored-THSs show a negatively charged surface, being stabilized by repulsive forces. Hence, the overall interaction between the surface of the colored-THSs with water molecules and, consequently, the adsorption of CIP, is altered. As a result, after 60 minutes of dark equilibration, CIP adsorption on the photocatalysts surface ranged from 2% for W_THS to 20% for DG_THS80 and 30% for TiO_2 Reference.

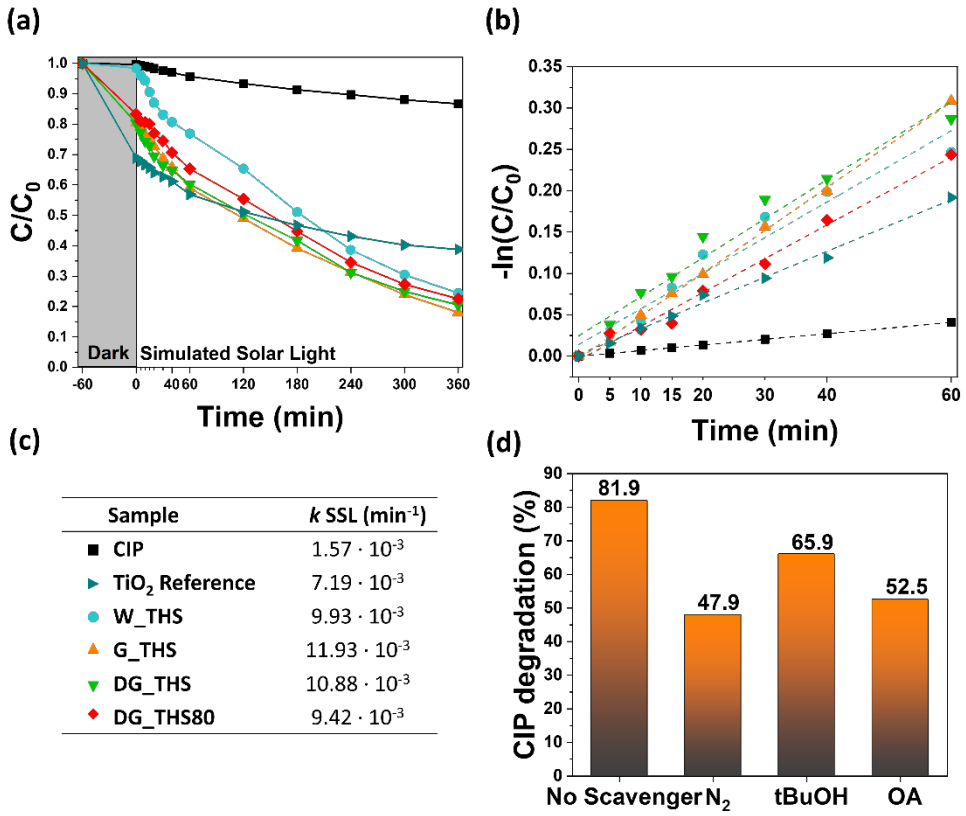

Figure 4.5 (a) Photocatalytic degradation of CIP as a function of irradiation time with and without catalysts (CIP curve) under simulated solar light irradiation. **(b)** CIP degradation kinetics with linear fits of the experimental data in dashed lines. **(c)** Legend and kinetic constant values for all the samples under simulated solar light (SSL). **(d)** Scavenger experiments of the active species for the degradation of CIP in presence of G_THS.

Upon 360 min under simulated solar light irradiation, all the synthesized samples exhibited superior degradation rate of CIP with respect to TiO_2 Reference (CIP degradation only at 61.2% with a kinetic constant of 7.2 10^{-3} · min^{-1}). The best performing samples were G_THS and DG_THS. In detail, G_THS degraded 81.9% of CIP in 6 hours with a kinetic constant of 11.9 10^{-3} · min^{-1}. Remarkably, DG_THS80 with its highest hydrogenation content, showed reduced photocatalytic activity among the colored samples. The role of surface defects such as Ti^{3+} centers and Ov, notably present in DG_THS80, have been widely discussed in literature and as mentioned in **Chapter 3**, their concentration has a strong impact on the overall photocatalytic activity.[29,30] Despite the increased absorbance ability toward higher wavelengths up to NIR region, a too high number of defects, acting as recombination centers for photogenerated electron hole pairs, may boost the recombination

rate and cause a decrease in the overall photocatalytic efficiency. In G_THS the lower amount of surface defects prevents charge-carriers recombination, simultaneously promoting the conversion of oxygen molecules into superoxide radicals, necessary for CIP photodegradation.[31] Therefore, achieving optimal photocatalysis requires a precise balance between light absorption and catalytic activity.

The main active species responsible for CIP degradation were investigated by performing free radical trapping experiments on G_THS, the best performing sample. Free radical trapping experiments are frequently reported in literature, using several types of scavengers. In this case, N_2 as superoxide radicals (O^{2-}) scavenger, Oxalic Acid (OA) as holes (h^+) scavenger and tert-butanol (tBuOH) as OH scavenger was selected. As can be noticed from **Figure 4.5d**, G_THS photocatalytic efficiency is strongly inhibited when N_2 and OA are introduced into the system, while barely influenced in presence of tBuOH. Therefore, it can be assumed that superoxide radicals and holes should be the two major reactive species involved in the CIP degradation by G_THS under simulated solar light irradiation.

The hydrogenated THSs exhibit enhanced absorbance in the visible region. Thus, for the best performing sample G_THS, photocatalytic activity was also evaluated under both UV and Vis light to compare the obtained results and examine wavelength dependence. As expected, G_THS displayed notable activity under both UV and visible light, achieving CIP degradation rates of 98% and 54%, respectively, following 180 minutes of irradiation. Furthermore, a 3-cycle stability and reusability test was carried out, highlighting not only a slight improvement in degradation efficiency (+ 5%) but also a decline in CIP adsorption during the dark period from a 20% in the first cycle to an 11% in the last cycle. This behavior suggests the adsorption of degradation by-products on active sites, facilitating faster radical production. Further details on photocatalytic tests under UV and Vis irradiation and stability tests can be found in **Paper-I Supporting Information**.

4.1.4 Conclusions

In this section an affordable and easy way of synthesis to produce tunable hydrogenated or colored titania hollow spheres (THSs) composed of hierarchically assembled nanoparticles has been proposed. The hollow microstructures, combined with the defect engineered surface, enable the utilization of solar light irradiation toward a broader spectral range (200-1200 nm) compared to the untreated counterpart. In addition, a highly efficient exploitation of photogenerated charges for the photocatalytic degradation of a common water contaminant, like CIP, was recorded. The most effective photocatalyst showed an 82% degradation efficiency under simulated solar light irradiation, at room temperature and standard atmospheric pressure. The investigation revealed a correlation between the hydrogenation degree, associated with the presence of Ov on the catalyst surface, and the enhancement of both optical absorption and overall photocatalytic activity of THS samples. Additionally, as monitored by magnetic resonance, it has been highlighted that the hydrogenation treatment process undoubtedly introduces defects not present in the pristine white THS.

Taking advantage of the design, the recorded functionality, and comprehension of the physicochemical properties, colored-THSs may represent a promising strategy to develop a new generation of efficient photocatalysts. Consequently, this section offers insight to produce cheap, environmentally friendly, stable and efficient photocatalysts, showcasing great potential for the advancement of new technology, concerning the application not only for water remediation, but also for energy in solar fuel production.

Paper-II

L. Liccardo, P. Moras, P. M. Sheverdyaeva, A. Vomiero, A. Caballero, G. Colón, E. Moretti, Surface Defect Engineered Nano-Cu/TiO_2 Photocatalysts for Hydrogen Production. *Adv. Sustainable Syst.* 2023, 2300418. https://doi.org/10.1002/adsu.202300418

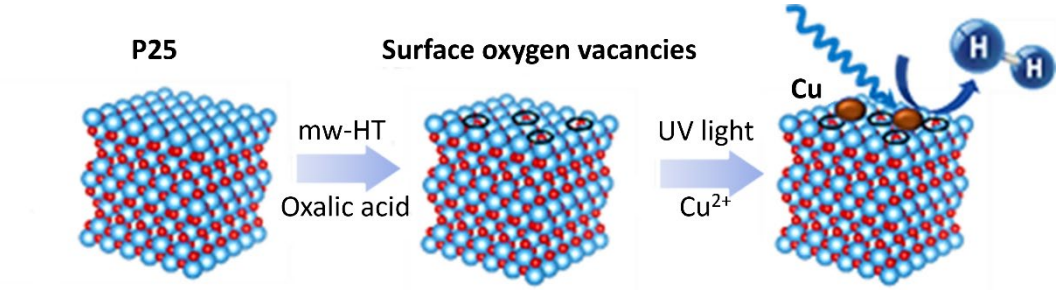

4.2 Surface defects in nano-Cu/TiO_2 particles

Chapter 1 deeply examines how recent events have caused a global energy crisis in which natural gas is at the forefront, significantly leading to an increase in electricity costs worldwide.[32] In detail, concern for the potential return to the high use of traditional biomass, resulting in increased greenhouse gas emissions, was highlighted. Oil and coal offer temporary solutions, which are inadequate in the long run.[33] Consequently, embracing low-emission alternatives as a more sustainable energy solution should be center stage.

In this frame, a clean-energy economy toward renewable energy sources is emerging and hydrogen, as a clean energy carrier, has a leading role in this transition. Hydrogen is considered an ideal candidate thanks to its versatility, including the possibility to be generated from several processes and renewable sources, such as biomass or water, by using solar energy that holds the ability to provide energy exceeding the daily total global energy consumption.[34]

In the field of heterogeneous photocatalysis, alcohol photocatalytic reforming for the H_2 production stands as a good option, compared with other strategies such as conventional water splitting.[11,35] In general, as widely stated in **Chapter 2**, engineered semiconductor photocatalysts with customized properties are essential to reach high photocatalytic activity. Thus, processes such as side or back reactions, rapid photogenerated charge-carriers recombination, and catalyst deactivation due to low stability should be avoided or strongly delayed.[36,37] Overcoming these issues is crucial for the practical application of these systems on a larger scale.

As anticipated in **Chapter 3**, among various photocatalysts, commercial titania P25 is widely used as target material thanks to its outstanding performances.[34] P25 is composed by a mixture of anatase and rutile phases with an average crystallite size of ~20 nm, having all the essential features to display strong photoactivity that can be further improved.[38,39] Typically, enhancing TiO_2 efficiency involves a series of approaches to tune its optical and electronic properties.[40–45] This can be achieved

by metal co-catalyst loading, while simultaneously varying the chemical surface composition.[38,46,47] In fact, metal co-catalyst loading is recognized as a good strategy to hinder the fast charge-carriers recombination. However, together with this conventional method, surface defects engineering has emerged as a novel approach to enhance photocatalytic efficiency. Surface defects play a crucial role by inducing alterations in the charge distribution around titanium and oxygen atoms inside TiO_2 lattice, by enhancing the photocarriers separation efficiency, promoting the adsorption of sacrificial agents and finally, extending the range of light absorption of the material.[48]

Therefore, this section examines surface defect engineered nano-Cu/TiO_2 (Cu2.0/gOx/P25 200) photocatalysts synthesized through an easy and cheap microwave (mw)-assisted hydrothermal synthesis, followed by the loading of copper metal co-catalyst through *in-situ* chemical reduction deposition procedure. In detail, the combination of different methods, like surface engineering and metal co-catalyst, is proposed as a feasible strategy to improve commercial P25 properties. Cu co-catalyst seem to enhance e^-—h^+ pairs separation efficiency, boosting the ability to perform photochemical reactions.[48] Whereas the introduction of surface defects, thanks to the presence of mid-gap states below TiO_2 CB, leads to an improvement of the absorbance ability toward visible light, and promotes electron transfer increasing the photocatalytic activity for the H_2 production. Additionally, benefiting from the excellent P25 titania properties, including high surface-to-volume ratio and stability, results in an easy way to improve the overall performance in light-driven chemical processes.

4.2.1 Morphology and crystal structure

Surface defects engineered nano-TiO_2 photocatalysts were obtained through an easy mw-assisted hydrothermal synthesis, preparing a suspension of commercial P25 titania in an aqueous solution of oxalic acid (Ox) in different molar ratios (Ox/P25). Samples were labeled as gOx/P25 200, where *g* stands for the grams of

oxalic acid and 200 for the selected temperature in Celsius degrees (**Figure 4.6a**, step 1 and 2). Subsequently, during the photocatalytic tests under UV light irradiation (using a 365 nm UV LED array equipped in the photoreactor), an in-situ photodeposition was used to add nominal 2.0 wt% of Cu (labeled as $Cu_{2.0}$) co-catalyst and gain the final photocatalysts labeled as $Cu_{2.0}$/gOx/P25 200.

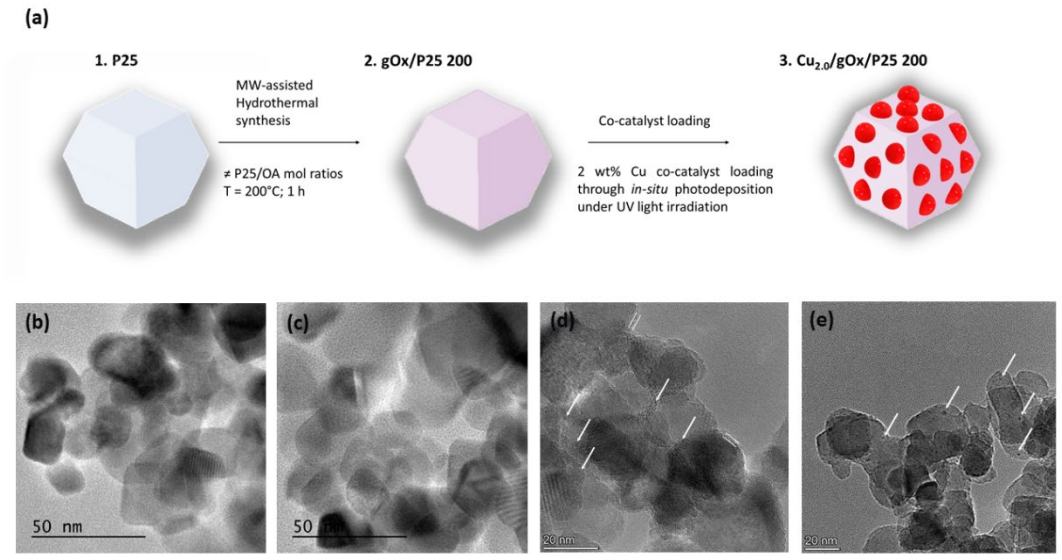

Figure 4.1 (a) Synthesis scheme. TEM images of **(b)** bare P25 and **(c)** 2.5Ox/P25 200. HR-TEM images for **(d)** $Cu_{2.0}$/3.0Ox/P25 200 and **(e)** $Cu_{2.0}$/P25 200 with white arrows indicating Cu clusters.

The crystallinity of the as-synthesized materials was investigated by XRD and micro-Raman analysis. As depicted in **Figure 4.7a, b** all the gOx/P25 200 samples displayed the typical pattern of commercial P25, including both rutile and anatase phases. From XRD patterns (**Figure 4.7a**) and according to JCPDS card number 21-1272, anatase phase is the most evident from the intense peaks at 2θ 25.3°, 37.7°, 48.0°, 53.9° and 55.02° related to (101), (004), (200), (105) and (211) reflections. The oxalic acid treatment did not affect the overall crystal structure of commercial P25. In fact, all the gOx/P25 200 samples retained the crystal structure of the bare P25. This is also confirmed by the more sensitive micro-Raman analysis. In fact, as shown in **Figure 4.7b**, the TiO_2 anatase six main Raman active modes (A_{1g} + $2B_{1g}$ + $3E_g$ symmetries) are detected at 143, 196, 398, 519 (overlapped with 515 cm^{-1} band), 639 cm^{-1}, corresponding to E_g, E_g, B_{1g}, A_{1g}, B_{1g} and E_g vibrational modes. [38,49] Expectedly, TiO_2 rutile Raman active modes can only be estimated at 140 (B_{1g}), 235

(multiphoton process), 445 (E_g), 609 (A_{1g}), and 825 cm^{-1} (B_{2g}).[50] Moreover, the addition of oxalic acid during the hydrothermal synthesis did not influence either the shape or the morphological and textural properties of commercial P25 as evidenced by BET (Brunauer-Emmett-Teller) analysis, performed through N_2 physisorption, and TEM micrographs (**Figure 4.6b, c** and **Figure 4.7c, d**).

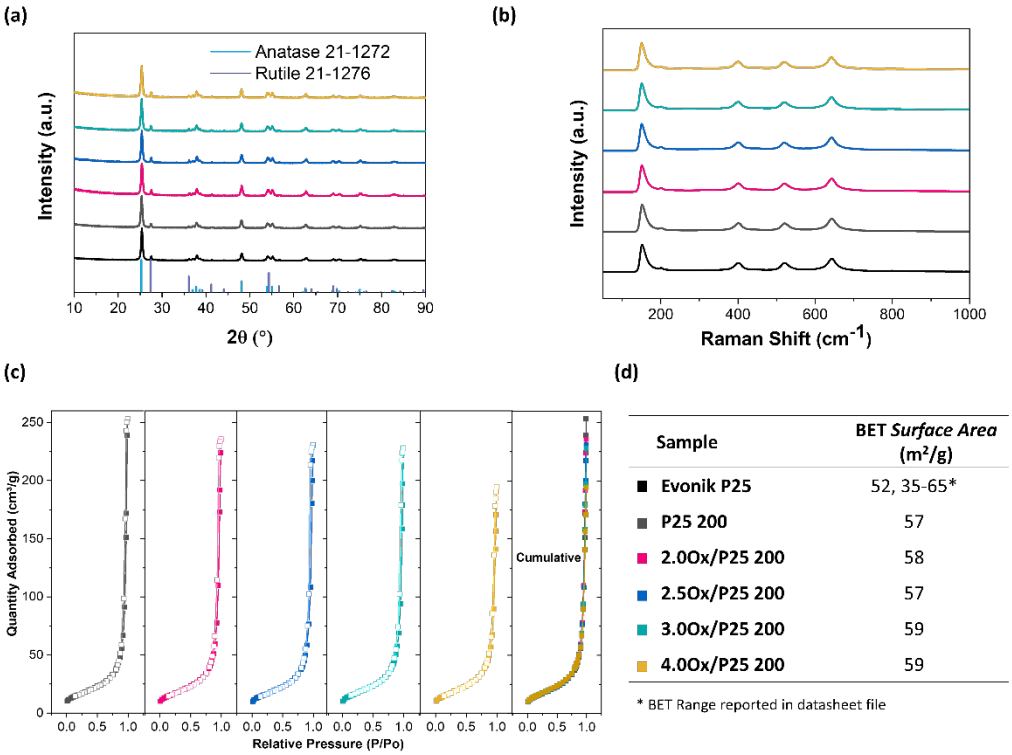

Figure 4.2 (a) XRD patterns; **(b)** Raman spectra; **(c)** N_2 adsorption-desorption isotherms for P25 200 and gOx/P25 200 samples; **(d)** BET surface area values for all the samples including the Evonik P25 reference. All the curves in (a), (b) and (c) follow the color palette reported in (d).

In detail, no relevant differences on BET surface area values, calculated from N_2 adsorption-desorption isotherms, were detected and all the gOx/P25 200 samples showed similar values compared to the bare commercial P25 (**Figure 4.7d**). These results suggested that the oxalic acid treatment process led to surface modifications. Observing the HR-TEM micrographs in **Figure 4.6d, e**, it is evident that the hydrothermal treatment in acidic conditions led to an increase in the surface rugosity of gOx/P25 200 samples. This is confirmed by the loss of anatase planes and the presence of a 2-3 nm well-defined amorphous shell at the surface, not occurring in the P25 sample hydrothermally treated with water (**Figure 4.6d** vs **4.6e**). In

addition, surface modifications have also affected Cu co-catalyst deposition (white arrows in **Figure 4.6d, e**), thus the size of Cu clusters was smaller in $Cu_{2.0}$/gOx/P25 200 samples than P25 200 sample (i.e., 1-2 nm versus 5-6 nm for $Cu_{2.0}$/3.0Ox/P25 200 and $Cu_{2.0}$/P25 200, respectively).

4.2.2 Detection of defects

As already mentioned, the presence of defects such as Ti^{3+} and oxygen vacancies, resulting in the introduction of continuos energy band states directly below the CB of TiO_2, can be investigated by combining the use of optical characterizations and X-ray photoemission spectroscopy. The DRUV-Vis-NIR spectra (**Figure 4.8a**) showed the the main absorption feature related to the typical optical bandgap of TiO_2. This feature is responsible for the strong absorption edge at ~370 nm and it is associated to the O^{2-} (2p) → Ti^{4+} (3d) trasition. Noticeably, a slight red-shift of the primary band towards higher wavelengths compared to the pure P25 reference was observed. The oxalic acid hydrothermal treatment at 200°C enhanced the absorbance ability within the 350-400 nm range, when compared to the pure P25 reference (**Figure 4.8b**). This prompted consideration toward the existence of surface defects, like Ti^{3+} species and oxygen vacancies as supported from a slight decrease of the bandgap energy values, calculated from the Tauc Plot through the intercept method (**Figure 4.8c, d**).[48,51] Since the enhancement of light absorption in the vis-NIR region can be enabled by the presence of a disordered surface layer or surface defects[14,16,21], the NIR region was also explored (refer to **Figure 4.8a,b**). Clear differences across all the spectra compared to the untreated P25 were detected. Notably, a broad band centered at 1450 nm and an increase in the absorbance ability starting from 850 nm were observed. The absorption feature at 1450 nm was likely due to water molecules adsorbed onto the surface of the treated samples, P25 200 and gOx/P25 200, as opposed to the reference untreated P25. Both the use of oxalic acid and the 200°C temperature treatment appeared

to induce surface modifications, altering the composition of functional groups exposed on the surface of the photocatalysts.

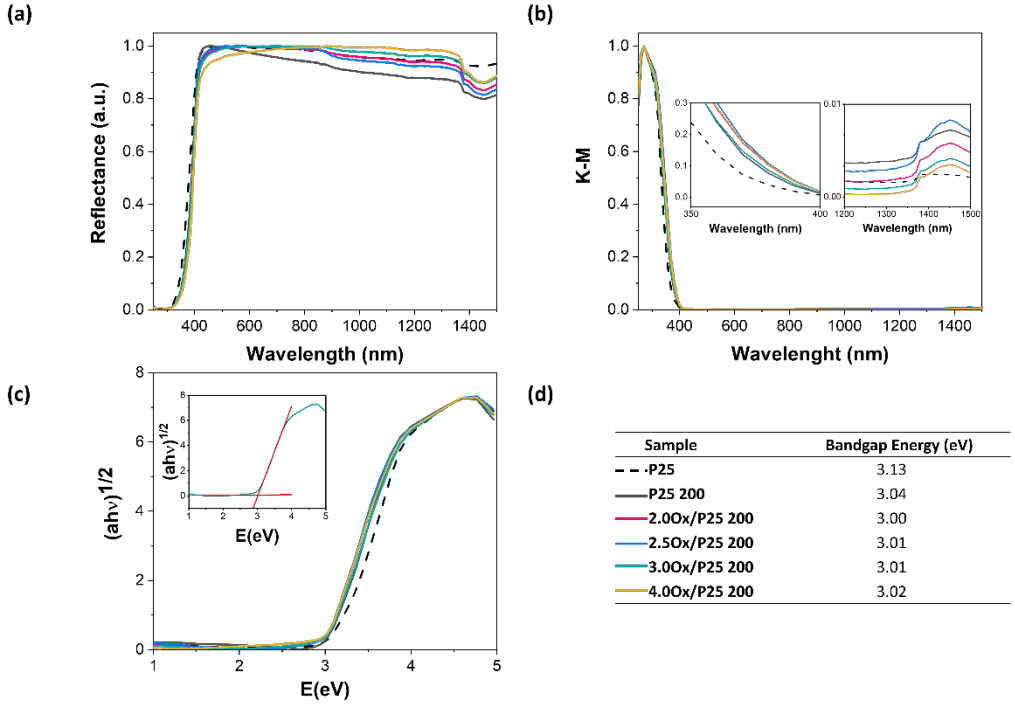

Figure 4.3 (a) DRUV-vis-NIR spectra; **(b)** Kubelka-Munk functions with inset-graphs focusing on the band changes in UV and NIR region; **(c)** Tauc plots and **(d)** Bandgap energies comparison for all the samples, including Evonik P25 reference.

Additionally, the appearance of that broad band at 1450 nm, could be attributed to a higher number of surface oxygen vacancies, also known for their affinity to bind water molecules.[46] This was also proven by XPS analysis. The XPS core level analysis for all the samples is shown in **Figure 4.9a**. All the core levels spectra were acquired at hν = 750 eV. Focusing on the O*1s* spectra from lower to higher binding energies, the fitted four components correspond to O^{2-} of stoichiometric TiO_2 (530.20 - 530.40 eV), -OH groups adsorbed on TiO_2 surface (531.60 - 532.20 eV), -O (532.65 - 532.95 eV) and -OH (534.05 - 534.3 eV) groups bound to C from surface contaminants or H_2O molecules adsorbed on TiO_2 surface.[25,26] Notably, the latter component displayed an increasing trend along the spectra, potentially indicating a rising density of surface oxygen vacancies. Concerning the Ti*2p* spectra, no

evidence of Ti^{3+} centers was detected, as evidenced by the fitted doublet associated with Ti^{4+}.

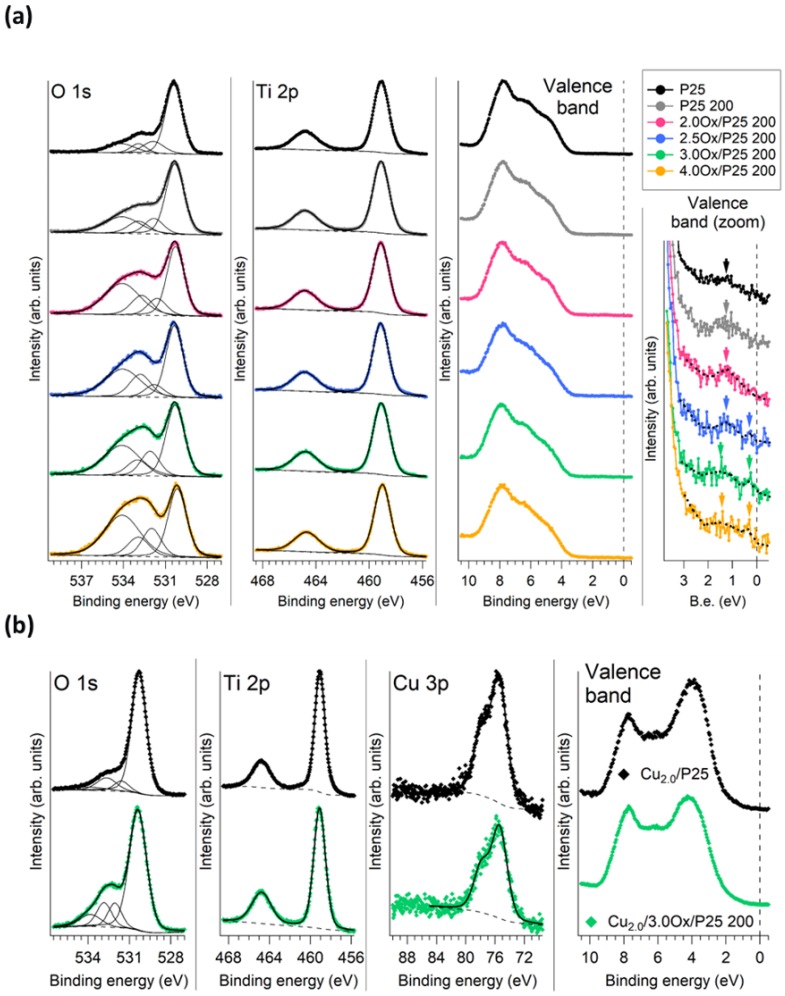

Figure 4.4 (a) O1s, Ti2p and valence band spectra of the P25, P25 200 and gOx/P25 200 samples. The zoomed valence band spectra indicate the presence of defect states (arrows) in the gap of all samples. Dotted lines are guides to the eye for the identification of the defect-related peaks. **(b)** O1s, Ti2p, Cu3p and valence band spectra of the $Cu_{2.0}$/P25 (top) and $Cu_{2.0}$/3.0Ox/P25 200 (bottom) samples.

The latter statement is also confirmed by the O/Ti atomic ratios (**Table 4.1**), derived from the area of O^{2-} peak and Ti^{4+} doublet normalized for the respective photoemission cross sections at hv = 750 eV (0.24 and 0.7).[52] In fact, for all the samples it is 2.09±0.09, thus very close to the stoichiometric ratio.

Table 4.1 O/Ti ratio in P25, P25 200 and gOx/P25 200 samples.

Sample	O/Ti ratio
P25	2.10
P25 200	2.05
2.0Ox/P25 200	2.02
2.5Ox/P25 200	2.12
3.0Ox/P25 200	2.17
4.0Ox/P25 200	2.12

The valence band spectra at hv = 468 eV showed minimal differences in the O2p-derived states (4-9 eV binding energy), but in the gap region (**Figure 4.9a**, valence band zoom), a feature related to O vacancy at 1.25 eV increased sequentially for P25, P25 200, and 2.0Ox/P25 200 samples. Conversely, the other three samples exhibited a significant broadening of this feature, forming two peaks at 1.45 and 0.30 eV. This behavior can be associated with surface modifications induced by oxalic acid treatments, giving rise to the observed amorphous shell in **Figure 4.6d**. Even if the discussed data do not allow to determine the exact origin of these new mid-gap states, their location aligns with the defect states near the bottom of TiO_2 CB.

Further evidence about the presence of surface modifications came from photoluminescence (PL) emission spectroscopy. As widely discussed in **Chapter 2** and **3**, emission processes in semiconductors are highly related to photogenerated charge carriers recombination[53] and one of the most significant TiO_2 drawbacks is its fast e^-—h^+ pairs recombination. Moreover, the higher the recombination rate, the higher the PL intensity. Therefore, PL emission spectra for all gOX/P25 200 samples (including P25 reference) in the range 380-600 nm with an excitation wavelength of 350 nm were recorded (**Figure 4.10**). As expected, the highest emission intensity

was acquired for bare P25 catalyst (dashed black line in **Figure 4.10**). It is important to highlight that non-radiative recombination pathways can reduce the overall PL intensity. However, considering similar non-radiative recombination channels across all samples, the existence of surface defects or adsorbed water molecules reduced the rate of radiative recombination, leading to decreased emission intensities for all the treated samples. Oxygen vacancies, i.e. the presence of -OH groups or H_2O molecules adsorbed on TiO_2 surface, typically work as trapping centers for photogenerated electrons, decreasing the e^-—h^+ pairs radiative recombination by simultaneously promoting electron transfer processes.[54,55] Accordingly, the overall charge-carriers separation efficiency can be enhanced.

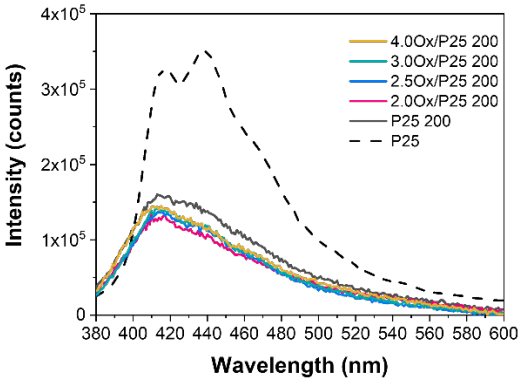

Figure 4.5 Photoluminescence spectra for all gOX/P25 200 samples, including Evonik P25 reference.

Additional investigations were conducted by performing XPS analysis on $Cu_{2.0}$/P25 and $Cu_{2.0}$/3Ox/P25 200 (**Figure 4.9b**). Notably, the Cu*3p* peaks binding energy ($Cu3p_{3/2}$ at 75.40 eV) and the lack of CuO characteristic correlation features toward high binding energies,[56] suggested the presence of Cu_2O on the surface of the Cu co-catalyst.[57] Moreover, the O*1s* spectra showed variations from the initial O*1s* spectra before the introduction of Cu in the relative weight of the peak at 530.40 eV, derived from the overlapping O^{2-} components of TiO_2 and Cu_2O. There were no significant differences in the Ti*2p* spectra, which were similar to those observed for bare P25 and gOx/P25 200 samples. The wide valence band feature at about 4.00 eV can be attributed to the Cu*3d* states of copper(I) surface oxide.

Interestingly, the photoemission signal originating from Cu4sp states, overlapping with the bandgap region of the P25 and 3.0Ox/P25 200 substrates, does not allow the identification of defect states close to the Fermi level.

4.2.3 H_2 production from methanol photoreforming

The H_2 production through methanol reforming under UV light, at room temperature and atmospheric pressure, was monitored to evaluate the photocatalytic activity of gOx/P25 200 samples. A continuous flow reactor purchased from Apria System was used. **Figure 4.11** shows the H_2 production rates and the apparent quantum yield (AQY) evolution over time referred to methanol photoreforming reaction. In addition, according to what is reported in literature and experimental results provided in this work, the band scheme diagram for e^-—h^+ pairs separation in $Cu_{2.0}$/gOx/P25 200 catalysts was proposed (**Figure 4.11d**).[54,55,58] As mentioned before, the loading of nominal 2.0 wt% Cu co-catalyst was obtained through the in-situ photoreduction while starting the photocatalytic test, meaning that copper nanoparticles (NPs) were created after the generation of e^-—h^+ pairs upon UV light irradiation, initiating oxidation and reduction reactions. During the photocatalysis, surface defects may have a crucial role acting as trapping states for electrons. Thus, e^-—h^+ pairs separation efficiency and reduction reactions rate can be improved, benefiting not only the formation of Cu NPs on the surface of gOx/P25 200 catalysts, but also the overall H_2 production. Therefore, as evidenced by a 15-minute delay on the H_2 production (see the flat region between 0 min and 30 min in **Figure 4.11a**), Cu NPs deposition occurs before the beginning of the photocatalytic reforming reaction. Observing the H_2 production rates curves in **Figure 4.11**, the mw-assisted hydrothermal synthesis significantly enhanced the photoreactivity when the oxalic acid loading exceeded the amount of 2.0 g but remained below 4.0 g. In fact, the optimum sample ($Cu_{2.0}$/3Ox/P25 200) showed excellent photocatalytic production rate of 6.8 $mmol \cdot h^{-1} \cdot g^{-1}$, twice higher rate than the pristine system ($Cu_{2.0}$/P25).

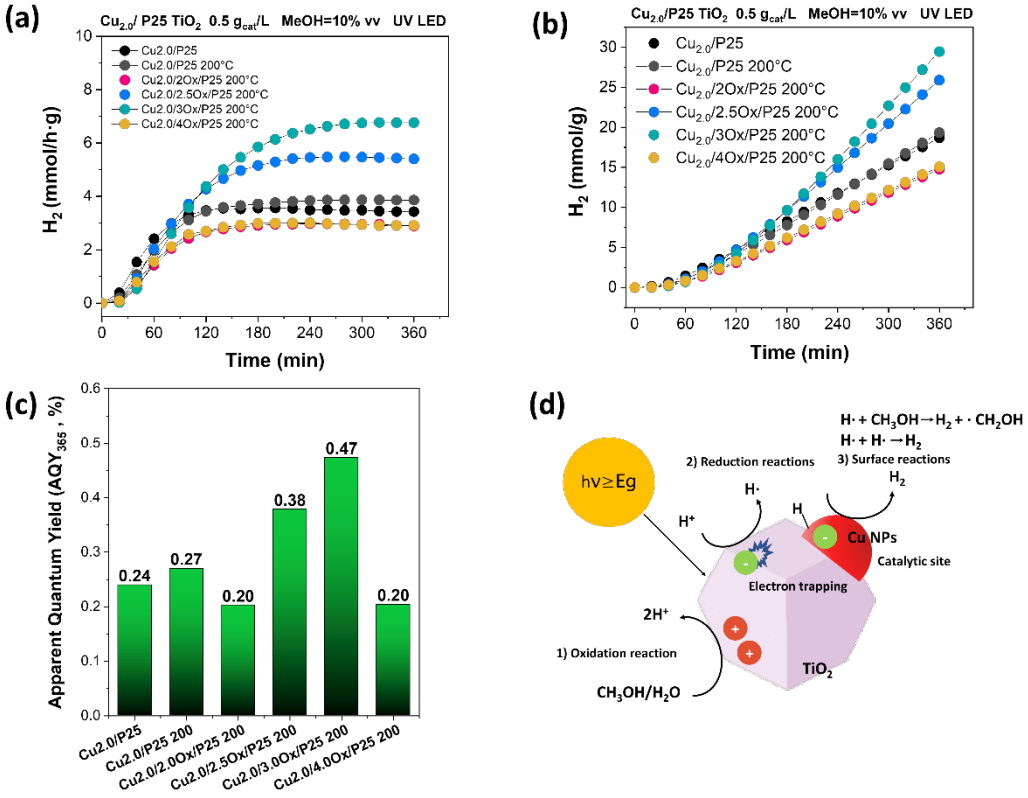

Figure 4.6 (a) H_2 production rates; **(b)** H_2 rates; **(c)** calculated AQYs for $Cu_{2.0}$/P25 $Cu_{2.0}$/P25 200 and $Cu_{2.0}$/gOx/P25 200 photocatalysts; **(d)** Scheme diagram of $Cu_{2.0}$/gOx/P25 200 system.

In addition, a stability test for the best performing sample ($Cu_{2.0}$/3Ox/P25 200) was carried out, showing a rather stable behavior after a long-time reaction time of 12 hours (**Figure 4.12**). It has to be pointed out that the amount of surface defects is a crucial factor that influences the overall H_2 production. In fact, when the system was treated with oxalic acid content lower than 2.5 g or higher than 3.0 g, the efficiency of the system decreased, as marked by H_2 yields evaluated at 6 hours of experiment expressed in mmol·g^{-1} and the calculated AQY (**Figure 4.11b, c**).

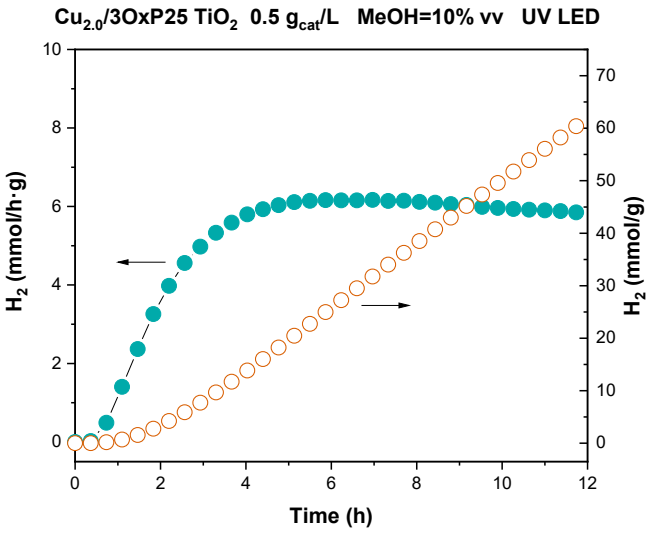

Figure 4.7 H_2 production rate and yield for $Cu_{2.0}$/3Ox/P25 200 photocatalysts system.

In this frame, $Cu_{2.0}$/3Ox/P25 200 sample demonstrates superior performance, achieving an H_2 yield of 29.5 mmol·g^{-1} and an AQY of 0.47%, surpassing $Cu_{2.0}$/P25 significantly. Additionally, the H_2 production reaction reached a steady state after 6 hours of irradiation (flat region after 180 min in **Figure 4.11a**), leading to the conclusion that the catalyst surface defects remained stable.

4.2.4 Conclusions

This section dealt with an innovative synthesis to improve the photoactivity of the well-known commercial P25 titania based on the combination of two approaches, namely surface-defects engineering and Cu co-catalyst loading through an in-situ photodeposition method. The photocatalytic activity of the as-synthesized $Cu_{2.0}$/gOx/P25 200 photocatalysts was evaluated monitoring the H_2 production through methanol photoreforming reaction under UV light irradiation. The best performing sample ($Cu_{2.0}$/3Ox/P25 200) exhibited outstanding photocatalytic H_2 production rate of 6.8 mmol·h^{-1}·g^{-1}, twice as high as the pristine $Cu_{2.0}$/P25 system, as also proven by the calculated AQY. The synergic use of XPS and optical

characterizations, drove to the conclusion that the notable enhancement in the final performances of the system can be attributed to the presence of surface defects, specifically oxygen vacancies, along with the use of copper as a co-catalyst. Surface-engineered commercial P25 nanoparticles coupled with Cu co-catalyst can enhance the electron-hole separation efficiency, extend the absorbance ability for the creation of mid-gap states below the TiO_2 CB and, consequently, boost the overall photocatalytic activity.

In conclusion, customizing the surface properties of commercial P25 presents a promising strategy to overcome the common limits of TiO_2-based photocatalysts. This approach opens the way for advancing new technologies for large-scale energy applications.

4.3 References

[1] M. Telkhozhayeva, B. Hirsch, R. Konar, E. Teblum, R. Lavi, M. Weitman, B. Malik, E. Moretti, G. D. Nessim, *Appl Catal B* **2022**, *318*, 121872.

[2] E. Moretti, E. Cattaruzza, C. Flora, A. Talon, E. Casini, A. Vomiero, *Appl Surf Sci* **2021**, *553*, 149535.

[3] E. E. Mitsika, C. Christophoridis, N. Kouinoglou, N. Lazaridis, C. K. Zacharis, K. Fytianos, *J Hazard Mater* **2021**, *403*, 123819.

[4] S. Wu, Y. H. Hu, *Chemical Engineering Journal* **2021**, *409*, 127739.

[5] C. Alberoni, I. Barroso-Martin, A. Infantes-Molina, E. Rodriguez-Castellon, A. Talon, H. Zhao, S. You, A. Vomiero, E. Moretti, *Mater Chem Front* **2021**, *5*, 4138.

[6] J. L. Wilkinson, A. B. A. Boxall, D. W. Kolpin, K. M. Y. Leung, R. W. S. Lai, D. Wong, R. Ntchantcho, J. Pizarro, J. Mart, S. Echeverr, J. Garric, A. Chaumot, P. Gibba, I. Kunchulia, S. Seidensticker, G. Lyberatos, J. M. Morales-salda, H. Kang, *PNAS* **2022**, *119*, 1.

[7] D. Ma, H. Yi, C. Lai, X. Liu, X. Huo, Z. An, L. Li, Y. Fu, B. Li, M. Zhang, L. Qin, S. Liu, L. Yang, *Chemosphere* **2021**, *275*, 130104.

[8] I. Concina, Z. H. Ibupoto, A. Vomiero, *Adv Energy Mater* **2017**, *7*, 1.

[9] J. Liu, N. Ma, W. Wu, Q. He, *Chemical Engineering Journal* **2020**, *393*, 124719.

[10] J. Xiong, J. Di, J. Xia, W. Zhu, H. Li, *Adv Funct Mater* **2018**, *28*, 1.

[11] L. Liccardo, E. Lushaj, L. Dal Compare, E. Moretti, A. Vomiero, *Small Science* **2022**, *2*, 2100104.

[12] L. Jiang, S. Zhou, J. Yang, H. Wang, H. Yu, H. Chen, Y. Zhao, X. Yuan, W. Chu, H. Li, *Adv Funct Mater* **2022**, *32*, 1.

[13] X. Liu, G. Zhu, X. Wang, X. Yuan, T. Lin, F. Huang, *Adv Energy Mater* **2016**, *6*, 1600452.

[14] Y. Wang, J. Cai, M. Wu, H. Zhang, M. Meng, Y. Tian, T. Ding, J. Gong, Z. Jiang, X. Li, *ACS Appl Mater Interfaces* **2016**, *8*, 23006.

[15] W. Hu, W. Zhou, K. Zhang, X. Zhang, L. Wang, B. Jiang, G. Tian, D. Zhao, H. Fu, *J Mater Chem A Mater* **2016**, *4*, 7495.

[16] X. Chen, L. Liu, P. Y. Yu, S. S. Mao, *Science* **2011**, *331*, 746.

[17] A. Naldoni, M. Altomare, G. Zoppellaro, N. Liu, Š. Kment, R. Zbořil, P. Schmuki, *ACS Catal* **2019**, *9*, 345.

[18] A. Naldoni, M. Allieta, S. Santangelo, M. Marelli, F. Fabbri, S. Cappelli, C. L. Bianchi, R. Psaro, V. Dal Santo, *J Am Chem Soc* **2012**, *134*, 7600.

[19] M. Plodinec, A. Gajović, G. Jakša, K. Žagar, M. Čeh, *J Alloys Compd* **2014**, *591*, 147.

[20] S. Chen, Y. Xiao, Y. Wang, Z. Hu, H. Zhao, W. Xie, *Nanomaterials* **2018**, *8*, 245.

[21] T. Xia, Y. Zhang, J. Murowchick, X. Chen, *Catal Today* **2014**, *225*, 2.

[22] T. S. Rajaraman, S. P. Parikh, V. G. Gandhi, *Chemical Engineering Journal* **2020**, *389*, 123918.

[23] J. J. Yeh, I. Lindau, *At Data Nucl Data Tables* **1985**, *32*, 1.

[24] X. Hu, X. Hu, Q. Peng, L. Zhou, X. Tan, L. Jiang, C. Tang, H. Wang, S. Liu, Y. Wang, Z. Ning, *Chemical Engineering Journal* **2020**, *380*, 122366.

[25] B. Gupta, N. Kumar, K. Panda, V. Kanan, S. Joshi, I. Visoly-Fisher, *Sci Rep* **2017**, *7*, 45030.

[26] I. Luciu, R. Bartali, N. Laidani, *J Phys D Appl Phys* **2012**, *45*, 345302.

[27] Y. Wang, K. I. Saitow, *Chemistry of Materials* **2020**, *32*, 9190.

[28] X. Pan, M. Q. Yang, X. Fu, N. Zhang, Y. J. Xu, *Nanoscale* **2013**, *5*, 3601.

[29] X. Wang, L. Mayrhofer, M. Hoefer, S. Estrade, L. Lopez-Conesa, H. Zhou, Y. Lin, F. Peiró, Z. Fan, H. Shen, L. Schaefer, M. Moseler, G. Braeuer, A. Waag, *Adv Energy Mater* **2019**, *9*, 1.

[30] Z. Li, S. Wang, J. Wu, W. Zhou, *Renewable and Sustainable Energy Reviews* **2022**, *156*, 111980.

[31] L. N. Costa, F. X. Nobre, A. O. Lobo, J. M. E. de Matos, *Environ Nanotechnol Monit Manag* **2021**, *16*, 100466.

[32] International Energy Agency, *International Energy Agency (IEA) World Energy Outlook 2022*, **2022**.

[33] World Meteorological Organization (WMO), *WMO Global Annual to Decadal Climate Update*, Geneva, **2023**.

[34] A. Kubacka, M. Fernández-García, G. Colón, *Chem Rev* **2012**, *112*, 1555.

[35] G. Colón, *Appl Catal A Gen* **2016**, *518*, 48.

[36] M. I. Maldonado, A. López-Martín, G. Colón, J. Peral, J. I. Martínez-Costa, S. Malato, *Appl Catal B* **2018**, *229*, 15.

[37] A. Ruiz-Aguirre, J. G. Villachica-Llamosas, M. I. Polo-López, A. Cabrera-Reina, G. Colón, J. Peral, S. Malato, *Energy* **2022**, *260*, 125199.

[38] H. Lu, B. Zhao, R. Pan, J. Yao, J. Qiu, L. Luo, Y. Liu, *RSC Adv* **2014**, *4*, 1128.

[39] L. Mino, G. Spoto, S. Bordiga, A. Zecchina, *Journal of Physical Chemistry C* **2012**, *116*, 17008.

[40] R. Hossain, M. A. Uddin, M. A. Khan, *The Journal of Physical Chemistry C* **2023**, *127*, 10897.

[41] C. J. Querebillo, *Nanomaterials* **2023**, *13*, 982.

[42] L. Liao, M. Wang, Z. Li, X. Wang, W. Zhou, *Nanomaterials* **2023**, *13*, 468.

[43] Y. Zhang, J. Yan, *Chemical Engineering Journal* **2023**, *472*, 144831.

[44] R. B. Domínguez-Espíndola, D. M. Arias, C. Rodríguez-González, P. J. Sebastian, *Appl Therm Eng* **2022**, *216*, 119009.

[45] L. Biswal, R. Mohanty, S. Nayak, K. Parida, *J Environ Chem Eng* **2022**, *10*, 107211.

[46] L. Liccardo, M. Bordin, P. M. Sheverdyaeva, M. Belli, P. Moras, A. Vomiero, E. Moretti, *Adv Funct Mater* **2023**, 2212486.

[47] K. C. Christoforidis, P. Fornasiero, *ChemCatChem* **2019**, *11*, 368.

[48] G. Colón, M. C. Hidalgo, G. Munuera, I. Ferino, M. G. Cutrufello, J. A. Navío, *Appl Catal B* **2006**, *63*, 45.

[49] S. Wang, L. Yi, J. E. Halpert, X. Lai, Y. Liu, H. Cao, R. Yu, D. Wang, Y. Li, *Small* **2012**, *8*, 265.

[50] M. González-Tejero, J. G. Villachica-Llamosas, A. Ruiz-Aguirre, G. Colón, *ACS Appl Energy Mater* **2023**, *6*, 4007.

[51] P. Kubelka, F. Munk, *Z. Tech. Phys* **1931**, *12*, 593.

[52] J. J. Yeh, *Atomic Calculation of Photoionization Cross-Section and Asymmetry Parameters*, Gordon And Breach Science Publishers, Langhorne, PE (USA), **1993**.

[53] J. Ma, T. J. Miao, J. Tang, *Chem Soc Rev* **2022**, *51*, 5777.

[54] L. Yan, C. Jing, *Journal of Physical Chemistry Letters* **2020**, *11*, 9485.

[55] E. Han, K. Vijayarangamuthu, J. sang Youn, Y. K. Park, S. C. Jung, K. J. Jeon, *Catal Today* **2018**, *303*, 305.

[56] I. Khalakhan, M. Vorokhta, X. Xie, L. Piliai, I. Matolínová, *J Electron Spectros Relat Phenomena* **2021**, *246*, 147027.

[57] T. Robert, M. Bartel, G. Offergeld, *Surf Sci* **1972**, *33*, 123.

[58] F. Platero, A. López-Martín, A. Caballero, G. Colón, *ChemCatChem* **2021**, *13*, 3878.

Chapter 5 – *Homojunctions & Heterojunctions*

The creation of homojunctions and heterojunctions is frequently regarded as an effective strategy for increasing the performance of TiO_2-based photocatalysts. The main body of this chapter is based on the appended Paper-III, provided at the end of the dissertation and available under license by Elsevier, and a submitted under review Paper-IV. In detail, the first section based on Paper-III is focused on TiO_2/TiO_{2-x} homojunctions, obtained by combining nanorods (NRs) hydrothermal growth and sputtering layer deposition technique, as easily recoverable photocatalysts for environmental applications in industrial processes such as wastewater purification from dyes. The second section, based on Paper-IV, is focused on heterojunction formation between atomic layered deposited TiO_2 ultrathin films and 1D hematite nanorod arrays. To assess the role of TiO_2 overlayer thickness, photoelectrochemical water splitting (PEC WS) tests of TiO_2/Fe_2O_3 heterojunctions were carried out, under both UV and visible light irradiation.

Paper-III

N. Spigariol,[1] L. Liccardo,[1] E. Lushaj, E. Rodríguez-Castellón, I. B. Martin, F. Polo, A. Vomiero, E. Cattaruzza, E. Moretti,

Titania nanorods array homojunction with sub-stoichiometric TiO_2 for enhanced methylene blue photodegradation. *Catalysis Today* 2023, 419, 114134. https://doi.org/10.1016/j.cattod.2023.114134

[1] These authors contributed equally to this work.

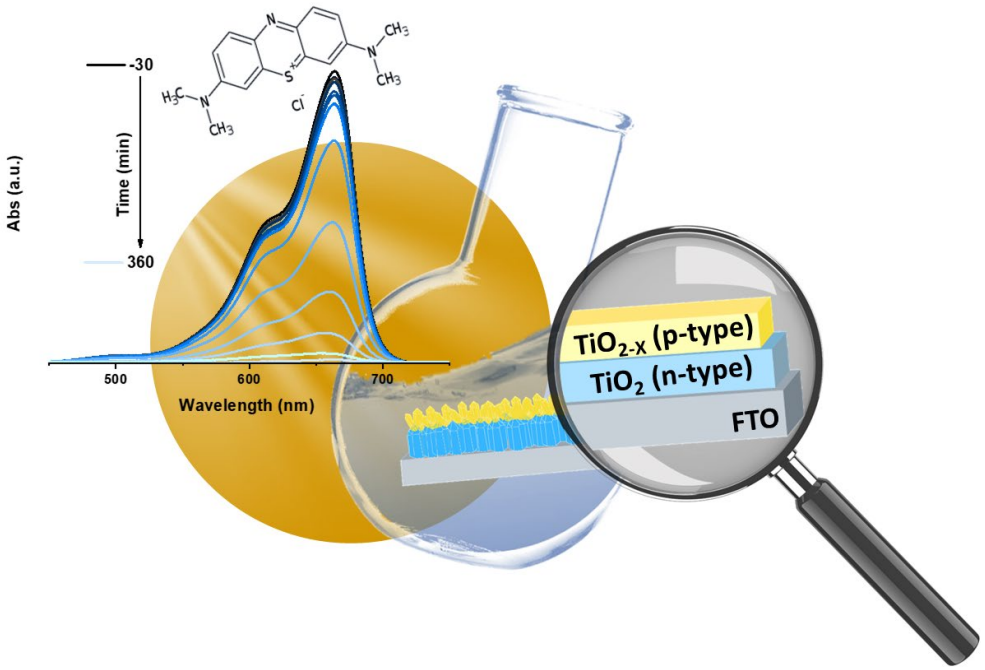

5.1 TiO_2 NRs array homojunctions

As described in **Chapter 1**, water pollution stands as a critical concern due to the high release and spread of numerous pollutants from industrial activities. Among all, the textile sector plays a pivotal role by releasing substantial amounts of dyes caused by the incomplete fabric fixation and resistance to oxidizing and reducing agents.[1–3] The United States Environmental Protection Agency (US EPA) mentions that around 40 liters of clean water per kilogram of fabrics are needed during a standard dyeing process. This leads to adverse effects on ecosystems and human health,[4,5] particularly when untreated wastewater is directly discharged into the environment. Thus, AOPs have been gaining attention to promote the photo-oxidation and degradation of a wide range of wastewater contaminants.[6]

As reported in **Chapter 2**, in his forward-thinking 1912 article, Giacomo Ciamician highlighted that photochemistry can be considered a sustainable way to easily perform chemical reactions and degrade pollutants by harnessing solar energy.[7] Thus, solar-driven heterogeneous photocatalysis is introduced for the great potential of semiconductors, including TiO_2, to interact with suitable wavelengths and produce e^-–h^+ pairs able to degrade dyes via radical reactions.[8,9]

In **Chapter 3**, the versatility and the ease of synthesis of TiO_2 nanomaterials have been pointed out. Several techniques can be applied to obtain the desired shape and morphology. In this frame, techniques like radiofrequency (RF) magnetron sputtering, a physical vapor deposition (PVD) method, are extensively employed to obtain thin films possessing controlled thickness, desired composition, high purity, and excellent adhesion to the substrate.[10,11] In addition, the possibility to use thin films deposited on a suitable substrate, including TiO_2 or TiO_{2-x} films, opens the way to the creation of easily recoverable catalysts.

However, the design and combination of suitable morphologies is one of the most attractive strategies to enhance the overall performance for a selected photocatalyst.[12] Among all the TiO_2 shapes, rutile NRs grown on the conductive side of

fluorine-doped tin oxide (FTO) glasses have been extensively investigated and considered promising in the field of heterogeneous catalysis thanks to their potential recoverability in wastewater treatment processes. Furthermore, several studies have shown that the rutile rod configuration, enhancing the charge carriers recombination delay and showing an increased number of surface active sites, may improve the overall organic pollutants photodegradation efficiency under UV light. Specifically, the prolonged delay in the recombination of e^-–h^+ pairs can be attributed to several factors, including quantum confinement effects (i.e., nanorods have a radius smaller than the exciton Bohr radius) and the presence of trapping centers both at the material surface and bulk. [13,14]

Several studies have reported the effectiveness of oxygen vacancies-doped TiO_2 NRs array homojunction in significantly increasing the UV-Visible driven photocatalytic processes compared to the bare material.[15,16] Thus, the introduction of substoichiometric TiO_{2-x} thin films through the radiofrequency (RF) sputtering deposition method with a precise control on the oxygen vacancies concentration (i.e., decreasing the partial pressure of oxygen in the working gas) is proposed as a good approach to effectively build a TiO_2/TiO_{2-x} homojunction. In principle, the creation of a homojunction between the TiO_2 NRs array and the substoichiometric TiO_{2-x} thin film leads to several advantages. As anticipated in **Chapter 3**, the composite system will induce changes in the electronic structure, leading to broadened absorbance ability toward visible light and increased photocatalytic properties compared to the bare material. The interaction between the two components of the homojunction compensates for the limits of each material. From one side, according to the oxygen vacancies concentration, TiO_{2-x} surface layer will show a narrower and tunable bandgap, leading to an increase in the overall light absorption overcoming the major TiO_2 limit.[17,18] From the other, the fast charge-carriers recombination in TiO_{2-x} overlayer (due to the presence of a high number of Ov) is delayed.[16,19]

In this section the role of the TiO_{2-x} overlayer deposited through the RF magnetron sputtering is investigated by monitoring the photocatalytic performances of pure

and sputtered TiO_2 NRs samples. The number of cycles for the creation of the seed layer to grow TiO_2 NRs and the O_2 partial pressure of the vacuum chamber in the sputtering deposition were tuned to optimize the homojunction properties. All the photocatalysts were tested for methylene blue (MB) photodegradation reaction, under UV and simulated solar light irradiation at room temperature and atmospheric pressure. A deep correlation between the photocatalytic activity and the physicochemical and optical properties of the homojunctions is proposed.

5.1.1 Morphology and crystal structure

To obtain TiO_2/TiO_{2-x} homojunctions, titania NRs (TNR) were first synthesized through a hydrothermal growth method, which involved the use of two different solutions, a seed layer solution and a NRs growth solution, respectively. Before the hydrothermal treatment, the seed solution was deposited over the conductive surface of a FTO glass by means of a spin coater. According to the number of repetitions of the seed layer deposition, samples were labelled as single layer (SL) or double layer (DL). The desired homojunction was finally obtained by physical vapor deposition. TiO_{2-x} nanostructures were deposited over TNR surface by reactive sputtering deposition in a custom-made RF magnetron sputtering deposition system. Each sputtering deposition involved a target of pure metallic titanium using a 13.56 MHz RF source and three reactive O_2 in Ar atmospheres (or working gas compositions): 90%+10%, 85%+15% and 80%+20%. Samples are referred to as XTNRY, where X stands for SL or DL and Y for 10, 15, 20 % of O_2 in Ar. For instance, sample SLTNR10 is made using a single layer of seed solution and it has been sputtered under a 10% O_2 in Ar atmosphere (further details in **Table 5.1** and appendix A).

Table 5.1 Sample label, layer type, working gas composition and deposition time of the synthesized photocatalysts.

Label	Seed layer type	*Ar+O_2 (%)	Gas deposition time (s)
SLTNR	Single	-	-
DLTNR	Double	-	-
SLTNR10	Single	90+10	3600
DLTNR10	Double	90+10	3600
SLTNR15	Single	85+15	4000
DLTNR15	Double	85+15	4000
SLTNR20	Single	80+20	4685
DLTNR20	Double	80+20	4685

* total pressure = $50 \cdot 10^{-4}$ mbar

FE-SEM images of TNR samples before and after the sputtering layer deposition are reported in **Figure 5.1(a-d)**. Both the SL and DL series showed the presence of nanostructured vertically aligned TNRs, which were strongly packed and uniformly distributed on the FTO glass surface. Each rod appeared with a square cross-section geometry and a relatively uniform average size of 78 ± 4 nm for SL and 68 ± 5 nm for DL, respectively (further details on the calculation methods applied are reported in **Appendix A**). In addition, the cross-section imaging analysis (**Figure 5.1d**) revealed an average TNR layer thickness of 310 ± 63 nm for SLTNR and 350 ± 84 nm for DLTNR. **Figure 5.1c-d** shows FE-SEM images of the sputtered samples, revealing the presence of the overlayer of thinner TiO_{2-x} nanorods on the pristine TNR surface, proving the effectiveness of the sputtering deposition.

Furthermore, atomic force microscopy (AFM) topography images of SLTNR and SLTNR15 nanorod arrays (**Figure 5.2a,b**) acquired in tapping mode, further proved the overall SEM findings. In fact, both SLTNR and SLTNR15 nanorod arrays showed an overall uniform coverage and further evidence of thinner nanorods in the sputtered sample, implying a subsequent growth onto the existing nanostructures. In

addition, the acquisition of line profiles allowed to estimate the lateral size of SLTNR and SLTNR15 (see in **Paper-III**, supporting information).

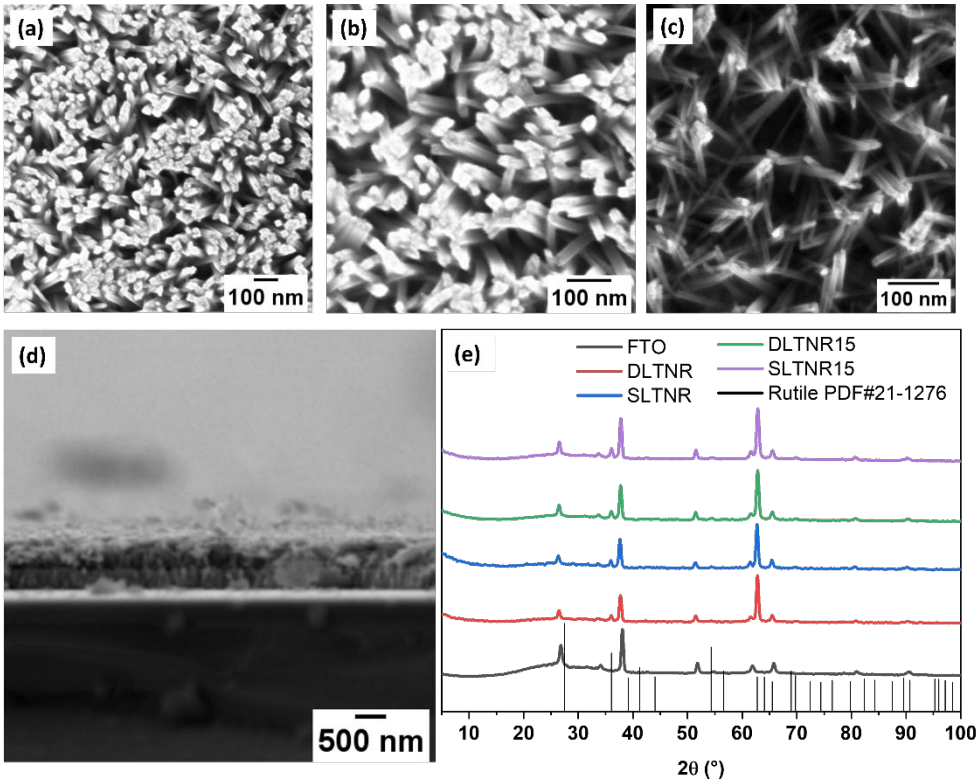

Figure 5.1 (a-d) SEM images of bare **(a)** SLTNR and **(b)** DLTNR at different magnifications and after the sputtering deposition **(c)** from top and **(d)** cross-section view **(e)** XRD diffractogram comparing pristine FTO glass and both stages of seed (SLTNR, DLTNR) and sputtered layers (SLTNR15 and DLTNR15).

In the SLTNR sample, nanorods spanning approximately 75 nm to 87 nm in lateral dimension were identified, whereas the sputtered sample (SLTNR15) displayed a smoother and more consistent surface, featuring elements with a reduced diameter ranging from about 17-25 nm.

Discrepancies based on profile irregularities can be highlighted by surface roughness parameter. In this case, since TNRs are showing vertical profiles, surface roughness was assessed through amplitude parameters, among which the root mean square (rms) roughness (Rq) is included. Rq represents the standard deviation of the Z height,[20] and the extrapolated values for SLTNR and SLTNR15 were 19.6 nm and 2.2 nm, respectively. The higher Rq value for SLTNR can be attributed

to the weak packing of nanostructures, as previously observed in FE-SEM analyses (**Figure 5.1**). The decline in roughness highlighted by AFM findings further indicates that the incorporation of sub-stoichiometric TiO_{2-x} induced a subsequent growth of thinner nanorods over the bare TiO_2 nanostructures.

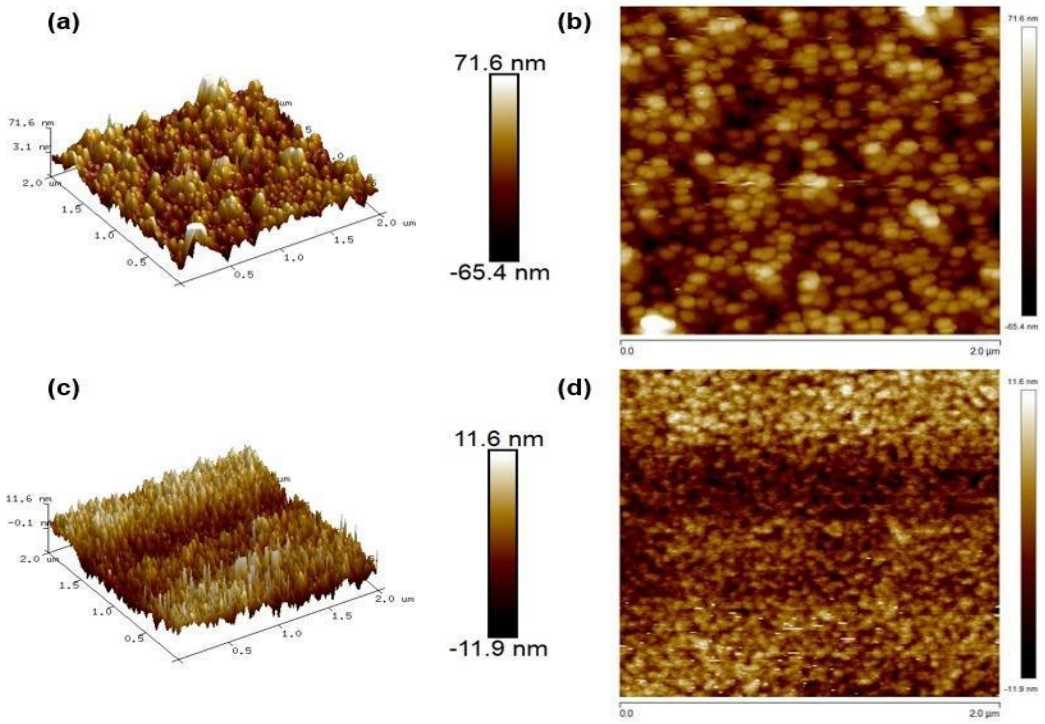

Figure 5.2 AFM 3D morphologies of **(a)** SLTNR and **(c)** SLTNR15 samples. AFM 2D images of **(b)** SLTNR and **(d)** SLTNR15 nanorod arrays.

Concerning the crystalline structure, the XRD patterns for all the samples are shown in **Figure 5.2e**. In both the SLTNR and DLTNR samples, a peak can be detected at 2θ of 36°, corresponding to the (101) peak associated with the rutile crystalline phase. The 2θ peak at 64° was identified as the (002) peak, indicating the vertically aligned structure of the rods growing perpendicular to the surface of the FTO along the [001] direction.[21] As a result, it is evident the preferential orientation growth towards the rutile phase, indicating a single crystal growth perpendicular to the FTO substrate. It is worth noting that several factors may significantly influence the TNR growth. One crucial parameter is the titanium precursor amount

in both the seed and hydrothermal growth solutions used in the synthetic procedure. In fact, the crystallinity of rutile nanorods was enhanced by the increasing concentration of titanium butoxide, used as Ti source.

5.1.2 Surface composition and optical properties

The surface chemical composition (atomic percent concentration, at. %) before and after 1 minute Ar^+ etching for all the samples is shown in **Table 5.2**. A high content of surface carbon was detected, thus high-resolution C1s core level spectra are depicted in **Figure 5.3** (left panel). All the C1s core level spectra can be fitted with four components at 284.8, 286.2, 287.5 and 288.7 eV. The main contribution at 284.8 eV was assigned to the presence of -C-C- and -C=C- bonds. The second, at 286.1-286.3 eV was attributed to C-O and C-N groups. In addition, at 287.5-287.6 eV and 288.7-288.8 eV appeared two weak components that can be assigned to residual C=O and carboxylate groups, respectively.[22,23] Following Ar^+ etching, a significant reduction in the carbon content is observed, suggesting that the major contribution originated from adventitious carbon contamination.

Table 5.2 Surface chemical composition (at. %) determined by XPS.

Sample	C	O	N	Ti	Si
DLTNR10	44.7	42.0	-	13.3	-
SLTNR10	48.3	37.6	2.5	11.6	-
DLTNR15	44.8	40.3	1.3	13.6	-
DLTNR20	45.1	38.2	1.2	11.5	4.0
SLTNR20	47.3	36.9	1.6	9.9	4.3
DLTNR10*	10.9	61.7	-	27.4	-
SLTNR10*	12.3	60.1	1.0	26.6	-
DLTNR15*	11.2	60.7	0.8	27.3	-
DLTNR20*	9.20	61.6	0.8	30.0	1.4
SLTNR20*	10.5	59.4	1.1	26.9	2.1

*After 1 min Ar^+ etching

From Ti*2p* core level spectra (**Figure 5.3**, on the center), the Ti$2p_{3/2}$ signal at binding energies 458.4-458.6 eV and attributed to the presence of Ti^{4+} was detected.[24] However, upon the 1 min Ar^+ etching procedure needed to remove surface contamination, the presence of sub-stoichiometric titania was proved. In fact, a 2p doublet, overlapping the Ti^{4+} signals, was detected at lower binding energies (**Figure 5.3**, on the right). In all the sputtered samples the mean distance between these 2p signals was estimated to be 1.5 eV.

In addition, in **Table 5.2**. is reported the presence of N and Si for some samples. Nitrogen may be ascribed to contamination resulting from mishandling during sample preparation. In fact, Ar^+ etching led to a decrease in its content, proving its existence only at the surface of the sample. Instead, the presence of Si in DLTNR20 and SLTNR20 was probably due to the leaching of the FTO glass following the hydrothermal conditions. However, no traces of F and Sn coming from FTO were detected for all the studied samples.

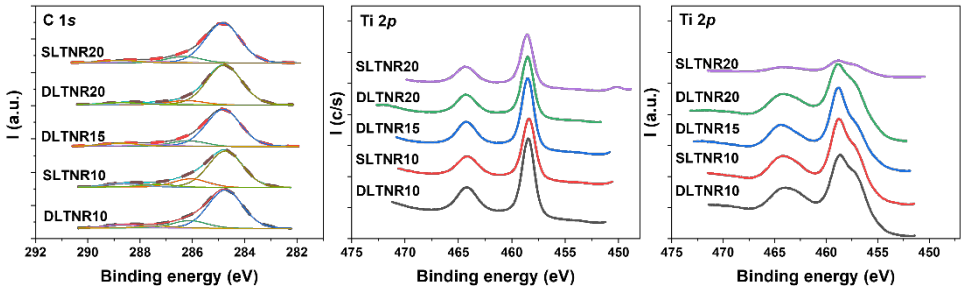

Figure 5.3 High resolution XPS bands: **C 1s** (on the left), **Ti 2p** before (on the center) and after (on the right) mild Ar^+ sputtering for removing surface contamination.

Concerning the optical properties of the prepared junctions, the UV-Vis absorption spectra are shown in **Figure 5.4**. Both SL and DL TNR samples showed the typical TiO_2 UV strong absorption band, slightly shifted toward the visible region compared with the bare FTO glass profile. It has to be pointed out that the oscillations detected above 400 nm may be related to interference effects from internal reflections. Notably, the homojunction creation caused the redshift in the absorption edge, leading to an extension of the overall absorption towards higher wavelengths up to ~800 nm. As expected, the red-shift intensity increased with

decreasing of oxygen concentration in deposition working gas (from 30 to 10 %), thus with TiO_2 becoming more sub-stoichiometric. In addition, after the sputtering deposition, the overall absorption increased in the full visible spectral range. Consequently, the TiO_2/TiO_{2-x} homojunction creation effectively improved the overall spectral response.[15] This is also confirmed by the indirect bandgap energies (values in **Figure 5.4**, right panel) calculated from Tauc plots (**Figure 5.4c,d**).[25] As expected, there is a clear correlation between the bandgap values and the increasing stoichiometry in the composition of the deposited TiO_{2-x} layer. The lowest measured value was accounted for SLTNR10 sputtered sample (2.8 eV), whereas the highest was for SLTNR20 sample (3.4 eV).

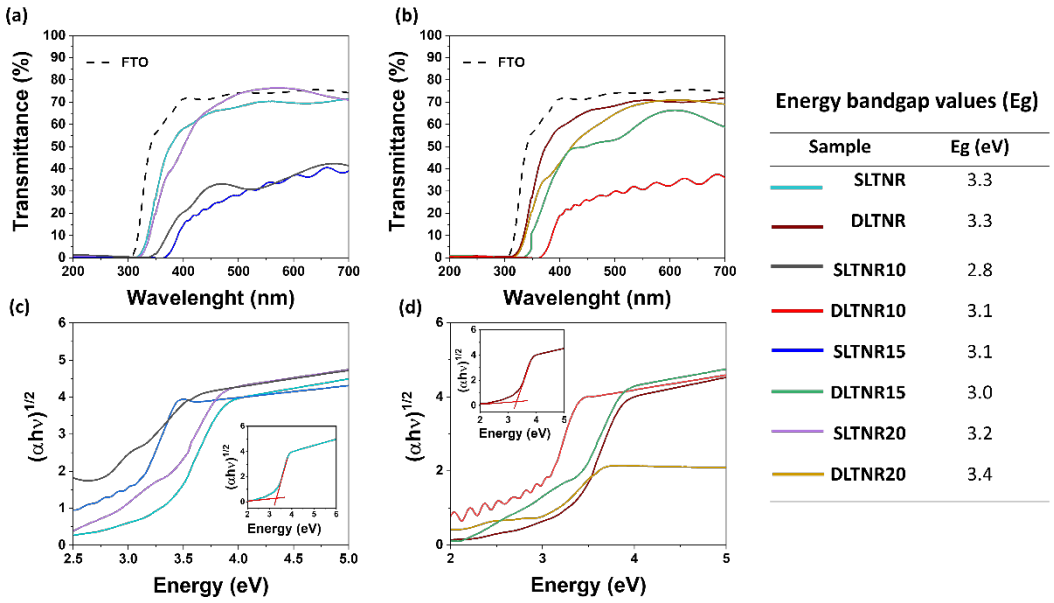

Figure 5.4 Transmittance UV-Vis spectra (top) and Tauc plots (bottom) referring to **(a, c)** SLTNRX series and **(b, d)** DLTNRX series. The energy bandgap values are listed in the inset table.

5.1.3 Photodegradation of Methylene Blue

XTNRY photocatalytic actvity was evaluated monitoring Methylene Blue (MB) photodegradation, following the evolution over light irradiation time of its

maximum absorption band at 664 nm. MB was selected as photocatalytic probe molecule since it is a well-known pollutant dye, being a hardly degradable heterocyclic aromatic compound. Moreover, MB photodegradation pathway in presence of TiO_2 systems under UV light, is deeply investigated and easily detectable. In fact, it is based on the conversion toward harmless and less complex molecules such as CO_2, nitrate, ammonium and sulfate ions.[26] However, Leuco Methylene Blue (LMB), the colorless reduced form of MB, can be produced causing the back-creation of the starting MB molecules. Thus, the presence of LMB was also investigated, by monitoring its typical absorption around 520 nm.[27] Each experiment was carried out at room temperature and atmospheric pressure, under both UV and simulated solar (SS) light irradiation, recording UV-Vis spectra in the range 300-800 nm at different photoreaction times. As showed in **Figure 5.5a,b**, the decrease in the absorption peak at 664 nm can be ascribed to the decomposition of benzene rings and heteropoly aromatic bonds in MB undergoing photodegradation in presence of XTNRY photocatalysts. Additionally, the presence of LMB was not detected neither under UV nor SS light experiments.

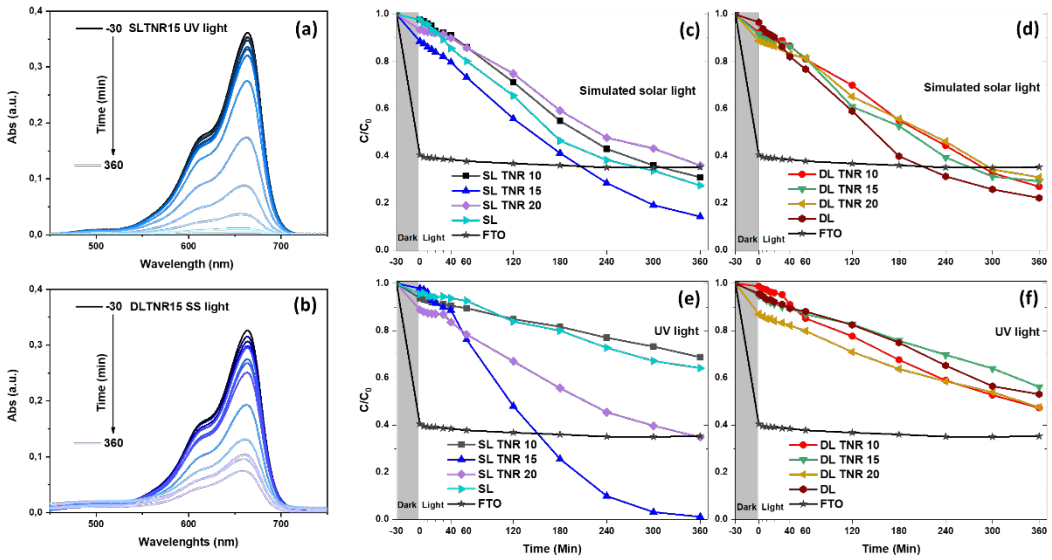

Figure 5.5 Methylene blue **(a,b)** absorption spectra for SLTNR15 under UV and DLTNR15 under simulated solar (SS) light. Photodegradation curves of the investigated samples under **(c, d)** simulated solar light and **(e, f)** UV light irradiation at room temperature and atmospheric pressure.

In **Figure 5.5(c-f)** the C/C_0 curves for all XTNRY samples under both UV and SS light irradiation are reported. Moreover, degradation efficiencies, pseudo-first order kinetic constant values with relative uncertainties k ± δk ($10^{-3} \cdot min^{-1}$), calculated from the non-stationary regime data during light irradiation, are listed in **Table 5.3** (further details in **Paper-III**, supporting information). The adsorption phenomena under dark equilibration time can be observed from the C/C_0 curves. As mentioned before, the pH of the system related to the point of zero charge (pH_{zpc}) of the material highly influences the adsorption of the probe molecules onto the catalyst surface. Specifically, the MB solution pH (~6.2) is higher than the FTO pH_{zpc}. In fact, FTO showed the highest ability to adsorb MB molecules with a consequent strong reduction in the MB concentration (up to 40%). Interestingly, regarding the adsorption in XTNRY samples, a correlation can be noticed between the decrease in MB concentration (from 2% to 17%) and the increase in the O_2% in Ar. In detail, the presence of a TiO_{2-x} overlayer, showcasing an increased quantity of surface-exposed hydroxyl groups, results in a greater tendency for interactions with the exposed functional groups of MB dye. When exposed to UV light, all XTNRY photocatalysts demonstrate remarkable catalytic performances, resulting in a considerable degradation efficiency ($\%Dr_{UV}$), varying from 30% to 99%.

Table 5.3 Degradation efficiency (% Dr) and k values for all the samples both under UV and Simulated Solar Light (SS) irradiation.

Sample	$\%Dr_{UV}$	$\%Dr_{SS}$	$k_{UV} \pm \delta k_{UV}$ ($10^{-3} \cdot min^{-1}$)	$k_{SS} \pm \delta k_{SS}$ ($10^{-3} \cdot min^{-1}$)
SLTNR	36	73	-	-
DLTNR	43	78	-	-
SLTNR10	32	70	1.6 ± 0.2	4.9 ± 0.4
DLTNR10	53	65	8.0 ± 1.0	4.2 ± 0.6
SLTNR15	99	86	9.0 ± 1.0	6.8 ± 0.5
DLTNR15	44	70	2.8 ± 0.4	3.5 ± 0.5
SLTNR20	66	65	4.9 ± 0.5	6.3 ± 0.5
DLTNR20	53	70	2.4 ± 0.3	3.0 ± 0.4

Figure 5(c-f) illustrates that both bare single layer (SL) and double layer (DL) TNR samples exhibited photocatalytic activity, resulting in behavior conforming with the sputtered samples. Among these, SLTNR15 displays the highest photoactivity, showcasing a kinetic constant for MB degradation of approximately $9 \cdot 10^{-3} \cdot min^{-1}$ and achieving a remarkable 99% dye degradation after 360 minutes. Despite similar band gap energy values, the SLTNR15 sample, as derived from XRD analysis and SEM images, showed a desired morphology aligned vertically compared to DLTNR15 (having the same stoichiometry). The significant improvement of SLTNR15 in the overall photocatalytic efficiency can be attributed to the synergistic effect among crystalline structure, morphology and oxygen content in sub-stoichiometric sputtering deposition. The same result can be observed by comparing the photodegradation profiles of all samples, with SLTNRY series being more efficient than DLTNRY series. The aim of this investigation was to design TiO_2/TiO_{2-x} homojunctions to improve photocatalytic efficiency when exposed to solar light. Overall, each sample exhibited an extended efficiency in degrading MB under simulated solar light, without any exceptions (**Table 5.3**). The catalytic performance of these systems aligns with their optical characterization: the redshift in band edge absorption potentially accounts for the increase in photocatalytic efficiency. The most effective sample remained SLTNR15, achieving an 86% degradation of MB with a k value of approximately $7 \cdot 10^{-3} \cdot min^{-1}$, thereby validating previous results. Furthermore, the peculiar synthetic strategy by using FTO glasses enables to easily recover the photocatalyst from the slurry system, useful for a future large-scale practical application. Thus, stability and reusability tests were carried out on the best performing sample (i.e., SLTNR15) under UV light. Upon a 3-cycle reusability test (**Figure 5.6a**), SLTNR15 exhibited not only persistent MB degradation activity, but also enhanced photodegradation efficiency. Consequently, SLTNR15 showed excellent physico-chemical stability opening the way for potential long-term applicability in water treatment.

Finally, to complete the photocatalytic activity characterization, SLTNR15 was also evaluated by performing the same MB photodegradation test under UV light but

varying the solution pH (**Figure 5.6b**) and simulating acidic (pH = 4) or alkaline conditions (pH = 9). As stated in **Chapter 3**, TiO_2 surface is highly sensitive to the solution pH and its pH_{zpc} was evaluated to be in the range 5.0-6.2.[28–32] Since TiO_2 surface is rich in -OH terminal groups, it is positively charged when the solution pH is below the pH_{zpc}. Conversely, it is negatively charged when the solution pH is above the pH_{zpc} (i.e., deprotonation of -OH groups). Thus, in acidic conditions the positively charged surface of SLTNR15 attracted a higher number of MB molecules, that can be almost completely degraded after 360 min of light irradiation, without any adsorption phenomena (**Figure 5.6b**). On the contrary, in alkaline conditions the -OH groups are deprotonated, and the MB adsorption easily occurred due to electrostatic interactions. Thus, the strong decrease in the C/C_0 curve at pH = 9 was almost completely caused by adsorption phenomena.

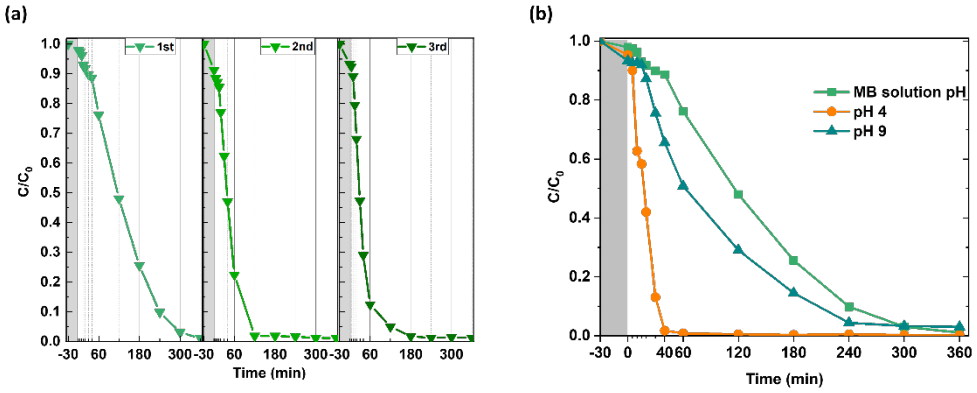

Figure 5.6 (a) Reusability test and **(b)** photocatalytic activity behavior in acidic and alkaline conditions for sample SLTNR15 performed under UV light irradiation.

5.1.4 Conclusions

TiO_2 thin films are extensively used in heterogeneous photocatalysis for degrading organic pollutants in wastewater. To enhance surface-to-volume ratio, optimize adsorption/desorption phenomena, mitigate rapid charge recombination, and reduce the wide TiO_2 band gap, a homojunction involving two distinct oxygen-rich/deficient TiO_2 layers was proposed. TiO_2 vertically aligned nanorods were grown on the conductive side of FTO glass through hydrothermal treatment under

acidic conditions, optimizing the synthesis by varying the spin coating seeding procedure. SEM micrographs indicated an average diameter of (78 ± 4) nm for SL and (68 ± 5) nm for DL samples, proving the influence of seed layer deposition on diameter growth. Using RF magnetron sputtering deposition, a uniform overlayer of thin TiO_{2-x} nanorods was created to form various homojunctions by tuning oxygen partial pressure in the sputtering argon atmosphere (10%, 15%, and 20%). XPS results suggested the presence of oxygen vacancies as confirmed by other studies. Both TiO_2 nanorods and TiO_{2-x} layers exhibited the same rutile crystalline phase, confirmed by XRD patterns. AFM investigations aligned with SEM findings, showing uniform nanorod arrays with average lateral dimensions of 80 nm for SLTNR sample and approximately 20 nm for the sputtered sample SLTNR15. Additionally, AFM confirmed the introduction of sub-stoichiometric titania thin film, revealed by the decrease in surface roughness parameter. Photocatalytic activity was finally assessed by monitoring MB photodegradation under UV and simulated solar light irradiation. The best-performing sample (SLTNR15) demonstrated MB degradation efficiencies up to 99% under UV and 85% under simulated solar light irradiation, respectively. These promising results lay the groundwork for potential large-scale environmental applications in the industrial dye degradation processes.

Paper-IV

J. Wang, L. Liccardo, H. Habibimarkani, E. Wierzbicka, T. Schultz, N. Koch, E. Moretti, N. Pinna, Precise control of TiO_2 overlayer on hematite nanorod arrays by ALD for the photoelectrochemical water splitting. *Sustain. Energy Fuels.* 2024, Submitted and under review.

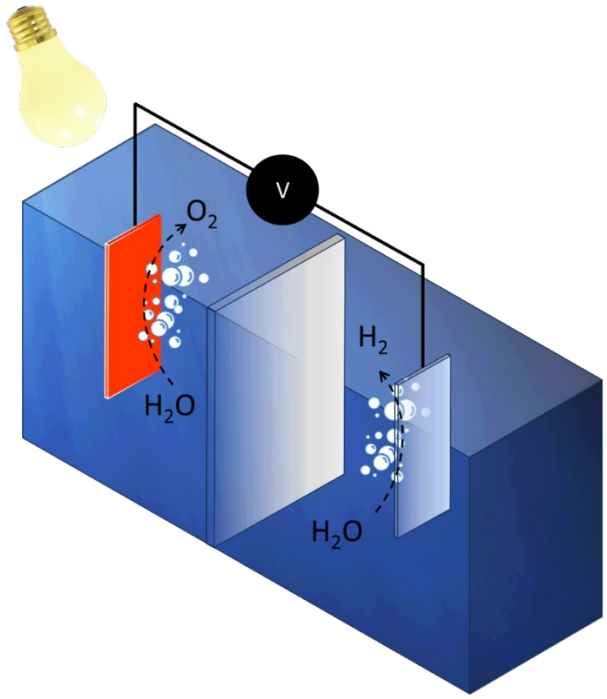

5.2 TiO_2/α-Fe_2O_3 NRs array heterojunctions

In the frame of energy crisis, as introduced in **Chapter 1**, developing novel technologies able to efficiently harvest and convert solar light into chemical fuels is urgently needed.[33,34] One of the most studied technologies is based on photoelectrochemical water splitting (PEC WS) using semiconductor nanomaterials. However, the efficiency values are still low for practical applications.[35–37] For instance, one of the most promising and used n-type photoanode materials is hematite (α-Fe_2O_3) thanks to its properties including favorable optical band gap (2.0-2.2 eV), chemical stability, earth abundance and relatively low cost.[38,39] Specifically, one-dimensional (1D) hematite nanostructures such as nanosheets, nanowires, nanorods, and nanotubes can improve charge creation efficiency in PEC water splitting thanks to their unique morphology and high surface-to-volume ratio.[40–43] However, hematite WS efficiency is highly limited by the e^-–h^+ pairs very short lifetime, short h^+ diffusion length (2−4 nm), poor charge-carriers mobility and fast recombination rates.[44,45] Among all the strategies applied to overcome these issues and improve PEC performances, [12,46,47] the creation of heterojunctions and surface modification exploiting the favorable properties of TiO_2 seems to be highly effective.[48–50] In literature numerous studies have been focused on TiO_2 overlayer modifications for applications in PEC WS.[44,51] In fact, a TiO_2 overlayer with optimized thickness can increase electronic conductivity and suppress surface charge-carriers recombination.[48,49,52] However, the precise control over the morphology and thickness of TiO_2 overlayer still remains a challenge. In addition, there is a lack of studies regarding the effects of TiO_2 overlayer thickness on PEC performance and charge transfer mechanisms at the semiconductor-electrolyte interface.

Several methods, including spin coating, atomic layer deposition (ALD), sputtering, chemical bath deposition and dip coating, can be used to deposit the TiO_2 overlayer. [51,53–56] Among all, ALD allows the conformal and homogeneous coating on high aspect ratio substrates with the possibility to precisely control the film

thickness at the Ångström scale.[57–59] Improvements in creating consistent TiO_2 overlayer on hematite via ALD technique have been already achieved. [57,60,61] However, obtaining a conformal, pinhole-free, and high-quality ultrathin TiO_2 film remains challenging primarily because of restricted comprehension of TiO_2 growth at early stages.

Therefore, this section is focused on the creation of heterojunctions between ALD TiO_2 continuous ultrathin films and 1D hematite nanorod arrays. Thanks to the use of ALD method the morphology and thickness of TiO_2 overlayer can be accurately controlled and tuned. Furthermore, the creation of TiO_2/α-Fe_2O_3 NRs array heterojunctions can open the possibility to improve and extend the optical properties of each semiconductor by enabling the use of both UV and visible light irradiation.[62,63] Thus, morphology of the resulting system was deeply characterized by high-resolution transmission electron microscopy (HR-TEM) and high-angle annular dark field scanning transmission microscopy (HAADF-STEM). The energy level alignment was then analyzed by X-ray photoemission spectroscopy (XPS). Additionally, the role of TiO_2 overlayer and the charge transfer mechanism in PEC WS is deeply discussed in this section, by monitoring the PEC performances of TiO_2/α-Fe_2O_3 system as a function of TiO_2 thickness. Accordingly, this section offers a promising approach to clarify the functions of TiO_2 overlayer and the charge transfer mechanisms involved during PEC WS process using the final photoanode.

5.2.1 Morphology and structure

The synthesis procedure to obtain ALD-grown TiO_2 films on α-Fe_2O_3 NRs array and create the final TiO_2/α-Fe_2O_3 heterojunction is represented in **Figure 5.7a**. In detail, vertically aligned β-FeOOH NRs were first grown on a conductive FTO glass by hydrothermal method and subsequently converted into α-Fe_2O_3 NRs through an annealing process. The final TiO_2/α-Fe_2O_3 heterojunction was then obtained by

depositing TiO_2 overlayer with various thickness by ALD. The samples were referred to as TiO_2 -X/Fe_2O_3, where X indicates the number of ALD cycles.

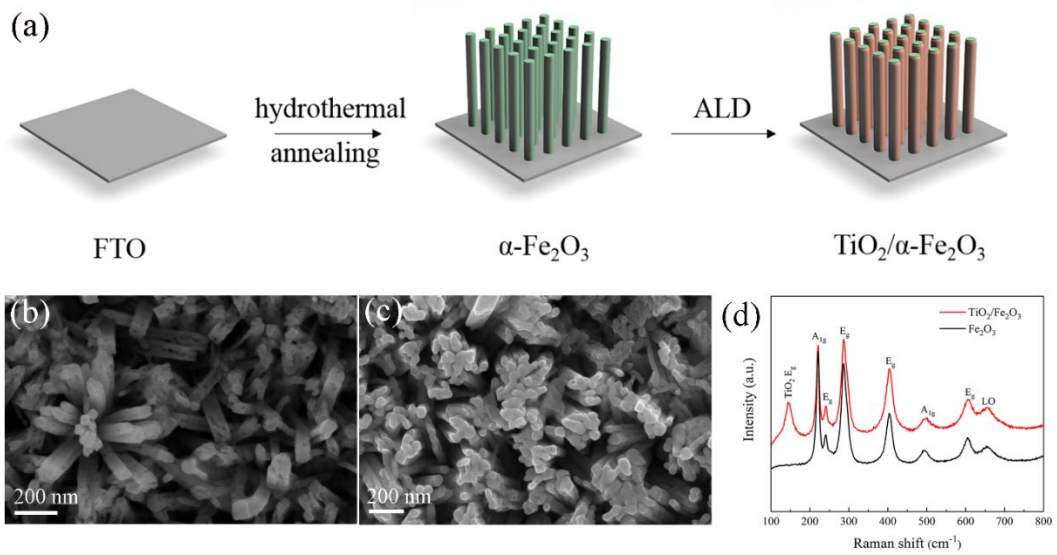

Figure 5.7 (a) Schematic view of the synthesis process for TiO_2/α-Fe_2O_3 hierarchical nanostructure. FE-SEM images of **(b)** pristine hematite nanorods and **(c)** 40ALD cycles of TiO_2 deposited on pristine hematite. **(d)** Raman-active modes of pristine hematite and TiO_2 deposited on hematite.

It must be pointed out that numerous characterization techniques, including XRD, TEM and HR-TEM, UV-vis-NIR spectroscopy, have been used to investigate the as-synthesized TiO_2/α-Fe_2O_3 system. However, this paragraph only delves into the most interesting findings.

The morphology and homogeneity of both α-Fe_2O_3 and TiO_2/α-Fe_2O_3 NRs array was investigated using FE-SEM. In **Figure 5.7b**, it is evident that the vertically aligned orientation of bare α-Fe_2O_3 NRs on the FTO substrate, with diameters ranging from approximately 60 to 80 nm. The TiO_2-40/Fe_2O_3 NRs array displayed a well-maintained NRs morphology, with the only difference that the presence of TiO_2 overlayer made the rods smoother and highly packed (**Figure 5.7b**). The presence of TiO_2 films and their thickness were investigated by means of several techniques including HR-TEM and XRD analysis (further details on **Appendix A**). Here, Raman spectra is presented to show the effect on the crystallinity of ALD-TiO_2 coating over bare α-Fe_2O_3 NRs (**Figure 5.7d**). The peaks at 220, 241, 286, 404, 494 and 606cm^{-1}

confirmed the presence of hematite crystalline structure. Moreover, the lattice oxygen (LO) peak centered at 658 cm^{-1} and attributed to the disorder-induced breaking of Raman symmetry properties, was detected.[46,64] After the TiO_2 ALD treatment, the intense peak located at 144 cm^{-1} and attributed to E_g mode of anatase TiO_2 was observed.[49] However, the overall structure of α-Fe_2O_3 nanorods was not affected by ALD of TiO_2.

Figure 5.8 displays the HAADF-STEM images along with the corresponding elemental mappings for the entire series of TiO_2-coated hematite samples. In **Figure 5.8a**, small TiO_2 nuclei randomly deposited on the α-Fe_2O_3 NRs after 10 ALD cycles were observed. At higher number ALD cycles, the nuclei seem to gradually increase, and tiny nanocrystallites coalesce together, eventually forming an extremely thin and cohesive TiO_2 layer. The HAADF-STEM images acquired for TiO_2-20/Fe_2O_3, TiO_2-40/Fe_2O_3, TiO_2-80/Fe_2O_3, and TiO_2-150/Fe_2O_3 exhibited a consistent and uniform deposition of TiO_2 on α-Fe_2O_3 NRs. The distinct phases of TiO_2 were easily detectable due to their different Z-contrast, indicating a conformal and homogeneous coating over α-Fe_2O_3 NRs for all the samples. As depicted in **Figure 5.8(b-e)**, the average thickness of TiO_2 films was 1.7, 3.5, 6.8, and 13.2 nm for 20, 40, 80, and 150 ALD cycles, respectively. This suggested a well-defined linear relationship between the TiO_2 shell thickness and the number of ALD cycles, showing a slope of 0.88 Å GPC (growth per cycle). Additionally, the corresponding elemental maps indicated a homogenous distribution of Ti and O elements α-Fe_2O_3 NRs for all the samples.

The chemical surface composition and states for all the samples were evaluated by high-resolution XPS. In this paragraph, only the extrapolation of the VB offset ($\Delta E_{V\text{-}TiO2/\alpha\text{-}Fe2O3}$) and the corresponding core level and valence band spectra are discussed and reported in **Figure 5.9**. Assuming an identical energy gap between the VB and the core levels for both the pristine material and the heterostructure, $\Delta E_V^{Fe2O3/TiO2}$ can be calculated according to **equation 5.1**.[65,66]

$$\Delta E_V^{Fe_2O_3/TiO_2} = \left(E_{Ti2p_{3/2}}^{TiO_2} - E_V^{TiO_2}\right) - \left(E_{Fe3p_{3/2}}^{Fe_2O_3} - E_V^{Fe_2O_3}\right) - \left(E_{Ti2p_{3/2}}^{Fe_2O_3/TiO_2} - E_{Fe3p_{3/2}}^{Fe_2O_3/TiO_2}\right) \qquad (5.1)$$

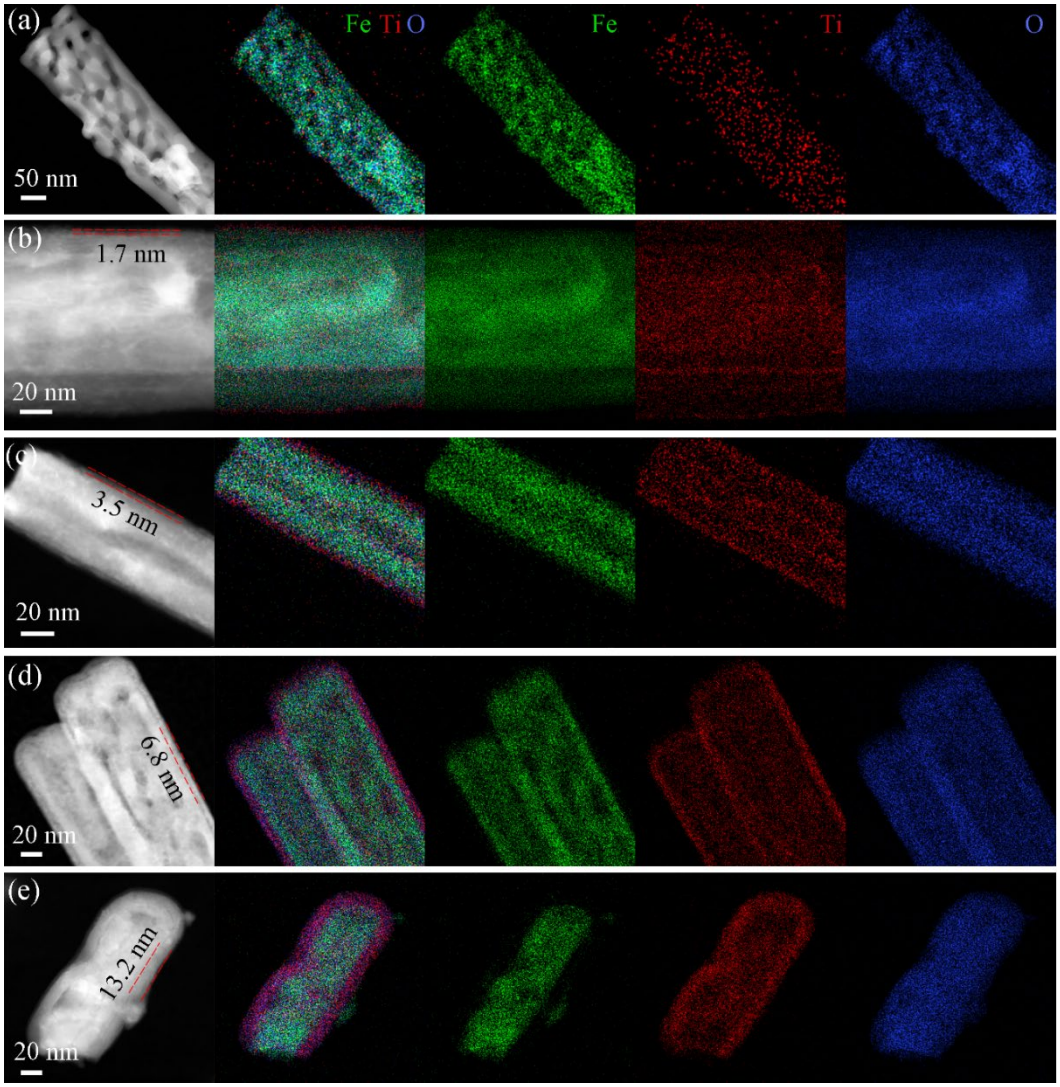

Figure 5.8 HAADF-STEM and corresponding EDX elemental maps for **(a)** TiO_2-10/Fe_2O_3, **(b)** TiO_2-20/Fe_2O_3, **(c)** TiO_2-40/Fe_2O_3, **(d)** TiO_2-80/Fe_2O_3 and **(e)** TiO_2-150/Fe_2O_3.

The binding energy of the core levels was evaluated by determining the peak position through the fitting procedure, whereas VB onsets were determined by linearly extrapolating the leading edges. Consequently, placing the α-Fe_2O_3 VB closer to the Fermi level a valence band offset of 0.83 eV was calculated. Considering the band gaps of 2.05eV determined by DRUV-vis-NIR spectroscopy (details on **Appendix A**), it can be assumed that the α-Fe_2O_3/TiO_2 interface forms a straddling gap (type I heterostructure) with a conduction band offset of 0.30 eV **(Figure 5.9e**).

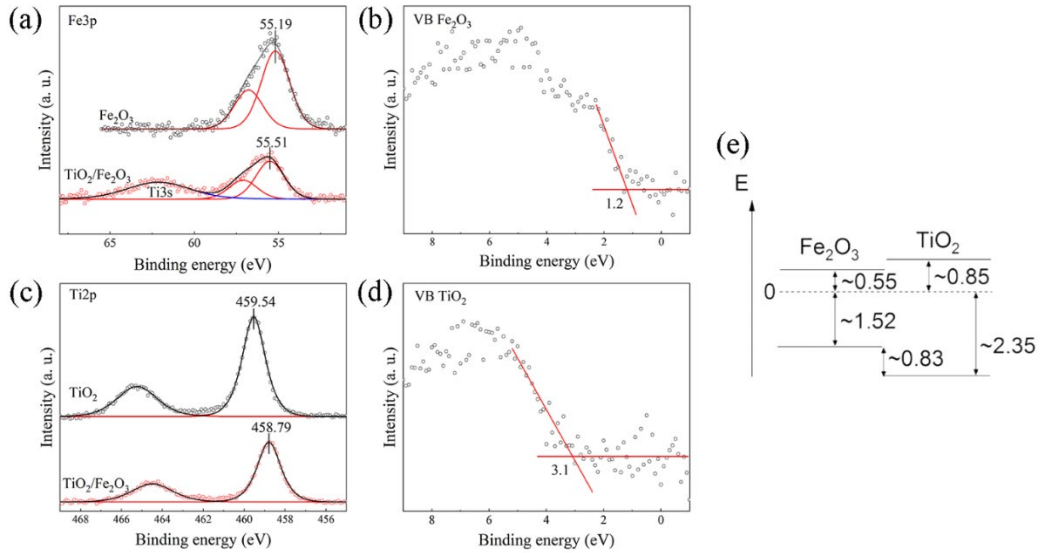

Figure 5.9 (a) Fe3p core level spectra of Fe_2O_3 (black) and TiO_2-20/Fe_2O_3 (red). Shirley backgrounds have been removed. **(b)** Valence band spectrum of Fe_2O_3 with a linear extrapolation of the valence band onset. **(c)** Ti2p core level spectra of TiO_2 (black) and TiO_2-20/Fe_2O_3 (red). Shirley backgrounds have been removed. **(d)** Valence band spectrum of TiO_2 with a linear extrapolation of the valence band onset. **(e)** Schematic energy level diagram of TiO_2/Fe_2O_3.

5.2.2 Photoelectrochemical activity

PEC performances were investigated for both pristine α-Fe_2O_3 NRs and modified TiO_2-X/Fe_2O_3 systems, under both UV and visible light irradiation (details on **Appendix A**). In **Figure 5.10** are reported the PEC measurements for all the samples under visible light. From the photocurrent-potential (J-V) curves, it can be stated that TiO_2-X/Fe_2O_3 photoanodes showed a lower overpotential for water oxidation reaction and a cathodic shift of the onset potential (**Figure 5.10a**). The ALD-TiO_2 coating significantly improved the photocurrent density. The measurements of photocurrent response under visible light at 0.5 V bias versus Hg/HgO are reported in **Figure 5.10b** for all the samples. For α-Fe_2O_3 a low photocurrent density of 0.01 $mA \cdot cm^{-2}$ was recorded. This low value is attributed to the fast charge-carriers recombination rate. As mentioned above, TiO_2-X/Fe_2O_3 heterojunctions are formed by a low bandgap semiconductor (i.e., α-Fe_2O_3) able to absorb visible light and a wide bandgap semiconductor (i.e., TiO_2) that can be activated only under UV light. Thus, under visible light, the photocurrent response was attributed exclusively to

α-Fe_2O_3. However, TiO_2-X/Fe_2O_3 heterojunctions displayed improved photocurrent densities compared to bare α-Fe_2O_3 photoanode. In this case, TiO_2 acts as a passivation layer by passivating surface states, reducing e^-–h^+ pairs recombination, enhancing the hole transfer, thus improving the overall photocurrent response.[48,52,67] In detail, the highest photocurrent density was recorded for TiO_2-20/Fe_2O_3 (~1.7 nm), which was ~27 times higher than that obtained for pristine hematite. The thickness of TiO_2 overlayer clearly played a pivotal role in preventing parasitic light absorption and enhancing charge-transfer from hematite to electrolyte.[68] In fact, when the TiO_2 overlayer thickness is too high, the hole transfer efficiency decreased, hematite light absorption was hindered, and the photocurrent response dramatically declined. Notably, upon visible light illumination, photogenerated holes in pristine hematite migrate and accumulate at SCLJ (semiconductor/liquid junction) due to the presence of surface trap states. This process triggers the appearance of large anodic transient peaks, that gradually decay as an equilibrium between charge-transfer and recombination at the interface is achieved.[69] Conversely, under dark conditions, cathodic transient peaks exceed and subsequently decay to zero, as electrons diffuse from the external circuit and recombine with accumulated holes at SCLJ.[44,52] This transient photocurrent spike notably decreased after TiO_2 deposition and remained consistent across multiple ALD cycles. This outcome underscores the efficacy of the TiO_2 passivating overlayer. Consequently, as mentioned before, α-Fe_2O_3 primarily acts as a light-absorbing layer, absorbing visible light and generating electron-hole pairs.

EIS (Electrochemical Impedance Spectroscopy) was conducted under light exposure to examine charge transfer kinetics at the interface. **Figure 5.10c** shows Nyquist plots for both untreated α-Fe_2O_3 NRs and TiO_2-20/Fe_2O_3 final photoanode. Inset in **Figure 5.10c** highlights the high-frequency region. Generally, Nyquist plots consist of a small semicircle at high frequencies and a sloping line at low frequencies.[70,71] In comparison with untreated α-Fe_2O_3 NRs, TiO_2-20/Fe_2O_3 exhibited a considerably smaller radius at high frequency. This suggests that TiO_2-20/Fe_2O_3 possessed a reduced charge transfer resistance, thanks to TiO_2 passivation effect.

This enhancement could significantly boost charge transfer, separation, and ultimately improve the performance of photoelectrochemical (PEC) water splitting.

The open circuit potential (OCP) of α-Fe_2O_3 NRs and TiO_2-20/Fe_2O_3 was examined in dark and under illumination conditions to analyze photogenerated carriers behavior (**Figure 5.10d**). Under illumination, both the OCP of α-Fe_2O_3 NRs and TiO_2-20/Fe_2O_3 shifted to a negative potential, with TiO_2-20/Fe_2O_3 showing an even more negative shift. Consequently, both photoanodes can be classified as n-type semiconductors, aligning with XPS findings. Both samples exhibited similar trends, generating comparable photogenerated electrons that accumulated on photoanode surfaces, causing a negative potential shift and a sudden OCP increase. Simultaneously, photogenerated electron-hole recombination occurred, leading to an OCP decrease until reaching a relatively stable state. α-Fe_2O_3 NRs and TiO_2-20/Fe_2O_3 demonstrated comparable potential changes, but TiO_2-20/Fe_2O_3 photoanode displayed greater stability due to TiO_2-20 passivation effect and lower photogenerated e^-–h^+ pairs recombination rates. After 20 seconds of irradiation followed by dark conditions, the OCP continued to decrease due to high e^-–h^+ pairs recombination. Photovoltages for pristine α-Fe_2O_3 NRs and TiO_2-20/Fe_2O_3 were 14.7 mV and 36.0 mV, respectively, derived from the dark-light OCP difference. TiO_2-20/Fe_2O_3 exhibited a significantly higher photovoltage.

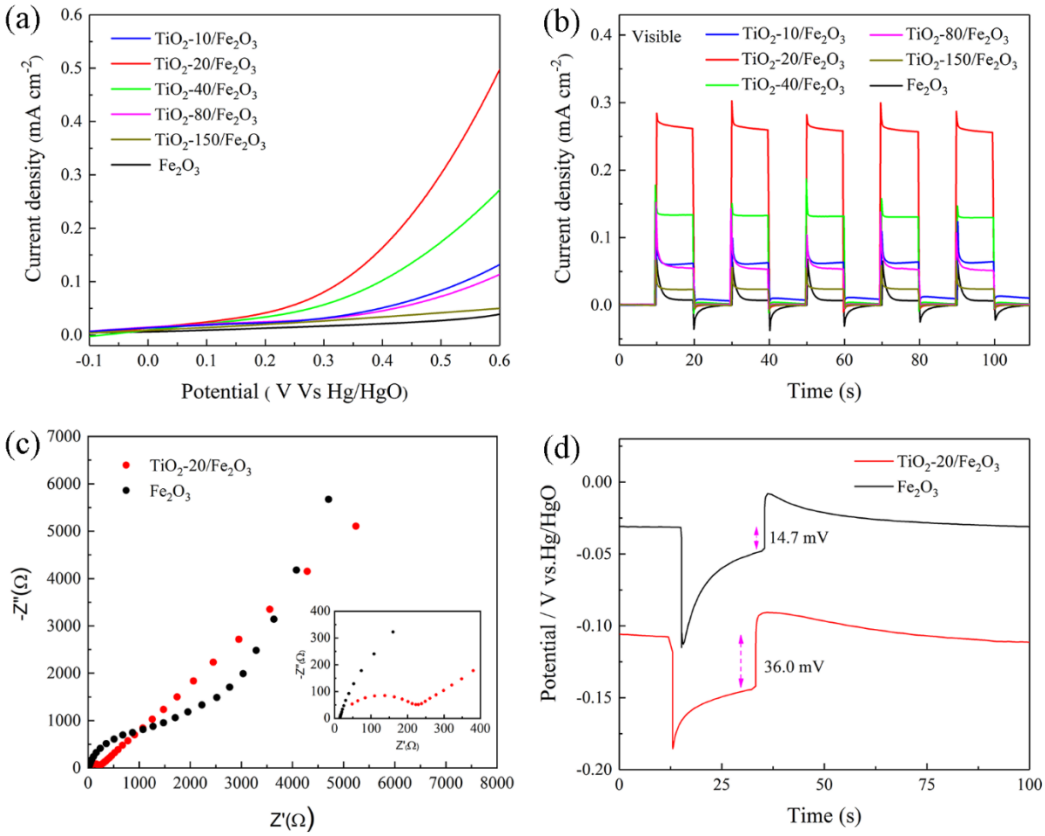

Figure 5.10 (a) Photocurrent versus potential plots of a different number of ALD cycles for TiO_2 coated hematite photoanodes under visible light irradiation. **(b)** Time-based photocurrent density at 0.5 V bias vs. Hg/HgO with the light off and on for 10s. **(c)** Nyquist plots of pristine Fe_2O_3 and TiO_2-20/Fe_2O_3 photoanodes measured under light illumination. **(d)** OCP curves of pristine Fe_2O_3 and TiO_2-20/Fe_2O_3 photoanodes with the light on for 20 s.

Additionally, to further investigate the photoresponse properties of TiO_2-X/Fe_2O_3 heterojunctions, it is reported the incident photon-to-current efficiency (IPCE) values calculated following equation 5.2:

$$\mathrm{IPCE}(\%) = \frac{1240 \cdot J_{photo}}{\lambda \cdot P_{light}} \cdot 100 \qquad (5.2)$$

where J_{photo} is the photocurrent density (mA·cm^{-2}) under visible light, λ is the wavelength of the incident light (nm), and P_{light} is the light power density (mW·cm^{-2}).[51,72]

The optimized TiO_2-20/Fe_2O_3 sample reached a maximum IPCE of 1.35% at 430 nm, significantly surpassing the 0.05% achieved by pristine α-Fe_2O_3 NRs photoanode. This considerable enhancement in photoconversion efficiency highlighted the

extended use of photoinduced carriers in TiO_2-coated hematite photoanodes, aligning with the trends observed in the J-V measurements depicted in **Figure 5.10a**.

To deeply verify the role of ALD-TiO_2, the photocurrent response was also evaluated under UV illumination. It is worth highlighting that, compared with the above discussed results, an opposite trend was observed. Briefly, the photocurrent response increased with a further growth of TiO_2 overlayer thickness (i.e., from 6.8 to 13.2 nm, 80 ALD to 150 ALD), reaching a value of 0.14 mA $\cdot cm^{-2}$ for TiO_2-150/Fe_2O_3. As expected, the photocurrent response was consequently restricted to TiO_2 overlayer. The opposite trend is depicted in **Figure 5.11**. The thickness of TiO_2 overlayer should be optimized for TiO_2 to act as a passivation layer. In fact, when the TiO_2 thickness is below 6.8 nm, TiO_2 does not absorb efficiently UV light to create e^-–h^+ pairs, consequently acting as passivation layer. Thus, the trend is similar to that observed under visible light. Conversely, when the TiO_2 thickness is higher enough than the optimal value of 1.7 nm (i.e., corresponding to 20-ALD cycles), TiO_2 component hinders the holes transfer from the hematite component and absorbs the UV light being the active layer in water oxidation reaction.

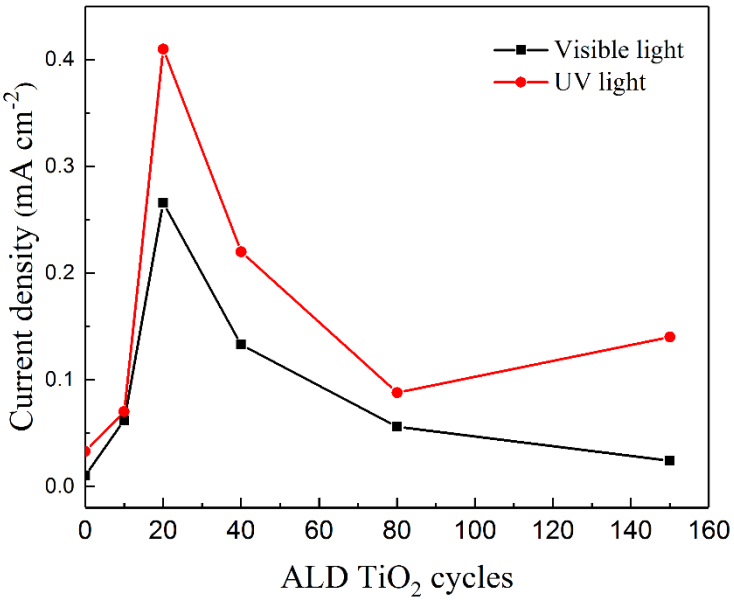

Figure 5.11 Current densities of hematite photoanodes with different ALD-TiO_2 cycles at 0.5 V bias vs. Hg/HgO, 1M KOH, under visible light and UV light irradiation, respectively.

5.2.3 Charge Transfer Mechanism

Based on previous results and discussion, the schematic diagram of charge separation and transport mechanism under both UV and visible light is proposed in **Figure 5.12**. As previously mentioned, TiO_2-X/Fe_2O_3 system can be considered a Type-I heterojunction. Furthermore, the number of ALD cycles is crucial for TiO_2 to weather act as passivation or active layer under UV light. Under visible light, α-Fe_2O_3 NRs, showing a suitable bandgap energy (~2.1 eV), can produce e^-–h^+ pairs in the CB and VB, respectively. The photogenerated electrons may be transferred through the external circuit, driven by the bias voltage (**Figure 5.12a**). Conversely, photogenerated holes cannot be transferred to the TiO_2 VB, due to the unfavorable band edge alignment in the Type-I heterojunction. Therefore, TiO_2 only acts as a passivation layer. Whereas, under UV illumination both α-Fe_2O_3 NRs and TiO_2 overlayer show suitable bandgap to bring e^-–h^+ pairs formation. The photogenerated electrons in TiO_2 CB can move towards α-Fe_2O_3 CB, located at a suitable and more positive potential. Consequently, electrons within α-Fe_2O_3 can travel through the external circuit. Meanwhile, the photoinduced holes in α-Fe_2O_3 can cross the TiO_2 thin layer by tunneling effect to participate in the oxidation reaction.[68,73,74] Moreover, photogenerated holes in TiO_2 VB may either directly react with electrolyte, or transfer to α-Fe_2O_3 VB and then cross the TiO_2 thin layer to finally give the water oxidation reaction (**Figure 5.12b**).

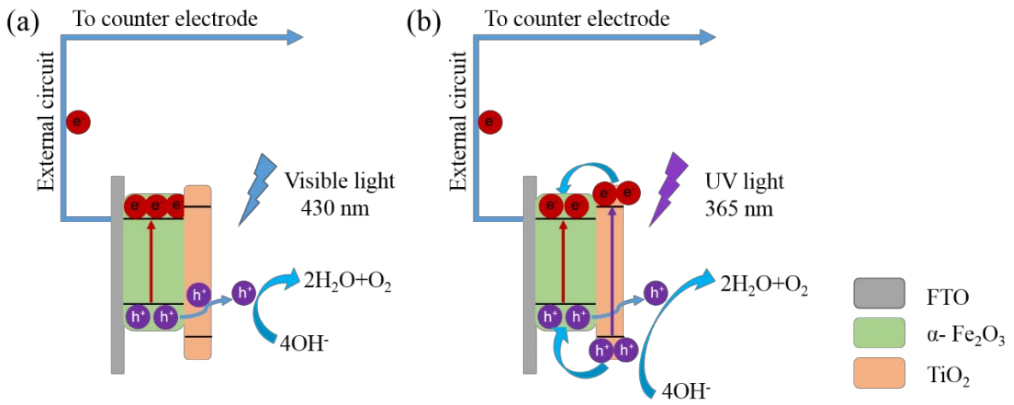

Figure 5.1 Schematic illustration of the charge-transfer pathways in the TiO2/Fe2O3 system under visible light and UV light.

5.2.4 Conclusions

TiO_2-X/Fe_2O_3 heterojunctions were synthesized using both hydrothermal methods and atomic layer deposition. The resulting samples exhibited a uniform and conformal coating of TiO_2 on α-Fe_2O_3 NRs, with precise control over the morphology and thickness of the TiO_2 overlayer. Comparative studies were conducted on pristine hematite and hematite coated tuning TiO_2 thicknesses to evaluate their photocurrent response under visible and UV light. The presence of TiO_2 overlayer notably enhanced the photocurrent response compared to pristine hematite, with response being highly related to the TiO_2 overlayer thickness. Optimal photoanode performance was observed with a 1.7 nm coating (TiO_2-20/Fe_2O_3) under both visible and UV light. Specifically, the photocurrent density of TiO_2-20/Fe_2O_3 reached 0.27 mA·cm^{-2} at 0.5 V vs. Hg/HgO under visible light, ~27 times higher than pristine α-Fe_2O_3. The TiO_2 overlayer acted as a passivation layer under visible light, facilitating the transfer of photogenerated holes and reducing surface recombination rates of electron-hole pairs, with α-Fe_2O_3 generating electron-hole pairs. Under UV light, TiO_2 served mainly as passivation layer at lower thickness (≤ 6.8 nm). However, at higher thickness, TiO_2 may act as light absorber layer as well, reducing the contribution of α-Fe_2O_3. This section not only offered comprehensive insights into the impact of TiO_2 overlayer on the photoelectrochemical (PEC) water splitting

performance of α-Fe_2O_3, but also laid the groundwork for the design and development of high-performance photoanodes.

5.3 References

[1] T. O. Ajiboye, O. A. Oyewo, D. C. Onwudiwe, *Chemosphere* **2021**, *262*, 128379.

[2] S. Anandan, V. Kumar Ponnusamy, M. Ashokkumar, *Ultrason Sonochem* **2020**, *67*, 105130.

[3] S. Varjani, P. Rakholiya, T. Shindhal, A. V. Shah, H. H. Ngo, *Journal of Water Process Engineering* **2021**, *39*, 101734.

[4] C. R. Holkar, A. J. Jadhav, D. V. Pinjari, N. M. Mahamuni, A. B. Pandit, *J Environ Manage* **2016**, *182*, 351.

[5] C. Alberoni, I. Barroso-Martin, A. Infantes-Molina, E. Rodriguez-Castellon, A. Talon, H. Zhao, S. You, A. Vomiero, E. Moretti, *Mater Chem Front* **2021**, *5*, 4138.

[6] M. Telkhozhayeva, B. Hirsch, R. Konar, E. Teblum, R. Lavi, M. Weitman, B. Malik, E. Moretti, G. D. Nessim, *Appl Catal B* **2022**, *318*, 121872.

[7] G. Ciamician, *Science* **1912**, *36*, 385.

[8] D. Ma, H. Yi, C. Lai, X. Liu, X. Huo, Z. An, L. Li, Y. Fu, B. Li, M. Zhang, L. Qin, S. Liu, L. Yang, *Chemosphere* **2021**, *275*, 130104.

[9] P. Naliwajko, J. Strunk, *Heterogeneous Photocatalysis* **2021**, 101.

[10] M. T. Noman, M. A. Ashraf, A. Ali, *Environmental Science and Pollution Research* **2019**, *26*, 3262.

[11] E. Moretti, E. Cattaruzza, C. Flora, A. Talon, E. Casini, A. Vomiero, *Appl Surf Sci* **2021**, *553*, 149535.

[12] L. Liccardo, E. Lushaj, L. Dal Compare, E. Moretti, A. Vomiero, *Small Science* **2022**, *2*, 2100104.

[13] J. Liu, L. Zhu, S. Xiang, H. Wang, H. Liu, W. Li, H. Chen, *ACS Sustain Chem Eng* **2019**, *7*, 16927.

[14] Q. Guo, C. Zhou, Z. Ma, X. Yang, *Advanced Materials* **2019**, *31*, 1901997.

[15] L. Pan, S. Wang, J. Xie, L. Wang, X. Zhang, J. J. Zou, *Nano Energy* **2016**, *28*, 296.

[16] M. Iraj, F. D. Nayeri, E. Asl-Soleimani, K. Narimani, *J Alloys Compd* **2016**, *659*, 44.

[17] Z. Li, S. Wang, J. Wu, W. Zhou, *Renewable and Sustainable Energy Reviews* **2022**, *156*, 111980.

[18] X. Wang, L. Mayrhofer, M. Hoefer, S. Estrade, L. Lopez-Conesa, H. Zhou, Y. Lin, F. Peiró, Z. Fan, H. Shen, L. Schaefer, M. Moseler, G. Braeuer, A. Waag, *Adv Energy Mater* **2019**, *9*, 1.

[19] Z. Miao, G. Wang, L. Li, C. Wang, X. Zhang, *J Mater Sci* **2019**, *54*, 14320.

[20] S. Kaya, O. Ozturk, L. Arda, *Ceram Int* **2020**, *46*, 15183.

[21] J. Yang, J. Du, X. Li, Y. Liu, C. Jiang, W. Qi, K. Zhang, C. Gong, R. Li, M. Luo, H. Peng, *Nanomaterials* **2019**, *9*, 526.

[22] D. Polidoro, A. Perosa, E. Rodríguez-Castellón, P. Canton, L. Castoldi, D. Rodríguez-Padrón, M. Selva, *ACS Sustain Chem Eng* **2022**, *10*, 13835.

[23] D. Rodríguez-Padrón, M. Algarra, L. A. C. Tarelho, J. Frade, A. Franco, G. De Miguel, J. Jiménez, E. Rodríguez-Castellón, R. Luque, *ACS Sustain Chem Eng* **2018**, *6*, 7200.

[24] E. Rodríguez-Aguado, A. Infantes-Molina, A. Talon, L. Storaro, L. León-Reina, E. Rodríguez-Castellón, E. Moretti, *Int J Hydrogen Energy* **2019**, *44*, 923.

[25] P. Makuła, M. Pacia, W. Macyk, *Journal of Physical Chemistry Letters* **2018**, *9*, 6814.

[26] A. Houas, H. Lachheb, M. Ksibi, E. Elaloui, C. Guillard, J. M. Herrmann, *Appl Catal B* **2001**, *31*, 145.

[27] M. Basu, A. K. Sinha, M. Pradhan, S. Sarkar, A. Pal, C. Mondal, T. Pal, *Journal of Physical Chemistry C* **2012**, *116*, 25741.

[28] S. Haq, W. Rehman, M. Waseem, V. Nair, P. Dhar, R. Vinu, *RSC Adv* **2016**, *6*, 18204.

[29] L. Tan, Z. Liu, C. Zhou, L. Ding, *Journal of Nanoparticle Research* **2021**, *23*, 191.

[30] Q. Xiang, X. Ma, D. Zhang, H. Zhou, Y. Liao, H. Zhang, S. Xu, I. Levchenko, K. Bazaka, *J Colloid Interface Sci* **2019**, *556*, 376.

[31] M. Zeng, *Bull Korean Chem Soc* **2013**, *34*, 953.

[32] C. Navas-Cárdenas, N. Benito, E. E. Wolf, F. Gracia, *Int J Hydrogen Energy* **2022**, *47*, 20867.

[33] K. B. Ibrahim, T. A. Shifa, P. Moras, E. Moretti, A. Vomiero, *Small* **2023**, *19*, 2204765.

[34] K. B. Ibrahim, T. A. Shifa, M. Bordin, E. Moretti, H. Wu, A. Vomiero, *Small Methods* **2023**, *7*, 2300348.

[35] Y. W. Phuan, W.-J. Ong, M. N. Chong, J. D. Ocon, *Journal of Photochemistry and Photobiology C: Photochemistry Reviews* **2017**, *33*, 54.

[36] Y. Yang, S. Niu, D. Han, T. Liu, G. Wang, Y. Li, *Adv Energy Mater* **2017**, *7*, 1700555.

[37] J. Joy, J. Mathew, S. C. George, *Int J Hydrogen Energy* **2018**, *43*, 4804.

[38] S. Kment, F. Riboni, S. Pausova, L. Wang, L. Wang, H. Han, Z. Hubicka, J. Krysa, P. Schmuki, R. Zboril, *Chem Soc Rev* **2017**, *46*, 3716.

[39] M. Mishra, D.-M. Chun, *Appl Catal A Gen* **2015**, *498*, 126.

[40] L. Li, Y. Yu, F. Meng, Y. Tan, R. J. Hamers, S. Jin, *Nano Lett* **2012**, *12*, 724.

[41] C. Li, A. Li, Z. Luo, J. Zhang, X. Chang, Z. Huang, T. Wang, J. Gong, *Angewandte Chemie* **2017**, *129*, 4214.

[42] M. Ji, J. Cai, Y. Ma, L. Qi, *ACS Appl Mater Interfaces* **2016**, *8*, 3651.

[43] Y. Li, X. Wei, B. Zhu, H. Wang, Y. Tang, T. C. Sum, X. Chen, *Nanoscale* **2016**, *8*, 11284.

[44] X. Yang, R. Liu, C. Du, P. Dai, Z. Zheng, D. Wang, *ACS Appl Mater Interfaces* **2014**, *6*, 12005.

[45] K.-Y. Yoon, J.-S. Lee, K. Kim, C. H. Bak, S.-I. Kim, J.-B. Kim, J.-H. Jang, *ACS Appl Mater Interfaces* **2014**, *6*, 22634.

[46] L. Palmolahti, H. Ali-Löytty, R. Khan, J. Saari, N. V. Tkachenko, M. Valden, *The Journal of Physical Chemistry C* **2020**, *124*, 13094.

[47] R. Franking, L. Li, M. A. Lukowski, F. Meng, Y. Tan, R. J. Hamers, S. Jin, *Energy Environ. Sci.* **2013**, *6*, 500.

[48] S. S. Mali, C. S. Shim, H. K. Park, J. Heo, P. S. Patil, C. K. Hong, *Chemistry of Materials* **2015**, *27*, 1541.

[49] X. Li, P. S. Bassi, P. P. Boix, Y. Fang, L. H. Wong, *ACS Appl Mater Interfaces* **2015**, *7*, 16960.

[50] D. Wang, Y. Chen, Y. Zhang, X. Zhang, N. Suzuki, C. Terashima, *Appl Surf Sci* **2017**, *422*, 913.

[51] F. Feng, C. Li, J. Jian, X. Qiao, H. Wang, L. Jia, *Chemical Engineering Journal* **2019**, *368*, 959.

[52] M. G. Ahmed, I. E. Kretschmer, T. A. Kandiel, A. Y. Ahmed, F. A. Rashwan, D. W. Bahnemann, *ACS Appl Mater Interfaces* **2015**, *7*, 24053.

[53] T. Imrich, R. Zazpe, H. Krýsová, Š. Paušová, F. Dvorak, J. Rodriguez-Pereira, J. Michalicka, O. Man, J. M. Macak, M. Neumann-Spallart, J. Krýsa, *J Photochem Photobiol A Chem* **2021**, *409*, 113126.

[54] R. Mechiakh, N. Ben Sedrine, R. Chtourou, R. Bensaha, *Appl Surf Sci* **2010**, *257*, 670.

[55] V. Bukauskas, S. Kaciulis, A. Mezzi, A. Mironas, G. Niaura, M. Rudzikas, I. Šimkienė, A. Šetkus, *Thin Solid Films* **2015**, *585*, 5.

[56] J. Wang, Z. Yin, F. Hermerschmidt, E. J. W. List-Kratochvil, N. Pinna, *Adv Mater Interfaces* **2021**, *8*, 2100759.

[57] C. Marichy, N. Pinna, *Coord Chem Rev* **2013**, *257*, 3232.

[58] N. Pinna, M. Knez, *Atomic Layer Deposition of Nanostructured Materials*, Wiley, **2011**.

[59] M. Leskelä, M. Ritala, *Thin Solid Films* **2002**, *409*, 138.

[60] C. Marichy, N. Pinna, *Adv Mater Interfaces* **2016**, *3*, 1600335.

[61] C. Marichy, M. Bechelany, N. Pinna, *Advanced Materials* **2012**, *24*, 1017.

[62] Y. Xia, L. Yin, *Physical Chemistry Chemical Physics* **2013**, *15*, 18627.

[63] K. Yao, P. Basnet, H. Sessions, G. K. Larsen, S. E. H. Murph, Y. Zhao, *Catal Today* **2016**, *270*, 51.

[64] Y. Liu, R. D. L. Smith, *ACS Appl Mater Interfaces* **2022**, *14*, 6615.

[65] E. A. Kraut, R. W. Grant, J. R. Waldrop, S. P. Kowalczyk, *Phys Rev Lett* **1980**, *44*, 1620.

[66] T. Schultz, M. Kneiß, P. Storm, D. Splith, H. von Wenckstern, M. Grundmann, N. Koch, *ACS Appl Mater Interfaces* **2020**, *12*, 8879.

[67] Z. Xing, F. Ren, H. Wu, L. Wu, X. Wang, J. Wang, D. Wan, G. Zhang, C. Jiang, *Sci Rep* **2017**, *7*, 43901.

[68] R. Liu, Z. Zheng, J. Spurgeon, X. Yang, *Energy Environ. Sci.* **2014**, *7*, 2504.

[69] K. Sivula, F. Le Formal, M. Grätzel, *ChemSusChem* **2011**, *4*, 432.

[70] X. Lv, S. Shao, Y. Xiao, J. Deng, *Appl Surf Sci* **2021**, *560*, 150036.

[71] X. Chai, H. Zhang, C. Cheng, *Semicond Sci Technol* **2017**, *32*, 114003.

[72] C. Shen, E. Wierzbicka, T. Schultz, R. Wang, N. Koch, N. Pinna, *Adv Mater Interfaces* **2022**, *9*, 2200643.

[73] Z. Luo, T. Wang, J. Zhang, C. Li, H. Li, J. Gong, *Angewandte Chemie International Edition* **2017**, *56*, 12878.

[74] C. Marichy, N. Donato, M. Latino, M. Georg Willinger, J.-P. Tessonnier, G. Neri, N. Pinna, *Nanotechnology* **2015**, *26*, 024004.

Chapter 6 – *Doping engineering*

Doping TiO_2 is an effective strategy to improve and expand photocatalytic capabilities. The main body of this chapter is based on the appended Paper-V, submitted under review. Thus, the first section, based on Paper-V, is focused on ceria-doped titania nano-octahedra (CeTNOh) derived from Ce-containing titanate nanowires, via ultrasonication-hydrothermal treatment from commercial titania (Degussa P25). Thanks to their favourable properties, CeTNOh are proposed as novel photocatalysts for the removal of ciprofloxacin, a common antibiotic, in aqueous solution under simulated solar light, at room temperature and atmospheric pressure. In addition, preliminary results on nitrogen-doped Titania Hollow Spheres (Nx-THS) are discussed in the second section of this chapter.

Paper-V

B. Shani, L. Liccardo, I. Barroso-Martín, M. Bordin, A. Infantes-Molina, E. Rodríguez-Castellón, A. Vomiero, E. Moretti, CeO_2-TiO_2 nano-octahedra as active photocatalysts for ciprofloxacin photodegradation under solar light. *Adv. Sustain. Syst.* 2024, Submitted and under review.

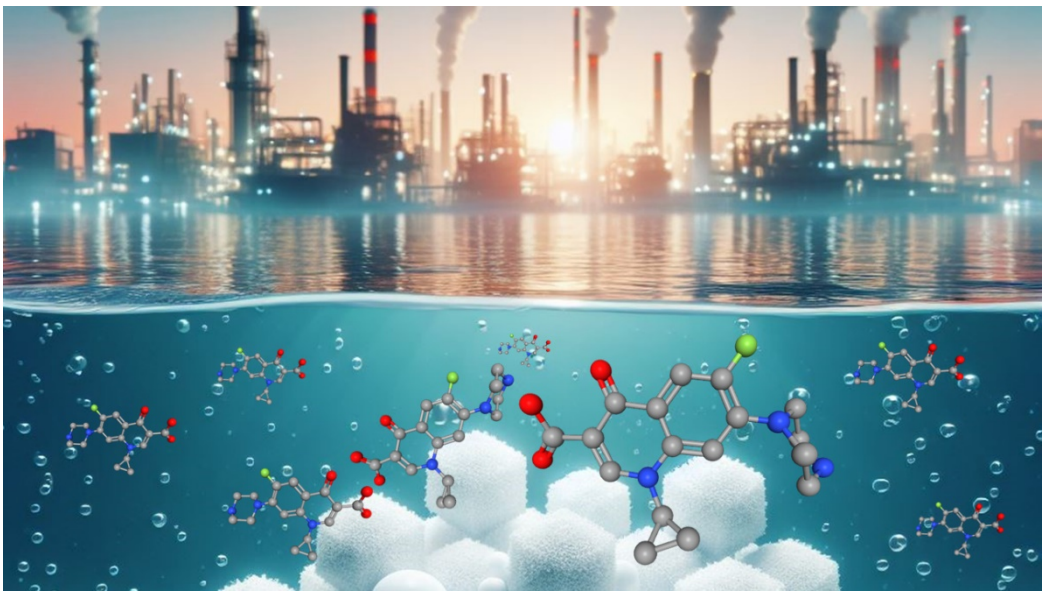

6.1 CeO_2-TiO_2 nano-octahedra

During this dissertation, it has been emphasized how environmental issues related to water contamination are of increasing concern. Special attention has been focused on hardly degradable and persistent complex molecules such as antibiotics, including ciprofloxacin (CIP). Titania is the most studied and exploited photocatalyst in UV-based AOPs operating at atmospheric pressure and room temperature (see **Chapter 1**).[1] However, the use of solar light as the main renewable energy source is a trend to consider. Thus, in this section, the combined use of two strategies, such as morphology engineering and doping, is proposed as efficient to overcome TiO_2 limits (i.e., wide bandgap energy and fast charge-carriers recombination).

From a morphological perspective, suitable nanostructures, including nanowires, nanospheres, hollow spheres, nanorods, nanooctahedra, in combination with appropriate exposure of specific TiO_2 facets has been reported to be highly beneficial for photocatalytic processes.[2–6] Specifically, in the frame of decahedron and octahedron morphologies, the exposed (101) anatase facets seem to have a pivotal role in increasing the photocatalytic oxidation of organic compounds.[7–9] In addition, the high photocatalytic activity of octahedral anatase crystals have been related to the presence of a well-crystallized surface with low density defects that lower or delay the recombination of e^-–h^+ pairs.[10,11]

As already mentioned, the TiO_2 doping with either noble metals and their alloys with non-noble metals like Cu[12,13] or reducible oxides like ceria (CeO_2), has been reported to be another efficient way to improve and enhance the catalytic performance (**Box 6.1**). Specifically, doping TiO_2 with CeO_2 seems to be a good possibility thanks to the promotion of oxygen mobility induced by the Ce^{3+}/Ce^{4+} redox pair. For instance, in the study proposed by Xu and co-workers, the presence of Ce^{4+} trapping sites have been related to the decrease in e^-–h^+ pairs recombination.[14]

Furthermore, the presence of ceria as doping agent has been also associated with the broadening of the absorption ability of pure titania toward visible light.[15]

Based on the above assumptions, in this section a set of TiO_2-doped samples showing octahedral morphology and different ceria loadings are presented as good photocatalysts for CIP photodegradation in aqueous media under simulated solar light. Additionally, the role of both morphology and ceria loading in the enhancement of photocatalytic activity of pure TiO_2 is deeply investigated.

Box 6.1: CeO_2

Cerium oxides stands out among lanthanide oxides in catalysis and photocatalysis due to its unique structural properties, including thermal stability, biocompatibility, excellent redox properties, fluorite-type construction, and oxygen storage capacity.[16,17] Cerium ($[Xe]4f^1\ 5d^1\ 6s^2$) is the first element in the lanthanide series where the lanthanoid contraction is not pronounced, allowing for the possibility to lose the 4f electron reaching the electronic configuration $[Xe]4f^0$. Cerium exhibits two possible oxidation states, namely Ce^{3+} and Ce^{4+} giving rise to two stable oxides, CeO_2 and Ce_2O_3, respectively. Cerium (IV) dioxide (CeO_2) or ceria, an n-type semiconductor, is produced through the oxidation of cerium (III) oxide (Ce_2O_3) in the presence of an excess of oxygen.[16,17] Notably, when there is a low amount of oxygen, cerium (IV) dioxide can undergo reduction and revert to cerium (III) oxide. Thus, this unique ability to selectively shuttle between Ce (III) and Ce (IV) states, referred to as oxygen storage capacity (OSC),[17] can be exploited in photocatalysis, enabling cerium materials to work as oxygen buffers promoting oxidative activities. Concerning the crystalline structure, CeO_2 exhibits a fluorite phase with a face-centered cubic lattice, where cerium cations are coordinated by eight oxygen anions.[18] During reduction processes, electrons are transferred from oxygen atoms to adjacent cerium atoms, leading to the reduction of Ce^{4+} to Ce^{3+} related to the formation of oxygen vacancies on both the

surface and the bulk of the material. The presence of oxygen vacancy defects and Ce^{3+} in the lattice of nonstoichiometric ceria, CeO_{2-x}, significantly enhances the performance of redox processes and catalytic reactions.[18–20] Ceria predominantly exists in three thermodynamically stable facets: (111), (110), and (100).[21] The (111) surface is the most stable, characterized by a repeating O−Ce−O−O−Ce-O layer structure with zero net dipole moment, thus it is less favored for vacancy defects. On the other hand, the (110) and (100) facets exhibit lower stability, and the order of reactivity for vacancy defect formation is (110) > (100) > (111), indicating that engineering crystals with different exposed facets can impact the overall redox activity and catalytic reactions of ceria.[21] While the theoretical bandgap of CeO_2 is ∼6.0 eV, the experimental bandgap is observed to be in the range 3.0-3.4 eV. Although the exact reason for the reduced bandgap remains controversial this discrepancy is likely attributed to the presence of mid-gap states and O 2p - Ce 4f transition.[22,23] Regarding charge dynamics in CeO_2, electron-hole recombination is a very fast process leading to poor photocatalytic activity. However, it is often selected as co-dopant to increase the overall photocatalytic activity of bare TiO_2. Taking advantage of the more positive CB potential of TiO_2 compared to CeO_2, photogenerated holes in the CeO_2 VB enable the oxidation of H_2O and OH^- ions into hydroxyl radicals, while electrons are transferred to the TiO_2 CB.[24] This efficient charge transfer in the composite structure enhances the separation rate and lifetime of photo-generated electron-hole pairs, leading significant improvements in the overall photocatalytic efficiency. Additionally, as light is absorbed and electrons are promoted to the CeO_2 CB, Ce^{3+} species are formed, enabling reactions with adsorbed oxygen to produce superoxide anion radicals and re-oxidation at Ce^{4+}.[24] Furthermore, the purpose of doping TiO_2 with Ce is to enhance photocatalytic activity in the visible region, thus narrowing the TiO_2 bandgap. In fact, the introduction of Ce^{3+} ions in the ceria−titania system creates additional states in the bandgap, attributed to the presence of oxygen vacancies and the partially occupied Ce^{3+} 4f levels, leading to an overall bandgap reduction.[25]

6.1.1 Morphology and crystal structure

To obtain the final catalysts, a modified ultrasonication-hydrothermal synthesis reported by Wei and co-workers[26] was followed. First, as shown in **Figure 6.1a**, potassium titanate nanowires (TNW) were synthesized hydrothermally, using a commercial P25 titania aqueous suspension under strong alkaline conditions. TNW were then used as precursors for the second step to obtain nano-octahedra via ultrasonication-hydrothermal synthesis. The ceria doping occurred during the first step, following the same procedure to obtain TNW. Upon step 1, the samples were labeled as CeTNWx, where Ce stands for ceria and x refers to the nominal wt.% CeO_2 loading (x = 0.75, 1 and 1.5). While, following step 2, the samples were referred to as TNOh for pure titania nano-octahedra and CeTNOhx for ceria-doped samples (details on **Appendix A**).

The crystalline structure for all the samples was investigated by performing high-angle X-ray powder diffraction analyses (**Figure 6.1(b, c)**), comparing the obtained patterns with anatase TiO_2 (JCPDS #21-1272), CeO_2 (JCPDS #00-034-0394) and $K_2Ti_6O_{13}$ (JCPDS #40.0403). As expected, $K_2Ti_6O_{13}$ phase was found to be present in TNW and CeTNWx samples, showing diffraction peaks at 2θ (°) 11.48, 24.11, 29.25 and 47.89 (**Figure 6.1b**). In **Figure 6.1c**, TNOh and TNOhx exhibited diffractograms with sharper and more intense peaks, indicating a higher level of crystallinity compared to TNWs. Evidence of the anatase polymorph formation was revealed by diffraction peaks observed at 2θ (°) 25.34, 38.61, 48.10, 55.13, 62.69, and 68.76°. This indicates that following the second hydrothermal treatment, a substantial portion of $K_2Ti_6O_{13}$ was successfully converted into the highly photoactive phase Anatase TiO_2.[27] Specifically, all the TNOh and TNOhx samples showed the most intense peak at 2θ (°) 25.34 related to the (101) crystal plane, that according to Bragg's law returns a d spacing of 0.35 nm, typical of the anatase phase. The amount of ceria doping was below the detection limit of the XRD technique thus, for all the TNOhx samples, no presence of CeO_2 was detected.

Using the Scherrer equation, the anatase mean crystallite size was estimated for both the nanowires and nano-octahedra, as detailed in **Table 6.1**. Remarkably, a noticeable trend emerged where the mean crystallite size demonstrated an increase with Ce loading, aligning with findings previously recorded in other Ce-Ti systems.[26,28]

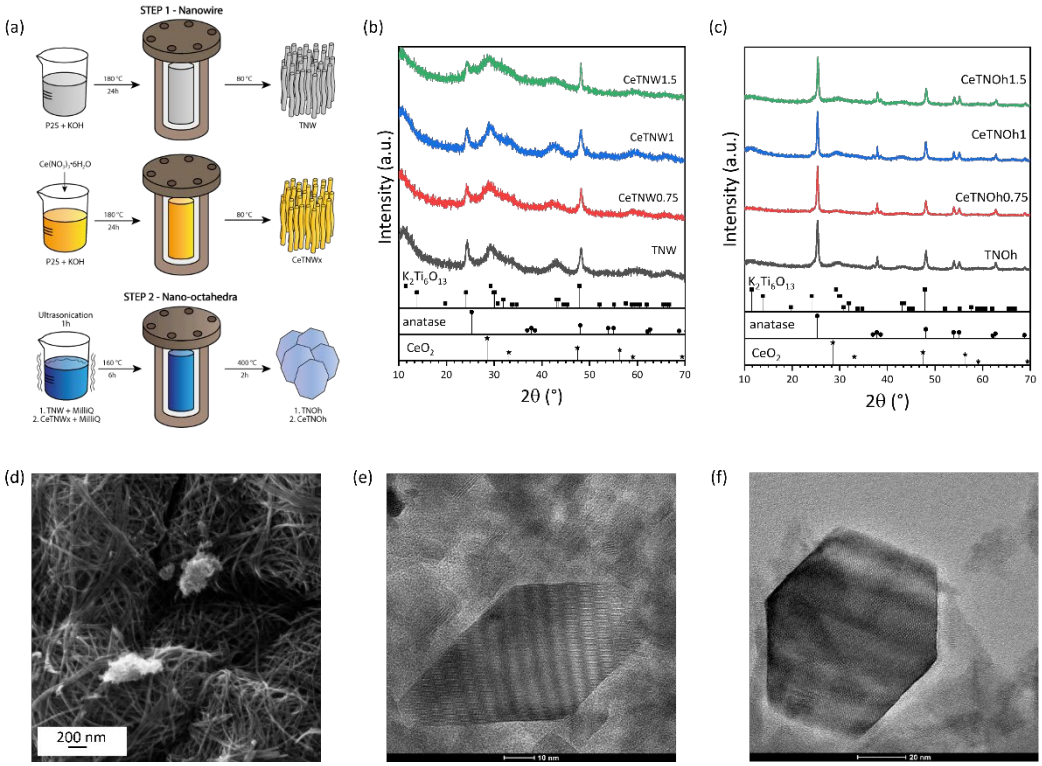

Figure 6.1 (a) Graphical overview of the catalyst's synthesis. **Step 1**: hydrothermal synthesis of TNW and CeTNW. **Step 2**: hydrothermal-ultrasonication synthesis of nano-octahedra. **(b)** High angle XRD pattern for CeTNWx set; **(c)** High angle XRD pattern for CeTNOhx set**; (d)** SEM image of TNW; HR-TEM micrographs of **(e)** TNOh and **(f)** CeTNOh0.75.

The morphology and elemental analysis for all the samples was evaluated by FE-SEM, HR-TEM and EDS-STEM. As shown in **Figure 6.1d** (taken as representative picture), P25 was successfully converted in TNW or CeTNWx during the hydrothermal treatment. Notably, CeTNW1 showed some changes in NWs length and diameter. In detail, the ceria addition led to a decrease in NWs length from 86 nm to 71 nm and a reduced diameter from 7 nm to 5 nm compared with pure TNW. The presence of homogeneously distributed cerium was confirmed by EDS analysis performed with STEM for the selected sample CeTNW1. Besides, the presence of

potassium and titanium related to the potassium titanate phase (already observed by XRD analysis) was also confirmed. As observed by HR-TEM images in **Figure 6.1e, f**, after the second step of the synthesis, both pure and Ce-doped samples showed well-defined octahedra nanoparticles with an average length of 63 nm and width of 31 nm (calculated by ImageJ software analysis). Furthermore, the size of nano-octahedra (NOh) increased in correlation with the ceria loading. Notably, the length and width measured 71 and 37 nm for CeTNOh0.75 and 91 and 45 nm for CeTNOh1, respectively. As already found for CeTNWx, EDS-STEM analyses revealed the presence of homogeneously disperse Ce inside the CeTNOhx without the formation of any aggregates.

N_2-physisorption and BET analysis were performed to assess textural properties, porosity and specific surface area of the samples in comparison with pristine commercial P25 (Degussa) used as a Ti precursor, and commercial Anatase TiO_2 (from Sigma-Aldrich). According to the IUPAC classification, TNW and TNOh and the relative Ce-doped samples, exhibited Type-IV isotherms with H3 hysteresis loop, typical of mesoporous materials.[29] The hydrothermal process to obtain TNWs is beneficial to reach high specific surface area.[30] In fact, both TNW and CeTNWx showed a very high specific surface area (SSA) ranging from 357 to 302 $m^2 \cdot g^{-1}$ and pore volume (V) of 0.65-0.96 $cm^3 \cdot g^{-1}$, significantly higher than the values reported for the bare commercial P25 titania (61 $m^2 \cdot g^{-1}$). There is no clear evidence of an established trend between Ce-content and enhancement of textural properties. As expected, both TNOh and CeTNOhx samples showed lower SSA compared to their nanowire precursors. Crystal growth, as observed in XRD results, along with thermal treatment, can lead to lack textural properties compared with titanate precursors.[31] However, the recorded SSA values for TNOh samples and their Ce-doped relatives were in the range 164-233 $m^2 \cdot g^{-1}$, about three times higher than the SSA of P25.

Table 6.2 Summary of the main properties related to structural and optical characterization for CeTNWx and CeTNOh samples.

Sample	Ce (wt.%)	Crystallite size (nm)	[1]BET SSA ($m^2 \cdot g^{-1}$)	[2]Pore V ($cm^3 \cdot g^{-1}$)	[3]Pore size (nm)	E_g (eV)
TNW	0.00	15.9	302	0.76	11.0	3.16
CeTNW0.75	0.75	17.0	357	0.96	14.6	3.07
CeTNW1	1.00	13.2	303	0.65	10.3	3.02
CeTNW1.5	1.50	32.5	355	0.93	13.3	2.99
TNOh	0.00	29.0	164	0.52	135	3.20
CeTNOh0.75	0.75	37.0	122	0.36	121	2.94
CeTNOh1	1.00	43.0	198	0.50	113	2.95
CeTNOh1.5	1.50	39.0	194	0.53	107	2.74
P25	-	-	61	0.10	6.8	3.20
Anatase	-	-	85	0.19	10.1	3.10

[1] N_2 physisorption values obtained at -196°C with BET method by N_2-physisorption at -196°C.

[2] Single point adsorption total pore volume of pores calculated at relative pressure $P/P_0 = 0,94$ by N_2-physisorption at -196°C.

[3] BJH Desorption average pore width by N_2 physisorption at -196°C.

6.1.2 Ce-doping

Ce content was investigated by the synergic use of Rutherford Backscattering Spectrometry (RBS) to follow the Ce profile within the samples and to obtain Ce:Ti atomic ratio, and high-resolution X-ray photoemission spectroscopy (XPS) to study the surface chemical composition. Briefly, a homogeneous Ce concentration was detected for all CeTNOhx samples, with a maximum Ce:Ti atomic ratio of 0.005:1 for CeTNOh1.5, while, as expected, no Ce species were detected in TNOh sample.

Concerning the XPS analysis, high-resolution Ti *2p*, O *1s*, and Ce *3d* core level spectra for both titanate nanowires and nano-octahedra are depicted in **Figure 6.2** and **Figure 6.3**, respectively.

The Ti 2p core level spectra can be fitted with the typical asymmetric doublet indicating the presence of Ti^{4+} species for both TNW/CeTNWx and TNOh/CeTNOhx series. In fact, the peaks at ~458.5 and 464.4 eV were assigned to Ti $2p_{3/2}$ and Ti $2p_{1/2}$, respectively, that showed a separation of 5.7 eV, normally ascribed to octahedrally coordinated Ti^{4+} ions.[30,32] In detail, the slight variations in binding energy between the main Ti $2p_{3/2}$ peaks at 458.7 eV for TNW/CeTNWx and 458.4 eV for

TNOh/CeTNOhx, can be ascribed to the different interactions between Ce and Ti species within the two series of samples.[33] Furthermore, when increasing Ce content in CeTNWx the main peak shifted to lower binding energies. Notably, K^+ and Ce^{3+} ions are showing similar ionic radii (i.e., 0.133 and 0.114 nm, respectively)[34] thus, the latter shift could be associated with the partial substitution of K^+ by Ce^{3+} ions within the TiO_2 lattice, that consequently bringed to the formation of Ti-O-Ce bonds.[35] Conversely, with the increasing in Ce content, the Ti $2p_{3/2}$ peak for CeTNOhx shifted toward higher binding energies. In this case, the presence of Ce may lead to higher mobility of electrons at the core level.[30,36]

Concerning the O *1s* core level spectra, three main components were needed to describe all the samples. In TNW/CeTNWx samples, the peak at ~530.2 eV was related to oxygen in stoichiometric TiO_2 lattice, while the second at 531.3 eV was associated with the presence of several species including surface adsorbed oxygen, defect oxide states and hydroxyl groups bonded to Ti. Moving toward higher binding energies, the last component in the range 532.5-533.5 eV can be attributed to adsorbed water molecules on the catalysts surface.[30,31,34] Remarkably, as for the already discussed Ti *2p* core level spectra, the main peak at ~530.2 eV shifted toward lower binding energies when increasing the Ce loadings in CeTNWx due to higher degree of interactions between Ce and Ti species. Regarding TNOh/CeTNOhx samples, the main peak associated with lattice oxygen was located at lower binding energies (~529.8 eV), suggesting an increasing on the contribution from CeO_2 lattice oxygen. Consequently, it can be suggested that the second step of the synthesis leads to CeO_2-TiO_2 heterojunction formation.[32] In this case, with the increasing in the cerium loading, a shift toward higher binding energies was observed, indicating an increased number of adsorbed reactive oxygen species with high mobility,[31,33] and a stronger interaction between Ce and Ti with the possible formation of a CeTiO solid solution.[35] It is worth noting that the intensity of the last component at 532.5-533.5 eV, decreased in TNOh/CeTNOhx samples compared to TNW/CeTNWx samples. This may be ascribed to the second hydrothermal

treatment followed by the calcination procedure, that led to the loss of superficially adsorbed water molecules.

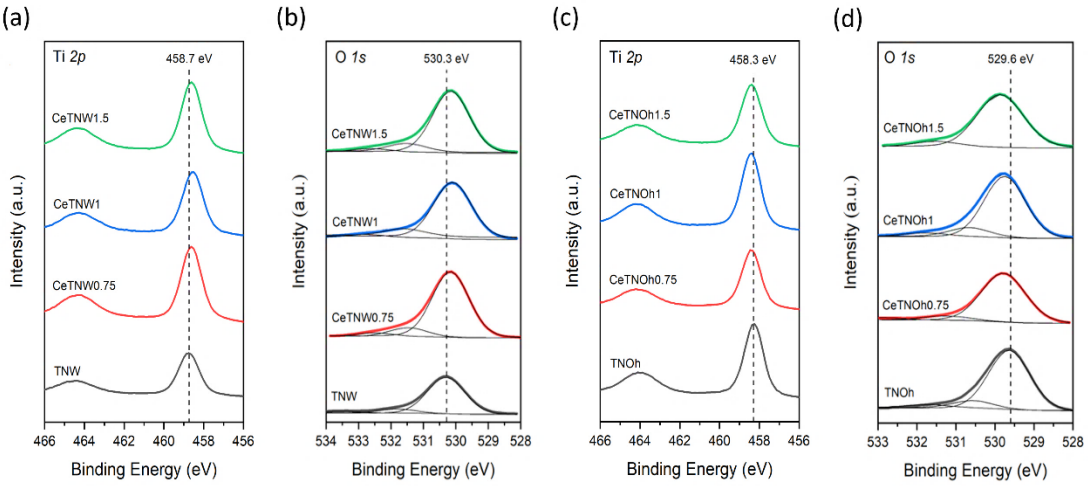

Figure 6.2 (a) Ti 2p core level spectra and **(b)** O 1s core level spectra for CeTNWx catalysts. **(c)** Ti 2p core level spectra and **(d)** O 1s core level spectra for CeTNOhx catalysts.

As shown in **Figure 6.3**, Ce 3d core level spectra displayed a low signal-to-noise ratio because of the low metal loading. However, the presence of both Ce^{4+} and Ce^{3+} species were detected for both CeTNWx and CeTNOhx samples, especially at higher Ce-loading due to stronger electronic interactions between Ce and Ti.[37] In fact, in all the Ce *3d* core level spectra, the following spin-orbit doublets associated to Ce^{4+} were recorded: v (~882.7 eV) and u (~901.3 eV); v" (~888.5 eV) and finally, satellite peaks associated with tetravalent Ce in Ce compounds, u" (~907.3 eV); v''' (~898.3 eV) and u''' (~916.9 eV).[36] Moreover, the Ce^{3+} presence was also observed, thanks to the presence of high binding energy doublets v' (~885.2 eV) and u' (~903.4 eV) and lowest binding energy states v_0 (~880.9 eV) and u_0 (~899.2 eV).[38] As already mentioned, the intensity of Ce^{3+} related peaks increased with the increase in the Ce-loading, indicating a stronger electronic interaction between Ce and Ti.[37] Noteworthy, the signals in CeTNOhx samples were more intense (**Figure 6.3b**), suggesting the presence of a higher number of superficially exposed Ce species.

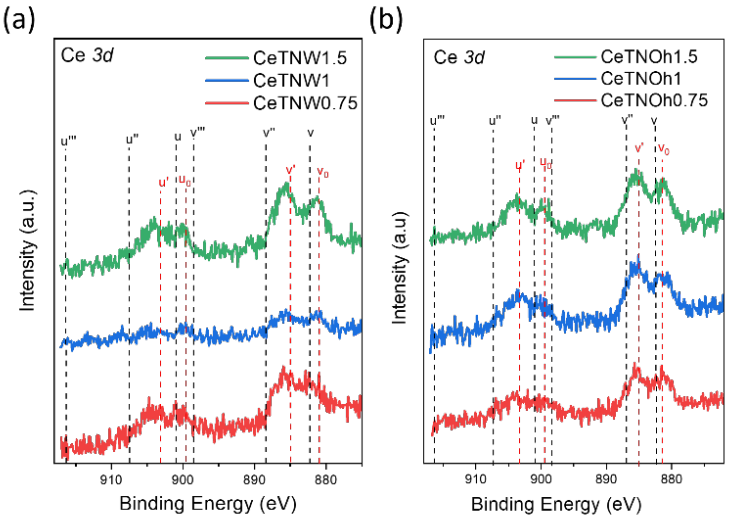

Figure 6.3 Ce 3d core level spectra for **(a)** CeTNWx and **(b)** CeTNOhx catalysts.

According to what is reported in literature, the coexistence of Ce^{3+} and Ce^{4+} species seems to enhance the photocatalytic performance in Ce-Ti systems. This enhancement is attributed to their electron transfer ability, that improves the efficient separation of photogenerated e^-–h^+ pairs.[32] Thus, to further study the charge-carriers dynamic and the photo-responsive behavior of the prepared materials, DRUV-Vis and PL spectroscopy were performed. DRUV-Vis spectra, Tauc plots and F(R) spectra for all the samples and the benchmark Sigma-Aldrich Anatase are reported in **Figure 6.4**. Band gap values were calculated from Tauc Plots, using the intercept of the extrapolated linear fit and they were collected in **Table 6.1** for both TNW/CeTNWx and TNOh/CeTNOhx series.

TNW and TNOh samples in their pure form displayed the characteristic absorption edge typical of TiO_2 materials at ~400 nm, indicating a wide bandgap absorption in the UV region.[39,40] From **Figure 6.4a, b**, it can be noticed that the Ce-doping resulted in a red-shift of the main absorbance peak, particularly pronounced in the nano-octahedra series. This shift can be attributed to the formation of Ce^{3+} species, which introduced localized mid-gap states within the bandgap of TiO_2

semiconductor.[41,42] Confirming what previously found from XPS measurements, the significant shift observed in the CeTNOhx series may be attributed to the formation of a CeO_2-TiO_2 heterojunction, characterized by a close contact between ceria and titania.[43]

This is more notably in the CeTNOhx F(R) spectra, as illustrated in **Figure 6.4c**. All samples exhibited the characteristic strong absorption band of titanium dioxide in the UV region, typically centered around 310 nm, with a broader profile observed for the pure TNOh sample. Additionally, in the case of CeTNOhx, the visible red-shift of the main band edges suggested the 4f to 5d transition of Ce^{3+} within the ligand environment of O^{2-} surrounding the TiO_2 nanoparticles. Thus, the prevalence of Ce^{3+} over Ce^{4+} species in the samples is further confirmed. Specifically, the lack of electrons in Ce ions in the +4 state hinders any transition from the ground state electronic configuration ($4f^0 5d^0$).[44]

The observed red-shift significantly impacted the band gap values, decreasing from 3.2 eV in the pure titanate nanowires to 2.99 eV in samples with the highest ceria content (**Figure 6.4d, e**). Moreover, this decrease is more prominent in CeTNOhx catalysts, where the band gap narrows from 3.2 eV for the pure TNOh sample to

2.74 eV for the CeTNOh1 sample. These values align with previously reported data for ceria-titania nanostructures.[23,45]

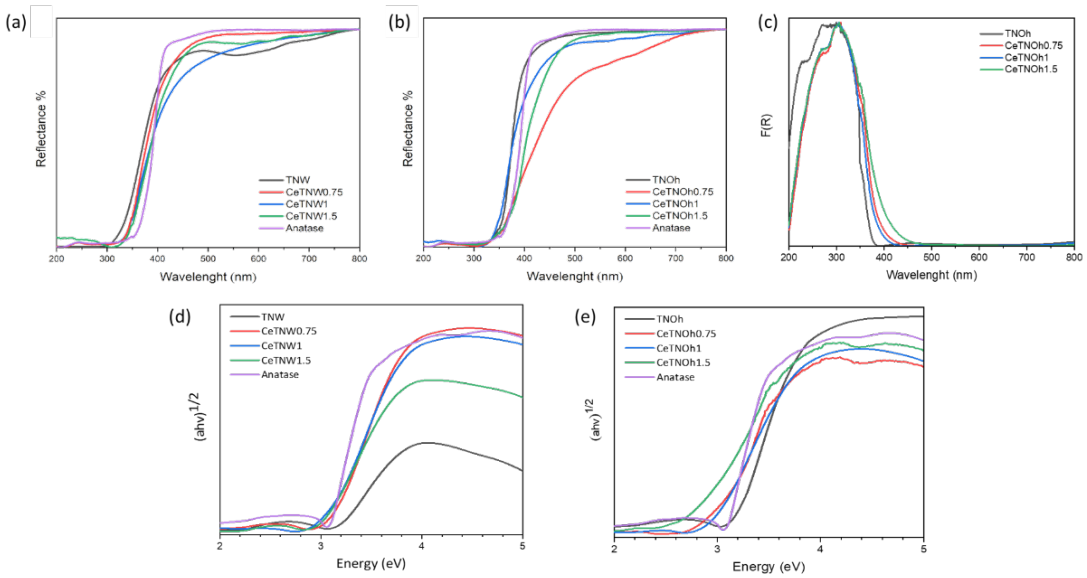

Figure 6.4 DRUV-Vis spectra for **(a)** CeTNWx and **(b)** CeTNOhx series; **(c)** F(R) spectra for CeTNOhx samples; Tauc plots for **(d)** CeTNWx and **(e)** CeTNOh series.

PL spectra for both pure TNOh and CeTNOhx catalysts were acquired by exciting the material at 350 nm with a cut-off filter at 370 nm. **Figure 6.5** illustrates that the undoped TNOh displayed a strong emission band ranging from 380 to 600 nm, characterized by multiple emission peaks. A detectable non-uniform emission trend was evident as the dopant content increased. Within the optimal doping threshold (up to 1 wt.%), energy transfer among Ce^{3+} ions occurred, leading to luminescence quenching, thereby delaying the recombination of charge carriers. However, beyond this optimal doping concentration, the dopant itself may become a radiative recombination center, subsequently increasing the rate of charge-carrier recombination and consequently, the PL intensity.

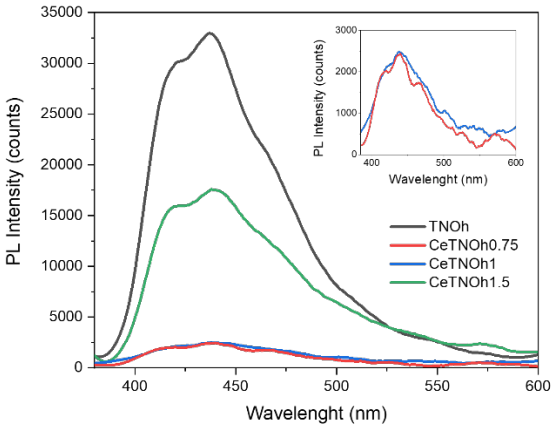

Figure 6.5 PL spectra for CeTNOhx samples.

6.1.3 Photodegradation of Ciprofloxacin

The evaluation of photocatalytic activity under simulated solar light irradiation, at room temperature and in an aqueous solution containing ciprofloxacin (CIP), was carried out for both pure titania nano-octahedra sample, TNOh, and all Ce-doped titania nano-octahedra systems, CeTNOhx. As shown in **Figure 6.6a** for representative TNOh sample, the photodegradation reaction of CIP over time was monitored by following the decrease of the main absorbance peak at 272 nm. The corresponding C/C_0 curves and kinetic studies as a function of irradiation time are reported in **Figure 6.6b, c**. CIP was chosen as the target molecule since it is highly stable under sunlight irradiation as confirmed by the C/C_0 curve which decreased slightly (by a ~13%) after 360 min of exposure. Upon equilibration time in dark conditions (30 min), CIP was partially adsorbed on the photocatalysts surface with a decrease in its concentration of ~20% for each sample, except for CeTNOh1.5, that adsorbed almost the 34% of drug. The higher amount of CeO_2 on CeTNOh1.5 surface observed from XPS results, may boost the interactions with CIP.[46] Under simulated solar light irradiation, a decrease in C/C_0 curves with the increase of reaction time was detected for all the samples. The best performing sample was CeTNOh0.75, with the best degradation efficiency of 83% within 360 min. As

reported in **Figure 6.6c**, despite the highest efficiency, apparent kinetic constant of CeTNOh0.75 ($6.1 \cdot 10^{-3}$ min^{-1}) was recorded to be notably lower than that showed by TNOh ($11.6 \cdot 10^{-3}$ min^{-1}). Thus, the introduction of ceria leads to a reduction in the rate of photodegradation but, simultaneously, creating CeO_2-TiO_2 systems proves to be a feasible approach to enhance the photodegradation capability.

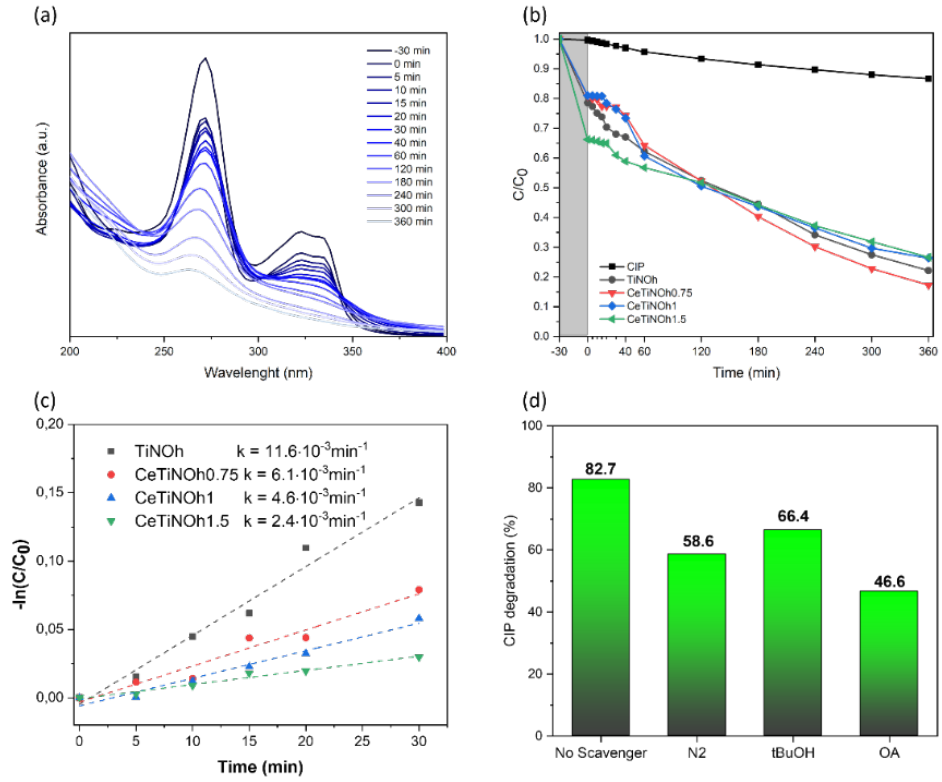

Figure 6.6 (a) UV-Visible absorption spectra recorded at different times, from 30 min under dark conditions to 360 min under simulated solar light irradiation, for the TNOh sample; **(b)** Photocatalytic degradation of CIP as a function of irradiation time with and with and without catalysts (CIP curve) under simulated solar light irradiation; **(c)** CIP degradation kinetics with linear fits of the experimental data in dashed lines; **(d)** Free radical trapping experiments results for CeTNOh0.75 photocatalyst.

This is achieved by extending the absorption range towards the visible region compared with bare sample, consequently decreasing its bandgap energy and minimizing the electron-hole recombination rate. In fact, the positive effect of Ce^{3+}/Ce^{4+} electron transfer properties on the photocatalytic activity, by enhancing the charge-carriers separation efficiency is well-known.[23] However, the separation

efficiency is strictly related to the concentration and distribution of the dopants, as well as the stability of the TiO_2 crystalline phase. Consequently, it is of extreme importance to reach the optimal amount of CeO_2 loading. In this case, the higher the ceria loading, the lower the photocatalytic activity. In fact, as demonstrated in **Figure 6.6b**, despite CeTNOh1.5 being the best solar light harvester within the series, the presence of CeO_2 in an amount higher than the 0.75 wt.% threshold, led to a decrease in photoactivity. The main active species responsible for CIP degradation were investigated by performing free radicals trapping experiments in presence of the best performing sample CeTNOh0.75 (**Figure 6.6d**). Briefly, the photocatalytic activity was significantly inhibited when oxalic acid (OA, h^+ scavenger) was added, while in presence of tert-butanol (tBuOH, OH scavenger) was barely affected. Hence, holes (h^+) should be the major reactive species involved in the CIP degradation by CeTNOh0.75 under simulated solar light irradiation.

Finally, stability and reusability tests are depicted in **Figure 6.7**. The 3-cycle reusability tests revealed that CeTNOh0.75 was still active, and the total CIP degradation percentage remained unchanged, suggesting the stability and the possibility of effectively recovering the photocatalyst from the slurry system.

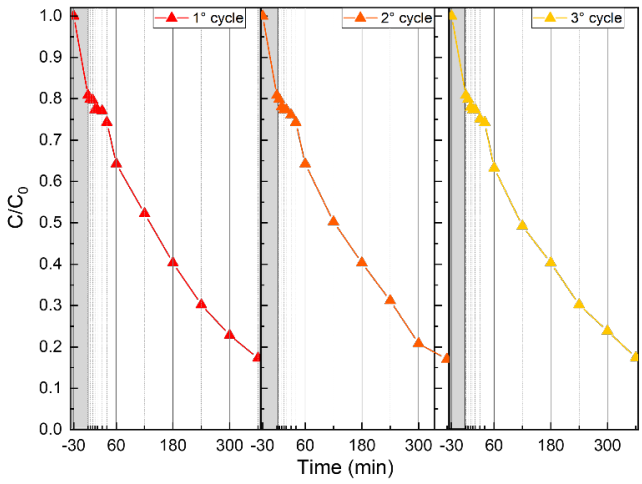

Figure 6.7 3-Cycles reusability test of the best performing sample CeTNOh0.75.

6.1.4 Conclusions

In this section an ultrasonication-hydrothermal route synthesis to obtain CeO_2 doped TiO_2 nano-octahedra was proposed. The use of characterization techniques, such as HR-TEM and XRD, confirmed the octahedral morphology and showed that samples were mainly in the anatase phase with the most intense peak related to (101) crystal planes. TNOh samples were mesoporous materials with a very high specific surface area, going from 122 to 194 $m^2\ g^{-1}$, 2-3 times higher than that of commercial anatase (Sigma-Aldrich). The photocatalytic activity was evaluated by monitoring ciprofloxacin degradation in water under simulated solar light irradiation at room temperature and atmospheric pressure. The properly designed morphology and the optimization in ceria-loading highly promoted ciprofloxacin degradation. The best performance was reached by CeTNOh0.75 sample, showing a degradation efficiency above 80%, after 360 min of exposure time. Low CeO_2 concentration was beneficial for photocatalytic activity, influencing the interactions between the catalyst and the target drug, thus the overall adsorption-desorption equilibrium. As demonstrated by optical characterizations, the presence of ceria improved the TNOh photo-response with a reduction in the bandgap energy up to 2.75 eV, and additionally, a red shift of the main absorption edge associated with oxygen vacancies was induced, due to the presence of Ce^{3+}/Ce^{4+} redox pair. PL measurements confirmed that the presence of CeO_2 enhanced the separation of photogenerated e^-–h^+ pairs by reducing the overall recombination rate. Additionally, the main species activated during the ciprofloxacin photodegradation reaction were holes as demonstrated by trapping experiments. Reusability test upon CeTNOh0.75 showed that the optimized sample was still stable and active after 3 catalytic cycles, opening the possibility for large-scale applications.

6.2 N-doped TiO_2 hollow spheres

As shown in the previous section, the combination of morphology and doping engineering can be used to successfully boost optical and electronic properties and simultaneously, overcome the fast charge-carriers recombination.[23]

In **Chapter 3** the possibility to tune both the TiO_2 crystalline and electronic band structure by doping with metal and non-metal elements have been introduced.

Since the pioneering work by Asahi and co-workers focused on visible light-driven photocatalytic ability of N-doped TiO_2 nanostructures,[47] several non-metal dopants (i.e., B, C, N, F, S, and Cl) have been widespread investigated.[48] However, nitrogen stands out as the most frequently used, primarily owing to its properties such as small ionization energy, stability, and comparable atomic size to oxygen, allowing its easy incorporation into TiO_2 crystal lattice.[48,49] N-doped TiO_2 materials have been widely used for various applications, including solar-driven AOPs, thanks to their excellent properties such as ease of synthesis, numerous nitrogen-containing precursors (e.g., aliphatic amines, nitrates, ammonium salts, urea, thiourea, ammonia), low cost, and chemical stability.[50] Moreover, N-doping by altering both the crystalline and the electronic band structures, may bring several improvements including surface modifications that enhance the reactant adsorption, and the enrichment of photoexcited e^-—h^+ pairs.[23,51]

When selecting the synthesis strategy, crucial parameters such as the optimal N-source concentration, and its distribution in the crystal structure, should be considered to prevent the creation of recombination centers.[52,53] Furthermore, to clarify the role of N in the photocatalytic activity, it is extremely important to deeply understand whether N species are interstitial or substitutional, their preferential distribution (i.e., at surface or bulk sites) and finally, how the electronic structure is influenced. [54] Thus, further investigations on N-doped TiO_2 materials are needed, to develop alternative and easy ways of synthesis that further extend their photocatalytic activity. In fact, several physical and chemical methods have

been investigated and applied to incorporate N into TiO_2 crystal lattice such as ball milling, sputtering deposition, sol-gel method, solvothermal and hydrothermal synthesis. Among all, the sol-gel method does not require sophisticated or expensive equipment and, thanks to its versatility, enables to select different TiO_2 precursors and N-sources, obtaining the desired physical and chemical properties.[49]

A fascinating way to further increase the optical properties of N-doped TiO_2 materials, is the proper design of the shape and the morphology. As deeply discussed in **Chapter 4**, TiO_2 hollow spheres (THSs) have shown their efficiency as photocatalysts thanks to their high surface area and intense light scattering ability. [55,56] However, despite the increased absorption probability, pure THSs still suffer from wide bandgap. Thus, in this section, morphology and doping engineering are combined to further enhance optical and photocatalytic properties of pure TiO_2. In this frame, preliminary results on N-doped Titania Hollow Spheres (N-THS) are introduced.

6.2.1 Morphology and crystal structure

Uniform submicrometric pure and N-doped TiO_2 hollow spheres, composed of hierarchically assembled nanoparticles, were obtained following a modified hard template-based approach combined with the sol-gel synthesis, already discussed and reported in **Paper-I**. In detail, the synthesis was carried out from step 1 to step 3 (**Figure 6.8a**), by performing the N-doping during the sol-gel method to obtain PMMA@TiO_2 core-shell system (step 2). To find the optimal concentration, four distinct formulations were selected at 0.5, 1.0, 2.0, 3.0 at % of N in TiO_2, respectively. The samples were referred to as THS for pure TiO_2 hollow spheres and Nx, for N-doped TiO_2 hollow spheres where x stands for the N content in at %. The surface morphology for all the as-synthesized samples was analysed by FE-SEM. As reported in **Figure 6.8b**, poly(methyl methacrilate) (PMMA) nanoparticles exhibited spherical shapes with high uniform size, showing an average diameter of 200 nm. In this case, the aim was to obtain THSs with lower diameter compared to

what already described in **Paper-I**. Thus, PMMA sacrificial templates with lower size were synthesized by finely tuning polymerization reaction temperature, and reagents concentration. Additionally, no agglomerated PMMA nanoparticles were observed. **Figure 6.8c, d** also reports pure THS and Nx, after the removal of the PMMA sacrificial templates through the calcination process at 450 °C. As previously demonstrated,[5] the hollow structure was successfully obtained thanks to the presence of clearly visible voids shown by some broken spheres. Both pure and N-doped THSs exhibited ordered structures and relatively rough surfaces, with uniform size, an average diameter of ~200 nm, and a shell thickness ranging from 30-50 nm. Overall, the N-doping strategy did not affect nor the morphology or the structure.

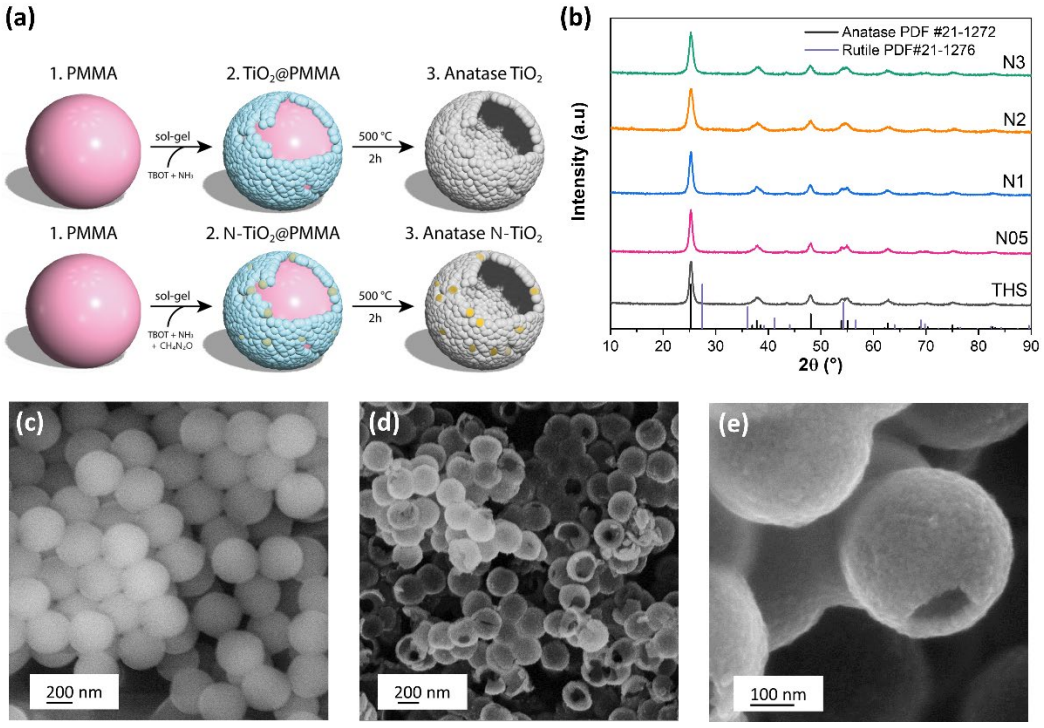

Figure 6.8 (a) Synthesis scheme; **(b)** X-ray diffraction patterns of THSs samples with TiO_2 anatase pdf #21-1272 and rutile pdf #21-1276 as references. FE-SEM images of **(c)** PMMA spheres **(d)** pure THS, and **(e)** N3 samples at different magnifications.

The crystal structure and phase identification were carried out by performing X-ray diffraction (XRD) analysis (**Figure 6.8**). According with the JCPDS card number 21-1272, all the samples showed the characteristic peaks of the anatase phase at 2θ

values at 25.3°, 36.9°, 37.8°, 38.6°, 48.1°, 53.9°,55.1°, and 62.7°. Meaning that the anatase crystalline structure has been retained upon the N-doping procedure. Furthermore, no traces of the characteristic peak of N element appeared, thus it may be evenly distributed in the crystal lattice.

6.2.2 N-doping

The effect of the N-doping on the optical and electronic properties of THSs were investigated by diffuse reflectance UV-visible-near infrared (DRUV-Vis-NIR) spectroscopy. All the spectra, shown in **Figure 6.9a**, were characterized by the main absorption feature related to TiO_2 optical bandgap (~3.1 eV), which induced the strong absorption edge at ~390 nm and associated to the transition O^{2-} (2p) → Ti^{4+} (3d). As previously investigated, the THS spectrum demonstrated the effectiveness of the hollow structure that leads to a flat reflectivity below 75% in the full range of wavelengths (390-1500 nm), except for N3. Hower, for all Nx samples, a clearly visible red-shift of the main band toward higher wavelength compared to bare THS was detected (**Figure 6.9b**). As expected, N-doping enables an increased absorbance ability in the region 380-400 nm compared to pure THS. Furthermore, the light absorption in the Vis-NIR region can be enhanced thanks to the creation of superficially disordered layer and the presence of defects induced by the N loading.[57] This is confirmed by the additional broad absorption band ranging from 500 nm to 1500 nm, which was detected when the N content was below 3 at %. Additionally, the onset of the absorption feature at higher wavelengths (> 500 nm) may be induced by the presence of additional localized states within the bandgap structure of TiO_2 (i.e., N 2p states above the TiO_2 VB or defect states below the TiO_2 CB), that leads to an overall bandgap energy reduction (**Figure 6.9c, d**).[47,58–60] Furthermore, the absorption peak centered at 1450 nm, which was less intense for N3, can be ascribed to the presence of water molecules adsorbed on the catalysts surface.

To better explain the increasing in the optical behavior and to extensively study the presence of localized states, synchrotron-based X-ray photoemission spectroscopy (XPS, VUV-Photoemission beamline) was performed, giving insights into the near-surface region of THS catalysts. O 1s and Ti 2p core levels were measured at 750 eV, while valence band states at 468 eV. For N1 sample core levels spectra only were acquired. No sign of N 1s was observed.

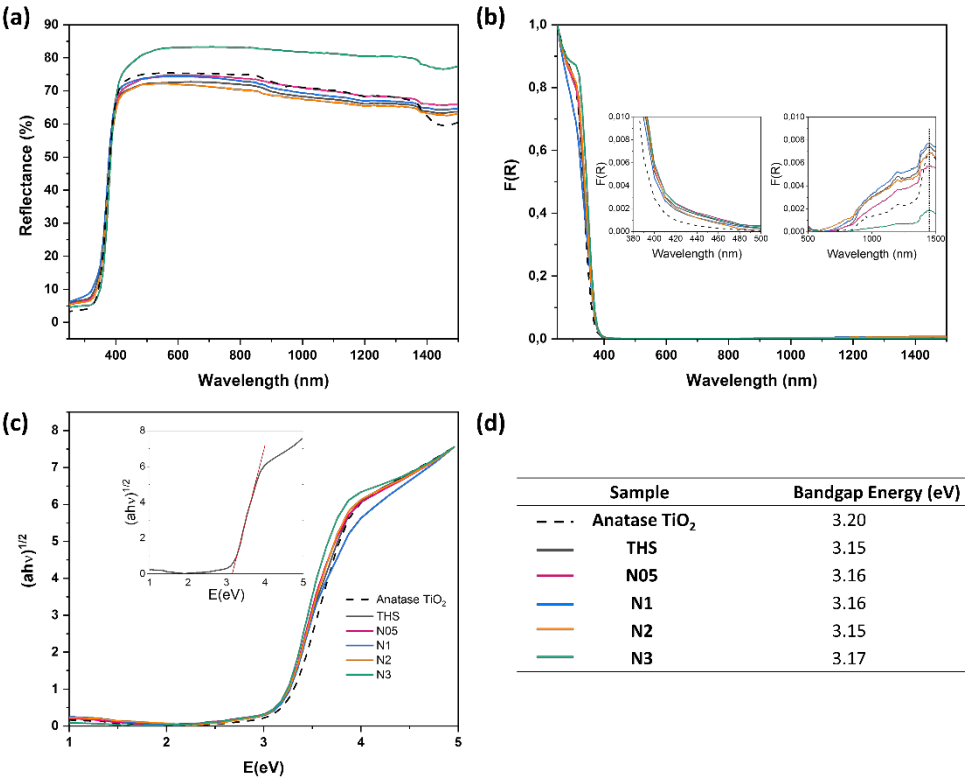

Sample	Bandgap Energy (eV)
Anatase TiO_2	3.20
THS	3.15
N05	3.16
N1	3.16
N2	3.15
N3	3.17

Figure 6.9 (a) DRUV-Vis-NIR spectra; **(b)** F(R) spectra calculated through Kubelka-Munk functions; **(c)** Tauc Plots and **(d)** bandgap energy values for all the samples including the Anatase TiO_2 reference.

Referring to **Figure 6.10**, O 1s levels could be fitted with two main components at 530.7 eV, and at 532.5 eV, attributed to O in stoichiometric TiO_2 (O^{2-}) and both C-O groups and OH groups, respectively. A third, minor component at 534.5 eV can

be attributed to the presence of water molecules adsorbed onto the catalysts surface, confirming what previously said by DRUV-Vis-NIR spectroscopy analysis.

All the Ti 2p spectra were fitted with a single doublet ($Ti2p_{3/2}$ at 459.45 eV) attributed to the presence of Ti^{4+}, as also confirmed by the O/Ti atomic ratios (**Table 6.2**) derived by normalizing the area of the relevant peaks to the respective photoemission cross sections (σ_O = 0.24 and σ_{Ti} = 0.7 at hν = 750 eV).[61]

Table 6.3 O/Ti ratios derived from the XPS spectra.

Sample	**THS**	**N0.5**	**N2**	**N3**
O/Ti	2.13	2.19	2.04	2.14

The valence band spectra at hν = 468 eV showed similar features related to the O2p-derived states (4-9 eV binding energy), but within the gap region (**Figure 6.10**, valence band zoom), a feature associated with O vacancy defect states was observed for all the N-doped samples. Pure THS showed a peak centered at 1.10 eV which shifted to higher binding energy for the N-doped samples. A very well-defined peak was observed for the N2 sample at 1.25 eV.

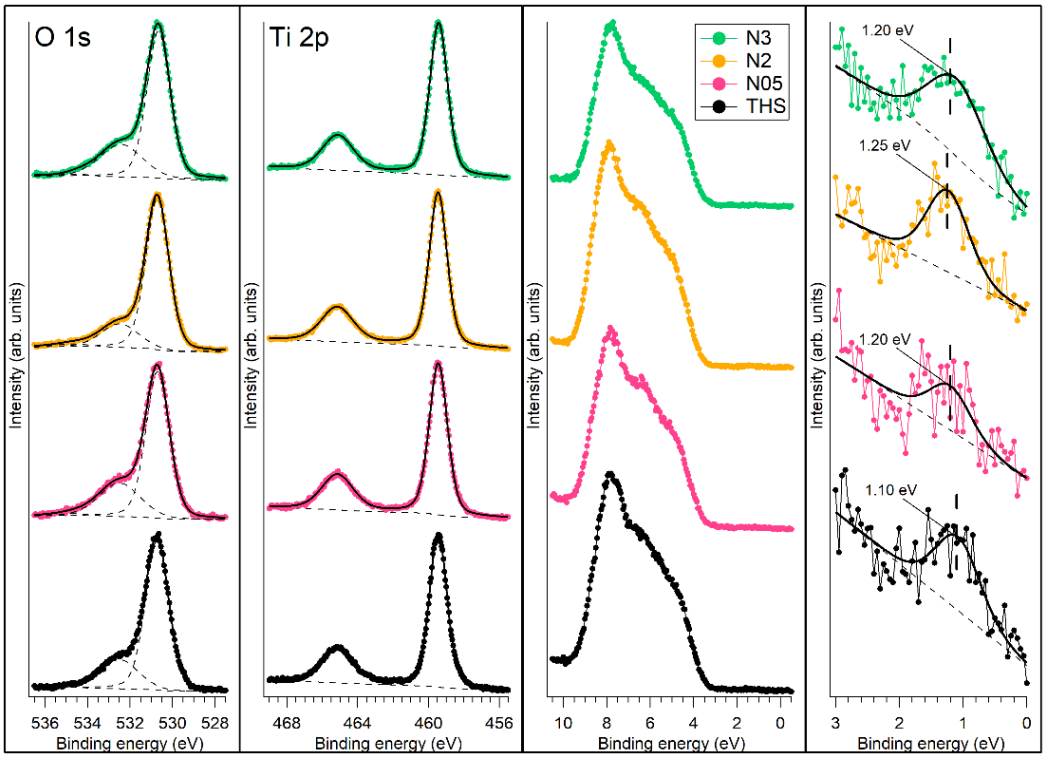

Figure 6.10 XPS analysis of the N3, N2, N0.5 and THS powder samples. O1s and Ti2p core level spectra were measured at hv = 750 eV, valence band spectra at hv = 468 eV.

6.2.3 Photodegradation of organic pollutants

The photocatalytic activity was investigated by monitoring organic pollutants degradation efficiency. Municipal wastewater typically contains multiple organic pollutants, and traces of various contaminants such as pharmaceuticals, personal care products, and industrial chemicals (see **Chapter 1**). Thus, assessing the mutual impacts of these contaminants on the efficiency of the selected photocatalyst is essential to determine its practical application.[62] In detail, the photodegradation of two different pollutants, namely metronidazole (MDZ) and Rhodamine B (RhB), and subsequently of their mixed solution to simulate a real environment, were evaluated. Photocatalytic tests were carried out at room temperature, under UV for aqueous solutions of RhB and the mixture, while both under UV and simulated solar light (SSL) for MDZ aqueous solution (preliminary results in **Figure 6.11** and

Figure 6.12). To plot the C/C_0 curves and measure the degradation efficiency (%Dr), the main MDZ and RhB absorbance peaks, at 320 nm and 554 nm, respectively, were monitored for 180 min under UV light and 360 min under SSL (**Figure 6.11c** and **Figure 6.12a**). Being a mixed solution much more difficult to degrade, the photocatalytic test was carried out for 360 min. The photolysis of the base MDZ and RhB were used as a reference (black curves).

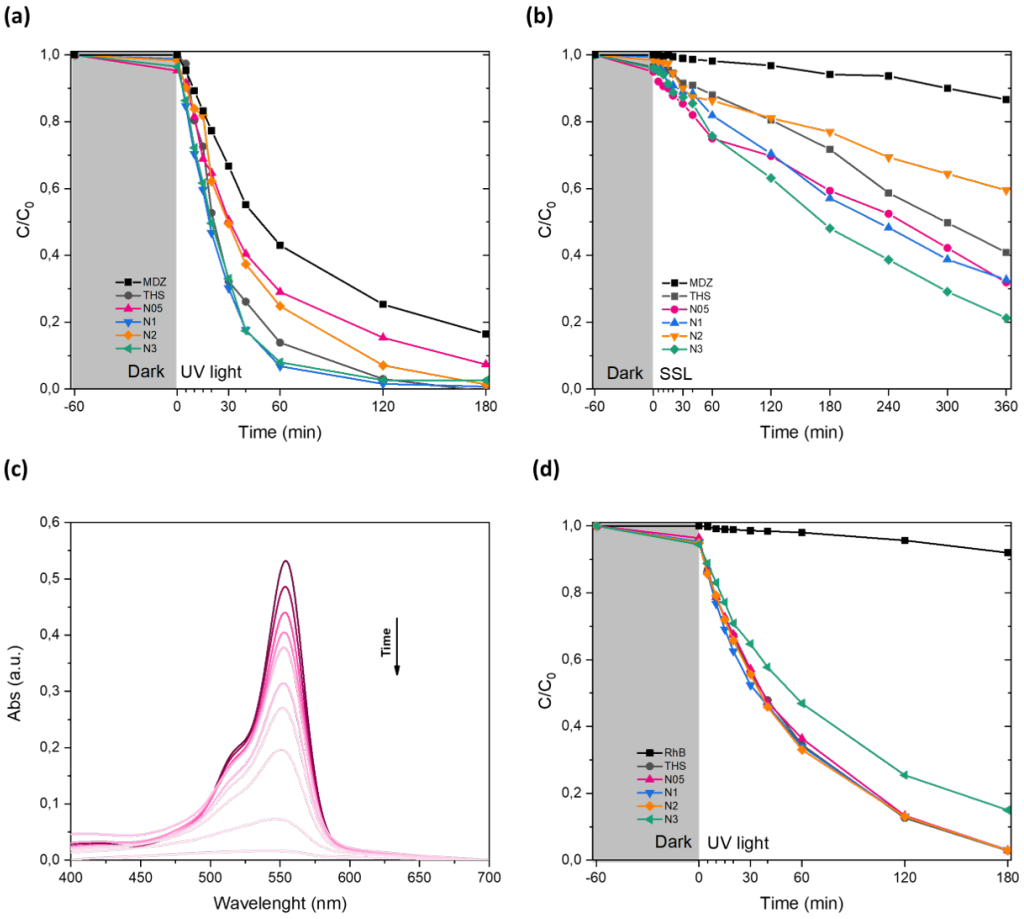

Figure 6.11 MDZ photodegradation as a function of time under **(a)** UV light and **(b)** SSL irradiation; **(c)** Absorbance spectra trend of the RhB solution during the UV light irradiation for THS sample taken as reference and **(d)** relative RhB photodegradation as a function of time under UV light irradiation.

Figure 6.11a, b shows the photocatalytic degradation of MDZ under UV and SSL, respectively. The concentration of MDZ (C) at a given exposure time with respect to its initial value (C_0) at -60 min (i.e., the equilibration time in the dark) was

monitored. Under UV light, bare MDZ is unstable reaching a maximum photolysis of ~80% after 180 min of exposure (**Figure 6.11a**). Conversely, RhB is highly stable even after 180 min of high energetic UV light exposure, reaching a maximum photolysis of ~8% (**Figure 6.11d**). After 60 min of equilibration in the dark and in presence of Nx photocatalysts, MDZ was hardly adsorbed on the catalysts surface, with a maximum value of 5 % for N05. As suggested by DRUV-Vis-NIR spectroscopy and XPS analysis, the presence of oxygen vacancies may lead to an increase in water molecules and hydroxyl groups, that affect the overall adsorption of organic molecules and degradation pathway.[63,64] The same assumption can be applied for RhB adsorption process (dark area, **Figure 6.11c**). Concerning MDZ photodegradation, the best performances were reached by bare THS and N1 under UV light and by N3 sample under SSL. In the case of RhB, all the samples showed excellent photocatalytic activity (reaching almost the 100 % of degradation efficiency), except for N3 sample. A similar trend was observed for the photodegradation of the mixed solution under UV light (**Figure 6.12**). Additionally, it can be stated that THS and N1 photocatalysts showed good selectivity for both RhB and MDZ. There is a clearly visible trend between the doping content and the photoactivity. The optimal N-doping was reached at 1 at% concentration, meaning that a trade-off between optical properties and catalytic activity is needed to maximize the photocatalytic efficiency under UV light. The final aim was to broaden the catalytic activity in a full-range of wavelengths, thus further analyses will be performed under SSL to better understand the photocatalytic activity of the N-doped THS samples.

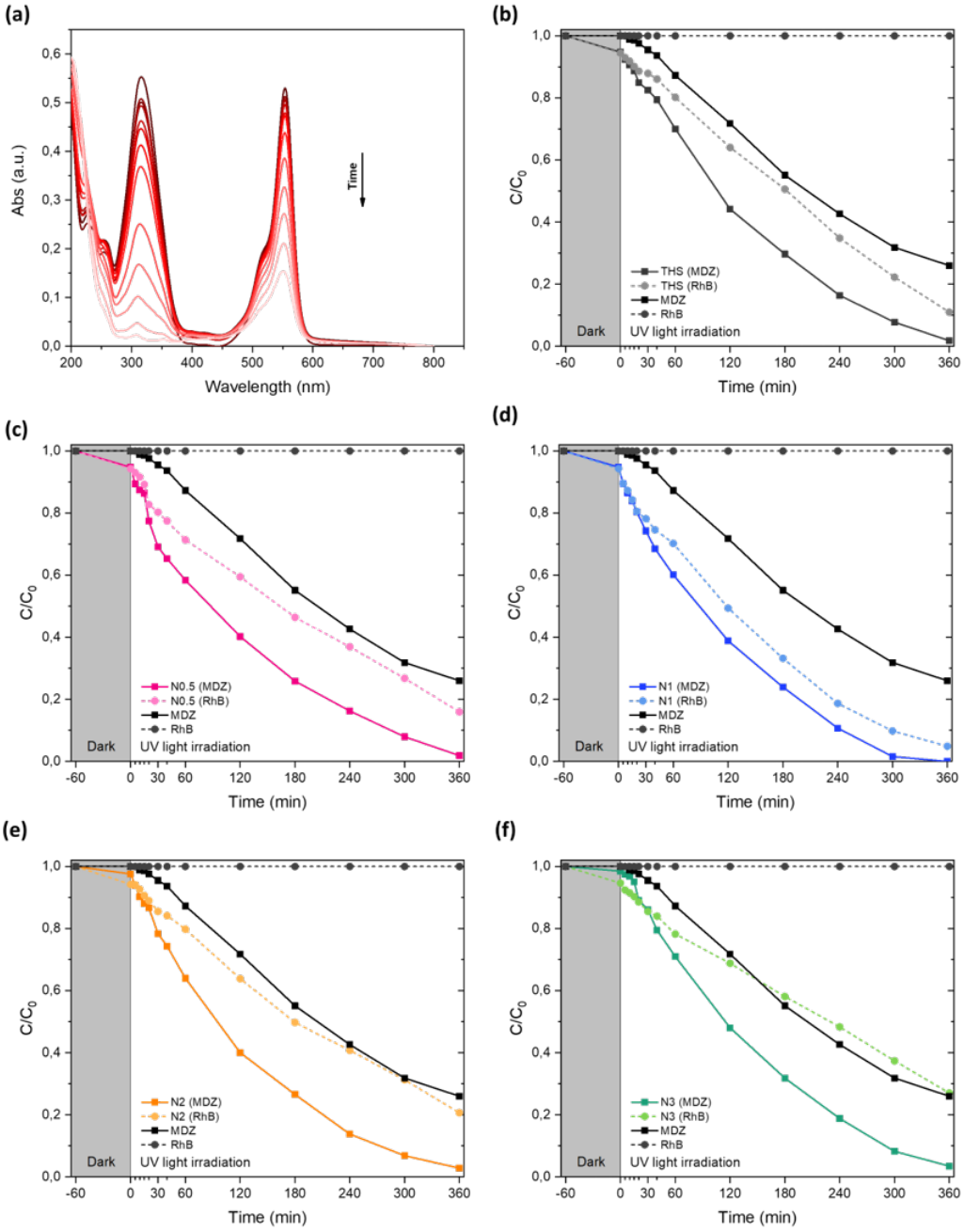

Figure 6.12 (a) Absorbance spectra trend of the mixed solution (MDZ + RhB) during the UV light irradiation for THS sample taken as reference. Relative C/C_0 curves as a function of time for **(b)** THS, **(c)** N05, **(d)** N1, **(e)** N2 and **(f)** N3 samples.

6.2.4 Conclusions

In this section preliminary results on nitrogen-doped Titania Hollow Spheres (Nx-THS) were discussed. Uniform submicrometric pure and N-doped TiO_2 hollow spheres, composed of hierarchically assembled nanoparticles, were synthesized following a modified hard template-based approach reported in **Paper-I**. The use of several characterization techniques, such as FE-SEM and XRD, confirmed the formation of a hollow structure and the presence of anatase phase, revealing that the N-doping strategy did not affect nor the morphology or the structure. Other analyses, including HR-TEM and Raman spectroscopy, have been planned to further investigate structural, textural and morphological properties of the materials. N-doping effects were investigated by combining the use of DRUV-Vis-NIR spectroscopy and high resolution XPS. N-doping improved the bare THS photoresponse, slightly reducing the bandgap energy and extending the main absorption edge toward visible light. Furthermore, the presence of a broad absorption band associated with oxygen vacancies was detected in the NIR region. The presence of oxygen vacancies was also confirmed by valence band analysis with the appearance of a new related feature within the bandgap region and clearly visible for the N2 sample. Electron Paramagnetic Resonance (EPR) spectroscopy will be useful to further localize and explain the N-doping effect. Finally, preliminary findings on photocatalytic activity evaluation confirmed that the proper design of the morphology and the optimization in N-loading may highly promote complex organic pollutants degradation at room temperature, under both UV and SSL. Further photocatalytic tests, such as mixture photodegradation efficiency evaluation under SSL, trapping experiments through the use of scavengers and stability/recyclability tests will be performed to reach a comprehensive overview of the photocatalytic behavior of N-doped titania samples compared to bare THS.

6.3 References

[1] M. Pelaez, N. T. Nolan, S. C. Pillai, M. K. Seery, P. Falaras, A. G. Kontos, P. S. M. Dunlop, J. W. J. Hamilton, J. A. Byrne, K. O'Shea, M. H. Entezari, D. D. Dionysiou, *Appl Catal B* **2012**, *125*, 331.

[2] E. Hosono, S. Fujihara, H. Imai, I. Honma, I. Masaki, H. Zhou, *ACS Nano* **2007**, *1*, 273.

[3] J. Du, J. Zhang, D. J. Kang, *CrystEngComm* **2011**, *13*, 4270.

[4] C.-T. Dinh, T.-D. Nguyen, F. Kleitz, T.-O. Do, *ACS Nano* **2009**, *3*, 3737.

[5] L. Liccardo, M. Bordin, P. M. Sheverdyaeva, M. Belli, P. Moras, A. Vomiero, E. Moretti, *Adv Funct Mater* **2023**, 2212486.

[6] M. Telkhozhayeva, B. Hirsch, R. Konar, E. Teblum, R. Lavi, M. Weitman, B. Malik, E. Moretti, G. D. Nessim, *Appl Catal B* **2022**, *318*, 121872.

[7] T.-Y. Lee, C.-Y. Lee, H.-T. Chiu, *ACS Omega* **2018**, *3*, 10225.

[8] H. G. Yang, C. H. Sun, S. Z. Qiao, J. Zou, G. Liu, S. C. Smith, H. M. Cheng, G. Q. Lu, *Nature* **2008**, *453*, 638.

[9] G. Liu, H. G. Yang, J. Pan, Y. Q. Yang, G. Q. (Max) Lu, H.-M. Cheng, *Chem Rev* **2014**, *114*, 9559.

[10] F. Amano, T. Yasumoto, O.-O. Prieto-Mahaney, S. Uchida, T. Shibayama, B. Ohtani, *Chemical Communications* **2009**, 2311.

[11] W. Chen, Q. Kuang, Q. Wang, Z. Xie, *RSC Adv* **2015**, *5*, 20396.

[12] I. Barroso-Martín, E. Moretti, A. Talon, L. Storaro, E. Rodríguez-Castellón, A. Infantes-Molina, *Materials* **2018**, *11*, 890.

[13] M. Telkhozhayeva, R. Konar, R. Lavi, E. Teblum, B. Malik, S. Ruthstein, E. Moretti, G. D. Nessim, *ACS Sustain Chem Eng* **2021**, *9*, 16103.

[14] Y. Xu, H. Chen, Z. Zeng, B. Lei, *Appl Surf Sci* **2006**, *252*, 8565.

[15] F. B. Li, X. Z. Li, M. F. Hou, K. W. Cheah, W. C. H. Choy, *Appl Catal A Gen* **2005**, *285*, 181.

[16] M. Kurian, *J Environ Chem Eng* **2020**, *8*, 104439.

[17] T. Montini, M. Melchionna, M. Monai, P. Fornasiero, *Chem Rev* **2016**, *116*, 5987.

[18] X. Huang, K. Zhang, B. Peng, G. Wang, M. Muhler, F. Wang, *ACS Catal* **2021**, *11*, 9618.

[19] Y. Ma, W. Gao, Z. Zhang, S. Zhang, Z. Tian, Y. Liu, J. C. Ho, Y. Qu, *Surf Sci Rep* **2018**, *73*, 1.

[20] M. L. Reni, A. S. Nesaraj, *Materials Research Innovations* **2021**, *25*, 276.

[21] A. Trovarelli, J. Llorca, *ACS Catal* **2017**, *7*, 4716.

[22] S. Xie, Z. Wang, F. Cheng, P. Zhang, W. Mai, Y. Tong, *Nano Energy* **2017**, *34*, 313.

[23] C. Alberoni, I. Barroso-Martin, A. Infantes-Molina, E. Rodriguez-Castellon, A. Talon, H. Zhao, S. You, A. Vomiero, E. Moretti, *Mater Chem Front* **2021**, *5*, 4138.

[24] M. Pudukudy, Q. Jia, J. Yuan, S. Megala, R. Rajendran, S. Shan, *Mater Sci Semicond Process* **2020**, *108*, 104891.

[25] A. C. Johnston-Peck, S. D. Senanayake, J. J. Plata, S. Kundu, W. Xu, L. Barrio, J. Graciani, J. Fdez. Sanz, R. M. Navarro, J. L. G. Fierro, E. A. Stach, J. A. Rodriguez, *The Journal of Physical Chemistry C* **2013**, *117*, 14463.

[26] Z. Wei, M. Endo-Kimura, C. Colbeau-Justin, B. Ohtani, E. Kowalska, *J Nanosci Nanotechnol* **2020**, *20*, 1278.

[27] R. Parimaladevi, M. Umadevi, T. N. Rekha, A. M. F. Benial, in *Nanotechnology in the Beverage Industry*, Elsevier, **2020**, pp. 3–24.

[28] B. Ohtani, *Journal of Photochemistry and Photobiology C: Photochemistry Reviews* **2010**, *11*, 157.

[29] X. Hu, X. Hu, Q. Peng, L. Zhou, X. Tan, L. Jiang, C. Tang, H. Wang, S. Liu, Y. Wang, Z. Ning, *Chemical Engineering Journal* **2020**, *380*, 122366.

[30] G. Greczynski, L. Hultman, *Prog Mater Sci* **2020**, *107*, 100591.

[31] Q. Lv, C. Wang, Y. He, M. Cai, D. Che, *Applied Sciences* **2020**, *10*, 2706.

[32] Y. Li, W. Li, F. Liu, M. Li, X. Qi, M. Xue, Y. Wang, F. Han, *Journal of Nanoparticle Research* **2020**, *22*, 122.

[33] N. Zhang, Z. Yang, Z. Chen, Y. Li, Y. Liao, Y. Li, M. Gong, Y. Chen, *Catalysts* **2018**, *8*, 246.

[34] M. Piumetti, S. Bensaid, N. Russo, D. Fino, *Appl Catal B* **2016**, *180*, 271.

[35] S. Watanabe, X. Ma, C. Song, *The Journal of Physical Chemistry C* **2009**, *113*, 14249.

[36] A. Kotani, T. Jo, J. C. Parlebas, *Adv Phys* **1988**, *37*, 37.

[37] R. Fiorenza, M. Bellardita, T. Barakat, S. Scirè, L. Palmisano, *J Photochem Photobiol A Chem* **2018**, *352*, 25.

[38] E. Bêche, P. Charvin, D. Perarnau, S. Abanades, G. Flamant, *Surface and Interface Analysis* **2008**, *40*, 264.

[39] S. Zhang, H. Liu, F. Gao, M. Fang, Y. Zhang, Y. Cai, K. Li, M. Kong, X. Tan, *J Alloys Compd* **2022**, *900*, 163492.

[40] Q. Wang, H. Zhu, B. Li, *Chemical Engineering Journal* **2019**, *378*, 122072.

[41] S. A. Ansari, M. M. Khan, M. O. Ansari, S. Kalathil, J. Lee, M. H. Cho, *RSC Adv.* **2014**, *4*, 16782.

[42] M. M. Khan, S. A. Ansari, D. Pradhan, D. H. Han, J. Lee, M. H. Cho, *Ind Eng Chem Res* **2014**, *53*, 9754.

[43] B. Huang, D. Yu, Z. Sheng, L. Yang, *Journal of Environmental Sciences* **2017**, *55*, 129.

[44] B. Choudhury, B. Borah, A. Choudhury, *Photochem Photobiol* **2012**, *88*, 257.

[45] Z. Wei, M. Janczarek, M. Endo, K. Wang, A. Balčytis, A. Nitta, M. G. Méndez-Medrano, C. Colbeau-Justin, S. Juodkazis, B. Ohtani, E. Kowalska, *Appl Catal B* **2018**, *237*, 574.

[46] S. Xing, T. Li, Y. Gao, J. Liu, *Optik (Stuttg)* **2019**, *183*, 266.

[47] R. Asahi, T. Morikawa, T. Ohwaki, K. Aoki, Y. Taga, *Science* **2001**, *293*, 269.

[48] W. Wang, M. O. Tadé, Z. Shao, *Prog Mater Sci* **2018**, *92*, 33.

[49] S. A. Ansari, M. M. Khan, M. O. Ansari, M. H. Cho, *New Journal of Chemistry* **2016**, *40*, 3000.

[50] A. Khlyustova, N. Sirotkin, T. Kusova, A. Kraev, V. Titov, A. Agafonov, *Mater Adv* **2020**, *1*, 1193.

[51] S. Sayegh, M. Abid, F. Tanos, M. Cretin, G. Lesage, F. Zaviska, E. Petit, B. Navarra, I. Iatsunskyi, E. Coy, R. Viter, V. Fedorenko, A. Ramanavicius, A. Razzouk, J. Stephan, M. Bechelany, *Colloids Surf A Physicochem Eng Asp* **2022**, *655*, 130213.

[52] J. Tao, T. Luttrell, M. Batzill, *Nat Chem* **2011**, *3*, 296.

[53] H. Xu, S. Ouyang, L. Liu, P. Reunchan, N. Umezawa, J. Ye, *J Mater Chem A Mater* **2014**, *2*, 12642.

[54] C. Di Valentin, E. Finazzi, G. Pacchioni, A. Selloni, S. Livraghi, M. C. Paganini, E. Giamello, *Chem Phys* **2007**, *339*, 44.

[55] R. Qian, H. Zong, J. Schneider, G. Zhou, T. Zhao, Y. Li, J. Yang, D. W. Bahnemann, J. H. Pan, *Catal Today* **2019**, *335*, 78.

[56] Y. Tamaki, K. Hara, R. Katoh, M. Tachiya, A. Furube, *The Journal of Physical Chemistry C* **2009**, *113*, 11741.

[57] L. Liccardo, P. Moras, P. M. Sheverdyaeva, A. Vomiero, A. Caballero, G. Colón, E. Moretti, *Adv Sustain Syst* **2023**, 2300418.

[58] R. Asahi, T. Morikawa, H. Irie, T. Ohwaki, *Chem Rev* **2014**, *114*, 9824.

[59] N. Serpone, *J Phys Chem B* **2006**, *110*, 24287.

[60] G. Barolo, S. Livraghi, M. Chiesa, M. C. Paganini, E. Giamello, *The Journal of Physical Chemistry C* **2012**, *116*, 20887.

[61] D. E. Parry, *Rapid Communications in Mass Spectrometry* **1994**, *8*, 579.

[62] J. Romão, G. Mul, *ACS Catal* **2016**, *6*, 1254.

[63] L. Y. Ozer, H. Apostoleris, F. Ravaux, S. I. Shylin, F. Mamedov, A. Lindblad, F. O. L. Johansson, M. Chiesa, S. Jacinto, G. Palmisano, *ChemCatChem* **2018**, *10*, 2949.

[64] M. Sarafraz, M. M. Amini, M. Adiban, A. Eslami, *Mater Sci Semicond Process* **2020**, *120*, 105258.

Chapter 7 – *General conclusions*

7.1 Outcomes

This dissertation critically explored emerging environmental and energy-related challenges trying to suggest sustainable solutions. With a focus on detrimental impacts of human activities on the environment, including global warming, and the presence of contaminants like pharmaceuticals in water sources, the urgency for newly effective wastewater treatment methods and sustainable energy production have been emphasized. While photo-driven advanced oxidation processes, particularly heterogeneous photocatalysis, have proven to be promising, their widespread application still faces some challenges. Thus, the entire thesis was focused on the design and development of new and efficient metal oxide-based nanostructured photocatalysts for hazardous organic contaminants photodegradation and H_2 production through photoelectrochemical water splitting (PEC WS) or photoreforming, aligning with Sustainable Development Goals 6 and 7 of Agenda 2030, towards a more environmentally conscious and sustainable future.

In detail, titanium dioxide (TiO_2) described in literature as the benchmark photocatalyst, suffers from several limits including its wide bandgap (3.0-3.2 eV), with a strong absorption capacity in the UV range and little absorption capacity in the visible light range, and fast charge-carriers recombination rate. Thus, from **Chapter 4** to **Chapter 6**, several strategies to tune its optical and electronical properties, based on different smart and low-cost synthetic approaches, were designed and deeply investigated. Moreover, a tight correlation between the materials properties and their photocatalytic activity was directly assessed, by using advanced experimental techniques.

Although conclusions were drawn for each investigation, general outcomes can be summarized as follows.

Chapter 4 was based on results shown in *Paper-I* and *Paper-II*, focusing on the use of surface engineering, *i.e.*, the possibility to create surface defects, and the synergistic effects of a suitable and controlled morphology to enhance the overall TiO_2 photoactivity toward visible light in two different applications (drugs photodegradation and methanol photoreforming).

Specifically, in the first section based on *Paper-I*, an affordable and straightforward synthesis method to obtain nanostructured hydrogenated (or colored) titania hollow spheres (THSs) was successfully proposed. The unique hollow microstructures, along with the defect-engineered surface, allowed efficient utilization of solar light across a broader spectral range (200-1200 nm) achieving an 82% photodegradation efficiency in presence of a common water contaminant (*i.e.,* ciprofloxacin) under simulated solar light irradiation at room temperature and standard atmospheric pressure. The correlation among hydrogenation degree, optical absorption, photocatalytic activity enhancement, and the introduction of defects was deeply investigated. In the second section based on *Paper-II*, an innovative microwave-assisted synthesis to enhance the photoactivity of the widely used commercial TiO_2 P25 was introduced. Precisely, surface-defects engineering and the in-situ Cu co-catalyst photodeposition demonstrated to be an effective strategy to enhance photocatalytic performance in the H_2 production through methanol photoreforming under UV light irradiation. In fact, the best performing sample demonstrated an exceptional photocatalytic H_2 production rate, doubling the bare Cu/P25 system performance. The synergistic use of X-ray photoelectron spectroscopy and DRUV-Vis-NIR spectroscopy revealed that the notable improvement could be attributed to the presence of oxygen vacancies at the catalyst surface in combination with the co-catalyst, that enhanced the electron-hole separation efficiency and the overall photocatalytic activity.

In **Chapter 5,** the possibility to build TiO_2/TiO_{2-x} homojunctions and α-Fe_2O_3/TiO_2 heterojunctions was proposed to enhance the photoactivity for both dye degradation and PEC WS. The first section based on *Paper-III* was focused on TiO_2/ TiO_{2-x} homojunctions, obtained by combining nanorods (NRs) hydrothermal growth and

sputtering layer deposition technique, as easily recoverable and efficient photocatalysts for wastewater purification from the benchmark dye methylene blue. Using several characterization techniques, it was demonstrated how the creation of a homojunction involving two distinct oxygen-rich/deficient TiO_2 NRs layers can be used to optimize the surface-to-volume ratio, adsorption/desorption phenomena, mitigate the rapid charge recombination, and reduce the wide TiO_2 band gap. The second section, based on submitted *Paper-IV*, was focused on heterojunction formation between atomic layered deposited TiO_2 ultrathin films, with precise control over the morphology and thickness, and 1D hematite nanorod arrays. To assess the role of TiO_2 overlayer thickness, photoelectrochemical water splitting (PEC WS) tests of α-Fe_2O_3/TiO_2 heterojunctions were carried out, under both UV and visible light irradiation. The presence of TiO_2 overlayer notably enhanced the photocurrent response compared to pristine hematite, with response highly related to the TiO_2 overlayer thickness. Notably, under UV light and at low thickness, TiO_2 acted as passivation layer. However, at higher thickness, TiO_2 served as both passivation and light absorber layer, reducing the contribution of α-Fe_2O_3 in PEC photoactivity.

Finally, in **Chapter 6**, TiO_2-doping strategy was considered and investigated. The first section, based on submitted *Paper-V*, was focused on ceria-doped titania nano-octahedra (CeTNOh) derived from Ce-containing titanate nanowires, via ultrasonication-hydrothermal treatment from commercial titania P25. TNOh samples were mesoporous materials with a very high specific surface area, at least 2 times higher than that of commercial anatase. The properly designed morphology and the optimization in ceria-loading highly promoted ciprofloxacin degradation, with the best performing sample showing a degradation efficiency above 80%, after 360 min of exposure time under simulated solar light irradiation. The optimal CeO_2 concentration was beneficial for photocatalytic activity, influencing the overall adsorption-desoprtion equilibrium and enhancing the TNOh photoresponse with a reduction in the bandgap energy up to 2.75 eV, associated with the presence of oxygen vacancies induced by Ce^{3+}/Ce^{4+} redox pair. Furthermore, the presence of cerium species enhanced the separation of photogenerated e^-–h^+ pairs by

reducing the overall recombination rate. Preliminary results on nitrogen-doped Titania Hollow Spheres (Nx-THS) were discussed in the second section of this chapter. Uniform submicrometric pure and N-doped TiO_2 hollow spheres, composed of hierarchically assembled nanoparticles, were successfully synthesized following a modified hard template-based approach reported in *Paper-I*. N-doping was found to enhance the photoresponse of bare titania hollow spheres (THS), reducing the bandgap energy and extending absorption into the visible-NIR light range. XPS valence band analysis confirmed the presence of oxygen vacancies in the N-doped samples. While initial photocatalytic activity evaluation demonstrated enhanced complex organic pollutants degradation under both UV and SSL at room temperature, further tests, including Electron Paramagnetic Resonance spectroscopy, mixture photodegradation efficiency evaluation under SSL, trapping experiments, and stability tests, will be conducted to comprehensively assess the N-doped samples photocatalytic activity compared to bare THS.

7.2 Ongoing & Future research

The research findings provided by the nanostructured systems designed, developed and described in this thesis may significantly boost and advance the practical exploitation of solar light for future large-scale applications in the field of heterogeneous photocatalysis. However, some extra experiments are proposed to obtain a deeper understanding of the as-synthesized materials and further improvements in the overall photocatalytic performance.

The combined use of surface and morphology engineering seems to be an attractive strategy for increasing photocatalytic performance. As a matter of fact, the creation and localization of surface defects together with the high control over the morphology, is highly challenging. In **Chapter 4**, two treatment processes were proposed to easily hydrogenate the catalyst surface while retaining both the morphology and the crystal structure. However, some alternative methods and/or

operating conditions could be explored. For instance, the hydrogenation of titania hollow spheres could be carried out by optimizing both the choice of the reducing agent, (*i.e*., alternative to $NaBH_4$), and the temperature of the thermal treatment. Furthermore, computational analysis would be very useful to deeply understand the amount of oxygen vacancies and their distribution onto the materials surface, allowing to design more efficient TiO_2-based photocatalysts.

The creation and evaluation of homojunctions and heterojunctions immobilized on a conductive substrate was presented in **Chapter 5** as a promising strategy to obtain efficient solar-driven and easily recoverable photocatalysts for water remediation and PEC WS. However, TiO_2/α-Fe_2O_3 system led to the creation of a Type-I heterojunction, which is less favorable for the holes transfer to the TiO_2 VB. Thus, different types of heterojunctions could also be considered. For instance, the coupling between TiO_{2-x} and α-Fe_2O_3 could lead to the creation of a direct Z-scheme heterojunction, decreasing the charge-carriers recombination probability (described in **Chapter 3**).

The last approach explored was the doping strategy proposed in **Chapter 6**. While it has been demonstrated that TiO_2 doping is a useful technique to enhance its electronic, optical, and photocatalytic properties, there are still some challenges to be faced including the dopant choice, the control in the doping levels and their distribution in the TiO_2 structure. Thus, further experiments such as exploring new dopant concentrations, as well as its localization in the crystal lattice, are crucial to further understand and tune the catalyst properties. The combination of EPR spectroscopy and computational studies could be a good strategy to deeply understand the dopants distribution and their effects on both the crystal and electronic structure. Concerning the preliminary results presented for N-doped titania hollow spheres, other analyses have been planned to further investigate the properties of the materials. HR-TEM, EDX, N_2-physisorption analysis and Raman spectroscopy will be useful to deeply understand structural, textural and morphological properties of the materials. Furthermore, on-going photocatalytic studies (*i.e.,* mixture photodegradation efficiency evaluation under SSL, trapping experiments and

stability tests) will allow to achieve a comprehensive overview of the photocatalytic behavior of the investigated systems.

7.3 Outlooks

Over the last decades, many efforts and scientific publications toward new efficient solar-driven metal-oxide based photocatalysts have been made. However, transitioning from laboratory-scale experiments to real-world applications still requires a comprehensive understanding of the scalability, efficiency, and economic viability of the processes.

The clean energy and environment transition could be achieved by integrating the newly designed photocatalysts into existing wastewater treatment plants or energy production facilities, always considering efficiency, and compatibility with conventional methods. Additionally, the successful implementation of sustainable solutions requires alignment with legislation and policies. Thus, enhancing the exchange of information between research and politics may facilitate the integration of innovative technologies into environmental protection and energy production strategies.

Besides the improvement of the benchmark TiO_2-based photocatalysts, there is a variety of potential materials to be explored. Thus, future investigations may lead to the discovery and development of novel metal-oxide based or other types of photocatalysts with tailored properties, including ternary oxides, 2D layered transition metal dichalcogenides, and carbon nitride-based materials. Exploring some cutting-edge methods, such as in-operando characterization techniques, can provide deeper insights into the correlation between catalyst properties and photocatalytic performance, driving toward further improvements in the design. Moreover, collaborations between researchers from different fields, such as materials

or physical science, engineering, and environmental science, can lead to innovative solutions to better address the challenges faced in heterogeneous photocatalysis.

In conclusion, by addressing these challenges, research in the field of heterogeneous photocatalysis can move forward to the promotion of sustainable methods and the mitigation of environmental issues.

Appendix A – *Methods*

A.1 Materials & synthetic methods

A.1.1 Colored-TiO_2 hollow spheres

Materials

The following commercial reagents were used in all the experimental phases without any further purification: milli-Q water (H_2O); nitrogen gas (N_2); methyl methacrylate (MMA, Merck ≥ 99.0%); 2,2'-azobis (2-methylpropionamidine) dihydrochloride (azobis, Merck 97%); deionized water (H_2O); ethanol absolute (EtOH, Merck ≥ 99.5%); titanium(IV) butoxide (TBOT, Merck 97%); ammonia solution 28 %w (NH_3, Merck ≥ 99.9%); sodium borohydride ($NaBH_4$, Merck ≥ 98%); argon (Ar, Merck ≥ 99.998%); Ciprofloxacin (CIP, Merck ≥ 98%); Titanium(IV) oxide (TiO_2 Reference, Anatase, Merck ≥ 99.5%).

Synthesis of White TiO_2 Hollow Spheres

The fabrication of white TiO_2 hollow spheres (W_THS) involved a hard template-based method. The initial step was the synthesis of PMMA templating spheres. MMA (12.5 wt%) was dispersed in Milli-Q water under vigorous magnetic stirring (700 rpm) while bubbling N_2 (g). Subsequently, the mixture was heated to 80°C, and the azobis initiator (0.19 wt%) was introduced. The reaction proceeded for 2 hours, yielding colloidal PMMA spheres. The reaction was promptly stopped by cooling in an ice bath, and the resulting PMMA spheres were separated via centrifugation (4000 rpm for 25 minutes). The products underwent multiple washes with deionized water and ethanol before finally being air-dried overnight.

The subsequent step involved coating the sacrificial template with a titanium precursor to create a TiO_2@PMMA core-shell system. Specifically, 1 wt% PMMA

spheres were dispersed in absolute ethanol and sonicated for 20 minutes. The system was then heated to 45°C and stirred at 500 rpm. 0.1 wt% of the ammonia solution and 1.5 wt% TBOT were added, and the reaction proceeded for 24 hours. The resulting product was collected through centrifugation and underwent several washes with deionized water and ethanol.

The final steps involved the removal of PMMA templates and the calcination process to produce THSs. In detail, the core-shell spheres were subjected to thermal treatment at 500°C for 2 hours (ramp rate 2°C/min) in an air flow, resulting in the formation of W_THSs.

Synthesis of Colored TiO_2 Hollow Spheres

To produce colored THSs, a mixture of W_THS and $NaBH_4$ in different ratios was thoroughly ground for 20 minutes. Subsequently, the resulting product was transferred to a tubular furnace, ready for the chemical vapor deposition (CVD) technique. Within the CVD chamber, the powder underwent thermal treatment at 350°C under an Ar atmosphere (flow rate 150 sccm) for either 60 or 80 minutes, depending on the desired samples (heating rate 10°C/min). After reaching room temperature, the colored THSs were meticulously washed with deionized water and ethanol to eliminate any unreacted $NaBH_4$. Finally, they were dried at 70°C overnight. The samples were labelled as X_THSn, where X indicated the color of the sample (W for white, G for gray, DG for dark gray), and n represented the CVD-annealing time, except when it was 60 minutes.

Specifically, G_THSs were produced by maintaining a weight ratio between $NaBH_4$ and W_THS ranging from 3 to 8, respectively, and employing a 60-minute CVD-annealing time. DG_THS and DG_THS80 samples were synthesized under identical operating conditions, with the only variation being the weight ratio between $NaBH_4$ and W_THS set at 1 to 2. In the case of DG_THS80, an extended CVD-annealing time of 80 minutes was applied.

A.1.2 Nano-Cu/TiO_2 particles

Materials

The following commercial reagents, without any further purification, were used: deionized water (H_2O); commercial TiO_2 (Evonik AEROXIDE TiO_2 P25); oxalic acid (Ox, $H_2C_2O_4$, Sigma-Aldrich 99.0%); copper (II)-nitrate trihydrate ($Cu(NO_3)_2 \cdot 3H_2O$, Merck ≥ 99.0%); methanol (MeOH, Merck ≥ 99.5%).

Photocatalysts preparation

Surface-defect-rich P25 photocatalysts were synthesized through a microwave-assisted hydrothermal reaction involving the combination of commercial P25 and oxalic acid. In a standard synthesis procedure, an aqueous dispersion of P25 was prepared under moderate magnetic stirring. Oxalic acid was introduced with fixed mole ratios (n/n) relative to P25, ranging from 3.7 to 7.2. After 30 minutes of stirring, the dispersion was transferred into a 100 mL Teflon-lined microwave reactor and heated at 200°C with 600 W for 1 hour. Upon cooling to room temperature, the precipitate was separated from the reaction mixture via filtration and underwent multiple washes with distilled water. Finally, the resulting samples were dried in an oven at 80°C overnight. The samples were denoted as gOx/P25200, where "g" represents the grams of oxalic acid, and "200" indicates the temperature used (e.g., 2Ox/P25 200).

To fully comprehend the role of oxalic acid and the impact of temperature on bare P25, a comparable procedure without the addition of oxalic acid was employed. This synthesis yielded a reference sample labeled as P25 200. The co-catalyst was loaded onto the surface of gOx/P25200 photocatalysts through in-situ photoreduction during the initial phase of the photocatalytic reaction. Specifically, 2 wt% of Cu^{2+} relative to the catalyst, using a 0.01 M solution of $Cu(NO_3)_2 \cdot 3H_2O$, was

directly added to the MeOH/H_2O solution used for the photocatalytic H_2 production under UV irradiation. The samples were labelled as $Cu_{2.0}$/gOx/P25 200. The deposited Cu loading was quantified using a Microwave Plasma-Atomic Emission Spectrometer (Agilent MP-AES 4210) for $Cu_{2.0}$/P25, $Cu_{2.0}$/P25 200, and $Cu_{2.0}$/3Ox/P25 200. The data, acquired after 5 readings, revealed a mean value of 1.8 wt% for all the samples.

A.1.3 TiO_2 NRs array homojunctions

Materials

Titanium(IV) butoxide (TBOT), absolute ethanol (EtOH), acetic acid (HAac), hydrochloric acid (37% v/v), sodium hydroxide and methylene blue (MB) were all analytical grade and purchased by Sigma Aldrich without further purification. Fluorine tin oxide (FTO) glasses were purchased by Pilkington.

FTO glasses treatment

FTO glasses were cleaned in an ultrasonic bath for 5 minutes three times each, with different solvents: absolute ethanol, deionized water, and acetone, respectively. Cleaned FTO glasses were then dried under nitrogen flow and then stored at room temperature.

TiO_2 NRs synthesis

The synthesis of Titania Nanorods (TNRs) involved a hydrothermal growth method. During the process, two different solutions were used, a seed layer solution (A) and a NR growth solution (B), respectively. Solution A was obtained by mixing 10^{-3} mol of titanium(IV) butoxide in an absolute ethanol and acetic acid solution in molar ratio 1:5 and under stirring for 2 h before the aging of 24h at room temperature.

The seed solution (A) was subsequently spin coated to the conductive side of an FTO glass, with a rotation speed of 500 rpm for 5 seconds followed by 3000 rpm for 30 seconds.

The FTO glass was then subjected to heating at 120 °C for 10 minutes in an air flow. The resulting samples were denoted as single layer (SL) or double layer (DL), depending on whether this procedure had been repeated once or twice, respectively. Subsequently, the samples were annealed in a furnace at 450 °C for 1 hour in an air flow.

For the 0.03 M titanium butoxide Solution B, $1.2 \cdot 10^{-3}$ mol of titanium butoxide was added to a solution of hydrochloric acid and deionized water (1:1 v/v). Solution B was stirred for 5 minutes until it became colorless and transparent. FTO substrates were located on a Teflon support inside a Teflon-lined stainless-steel autoclave (40 mL). Solution B was then introduced into the Teflon-lined autoclave, and the hydrothermal growth took place at 150 °C for 4 hours. Finally, the samples were rinsed with deionized water and dried at 60 °C for 2 hours.

TiO_2 NRs array homojunction creation

TiO_2/TiO_{2-x} homojunctions were created by physical vapor deposition (PVD). TiO_{2-x} nanostructures were synthesized via reactive sputtering deposition on the surface of TiO_2 NRs using a custom-made RF (radiofrequency) magnetron sputtering deposition apparatus. Depositions were carried out starting from a target of pure metallic titanium, employing a 13.56 MHz RF source and three reactive atmospheres of Ar+O_2: 90%+10%, 85%+15%, and 80%+20%. The total pressure was set at $50 \cdot 10^{-4}$ mbar under dynamic vacuum conditions, and the sample holder was rotated at 5 rpm during deposition to enhance the homogeneity of the film composition and thickness. The RF power applied to the 2-inch diameter titanium target was consistently set at 250 W. Throughout the deposition process, the temperature was maintained below 60°C to prevent induced phase transition. The deposition duration was approximately 1 hour, depending on the desired titanium film thickness,

which ranged from 50 to 60 nm (measured by a stylus profilometer with a relative uncertainty of around 20%), corresponding to the specific reactive atmosphere used.

A.1.4 TiO_2/α-Fe_2O_3 NRs array heterojunctions

Materials

Titanium tetrachloride ($TiCl_4$, 99%) from ABCR GmbH. Ozone (O_3) provided by a BMT803N ozone delivery system using pure oxygen at a pressure of 0.5 bar, and nitrogen (99.99%) were purchased from Air Liquide. Iron(III) chloride hexahydrate ($FeCl_3 \cdot 6H_2O$) and urea (CH_4N_2O) were acquired from Carl Roth and Sigma Aldrich, respectively. VWR GmbH provided absolute ethanol and acetone for synthesis. Water with a resistivity of 18.2 MΩ cm^{-1} was used in all syntheses. All other chemicals and reagents were of analytical grades. SnO_2: F transparent conducting glasses (FTO, TEC8, thickness 2.2 mm, resistance 6.70 ± 0.27 Ω/square) were purchased from Ossila.

Preparation of α-Fe_2O_3 nanorods

Hematite (α-Fe_2O_3) nanorod arrays were grown on FTO substrates using a hydrothermal method, followed by an annealing process in an air flow. Prior to the synthesis, meticulous cleaning of the FTO-glasses was crucial, involving ultrasonication with absolute acetone, absolute ethanol, and ultrapure water (MilliQ) successively, each for 10 minutes.

A solution containing 1.8 mmol $FeCl_3 \cdot 6H_2O$ and 4.2 mmol CH_4N_2O dissolved in 15 mL of water was stirred at room temperature for 20 minutes. Subsequently, the solution was transferred into a Teflon-lined stainless-steel autoclave, with the FTO substrates conductive side facing down, and then heated at 100 °C in the oven for 12 hours. The resulting β-FeOOH product formed a uniform yellow film on the FTO

substrates, which was thoroughly washed with absolute ethanol and water, followed by drying under nitrogen flow.

Following a two-step annealing treatment of β-FeOOH in a muffle furnace (250 °C for 30 minutes and 500 °C for 30 minutes with a heating rate of 10 °C/min), α-Fe_2O_3 hematite NRs were successfully obtained.

Preparation of TiO_2/Fe_2O_3 heterojunctions

PLAY 2018-01 (CTECHnano) thermal atomic layer deposition (ALD) system was used to deposit TiO_2 layer on hematite NRs and Si-wafers to subsequently determine the layer thickness. Firstly, the ALD chamber was evacuated, and the temperature stabilized. The pressure was maintained at 7.3×10^{-1} mbar under a 40 sccm of nitrogen flow. $TiCl_4$ and H_2O, the metal precursor and oxygen source, respectively, were stored in stainless steel canisters at room temperature. The manifold and the ALD chamber were maintained at 100 °C and 120 °C, respectively. Introducing $TiCl_4$ and H_2O into the ALD chamber occurred sequentially, with nitrogen employed as both purging and carrier gas. Typically, the pulse time, exposure time, and purge time were set at 0.5 s, 50 s, and 30 s for $TiCl_4$, and 0.15 s, 40 s, and 30 s for H_2O, respectively. Samples underwent deposition with 10, 20, 40, 80, and 150 ALD cycles. Following the TiO_2 coating, samples were annealed at 450 °C for 2 hours in air.

A.1.5 CeO_2-TiO_2 nano-octahedra

Materials

The following commercial materials were used without any further purification: commercial TiO_2 (Degussa P25); potassium hydroxide (KOH, Emsure, 85%); cerium nitrate hexahydrate ($Ce(NO_3)_3 \cdot 6H_2O$, Sigma Aldrich, 95%); nitric acid (HNO_3, Sigma-Aldrich, 70%); Milli-Q water.

Nano-octahedra synthesis

To produce the precursors for the nano-octahedra, potassium titanate nanowires (TNW) were initially synthesized based on a modified synthesis previously reported by Wei and co-workers.[1] In a standard procedure, 0.9 g of commercial titania (Degussa P25) were suspended in a 90 mL aqueous 10 M KOH solution and stirred for 1h at room temperature. The resulting solution was then transferred in an autoclave, and a hydrothermal reaction was carried out at 180 °C for 24h. The obtained powder was collected through vacuum filtration and washed with Milli-Q water, 0.1M HNO_3 solution, and hot Milli-Q water until a neutral pH was achieved. As a final step, TNW were dried at 80 °C overnight.

For the hydrothermal synthesis of ceria-doped TNW, a specified amount (1 wt.%, 0.75 wt.%, and 1.5 wt.%) of a 0.0105 M $Ce(NO_3)_3 \cdot 6H_2O$ solution was added to the stirring suspension of P25 in 10 M KOH after 30 minutes under stirring. This suspension was stirred for an additional 30 min and then hydrothermally treated, following the same procedure as for the pure TNW sample. The resulting samples were named CeTNWx, where "Ce" denotes ceria, and "x" represents the nominal wt.% CeO_2 loading (x = 0.75, 1, and 1.5).

Octahedral anatase nanoparticles were obtained from TNW and CeTNWx samples. In a standard procedure, nanowire precursors were ultrasonically dispersed in Milli-Q water for 1h at room temperature, and the resulting suspension was then transferred to an autoclave for a hydrothermal reaction at 160 °C for 6h. After the end of the reaction, the solid was recovered through centrifugation and dried under vacuum at 80 °C overnight. Subsequently, the dried solid underwent calcination at 400 °C for 2h following a heating rate ramp of $1°C \cdot min^{-1}$ in static air. The samples were labelled as TNOh for pure titania nano-octahedra and CeTNOhx for ceria-doped samples, where x represents the ceria loading used for the titanate precursors (x = 0.75, 1, and 1.5).

A.2 Characterization techniques

A.2.1 X-Ray Diffraction

X-ray Diffraction (XRD) is a powerful analytical technique used for determining the crystallographic structure of a material. In XRD, a sample is exposed to X-rays, that are diffracted by the crystal planes of the material. Bragg's law is the basic principle in X-ray diffraction that describes the constructive interference between the incident X-rays and the atomic spacing in the crystal lattice (equation A.1).

$$n\lambda = 2dsin(\theta) \quad \text{(A.1)}$$

Where n is an integer number that indicate the order of the diffraction peak, λ is the wavelength of the incident X-rays, d is the interplanar spacing in the crystal lattice, and θ is the angle of the incident beam.

This condition leads to the development of diffracted X-rays at specific angles, creating a diffraction pattern that can be analyzed to determine the crystal structure of the material. The resulting diffraction pattern, which consists of constructive and destructive interference of the diffracted X-rays, is then detected. Thus, by scanning the sample in a 2θ(°) range, all the possible diffractions of the crystal lattice can be obtained. Additionally, the crystallite size can be determined directly from the width of specific reflections on the XRD pattern using Scherrer's equation (A.2), where the crystallite mean size τ is inversely proportional to the full width at half maximum (FWHM) of the reflections. Materials with smaller crystallite sizes exhibit broader reflections with higher FWHM.

$$\tau = K\lambda/\beta cos(\theta) \quad \text{(A.2)}$$

Where τ is the crystallite mean size, K is a constant related to the peak shape, λ is the X-ray wavelength, β is the FWHM of the diffraction peak, and θ is the Bragg angle. It has to be pointed out that the reliability of Scherrer's equation is

influenced by factors like grain boundaries, dislocations, crystalline mismatch, intrinsic stress, impurities, and potential instrumental effects on the β value.[2]

In this thesis, the X-ray diffraction (XRD) analyses were carried out with PanAnalytical Empyrean X-ray diffractometer, or Siemens D-501 X-ray diffractometer equipped with a Ni filter and a graphite monochromator. X-ray source was Cu Kα radiation. The scan rate was set at 2° min^{-1} and the X-Ray diffraction patterns were collected in the 2θ range 10-90°. For sample identification, diffraction patterns were matched to the JCPDS (Joint Committee on Powder Diffraction Standards) database. Crystallite size for TNOh samples described in **Chapter 6**, were evaluated by Scherrer's equation (A.2).

A.2.2 Raman spectroscopy

Raman spectroscopy is a non-destructive analytical technique based on inelastic monochromatic light scattering in the UV, Vis, or NIR range and provides detailed information about chemical structure, phase, crystallinity and molecular interactions.

When a monochromatic laser beam hits the sample, most of the light is elastically scattered, giving rise to the Rayleigh scattering. However, a small portion of the light is inelastically scattered due to the interactions with molecular vibrations, changing its frequency (or wavelength) and giving rise to the so-called Raman scattering. Briefly, when the laser incoming photon with energy hv interacts with a molecule, it is excited from a vibrational state to one of the numerous virtual states existing between the ground and first electronic states. The observed scattering type is determined by the way the molecule relaxes following excitation. The less common and less intense, is the anti-Stokes scattering, that needs the molecule to be in a vibrational excited state before interacting with the photon. Thus, Raman measurements typically rely on Stokes scattering, that occurs when the molecule

is excited to a virtual state, and subsequently relaxes to a higher vibrational state, resulting in the inelastic scattering of the photon with lower energy (hv-ΔE).

Raman spectroscopy detects the energy difference between the incident and scattered photons related to the Stokes and anti-Stokes transitions, often measured as the wavenumber change (cm^{-1}) from the incident light source.

Raman spectroscopy relies on the polarizability of a molecular bond, which is a measure of its deformability in an electric field, determined by the ease with which electrons can be displaced in the bond, inducing a temporary dipole. When a bond shows a high concentration of not tightly bound electrons, it exhibits high polarizability, with high probability to induce temporary dipoles and resulting in a strong Raman signal. Hence, Raman is more responsive to the general electron distribution and molecular structure than specific functional groups, unlike infrared (IR) spectroscopy.[3]

Micro-Raman spectra shown in **Chapter 4** were collected using a LabRAM Jobin Yvon spectrometer equipped with a microscope. Laser radiation at 532 nm was used as excitation source at 5 mW. All measurements were acquired under the same conditions (2s of integration time and 30 accumulations) using a 100× magnification objective and a 125 mm pinhole.

A.2.3 X-ray Photoelectron Spectroscopy

X-ray photoelectron spectroscopy (XPS), also known as electron spectroscopy for chemical analysis (ESCA), is the most used non-destructive, analytical technique to deeply investigate the surface of a material. It can provide information about the elemental composition, chemical state, and electronic state of elements present in the outermost of a material.

As suggested by its name, XPS is based on photoelectric effect that occurs when irradiating a sample with X-rays, typically from a monochromatic X-ray source. In fact, when X-rays, having an appropriate energy, interact with the investigated

material, electrons (also called photoelectrons) can be ejected from the inner shells of its atoms. In fact, the photoelectric effect occurs only when the impinging X-rays have an energy (hv) higher than the binding energy of electrons in that material. The binding energy of each electron is related to the kinetic energy of an emitted electron according to the Eistein equation (A.3). Since atoms possess multiple orbitals at distinct energy states, XPS provides spectra of emitted electrons with varying binding energies (and consequently, kinetic energies).

$$E_k = E_{h\nu} - E_b - \varphi \quad \text{(A.3)}$$

Where E_k is the photoelectron kinetic energy measured by the instruments, E_{hv} is the energy of the incident X-rays (known and with a fixed value), E_b is the binding energy of a given electron and finally, ϕ is the work function of the spectrometer, given by the energy difference between the vacuum energy (E_v) and the Fermi level (E_f) of a material.

The kinetic energy and intensity (number of ejected electrons) of photoelectrons are thus detected and measured to produce the final XPS spectra. By analyzing the binding energies, the elemental composition of the sample can be determined. Additionally, the fine structure of the XPS spectrum allows for the identification of different chemical states of the elements, providing insights into the chemical environment and bonding configurations that give rise to chemical shifts.

Despite the numerous and interesting information given by XPS measurements, there are several parameters to consider that limits this technique, including the needed for high or ultra-high vacuum conditions (<10^{-9} millibar) or the source selection that influences the signal-to-noise ratio and determines the probing depth.[4] It is worth recalling that the inelastic mean free path of electrons increases with higher electron energy. Consequently, employing higher energy sources enables excited electrons from larger depths to reach the surface without collisions. This extended probing depth may be beneficial for reducing the relative impact of surface oxides or contaminants. This is particularly valuable for samples sensitive to sputter damage, where it is not possible to use the common Ar^+

etching method before analyses.[5] Thus, enhancing the overall quality of the XPS spectra can be achieved by conducting these measurements exploiting the synchrotron light radiation.

The XPS measurements performed on the samples described in **Chapter 4** (*i.e.,* colored-Titania hollow spheres; nano-Cu/TiO_2 particles) and in the *second section* of **Chapter 6** (*i.e.,* N-doped Titania hollow spheres), were carried out at the VUV-Photoemission beamline of the synchrotron Elettra (Trieste, Italy) using photons of 750 eV for the core level analysis and 469 eV for the valence band analysis. The spectra were acquired at room temperature with a Scienta R4000 electron spectrometer.

For Titania Nanorods array homojunctions described in **Chapter 5**, high-resolution core level spectra for C *1s*, O *1s*, Ti *2p*, and N *1s* were recorded on a Physical Electronics PHI 5700 spectrometer, using non-monochromatic Al-Kα radiation (1486.6 eV). The measurements were conducted in constant pass energy mode with a 720 µm diameter analysis area. A reference point for adventitious carbon (C *1s* at 284.8 eV) was established. While acknowledging the broad binding energy range of this signal (284.0–285.6 eV, as reported in literature), this reference was selected to provide reliable binding energy values for all detected XPS bands in our samples. To enhance accuracy, a Shirley-type background was subtracted from the signals, and deconvolution curves were fitted using a Gaussian–Lorentzian model in Multipak 9.0 software. Additionally, the materials underwent further analysis following etching with Ar^+ at 1 keV for 1 minute.

XPS measurements on α-Fe_2O_3 /TiO_2 heterojunctions (**Chapter 5**) were performed using a JEOL JPS-9030 spectrometer at $2 \cdot 10^{-9}$ mbar, equipped with hemispherical analyzer to detect the kinetic energy of the emitted electrons and using the K_α-radiation of a non-monochromatic Al X-ray source (1486.6 eV). The binding energy was calibrated by analysing a sputter-cleaned polycrystalline gold foil and setting the Au $4f_{7/2}$ peak to 84.00 eV. The core level spectra were fitted with CasaXPS, using Voigt-functions.[6]

Finally, XPS measurements on Ceria-doped titania nano-octahedra (**Chapter 6**) were carried out using a Physical Electronics spectrometer PHI 5700, with non-monochromatic Mg Kα radiation equipped with a multichannel detector. Spectra were collected with PHI ACCESS ESCA-V6.0 F software and a constant step mode of 29.35 eV. Binding energy values were referred to C *1s* peak of adventitious carbon contamination layer (284.8 eV) and the error in binding energy values was estimated to be ±0.1 eV. Recorded data were analysed with Multipak 9.5 software.

A.2.4 Diffuse Reflectance Spectroscopy

UV-Vis-NIR diffuse reflectance (DRUV-Vis-NIR) spectra were collected to investigate the optical absorption properties of all the synthesized catalysts shown in this thesis. Measurements were carried out by using a Perkin Elmer Lambda 1050+ UV-Vis-NIR spectrophotometer, equipped with an integrating sphere, for wavelengths ranging from 200 to 1500 nm. The use of integrating sphere geometry allowed to exclude the specular component of the reflected light.

The band gap (E_g) was determined using the Kubelka-Munk approach (Equation A.4).[7]

$$F(R_\infty) = \frac{(1-R_\infty)^2}{2R_\infty} = \frac{K}{S} \quad \text{(A.4)}$$

Where $F(R_\infty)$ is the Kubelka-Munk function, R_∞ is the diffuse reflectance, K is the absorption coefficient, and S is the scattering coefficient. Thanks to the Tauc method,[8] the band gap for TiO_2 semiconductors can be expressed using the following equation (A.5):

$$(F(R_\infty)h\nu)^{\frac{1}{2}} = B(h\nu - E_g) \quad \text{(A.5)}$$

Here, h is the Planck's constant, ν is the frequency of the light and B is a constant. By plotting $F(R_\infty)$ versus the energy expressed in eV, and by finding the x-axis intersection point of the linear fit of the Tauc plot, it is possible to estimate the band gap of a material.[8]

A.2.5 Photoluminescence

Photoluminescence (PL) spectroscopy was carried out to investigate the optical properties and charge-carriers recombination on surface engineered nano-Cu/TiO_2 and ceria doped samples in **Chapter 4** and **Chapter 6**, respectively.

All measurements were conducted under ambient conditions at room temperature using a FluoroLog 3–21 system from Horiba Jobin-Yvon. The system was equipped with a 450 W xenon arc lamp as the excitation source. The excitation wavelength was selected through a double Czerny–Turner monochromator, and the signal detection stage included an iHR300 single grating monochromator coupled to a Hamamatsu photomultiplier tube. For the visible range, model R928P was used, and for the NIR range, model R5509-73 N2-cooled was employed. The excitation wavelength was set at 350 nm, and photoluminescence (PL) spectra were recorded over a range of 380-600 nm. Additionally, a cut-off filter at 370 was used.

A.2.6 Electron Microscopies

Electron microscopy is a non-destructive powerful imaging technique, comprising scanning electron microscopy (SEM), transmission electron microscopy (TEM) and the hybrid version scanning transmission electron microscopy (STEM), that uses a beam of electrons instead of light to achieve much higher resolution than traditional light microscopy. The use of electron microscopy allows to visualize the ultrafine details of specimens at the nanoscale, providing invaluable insights into their structure and composition. SEM and TEM microscopes can produce strongly focused beams of electrons that interact with samples within a vacuum chamber. While SEM microscopes are primarily designed for surface examination, TEM microscopes focus on internal structural analysis.[9] Thus, the size and morphology of the samples, shown in this thesis, were investigated by TEM or high-resolution

TEM (HR-TEM), field-emission SEM (FE-SEM) and STEM, coupled with energy dispersive X-ray spectroscopy (EDX).

FE-SEM

Briefly, in SEM the electron beam is focused on a specific spot and sequentially scanned across the specimen. Signals emitted from each location are emitted and captured by detectors, with signal synchronized with the known position of the beam on the specimen. The modulation of signal intensity is used to define the corresponding image pixel, and the accumulated signals generate an image whose pixel distribution is determined by the selected scan pattern. Typically, electron energies in SEM are on the order of 1 to 30 keV.[9]

High resolution SEM images were collected with a FE-SEM Zeiss SUPRA-40 microscope, equipped with Everhart-Thornley Secondary Electron Detector, High efficiency In-lens Detector, angle selective backscatter (AsB) and annular-STEM (A-STEM) detectors for the detection of backscattered and transmitted electrons, respectively. An Oxford INCA X-Act silicon drift detector for EDX analysis was used. The electron gun acceleration voltage ranged from 5 to 15 kV, according to the analysis and investigated sample.

Samples were prepared following two methods, by dispersing a small quantity of powder in ethanol and drop-casting some droplets onto a silicon wafer, or by directly depositing the powders on the carbon tape.

TEM and HR-TEM

In TEM, the incident electron beam is directed onto a specific region of the specimen. Electrons that cross the specimen are lens-focused and gathered by a parallel detector to build an image. TEM works at higher electron energies compared to SEM, typically ranging from 80 to 300 keV, facilitating the electrons to penetrate through materials.[9] TEM and HR-TEM images for all the samples described were obtained by using FEI S/TEM TALOS F200s. In addition, STEM images and elemental mappings were collected with a High-Angle Annular Dark-Field (HAADF) detector

coupled with an EDX detector, operating at 200 kV. The average grain size distribution or mean particle size were evaluated by using ImageJ analysis software.

A.2.7 Atomic Force Microscopy

Among the scanning probe microscopies, Atomic Force Microscopy (AFM) is a high-resolution imaging technique used to study the surface of a sample at the atomic and molecular levels. In AFM, a sharp tip is mounted on a flexible cantilever, and the tip is brought close or in contact with the sample surface. As the tip scans across the specimen, interactions between the tip and the surface cause the cantilever to deflect, according to Hooke's law. This deflection is detected by a low-power laser reflected from the back of the cantilever onto a position-sensitive photodetector and used to generate a detailed topographic image of the sample surface at the nanoscale resolution. AFM is widely used in materials science, and nanotechnology, for its ability to provide three-dimensional images and precise measurements of surface properties at the atomic scale.[10] There are several operating modes that can be used, some available with standard AFM, while others that require additional modules. The most used are the contact and the tapping modes. Briefly, in contact mode, the AFM tip is continuously in contact with the sample surface under a constant repulsive force, and the deflection of the cantilever is used to map the topography of the specimen. Conversely, in tapping mode, the cantilever oscillates near its resonance frequency, intermittently tapping the sample surface, allowing for improved sensitivity and reduced lateral forces during imaging.[11]

In the first section described in **Chapter 5**, morphology of titania nanorods array was further investigated by using a Bruker Dimension ICON AFM in tapping operation mode with a Bruker SCM-PIT-V2 probe having a Platinum-Iridium coated electrically conductive tip (spring constant ~0.3 N/m, nominal tip radius ~25 nm).

A.2.8 N_2 physisorption measurements

N_2 physisorption, a widely used technique to characterize the surface area and porosity of materials involves the physical adsorption of gas molecules onto a solid surface, primarily governed by van der Waals forces. The amount of nitrogen gas adsorbed is measured as a function of relative pressure, and the resulting data are used to determine several key parameters, including specific surface area (SSA), pore size distribution and pore volume. Additionally, N_2 physisorption data typically generate adsorption isotherms, representing the adsorbed gas amount as a function of pressure at a constant temperature. The presence of adsorption hysteresis loops occurs when the adsorption and desorption curves do not coincide. The IUPAC (International Union of Pure and Applied Chemistry) classification recognizes various isotherms (**Figure A.1a**) and hysteresis loops (**Figure A.1b**), offering insights into porosity and adsorption mechanisms.[12] Briefly, Type I is indicative of microporous solids, with I(a) and (b) distinguishing between smaller and larger micropores, respectively. Types II, III, and VI belong to macro- or non-porous materials. Type IV characterizes mesoporous materials with Type V representing a specific version, revealing weak adsorbent-adsorbate interactions. Hysteresis loops (H1 to H5) provide further details, with variations indicating specific pore structures and interactions, such as uniform mesopores (H1), broad pore size distributions (H2, H2(a) and (b), non-rigid aggregates (H3), slit-shaped pores (H4), and structures with both open and partially blocked mesopores (H5).

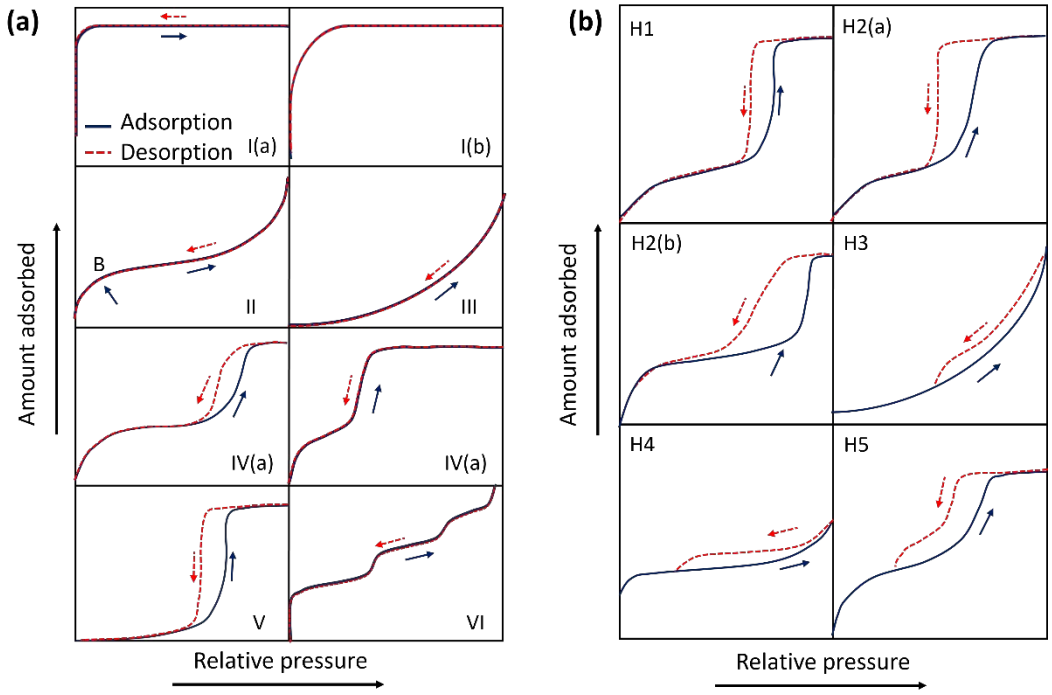

Figure A.1 Classification of physisorption **(a)** isotherms and **(b)** hysteresis loops by IUPAC.

In N_2 physisorption analysis, several mathematical models have been proposed to describe the equilibrium adsorption capacity of adsorbents. The most common method applied to Type II and Type IV isotherms, is the Brunauer-Emmett-Teller (BET) method and provides valuable information about textural properties of materials, including specific surface area (SSA, $m^2 \cdot g^{-1}$).[12,13]

Physisorption measurements of mesoporous materials, characterized by Type IV isotherms, enable the determination of total pore volume (Vp) and pore size distribution. Vp is obtained from vapor adsorption at a relative pressure close to unit (e.g., $p/p_0 = 0.95$). Pore size distribution can be assessed using the traditional BJH (Barrett, Joyner and Halenda) model, based on the desorption branch of the N_2 physisorption isotherm, and derived from the Kelvin equation. This model, while widely used, tends to underestimate pore diameter for micropores and narrow mesopores.[14,15] In contrast, the more recent and powerful DFT (density functional theory) model provides a theoretical description of the adsorption isotherm, offering a broader applicability range and increased accuracy, particularly for

micropores.[16,17] However, in this dissertation the BJH model was applied to determine the pore size distribution.

In **Chapter 4**, N_2 physisorption measurements at -196°C and BET surface area studies on nano-Cu/TiO_2 samples were performed using a Micromeritics 2000 instrument.

N_2 physisorption measurements at -196°C and BET surface area studies on ceria-doped TiO_2 nano-octahedra shown in **Chapter 6**, were performed with a Micromeritics ASAP 2420 instrument. Prior to the measurement, all the physisorbed species from the surface of the adsorbent were removed by carrying out an outgassing step at 150°C for 24h.

A.2.9 Electron Paramagnetic Resonance spectroscopy

Electron Paramagnetic Resonance (EPR), commonly known as Electron Spin Resonance (ESR), is a magnetic resonance spectroscopy technique that employs microwave radiation, in the range 3 - 400 GHz, to investigate species containing unpaired electrons, such as radicals, radical cations, and triplets, under the influence of an externally applied static magnetic field. Without going further in details, EPR spectroscopy is based on resonance signals caused by the applied magnetic field. In fact, as the strength of the applied magnetic field increases, the energy splitting (equation A.6) between energy levels for an electron spin widens, until it aligns with the frequency of microwave radiation, leading to the absorption of photons.

EPR is commonly employed to study systems where electrons exhibit both orbital and spin angular momentum. In such cases, a scaling factor is applied to accommodate the coupling between these two momenta. This is the *g*-factor, also known as the spectroscopic splitting factor or Landé *g*-factor, is a dimensionless quantity that describes the ratio of the magnetic moment of an electron to its angular momentum. It characterizes the splitting of electron spin energy levels (equation A.6) in a magnetic field.

$$\Delta E = h\nu = g \cdot \mu_B \cdot B \quad \text{(A.6)}$$

Where ΔE is the energy separation between the electron spin states, g is the g-factor, μ_B is the Bohr magneton, and B is the magnetic field strength.

The g-factor provides information about the electronic environment and the magnetic properties of the species studied in EPR spectroscopy. For free electrons, the g-factor is approximately 2 (i.e., 2.002319304386), but deviations from this value can occur due to the influence of the local environment and interactions with neighboring atoms or molecules. [18]

EPR investigations discussed in **Chapter 4** were performed by Dr. Matteo Belli using a Bruker Elexsys E580 instrument equipped with a standard X-band cylindrical cavity (ER-4118X-MD5). Powder samples were placed in fused quartz EPR tubes, and g-factor values around g = 2 were calibrated using an α-α'-diphenyl-β-picryl-hydrazyl (DPPH) standard (g = 2.0036 ± 0.0003). The analysis was carried out by the EASYSPIN software for MATLABTM. Firstly, background, oxygen vacancies, and Ti^{3+} centers were introduced in the fitting model revealing structured residuals for all hydrogenated samples. Subsequently, an axially symmetric powder pattern was incorporated into the model. While experimental limitations prevented the extraction of spin concentration in the spectra, relative quantitative considerations were feasible, and details are available in the main text and supplementary information of *Paper-I*.

A.2.10 Rutherford Backscattering Spectrometry

Rutherford Backscattering Spectrometry (RBS) is used for analyzing the composition and structure of materials. In RBS, a beam of high-energy ions (typically protons or alpha particles), is directed at a target material. As these ions interact with the atomic nuclei of the investigated material, some are backscattered. By measuring the energy and intensity of the backscattered ions, information about the

elemental composition and depth distribution of atoms within the target material can be obtained.[19]

RBS analysis mentioned in **Chapter 6**, was performed using a $^4He^+$ beam with energy E_0 of 2.0 MeV, and the backscattered beam was collected at backscattering angle $\theta = 160°$ in IBM geometry.

A.2.11 Photoelectrochemical characterizations

In general, electrochemical techniques can be divided into direct current methods, such as Linear Sweep Voltammetry (LSV) or chronoamperometry, and alternating current (AC) methods, such as Electrochemical Impedance Spectroscopy (EIS). Photoelectrochemical (PEC) measurements involve the study of the interaction of light with a photoactive working electrode (WE) immersed in an electrolyte solution. The experimental setup usually involves the use of a WE composed by photoactive materials (e.g., metal oxides like TiO_2 or α-Fe_2O_3) giving a PEC response, an electrolyte solution to facilitate the redox reactions at the electrode interface, a counter electrode (CE) and a reference electrode (RE) to complete the 3-electrode configuration PEC cell. Specifically, CE works as the site for the complementary half-reaction of water splitting, requiring a substantial surface area and rapid kinetics to prevent constraining the circuit current. Typically, Pt is commonly used for n-type photoanodes.[20] RE is employed to maintain the potential of the WE within a defined electrochemical potential scale. Commonly used REs include saturated calomel electrodes (SCEs) and Ag/AgCl. In publications related to PEC WS, the applied potential, measured with respect to SCE or Ag/AgCl RE, is often converted to the reversible hydrogen electrode (RHE) scale for convenient comparison of data reported in the literature.[21]

The photocurrent response versus the applied potential is commonly measured setting the Linear Sweep Voltammetry (LSV) mode in the potentiostat. Briefly, LSV involves the application of a linearly increasing or decreasing potential, over a

specific range, to the WE while measuring the resulting current flowing to the CE. The applied potential is swept at a constant rate expressed in volts per unit time (generally in the range 10-100 $mV \cdot s^{-1}$),[22] and the current response is recorded, generating a voltammogram. The direction of the sweep (anodic or cathodic) depends on the experimental setup. During an anodic sweep, the potential increases, while during a cathodic sweep, it decreases. As the potential sweep proceeds, the electrochemical reactions at the electrode interface lead to changes in the current. The photocurrent response at a fixed applied potential versus time, can be measured setting the Chronoamperometry (CA) mode of the potentiostat.

In general, CA is used to study the time-dependent behavior of electrochemical systems by applying a constant potential on the WE and monitoring the resulting photocurrent over time. The form of the CA curve depends on the diffusion of the analyte toward the electrode surface. Specifically, as the analyte undergoes a reaction at the electrode interface, its localized concentration decreases, leading to a gradual decay in current over time. This decay persists until either the analyte is entirely consumed, or an equilibrium is established with diffusion. This investigation is usually performed to test the stability of the photoelectrode.[22]

Electrochemical impedance spectroscopy (EIS) is a powerful technique used to study the electrical properties of electrochemical systems at the electrode-electrolyte interface. Shortly, it is based on the perturbation of the perturbation of the electrochemical system in equilibrium or steady state by applying a sinusoidal signal (AC voltage or AC current) across a broad range of frequencies and observing the sinusoidal response (current or voltage, respectively) to the applied perturbation. From the data analysis of EIS measurements, a Nyquist plot can be constructed. The Nyquist plot, represented as $-Z'' = f(Z')$, depicts the imaginary part of impedance (typically as $-Z''$) plotted against the real part of impedance (Z') for each excitation frequency.[23]

During an EIS experiment, direct current (dc) voltage typically refers to the Open Circuit Potential (OCP). OCP is the electrochemical potential of the system when no external current is applied. OCP is used as a reference point in EIS

measurements, and it is often measured before applying the small perturbation to the system to obtain impedance data. Analyzing changes in the OCP during an EIS experiment can provide information about the electrochemical processes occurring in the system, helping to characterize its behavior under different conditions.

Photoelectrochemical measurements described in **Chapter 5**, were performed at the Humboldt-Universität zu Berlin, under the supervision of Dr. Jiao Wang. The experimental setup is reported below.

PEC measurements were carried out on a Bio-Logic VMP3 potentiostat in a home-made three-electrode electrochemical system with a 0.385 cm^2 working area. Platinum sheet (1×1cm^2) and Hg/HgO were employed as CE and RE, respectively. 1M KOH (pH=13.6) was used as electrolyte. The electrolyte solution was degassed with Ar flow for 20 min before the PEC measurement to remove the dissolved oxygen. LEDs nominal wavelengths (λ =430 nm, M430L4 Spectrum) and (λ =365 nm M365L4 Spectrum) were used as the light sources. The light power density for LED illumination under 430 nm and 365 nm were 57 $mW \cdot cm^{-2}$ and 26 $mW \cdot cm^{-2}$, respectively. The LEDs power was measured with a Compact Power and Energy Meter (PM100D, ThorLabs). LSV curves were measured in the potential window -0.1 V to 0.6 V bias versus Hg/HgO with a scan rate of 10 mVs^{-1}. Electrochemical impedance spectroscopy (EIS) measurements were carried out in a frequency range from 100 kHz to 0.1 Hz with an amplitude of 5 mV.

A.3 Photocatalytic tests

A.3.1 Organic pollutants photodegradation

The degradation of target complex molecules is a good method to evaluate the photocatalytic activity of the synthesized materials. The evaluation of wavelength dependencies can be carried out by using different light irradiation sources, namely solar simulated light and both UV and visible (Vis) light irradiation. In all the test presented in this thesis, the UV and Vis photocatalytic tests were carried out under UV irradiation (365 nm) composed by six sets of 6 W UV-B lamps (Sankyo, Japan) or under a 13 W visible sodium lamp (Osram, Germany) for visible light irradiation. Moreover, the main photocatalytic tests were carried out under Sunlight Solar Simulator, AM1.5G filter, 100 W Xenon arc lamp (Abet Technologies, USA). During the photocatalysis the reactor was positioned under the solar lamp at a suitable distance to obtain the power of 1 sun (1350 W/m^2). The photon flux was measured by using a Si-based reference solar cell #15150 (Abet Technologies, USA) placed against the external wall of the photoreactor containing pure water. For all the tests, a 100 mL cylindrical concentric Pyrex-quartz photocatalytic reactor was used. According to the selected pollutant, the initial concentration was in the range of 10^{-5} – 10^{-6} M. For instance, ciprofloxacin optimal concentration was found to be 10^{-5} M. Additionally, the optimal photocatalyst amount (evaluated in mg/L) varied, according to the investigated material. All the photodegradations were performed at room temperature and atmospheric pressure. Prior to irradiation, the solutions were put in dark for 30 or 60 minutes to reach the adsorption/desorption equilibrium. At given time intervals, 1 mL of solution was collected from the reactor, filtered through a 0.45 mm PTFE Millipore disc to remove the catalyst powder and used for successive UV–Vis spectroscopy analysis. The degradation processes were observed following the maximum absorbance in the UV-Vis spectrum of the target molecule. Once calculated the concentration at that specific wavelength through the Lambert Beer law, it was possible to calculate the degradation rate

C/C_0, where C is the concentration after a given time, *t* and C_0 represents the initial concentration at *t = 0*. Kinetics study involved in the complex molecules photodegradation was carried out evaluating the data interval from 0 to 40 min and adopting the pseudo-first-order model (equation A.7):

$$ln\ \frac{C}{C_0} = -kt \quad \text{(A.7)}$$

where k is the pseudo-first order rate constant (min^{-1}), calculated as k = (2.303· slope).

A 3-cycles recycling test was performed to evaluate the stability and reusability of the investigated photocatalysts. Briefly, the most promising sample was collected by centrifugation, washed several times with deionized water, and then dried overnight after each photocatalytic cycle.

The main active species were investigated performing the free radical trapping experiments. In summary, three distinct photocatalytic experiments were conducted under identical conditions as described above, with the inclusion of tert-Butanol (tBuOH, 1mM), oxalic acid (OA, 1mM), and N_2 (g) as scavengers for OH, holes, and O^{2-}, respectively, in the reaction system.

A.3.2 Photoreforming

As described in **Chapter 1** and **4**, the photocatalytic activity of the samples can be evaluated by means of the H_2 evolution reaction from methanol photoreforming. Photocatalytic H_2 production tests were performed in a liquid-phase flow reactor system provided by Apria Systems. The photocatalyst was suspended in a methanol/ deionized water (MeOH/ H_2O) solution (10 % v/v) under N_2(g) flux at 50 $mL{\cdot}min^{-1}$ for 60 min before starting the reaction. Initiating the test involved setting the gas flow to 6 $mL{\cdot}min^{-1}$ and activating the lamp, which was a 365 nm UV LED array. Such low gas flow (6 $mL{\cdot}min^{-1}$) was set to reach very exigent conditions to see any small differences between the studied catalysts. A gas chromatographer

equipped with a thermal conductivity detector (Agilent 7890B GC) was useful to analyze the effluent gases and quantify the H_2 production. Equation 3 was used to estimate the apparent quantum yield (AQY) for the H_2 evolution reaction (equation A.8):[24]

$$AQY = \frac{2 \cdot n_{H_2}}{n_p} \left[\frac{mol \cdot s^{-1}}{mol \cdot s^{-1}}\right] \cdot 100 \quad \text{(A.8)}$$

where n_{H2} is the H_2 molecules number and n_p is the number of incident photons reaching the photocatalyst. n_p can be calculated from the ratio between the total incident energy and the energy of one photon. In this experimental setup, the total incident energy was calculated considering the 365 nm incident light used and the power density of the incident light (2100 $W \cdot m^{-2}$).

A.4 References

[1] Z. Wei, M. Endo-Kimura, C. Colbeau-Justin, B. Ohtani, E. Kowalska, *J Nanosci Nanotechnol* **2020**, *20*, 1278.

[2] Y. Waseda, E. Matsubara, K. Shinoda, *X-Ray Diffraction Crystallography*, Springer Berlin Heidelberg, Berlin, Heidelberg, **2011**.

[3] E. Smith, G. Dent, *Modern Raman Spectroscopy*, Wiley, **2019**.

[4] S. Hofmann, *Auger- and X-Ray Photoelectron Spectroscopy in Materials Science*, Springer Berlin Heidelberg, Berlin, Heidelberg, **2013**.

[5] G. Greczynski, L. Hultman, *J Appl Phys* **2022**, *132*.

[6] N. Fairley, V. Fernandez, M. Richard-Plouet, C. Guillot-Deudon, J. Walton, E. Smith, D. Flahaut, M. Greiner, M. Biesinger, S. Tougaard, D. Morgan, J. Baltrusaitis, *Applied Surface Science Advances* **2021**, *5*, 100112.

[7] P. Kubelka, F. Munk, *Z. Tech. Phys* **1931**, *12*, 593.

[8] P. Makuła, M. Pacia, W. Macyk, *Journal of Physical Chemistry Letters* **2018**, *9*, 6814.

[9] B. J. Inkson, in *Materials Characterization Using Nondestructive Evaluation (NDE) Methods*, Elsevier, **2016**, pp. 17–43.

[10] R. Tararam, P. S. Garcia, D. K. Deda, J. A. Varela, F. de Lima Leite, in *Nanocharacterization Techniques*, Elsevier, **2017**, pp. 37–64.

[11] D. Johnson, D. L. Oatley-Radcliffe, N. Hilal, in *Membrane Characterization*, Elsevier, **2017**, pp. 115–144.

[12] C. Schlumberger, M. Thommes, *Adv Mater Interfaces* **2021**, *8*.

[13] S. Brunauer, P. H. Emmett, E. Teller, *Adsorption of Gases in Multimolecular Layers*, **1938**.

[14] M. Thommes, K. A. Cychosz, *Adsorption* **2014**, *20*, 233.

[15] J. Landers, G. Yu. Gor, A. V. Neimark, *Colloids Surf A Physicochem Eng Asp* **2013**, *437*, 3.

[16] G. Leofanti, M. Padovan, G. Tozzola, B. Venturelli, *Catal Today* **1998**, *41*, 207.

[17] P. I. Ravikovitch, S. C. Ó Domhnaill, A. V Neimark, F. Schiith, K. K. Ungert, *Capillary Hysteresis in Nanopores: Theoretical and Experimental Studies of Nitrogen Adsorption on MCM-41*, **1995**.

[18] P. Bertrand, *Electron Paramagnetic Resonance Spectroscopy*, Springer International Publishing, Cham, **2020**.

[19] R. Escobar Galindo, R. Gago, D. Duday, C. Palacio, *Anal Bioanal Chem* **2010**, *396*, 2725.

[20] Z. Chen, H. N. Dinh, E. Miller, *Photoelectrochemical Water Splitting*, Springer New York, New York, NY, **2013**.

[21] van de Krol Roel, Grätzel Michael, *Photoelectrochemical Hydrogen Production*, Springer US, Boston, MA, **2012**.

[22] X. Shi, L. Cai, M. Ma, X. Zheng, J. H. Park, *ChemSusChem* **2015**, *8*, 3192.

[23] A. Ch. Lazanas, M. I. Prodromidis, *ACS Measurement Science Au* **2023**, *3*, 162.

[24] M. Qureshi, K. Takanabe, *Chemistry of Materials* **2017**, *29*, 158.

Appendix B – *Publications & Scientific contributions*

Paper-I

L. Liccardo, M. Bordin, P. M. Sheverdyaeva, M. Belli, P. Moras, A. Vomiero, E. Moretti, Surface Defect Engineering in Colored TiO_2 Hollow Spheres Toward Efficient Photocatalysis. *Adv. Funct. Mater.* 2023, 33, 2212486. https://doi.org/10.1002/adfm.202212486

ADVANCED FUNCTIONAL MATERIALS
www.afm-journal.de

Surface Defect Engineering in Colored TiO_2 Hollow Spheres Toward Efficient Photocatalysis

Letizia Liccardo, Matteo Bordin, Polina M. Sheverdyaeva, Matteo Belli, Paolo Moras, Alberto Vomiero, and Elisa Moretti**

Nanostructured TiO_2 is one of the best materials for photocatalysis, thanks to its high surface area and surface reactivity, but its large energy bandgap (3.2 eV) hinders the use of the entire solar spectrum. Here, it is proposed that defect-engineered nanostructured TiO_2 photocatalysts are obtained by hydrogenation strategy to extend its light absorption up to the near-infrared region. It is demonstrated that hydrogenated or colored TiO_2 hollow spheres (THS) composed of hierarchically assembled nanoparticles result in much broader exploitation of the solar spectrum (up to 1200 nm) and the engineered surface enhances the photogeneration of charges for photocatalytic processes. In turn, when applied for photodegradation of a targeted drug (Ciprofloxacin) this results in 82% degradation after 6 h under simulated sunlight. Valence band analysis by photoelectron spectroscopy revealed the presence of oxygen vacancies, whose surface density increases with the hydrogenation rate. Thus, a tight correlation between degree of hydrogenation and photocatalytic activity is directly established. Further insight comes from electron paramagnetic resonance, which evidences bulk Ti^{3+} centers only in hydrogenated THS. The results are anticipated to disclose a new path toward highly efficient photocatalytic titania in a series of applications targeting water remediation and solar fuel production.

1. Introduction

The development of efficient, low-cost, and environmentally friendly photocatalysts has attracted the interest of researchers for a series of applications, including production of "green fuels",[1–3] and water remediation from polluting dyes and drugs.[4]

Water contamination is one of the upfront issues to be solved.[5] Complex organic molecules and pharmaceuticals including antibiotics are gaining attention due to their abuse and their low degradability. In fact, antibiotics are largely detected in rivers and water surfaces with concentrations ranging from ng L^{-1} to µg L^{-1}. Hence, their release from wastewater industries is extremely dangerous both for the environment and human health.[6–8] Ciprofloxacin (CIP) is a broad-spectrum second-generation fluoroquinolone antibiotic and one of the most widely used and prescribed. Additionally, it has been proved that CIP is not only present in different water effluents all over the world, but it is also exceeding the safe concentration limit for antimicrobial resistance in several sites.[9] Unfortunately, most wastewater treatment plants are not suitable to eliminate pollutants effectively, so it is extremely important to look for new treatment strategies.

In this regard, photocatalytic advanced oxidation processes (AOPs), such as heterogeneous catalysis, seem to be promising to accelerate the oxidation and degradation of a wide range of organic pollutants. In fact, AOPs use the ability of semiconductor materials to interact with light and to create excitons, whose dissociation induces the formation of electron-hole pairs (e^-–h^+) that can degrade pollutant molecules via a radical mechanism, thus promoting their mineralization. The production of photogenerated e^-–h^+ is one of the crucial steps, thus boosting their creation and avoiding fast charge recombination is essential to have high photocatalytic activity.[10] This process requires the presence of an efficient and stable catalyst with a suitable bandgap, able to absorb as much solar light as possible.

Titania (TiO_2) is one of the most used photoactive materials, being at the same time non-toxic and cheap. However, its bandgap energy is in the range of 3.0–3.2 eV, so it can absorb light only in the ultraviolet (UV) region, which represents 4–5% of the total solar irradiance spectrum.[11,12] In addition,

L. Liccardo, M. Bordin, A. Vomiero, E. Moretti
Department of Molecular Sciences and Nanosystems
Ca' Foscari University of Venice
Via Torino 155 30172, Venezia Mestre, Italy
E-mail: alberto.vomiero@ltu.se; elisa.moretti@unive.it
P. M. Sheverdyaeva, P. Moras
Istituto di Struttura della Materia-CNR (ISM-CNR)
SS 14, Km 163.5 34149, Trieste, Italy
M. Belli
CNR-IMM
Unit of Agrate Brianza
Via C. Olivetti 2 20864, Agrate Brianza, Italy
A. Vomiero
Division of Materials Science
Department of Engineering Sciences and Mathematics
Luleå University of Technology
97187 Luleå, Sweden
The ORCID identification number(s) for the author(s) of this article can be found under https://doi.org/10.1002/adfm.202212486.

DOI: 10.1002/adfm.202212486

small titania nanoparticles, both in solution or assembled as mesoporous layers, are unable to scatter the impinging light and force it within a confined space, to increase the absorption probability. The development of low-energy gap systems able to confine and absorb light is still a challenge.

Hydrogenated titania is a sub-stoichiometric oxide (TiO_{2-x}), also called colored titania due to the very different colors it can assume (blue, gray, black). It is one of the best sunlight harvesters, as it can absorb light from the UV to the infrared (IR) region of the solar spectrum. Moreover, it has been demonstrated that the oxygen-vacancy-rich black TiO_2 has enhanced photoactivity in several oxidation reactions under visible light as compared to white (stoichiometric) TiO_2.[13,14] Suitable combinations of chemical structure and morphology can further enhance the photochemical activity of a nanostructured system,[15,16] since the functionality of a material can be strongly influenced by its shape and size.

An interesting architecture is represented by hierarchical structures, where small building blocks are assembled into more complex geometries. TiO_2 hollow spheres composed of self-assembled nanoparticles have been successfully applied as decently efficient photocatalysts, by combining the high surface area, and strong light scattering, which induces the light confinement within a small volume, thus increasing the absorption probability.[17,18] However, even the hierarchically assembled white titania hollow spheres suffer from very limited light absorption, due to the large bandgap of the material.

In the present work, colored TiO_2 hollow spheres (THSs), composed of hierarchically assembled nanoparticles, were synthesized by a hard template-based method (see **Figure 1**a), followed by chemical reduction under controlled conditions. Electron paramagnetic resonance (EPR) is used to monitor the presence of defects (Ti^{3+} centers and oxygen vacancies) in the bulk of the materials.[19] X-ray photoelectron spectroscopy (XPS) shows that the density of surface oxygen vacancies increases in a controllable fashion at every step of preparation of the THSs. Their catalytic activity was evaluated by monitoring the photodegradation at room temperature and atmospheric pressure (P_{atm}) of CIP (target molecule), under simulated solar light. We demonstrated that the hydrogenation content, related to the presence of oxygen vacancies, is responsible for the increase in the optical absorption capability of the catalysts (up to the near-IR, NIR, region) thus enhancing the overall photocatalytic efficiency for the investigated photocatalytic oxidation process. We anticipate our results to disclose a new path toward highly efficient photocatalytic titania in a series of applications targeting water remediation and solar fuel production.

2. Results and Discussion

2.1. Morphological and Structural Characterization

The surface morphology of THSs samples was analyzed using Field-emission scanning electron microscope (FESEM) (Figure S1, Supporting Information). Poly(methyl methacrylate) (PMMA) nanoparticles exhibited spherical shapes and uniform sizes with an average diameter of 300 nm. No agglomerated nanoparticles were observed. Figure S1 (Supporting Information) also reports white THS and the gray THS series, after the removal of PMMA through the calcination process. THSs were uniform in size, with diameters ranging from 350 to 400 nm. It is worth mentioning that samples were labeled as X_THSn, where X is referred to the color of the sample: W (white), G (gray), DG (dark gray) and n is the chemical vapor deposition (CVD)-annealing time when it is not 60 min.

The shell thickness was estimated to be ≈50 nm with a relatively rough surface. The appearance of some broken spheres revealed the presence of a void inside, thus confirming that hollow structures were obtained. After the chemical reduction treatment under annealing of W_THSs, no relevant morphological and structural changes were detected. The crystal structure and phase identification were studied through X-ray diffraction (XRD) (Figure S1, Supporting Information). All the THSs samples showed the characteristic peaks of the anatase phase at 2θ values 25.3°, 36.9°, 37.8°, 38.6°, 48.1°, 53.9°, 55.1°, and 62.7°, in agreement with the JCPDS (Joint Committee on Powder Diffraction Standards) card number 21–1272. The anatase crystalline structure has been preserved during the reduction process in all the colored samples, as confirmed by XRD (Figure S1, Supporting Information) and high-resolution transmission electron microscope (HRTEM) analysis (Figure 1b–g). From the HRTEM analysis, the grain size distribution of W_THSs is (9.4 ± 2.9) nm (Figure S2, Supporting Information). Lattice fringes are clearly visible in the polycrystalline structure of Figure 1c. The Selected Area Electron Diffraction (SAED) pattern (Figure 1d) revealed concentric circles, due to the polycrystallinity of THSs samples. The lattice spacing and the crystal phase agree with the results from XRD. The energy dispersive X-ray spectroscopy (EDS) analysis indicates that only Ti and O species can be detected in the W_THS selected sample (Figure 1e–g). The hollow shape was maintained during all the processing steps, including hydrogenation (Figure S1, Supporting Information).

2.2. Optical Characterization

All the diffuse reflectance UV–visible–near-infrared (DRUV-vis-NIR) spectra in **Figure 2**a are characterized by the main absorption feature related to the optical bandgap, which induces the strong absorption edge ≈390 nm (≈3.1 eV). The spectrum for W_THS demonstrates the effectiveness of the hollow sphere,[17] leading to a flat reflectivity below 75% in the full range of 390–1200 nm. Hydrogenation induces the onset of an additional broad absorption band from 500 nm up to (at least) 1200 nm, which is not present in the W_THS sample, whose intensity increases with increasing the wavelengths and the degree of hydrogenation. The light absorption in the vis–NIR region can be enhanced thanks to the disordered surface layer and the presence of surface defects (i.e., oxygen vacancies) generated by hydrogenation.[17,20,21] Our results reveal that the combination of a suitable morphology and the hydrogenation treatment enhanced light absorption in a broad spectral range. The onset of the absorption feature in the low-energy spectral region (>500 nm) may be explained by the presence of localized states below the TiO_2 conduction band (CB) minimum, introduced by the oxygen vacancies, as confirmed by both XPS and EPR analyses (see sections below).[22]

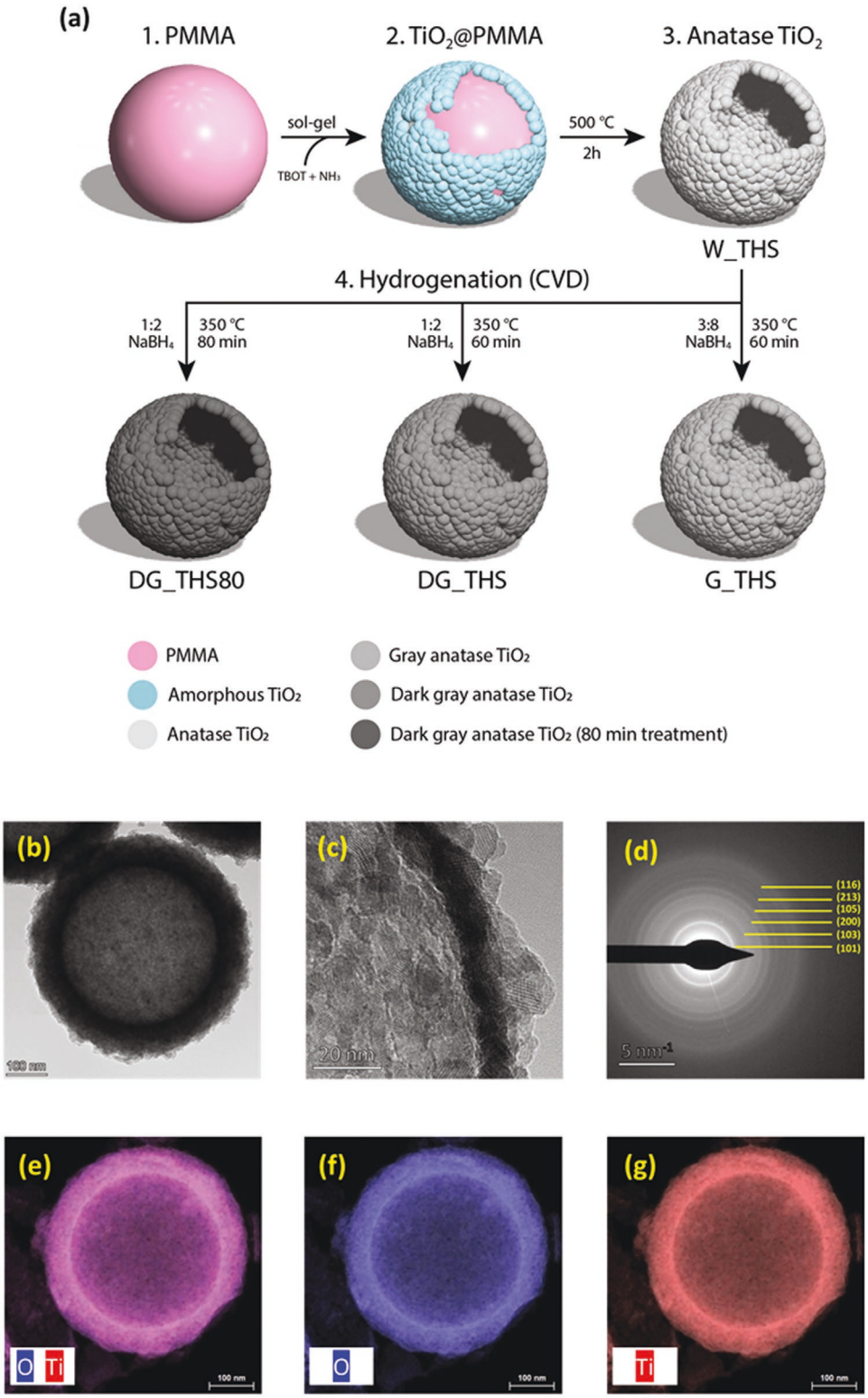

Figure 1. a) Synthesis scheme and b–g) HRTEM analysis of the W_THS sample. b,c) HRTEM images at different magnifications. d) SAED pattern with Miller indexes. e–g) EDS images showing the presence of Ti and O only.

2.3. Photoelectron Spectroscopy Analysis

The electronic structure of the four types of hollow spheres was analyzed by X-ray photoelectron spectroscopy (XPS). The survey spectra (Figure S3, Supporting Information) show the attenuation of the titania-related peaks along the sequence of the CVD preparation steps (Figure 1a), due to the gradual formation of a graphitic coating. Four peaks are necessary to describe the O1s

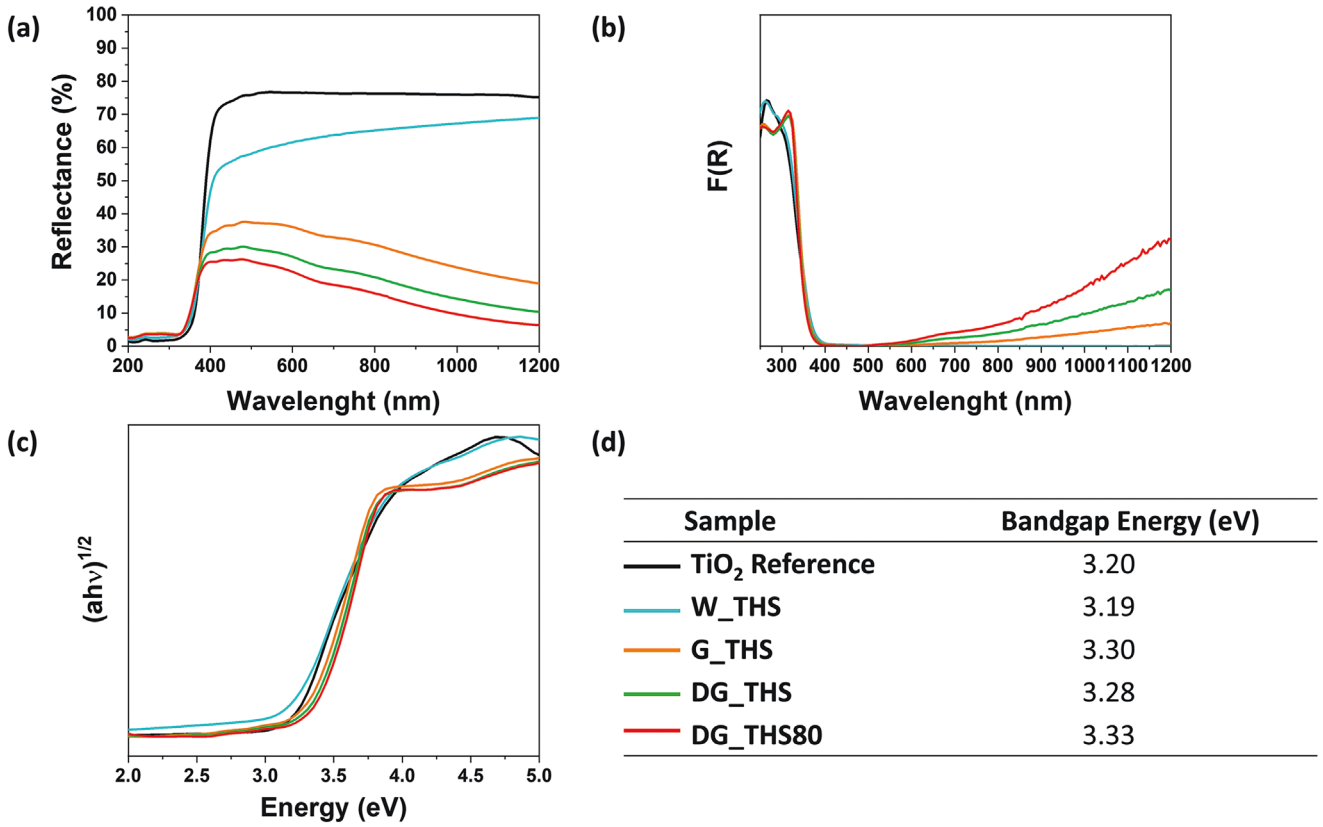

Figure 2. a) DRUV–Vis-NIR spectra, b) F(R) spectra calculated through Kubelka–Munk functions, c) Tauc Plots and d) bandgap energies comparison for all the samples, including the TiO_2 Reference.

spectra (**Figure 3**a, photon energy 750 eV). P1 at 530.65 eV and P2 at 531.85 eV are attributed to O in stoichiometric TiO_2 (O_2^-) and OH groups adsorbed on the surface of the THSs. Their ratio remains stable for all THSs (**Table 1**). P3 at 533.0 eV and P4 at 534.4 eV can be associated with C—O and C—OH groups, respectively,[23] and with the presence of adsorbed H_2O.[24] The increasing P3/P1 and P4/P1 ratios along the sequence of CVD cycles (Table 1) can indicate that reduced graphene oxide forms in parallel with the graphitic coating, as suggested by the Fourier Transform Infrared Spectroscopy (FT-IR) spectroscopy data of Figure S4 (Supporting Information). In addition, a higher water content can be ascribed to higher surface concentration of oxygen vacancies which tend to bind water. The Ti2p spectra are very similar for all samples (Figure 3b, with photon energy of 750 eV). They can be fitted with two doublets: the main doublet (D1) at high binding energy derives from Ti in stoichiometric TiO_2 (Ti^{4+}), while the minor doublet (D2) is due to Ti^{3+} defects that probably form during the thermal treatment at 500 °C (step 2 of Figure 1a).[25] The nearly constant D2/D1 ratio (4.2–5.3%, Table 1) shows that the surface concentration of Ti^{3+} is negligibly modified by the CVD preparation procedures at lower temperature (350 °C), which strongly affect the bulk concentration of Ti^{3+} (see Section 2.5). The P1/D1 ratio, normalized to the respective photoemission cross sections at 750 eV (0.24 for O1s and 0.7 for Ti2p),[26,27] is always very close to 2 (Table 1), as expected for stoichiometric TiO_2. The valence band analysis was carried out using resonant conditions (photon energy 469 eV) in order to probe the defect states (oxygen vacancies and Ti^{3+}) within the gap of stoichiometric TiO_2 with highest sensitivity. In Figure 3c the valence band spectra display strong O2p-related states between ≈3 and 10 eV (V1) and a low-intensity Ti3d-derived state at ≈1 eV (V2), which is better visualized in the inset. The binding energy of V2 shifts continuously from 1.10 to 0.95 eV from W_THS to DG_THS80, i.e., closer to the CB minimum. The V2/V1 ratio can be used to estimate the concentration of the defects in the near-surface region of the samples. As the concentration of the Ti^{3+} defects remains stable (Figure 3b), the higher V2/V1 ratio reflects the increasing concentration of oxygen vacancies with the CVD treatments (Table 1).

2.4. FT-IR Spectroscopy

Figure S4a (Supporting Information) shows the FT-IR spectra of W_THS, DG_THS, and DG_THS80. The titania characteristic absorption bands are the Ti—O—Ti symmetrical stretching at 686 cm^{-1} and the Ti—O vibration band located at 505 cm^{-1}.[28] The broad band at ≈3500 cm^{-1} corresponds to the stretching vibrations of OH groups.[29] Furthermore, the band located at 1631 cm^{-1} can be attributed to the combination of Ti—OH bending due to the H_2O molecules adsorbed on the sample's surface and to the C=C stretching vibration that can be associated with the presence of graphitic carbon. The band at

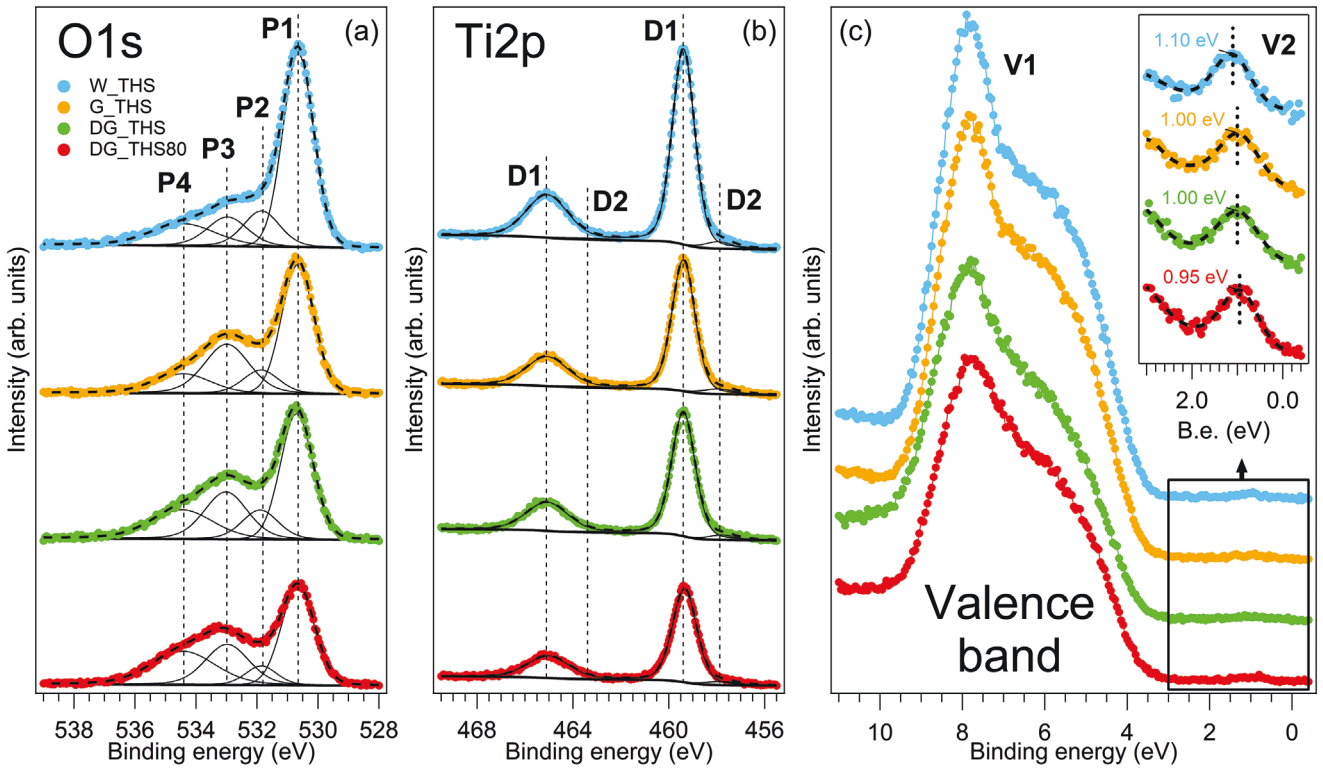

Figure 3. XPS characterization of the THSs. The spectra were collected at photon energy 750 eV for the a) O1s and b) Ti2p core levels and photon energy 468 eV for the c) valence band. The inset in panel (c) shows a zoom of the fundamental gap region of the THSs, where defect states (V2) are detected.

1570 cm^{-1} is attributed to the presence of aromatic C=C vibrations and the band at 1360 cm^{-1} to C−OH stretching, leading to the conclusion that there is the presence of graphitic carbon and graphene oxide on the surface of the hydrogenated samples.[28,30] These results are consistent with XPS analysis. Figure S4b (Supporting Information) shows the FT-IR spectra for the bare (W_THS) and the hydrogenated samples after and before the CIP photodegradation experiments, labeled as DG_THS, DG_THS80, and DG_THS photodeg, DG_THS80 photodeg, respectively. Slight differences can be detected between the spectra before and after the photocatalytic experiments. The main difference found in the used samples is the presence of two low-intensity bands located at ≈2850 and 2910 cm^{-1} associated to aromatic and aliphatic C−H stretching of CIP functional groups, which indicates that only a few of CIP molecules are adsorbed onto the surface of the photocatalysts.[30]

Table 1. Numerical values derived from the XPS data (shown in Figure 3).

Sample	W_THS	G_THS	DG_THS	DG_THS80
P2/P1 [%]	24	23	28	20
P3/P1 [%]	22	59	55	60
P4/P1 [%]	26	28	48	71
D2/D1 [%]	4.2	5.3	4.5	5.1
P1/D1	2.03	2.05	2.08	2.14
V2 binding energy [eV]	1.10	1.00	1.00	0.95
V2/V1 [%]	1.7	1.8	2.7	3.0

2.5. EPR Spectroscopy

Figure 4 shows the room temperature EPR spectra of THS with different degrees of hydrogenation in the $g = 2$ region. Data are reported after the removal of a parabolic background and the normalization to the maximum of each spectrum, to better appreciate its features.

W_THS shows a single transition, characterized by a small anisotropy, almost unobservable because of the signal line width ($g_\perp = 2.0021$, $g_\parallel = 2.0007$, Gaussian and Lorentzian peak-to-peak widths σ_{pp} and λ_{pp} of 0.22 and 0.17 mT respectively). This center is generally ascribed to oxygen vacancies (OV), though we observe a g factor slightly shifted to lower values with respect to the literature ($g = 2.002$–2.003).[19,25] Following hydrogenation, the OV signal is still present though with parameters closer to the expected values ($g_\perp = 2.0026$, $g_\parallel = 2.0016$, $\sigma_{pp} = 0.64$, $\lambda_{pp} = 0.38$). Moreover, three other centers emerge: a broader transitions at higher magnetic field values ($g_\perp = 1.988$, $g_\parallel = 1.978$, $\sigma_{pp} = 0.2$, $\lambda_{pp} = 1.2$); another weak center at intermediate g factor which is responsible for the strange asymmetric line shape of the OV center in the treated material ($g_\perp = 2.0004$, $g_\parallel = 1.9935$, $\sigma_{pp} = 0.54$, $\lambda_{pp} = 0.04$); an extremely broad peak (peak-to-peak width higher than 110 mT) centered around $g = 2.4$–2.45 (Figure S9, Supporting Information). The first center is generally attributed to paramagnetic Ti^{3+} centers.[19,25] The fact that no such signal is observed in W_THS while, for the same material, Ti^{3+} is observed by XPS may be related to the different parts of the sample the two techniques probe. If hydrogenation promotes the formation of Ti^{3+} at the surface

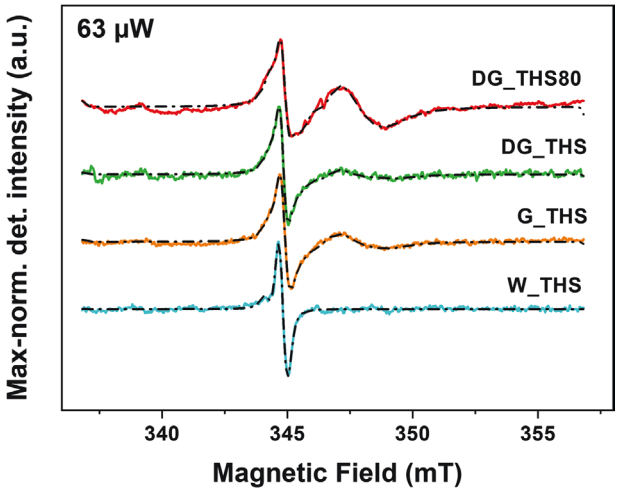

Figure 4. Stacked EPR spectra of THS with different degrees of hydrogenation. The applied power was selected not to saturate any of the signals. Ordinate scale represents data after the subtraction of a parabolic background, and normalization to the maximum value in each spectrum, to better visualize the relative weight of the various components. Fitting curves of the single spectra are also included (black dash-dot line) and the corresponding spin-Hamiltonian parameters can be found in (Figures S5–S9 and Tables S1–S4, Supporting Information).

and their diffusion into the bulk portion of the THS, Ti^{3+} centers too weak to be recorded by EPR in the pristine material may become observable. The interpretation of the second center is not straightforward. Despite the fact that it is present only together with the Ti^{3+} center, it does not fall in the typical g factor range of Ti^{3+} centers.[31–33] It is more probably a carbon-related center, possibly interacting with Ti^{3+} centers nearby. This attribution is suggested in the literature[34] and would be compatible with XPS characterization. Low-temperature EPR characterization may help to unravel this issue. The last center is responsible for the large negative background overlapping the $g = 2$ region. Such a background can be observed in various reports, but it is not often commented on. Its width and placement suggest that it is likely due to ferromagnetic resonance from magnetic impurities, which can give very large signals at unusual g factor values even if in trace amounts. This effect is due to the enhancement inherent in their intrinsic magnetization. Similar signals were observed in TiO_2 samples after 2 h ball milling, for example.[35] Presumably, it is not due to Fe contaminants, nor to ferromagnetic interactions between Ti^{3+} centers, which would both introduce well-defined features in a different g range, at least for a substitutional fraction.[31,36,37]

The intensity ratio of the Ti^{3+} component with respect to the OV component for G_THS, DG_THS, and DG_THS80 is roughly 1.5, 1.2, and 3.9, respectively, while it is identically 0 for W_THS which does not show Ti^{3+} even at large microwave power. The ratio of the C-related component with respect to the OV component is 0, 0.2, 0.3, and 0.4. for W_THS, G_THS, DG_THS, DG_THS80 respectively.

2.6. Photodegradation of Ciprofloxacin under Simulated Solar Light

The photocatalytic activity of all THS samples was evaluated under simulated solar light irradiation, in an aqueous solution and at room temperature (**Figure 5**a,b). In all cases, we monitored for 360 min the typical CIP main absorbance peak located at ≈273 nm. The photolysis of the base CIP was used as a reference (black curves). Figure 5a shows the photocatalytic degradation of CIP with and without catalysts in terms of the concentration of CIP C at a given exposure time with respect to its initial value C_0 at −60 min (60 min is the equilibration time before the exposure to the solar light). The C/C_0 curve of bare CIP decreases slightly (≈13%) over 360 min, thus confirming the substantial stability of CIP under sunlight irradiation. After 60 min of equilibration in the dark in the presence of TiO_2 Reference and THS samples, CIP is partially adsorbed on the surface of the photocatalysts, from 2% for W_THS to 20% for DG_THS80 and 30% for TiO_2 Reference. The efficiency of the photocatalytic degradation is known to depend crucially on the type of the adsorption phenomena involved, which are also affected by the pH of the solution. Indeed, the solution pH influences both the charge of the photocatalyst surface and the drug molecules as well as their possible interactions. The zero-point charge (pH_{zpc}) is defined as the pH at which the catalyst surface is uncharged. According to the literature, pH_{zpc} for stoichiometric TiO_2 is between 5 and 6. In addition, CIP shows different pKa associated to its functional groups and can take different charges according to the pH of the solution.[27,38] In general, in alkali conditions CIP is predominantly in its anionic form, on the contrary in cationic form in acidic conditions. Hence, in water at a neutral pH CIP is in its zwitterionic form so that it will interact weakly with the pure TiO_2 photocatalyst surface. When the hydrogenation content increases, the pH_{zpc} of the colored TiO_2 changes. In detail, values reported in literature are below the neutral pH, thus the hydrogenated particle suspensions in water (pH = 7) are stabilized by repulsive forces coming from their negatively charged surface. Oxygen vacancies may lead to an increase in the adsorption of water molecules thus hydroxylating the catalyst's surface, affecting the adsorption of CIP molecules and the overall degradation pathway.[39,40] This mechanism explains the marked decrease of C/C_0 as a function of the exposure time when THS samples were added to the solution.

For comparison purposes, a commercial white titania (pure anatase polymorph, as the THS samples) was also investigated under the same reaction conditions. All the synthesized samples showed excellent and improved photocatalytic activity with respect to the commercial TiO_2 Reference, which can degrade CIP only at 61%. The best-performing sample is G_THS, which degrades 82% of CIP within 360 min and presents a kinetic constant of 11.9 10^{-3} min^{-1} (the kinetic constants for all the samples are reported in Figure 5b,c). Interestingly, the high hydrogenation content of DG_THS80 is accompanied by lower photocatalytic activity among the colored samples. When dealing with hydrogenated TiO_2, the correlation between the physicochemical properties and the photocatalytic performances is complicated and often results in conflicting results.[22] In our case, XPS and EPR analysis confirmed the presence of surface defects such as Ti^{3+} centers and oxygen vacancies, which are highly visible in DG_THS80. The role of the oxygen vacancies and Ti^{3+} centers have been widely discussed in the literature and their concentration has an impact on the photocatalytic activity.[41,42] In fact, defects act as recombination centers for photogenerated electron-hole pairs and cause a decrease in the

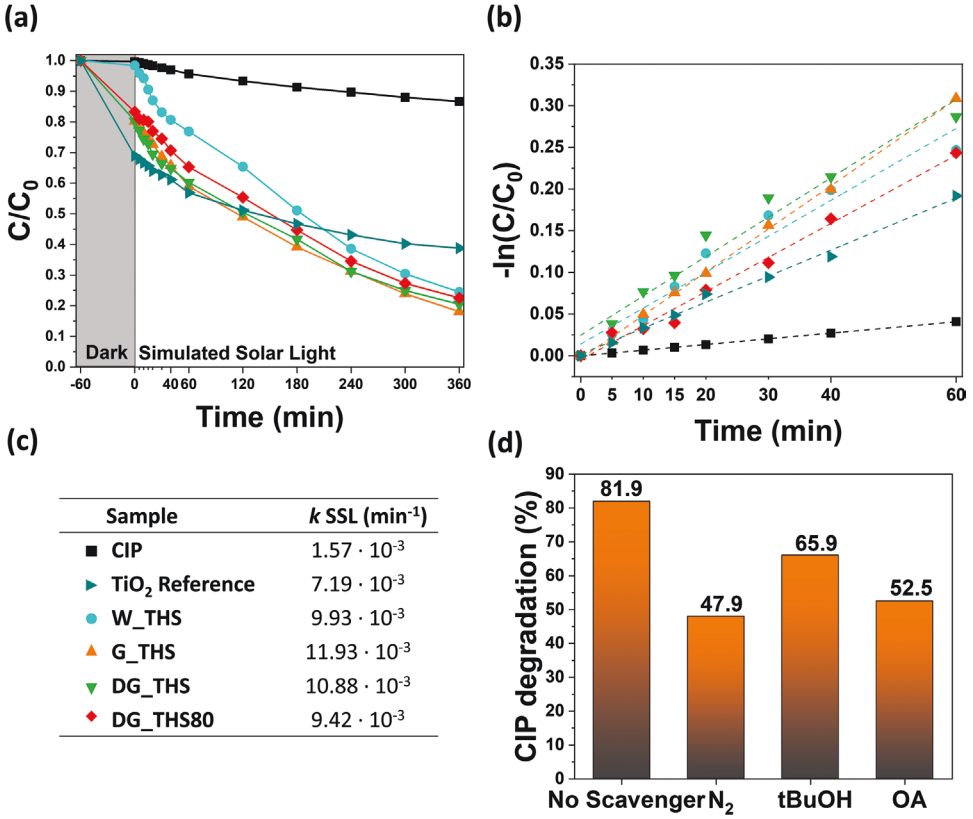

Figure 5. a) Photocatalytic degradation of CIP as a function of irradiation time with and without catalysts (CIP curve) under simulated solar light irradiation. b) CIP degradation kinetics with linear fits of the experimental data in dashed lines. c) Legend and kinetic constant values for all the samples under simulated solar light (SSL). d) Scavenger experiments of the active species for the degradation of CIP in presence of G_THS.

overall photocatalytic efficiency. However, the same Ti^{3+} sites and oxygen vacancies have been shown to be responsible for the increasing ability in absorbing a broader range of wavelengths up to the NIR region. Consequently, a trade-off between light absorption and catalytic activity is needed to maximize the photocatalysis. G_THS showed the lowest amount of surface defects. This feature prevents charge-carriers recombination, thus lowering the electrons trapping phenomena and promoting the conversion of oxygen molecules into superoxide radicals, necessary for CIP photodegradation.[43]

Another important point deserves to be discussed: the role of graphitic carbon on the photocatalytic properties. The combination of XPS and FT-IR analysis may help on the matter. In fact, XPS highlights the formation of graphitic coating along the sequence of the CVD preparation steps. The presence of carbon coating is also confirmed by FT-IR analysis of the samples DG_THS and DG_THS80 before the catalytic tests: the samples DG_THS and DG_THS80 clearly present the two FT-IR absorption bands at 1570 and 1360 cm^{-1}, which are not present in the sample W_THS. After the first cycle of photocatalysis, the FT-IR analysis was repeated (Figure S4, Supporting Information) and the two bands at 1570 and 1360 cm^{-1} disappeared. After three catalytic cycles, we also repeated the XPS measurement on sample DG_THS (Figure S10, Supporting Information), which indicated a drastic decrease in the surface graphitic carbon content. The experimental evidence from both FT-IR and XPS indicates strong reduction of graphitic carbon content in the DG sample series after the photocatalytic tests. Despite the strong modification of carbon content, the functional tests of Figure S11 (Supporting Information) demonstrate no variation in the photocatalytic activity during cycles 1, 2, and 3 of the reusability test. The combination of these data allows us to conclude that the surface graphitic carbon plays a negligible role in the functional properties of the material and tends to disappear during the re-use of the colored hollow spheres.

Since the peculiarity of the hydrogenated THSs is the broad absorbance in the visible region, we also evaluated the photocatalytic activity of the best-performing sample (i.e., G_THS) under both UV and vis light, in the same conditions used before, to compare the obtained results and examine wavelength dependence. As expected, G_THS photocatalyst is active both under UV and vis light, showing a CIP degradation of 98% and 54%, respectively, after 180 min of irradiation time (Figure S12, Supporting Information).

Stability and reusability test of the best-performing photocatalyst (G_THS), was carried out (Figure S11, Supporting Information). A slightly increased photocatalytic activity (+5%) was observed soon after the first-cycle test. Simultaneously, a decrease of the CIP adsorption process from 20% of adsorbed species during the first cycle to 11% during the third cycle in the dark period was recorded. This behavior can be attributed to the adsorption of degradation by-products on the active sites which leads, at the same time, to faster production of radicals. Finally, free radical trapping experiments were conducted to

investigate the main active species responsible for CIP degradation (Figure 5d). The photocatalytic efficiency of G_THS is significantly inhibited when N_2 (O_2^- scavenger) and OA (h^+ scavenger) are introduced into the system, while barely affected upon the addition of tBuOH (OH scavenger). Hence, superoxide radicals (O_2^-) and holes (h^+) should be the two major reactive species involved in the CIP degradation by G_THS under simulated solar light irradiation.

3. Conclusions

We have proposed an easy and cost-effective way to obtain hydrogenated and colored THS composed of hierarchically assembled nanoparticles as promising photocatalysts for water remediation. The hollow microstructures, in combination with the defect-engineered surface, enable the exploitation of solar light in a much broader spectral range (200–1200 nm), compared to the bare titania counterpart. We recorded highly effective exploitation of photogenerated charges in photocatalytic degradation of the well-known water contaminant CIP. The best-performing sample reached 82% of degradation efficiency under simulated solar light irradiation at room temperature and atmospheric pressure. We showed that the hydrogenation degree, related to the presence of oxygen vacancies on the catalyst's surface, seems to lead to an increase in the optical absorption and the overall photocatalytic activity of the samples. We showed also that hydrogenation undoubtedly introduces defects that are not present in pristine THS, as monitored by magnetic resonance. Benefitting from the design, the recorded functionality, and the understanding of physico-chemical properties of these materials, colored THS may offer a promising strategy to obtain novel and efficient photocatalysts. Therefore, this work provides inspiration to produce a cheap, environmentally friendly, stable, and efficient photocatalyst, which holds a great potential for the development of new technologies not only for water remediation applications but also for energy applications in the field of solar fuel production.

4. Experimental Section

Materials: The following commercial reagents, without any further purification, were used in all the experimental phases: milli-Q water (H_2O); nitrogen gas (N_2); methyl methacrylate (MMA, Merck ≥ 99.0%); 2,2′-azobis (2-methylpropionamidine) dihydrochloride (azobis, Merck 97%); deionized water (H_2O); ethanol absolute (EtOH, Merck ≥ 99.5%); titanium(IV) butoxide (TBOT, Merck 97%); ammonia solution 28%w (NH_3, Merck ≥ 99.9%); sodium borohydride ($NaBH_4$, Merck ≥ 98%); argon (Ar, Merck ≥ 99.998%); methylene blue (MB, Merck ≥ 82%); CIP (CIP, Merck ≥ 98%); Titanium(IV) oxide (TiO_2 Reference, Anatase, Merck ≥ 99.5%).

Synthesis of White TiO_2 Hollow Spheres: The synthesis of white TiO_2 hollow (W_THS) spheres involved a hard template-based approach. The first step was the synthesis of PMMA templating spheres. Briefly, MMA (12.5 wt.%) was dispersed in Milli-Q water under vigorous magnetic stirring (700 rpm), bubbling N_2 (g). Subsequently, the mixture was heated up to 80 °C and the azobis initiator (0.19 wt.%) was added. The reaction was carried out for 2 h, producing colloidal PMMA spheres. The reaction was rapidly stopped by cooling in an ice bath and the resulting PMMA spheres were separated by centrifugation (4000 rpm for 25 min). They were washed with deionized water and ethanol repeatedly. Finally, the product was dried in the air overnight.

The second step involved the coating of the sacrificial template using a titanium precursor to obtain a TiO_2@PMMA core-shell system. Specifically, 1 wt.% PMMA spheres were dispersed in absolute ethanol and sonicated for 20 min. The system was heated to 45 °C and stirred at 500 rpm. 0.1 wt.% of the ammonia solution and 1.5 wt.% TBOT were added, and the reaction was carried out for 24 h. The resulting product was collected by centrifugation and washed with deionized water and ethanol several times.

The removal of PMMA-templates and the calcination process are the last steps to produce THSs. In detail, the core-shell spheres were thermally treated at 500 °C for 2 h (ramp rate 2 °C min^{-1}) in airflow and W_THSs were obtained.

Synthesis of Colored TiO_2 Hollow Spheres: To obtain colored THSs, W_THS and $NaBH_4$ were mixed in different ratios and grounded for 20 min thoroughly. Then, the product was placed in a tubular furnace, ready for the chemical vapor deposition (CVD) technique. Inside the CVD, the powder was thermally treated at 350 °C under Ar atmosphere (flow rate 150 sccm) for 60 or 80 min (heating rate 10°C min^{-1}), according to the desired samples. After cooling to room temperature, the colored THSs were accurately rinsed several times with deionized water and ethanol to remove unreacted $NaBH_4$, and finally dried at 70 °C overnight. Samples were labeled as X_THSn, where X was referred to the color of the sample: W (white), G (gray), DG (dark gray) and n was the CVD-annealing time when it was not 60 min.

G_THSs were obtained using a weight ratio between $NaBH_4$ and W_THS of 3 to 8, respectively, and a 60 min CVD-annealing time. DG_THS and DG_THS80 samples were synthesized through the same operating conditions but using a weight ratio between $NaBH_4$ and W_THS of 1 to 2 and, in the case of DG_THS80 a CVD-annealing time of 80 min.

Characterization Techniques: Field-emission scanning electron microscopy (FESEM) was performed with Zeiss SUPRA 40 instruments. All micrographs were taken at a 5 kV electron gun accelerating voltage. High-resolution transmission electron microscopy (HRTEM), and energy dispersive X-ray analysis (EDX) elemental mapping were carried out on a FEI Talos F200S scanning/transmission electron microscope (S/TEM) at an acceleration voltage of 200 kV. The average grain size distribution was determined by grain size analysis software evaluation. The X-ray diffraction (XRD) analyses were carried out with PanAnalytical Empyrean XRD, equipped with Cu kα radiation. The scan rate was 2°min^{-1}. X-Ray diffraction patterns were collected in the range 10–80 2θ degrees. For sample identification, diffraction patterns were matched to the JCPDS database.

Fourier Transform Infrared Spectroscopy (FT-IR) was led using a Perkin-Elmer Spectrum 1000 spectrometer equipped with a Platinum Diamond attenuated total reflectance (ATR). FT-IR spectra were collected in the range 4000–400 cm^{-1}.

UV–is-NIR diffuse reflectance (DRUV-vis-NIR) spectra were collected with a Perkin Elmer Lambda 1050+ UV–vis-NIR spectrophotometer, equipped with an integrating sphere, for wavelengths ranging from 200 to 1200 nm. The bandgap (E_g) was determined using the Kubelka–Munk approach (Equation 1).[44]

$$F(R_\infty) = \frac{(1-R_\infty)^2}{2R_\infty} = \frac{K}{S} \quad (1)$$

Here, $F(R_\infty)$ is the Kubelka–Munk function, R_∞ is the diffuse reflectance, K is the absorption coefficient, and S is the scattering coefficient. Then by exploiting the Tauc method,[45] the bandgap for TiO_2 semiconductors can be expressed using the following equation Equation 2:

$$\left(F(R_\infty)h\nu\right)^{\frac{1}{2}} = B\left(h\nu - E_g\right) \quad (2)$$

Here, h is the Planck's constant, ν is the frequency of the light and B is a constant. By plotting $F(R_\infty)$ versus the energy expressed in eV, and

by finding the x-axis intersection point of the linear fit of the Tauc plot, it is possible to estimate the bandgap of a material.[45]

The XPS measurements were carried out at the VUV-Photoemission beamline of the synchrotron Elettra (Trieste, Italy).

Electron paramagnetic resonance investigations were performed with a Bruker Elexsys E580 instrument equipped with a standard X-band cylindrical cavity (ER-4118X-MD5). The powder samples were introduced in fused quartz EPR tubes. g factor values around $g = 2$ were calibrated with an α-α'-diphenyl-β-picryl-hydrazyl (DPPH) standard ($g = 2.0036 \pm 0.0003$), while for the large scan in Figure S9 (Supporting Information), the applied correction consisted in a linear extrapolation of the $g = 2$ correction and no correction at zero magnetic fields. Analysis routines made use of the EASYSPIN software for MATLAB™.[46] In particular, a first-stage analysis introducing background, OV, and Ti^{3+} centered in the fitting model showed structured residuals for all hydrogenated samples, in the form of an axially symmetric powder pattern which was thus introduced into the model. Experimental issues did not allow to extract the spin concentration of the different samples in the spectra, though relative quantitative considerations could be performed and are described in the main text and in the Supporting Information.

Photocatalytic Tests: The degradation of ciprofloxacin (CIP), an antibiotic, was chosen as a test reaction to evaluate the photocatalytic activity of the synthesized materials under solar simulated light and both UV and visible (vis) light irradiation to evaluate wavelength dependences of photocatalytic activity at several different wavelengths. The UV and vis photocatalysis reactions took place in a reactor system, where six sets of 6 W UV-B lamps (Sankyo, Japan) for UV irradiation (365 nm) and a 13 W visible sodium lamp (Osram, Germany) for visible light irradiation were used. The main photocatalytic test was carried out under Sunlight Solar Simulator, AM1.5G filter, 100 W Xenon arc lamp (Abet Technologies, USA). During the photocatalysis, the reactor was positioned under the solar lamp at a suitable distance to obtain a power of 1 sun (1350 W m^{-2}). The photon flux was measured by using a Si-based reference solar cell #15 150 (Abet Technologies, USA) leaned against the external wall of the photoreactor containing only pure water. A 100 mL cylindrical concentric Pyrex-quartz photocatalytic reactor was employed. The initial concentration of the target molecule was 2×10^{-5} M and the amount of photocatalyst was fixed at 125 mg L^{-1}. The photodegradation tests were performed at r.t. and P_{atm} and at solution's pH (pH = 5). Prior to irradiation, the solutions were put in dark for 60 min to reach the adsorption equilibrium. At given time intervals, 1 mL of solution was collected from the reactor, filtered through a 0.45 mm PTFE Millipore disc to remove the catalyst powder, and used for successive UV–vis spectroscopy analysis. A Perkin Elmer Lambda 1050+ UV–vis-NIR was used for these measurements. The degradation processes were observed following the maximum of absorbance (273 nm for CIP) in the UV–vis spectrum of the target molecule. Then, once calculated the concentration at this specific wavelength using the Lambert-Beer law, it was possible to calculate the degradation rate $\frac{C}{C_0}$, where C is the concentration after time t and C_0 represents the initial concentration at $t = 0$. Kinetics study involved in the CIP molecules photodegradation was carried out evaluating the data interval from 0 to 60 min and adopting the pseudo-first-order model:

$$ln\frac{C}{C_0} = -kt \tag{3}$$

where k is the pseudo-first-order rate constant (min^{-1}), calculated as

$$k = 2.303 \times \text{slope} \tag{4}$$

To evaluate the stability and reusability of the photocatalysts, a 3-cycle recycling test was performed. The best-performing sample was collected by centrifugation, washed with deionized water several times, and dried overnight after each photocatalytic cycle.

The main active species in the CIP degradation were investigated by performing the free radical trapping experiments. Briefly, three different photocatalytic tests were carried out using the same conditions as before but adding to the reaction system tert-Butanol (tBuOH, 1 mM), oxalic acid (OA, 1 mM) and N_2 (g) as OH, holes, and O_2^- scavengers, respectively.

Supporting Information

Supporting Information is available from the Wiley Online Library or from the author.

Acknowledgements

This work was carried out within the agreement "Convenzione operativa per collaborazione scientifica tra CNR ISM e Dipartimento di Scienze Molecolari e Nanosistemi Università Cà Foscari Venezia (Prot.n. 709, 14/04/2021)". Partial support through the project EUROFEL-ROADMAP ESFRI was gratefully acknowledged. The Kempe Foundation and the Knut och Alice Wallenberg Foundation were acknowledged for financial support. Elettra Sincrotrone Trieste was acknowledged for providing access to its synchrotron radiation facilities and for financial support under the SUI international project.

Conflict of Interest

The authors declare no conflict of interest.

Data Availability Statement

The data that support the findings of this study are available from the corresponding author upon reasonable request.

Keywords

colored-TiO_2, hierarchical nanostructures, hollow spheres, multiple reflections, photocatalysts, solar light, surface defects

Received: October 27, 2022
Revised: January 29, 2023
Published online:

[1] T. A. Shifa, F. Wang, Z. Cheng, P. He, Y. Liu, C. Jiang, Z. Wang, J. He, *Adv. Funct. Mater.* **2018**, *28*, 1800548.
[2] H. Luo, J. Barrio, N. Sunny, A. Li, L. Steier, N. Shah, I. E. L. Stephens, M. Titirici, *Adv. Energy Mater.* **2021**, *11*, 2101180.
[3] H. Zhang, C. Li, L. Lyu, C. Hu, *Appl. Catal. B* **2020**, *270*, 118874.
[4] M. Telkhozhayeva, B. Hirsch, R. Konar, E. Teblum, R. Lavi, M. Weitman, B. Malik, E. Moretti, G. D. Nessim, *Appl. Catal., B* **2022**, *318*, 121872.
[5] E. Moretti, E. Cattaruzza, C. Flora, A. Talon, E. Casini, A. Vomiero, *Appl. Surf. Sci.* **2021**, *553*, 149535.
[6] E. E. Mitsika, C. Christophoridis, N. Kouinoglou, N. Lazaridis, C. K. Zacharis, K. Fytianos, *J. Hazard. Mater.* **2021**, *403*, 123819.
[7] S. Wu, Y. H. Hu, *Chem. Eng. J.* **2021**, *409*, 127739.
[8] C. Alberoni, I. Barroso-Martín, A. Infantes-Molina, E. Rodríguez-Castellón, A. Talon, H. Zhao, S. You, A. Vomiero, E. Moretti, *Mater. Chem. Front.* **2021**, *5*, 4138.
[9] J. L. Wilkinson, A. B. A. Boxall, D. W. Kolpin, K. M. Y. Leung, R. W. S. Lai, D. Wong, R. Ntchantcho, J. Pizarro, J. Mart, S. Echeverr,

J. Garric, A. Chaumot, P. Gibba, I. Kunchulia, S. Seidensticker, G. Lyberatos, J. M. Morales-salda, H. Kang, *Proc. Natl. Acad. Sci. USA* **2022**, *119*, e2113947119.
[10] D. Ma, H. Yi, C. Lai, X. Liu, X. Huo, Z. An, L. Li, Y. Fu, B. Li, M. Zhang, L. Qin, S. Liu, L. Yang, *Chemosphere* **2021**, *275*, 130104.
[11] I. Concina, Z. H. Ibupoto, A. Vomiero, *Adv. Energy Mater.* **2017**, *7*, 1700706.
[12] J. Liu, N. Ma, W. Wu, Q. He, *Chem. Eng. J.* **2020**, *393*, 124719.
[13] L. Jiang, S. Zhou, J. Yang, H. Wang, H. Yu, H. Chen, Y. Zhao, X. Yuan, W. Chu, H. Li, *Adv. Funct. Mater.* **2022**, *32*, 2108977.
[14] X. Liu, G. Zhu, X. Wang, X. Yuan, T. Lin, F. Huang, *Adv. Energy Mater.* **2016**, *6*, 1600452.
[15] J. Xiong, J. Di, J. Xia, W. Zhu, H. Li, *Adv. Funct. Mater.* **2018**, *28*, 1801983.
[16] L. Liccardo, E. Lushaj, L. Dal Compare, E. Moretti, A. Vomiero, *Small Sci.* **2022**, *2*, 2100104.
[17] Y. Wang, J. Cai, M. Wu, H. Zhang, M. Meng, Y. Tian, T. Ding, J. Gong, Z. Jiang, X. Li, *ACS Appl. Mater. Interfaces* **2016**, *8*, 23006.
[18] W. Hu, W. Zhou, K. Zhang, X. Zhang, L. Wang, B. Jiang, G. Tian, D. Zhao, H. Fu, *J. Mater. Chem. A* **2016**, *4*, 7495.
[19] Y. Wang, K. I. Saitow, *Chem. Mater.* **2020**, *32*, 9190.
[20] X. Chen, L. Liu, P. Y. Yu, S. S. Mao, *Science* **2011**, *331*, 746.
[21] T. Xia, Y. Zhang, J. Murowchick, X. Chen, *Catal. Today* **2014**, *225*, 2.
[22] T. S. Rajaraman, S. P. Parikh, V. G. Gandhi, *Chem. Eng. J.* **2020**, *389*, 123918.
[23] B. Gupta, N. Kumar, K. Panda, V. Kanan, S. Joshi, I. Visoly-Fisher, *Sci. Rep.* **2017**, *7*, 45030.
[24] I. Luciu, R. Bartali, N. Laidani, *J. Phys. D* **2012**, *45*, 345302.
[25] X. Pan, M. Q. Yang, X. Fu, N. Zhang, Y. J. Xu, *Nanoscale* **2013**, *5*, 3601.
[26] J. J. Yeh, I. Lindau, *At. Data Nucl. Data Tables* **1985**, *32*, 1.
[27] X. Hu, X. Hu, Q. Peng, L. Zhou, X. Tan, L. Jiang, C. Tang, H. Wang, S. Liu, Y. Wang, Z. Ning, *Chem. Eng. J.* **2020**, *380*, 122366.
[28] D. Liang, C. Cui, H. Hub, Y. Wang, S. Xu, B. Ying, P. Li, B. Lu, H. Shen, *J. Alloys Compd.* **2014**, *582*, 236.
[29] M. M. Kumar, S. Badrinarayanan, M. Sastry, *Thin Solid Films* **2000**, *358*, 122.
[30] S. A. Khan, Z. Arshad, S. Shahid, I. Arshad, K. Rizwan, M. Sher, U. Fatima, *Compos. B Eng.* **2019**, *175*, 107120.
[31] M. Chiesa, S. Livraghi, E. Giamello, E. Albanese, G. Pacchioni, *Angew. Chem.* **2017**, *129*, 2648.
[32] M. Chiesa, M. C. Paganini, S. Livraghi, E. Giamello, *Phys. Chem. Chem. Phys.* **2013**, *15*, 9435.
[33] A. Naldoni, M. Altomare, G. Zoppellaro, N. Liu, Š. Kment, R. Zbořil, P. Schmuki, *ACS Catal.* **2019**, *9*, 345.
[34] I. Caretti, M. Keulemans, S. W. Verbruggen, S. Lenaerts, S. van Doorslaer, *Top. Catal.* **2015**, *58*, 776.
[35] S. Indris, R. Amade, P. Heitjans, M. Finger, A. Haeger, D. Hesse, W. Grünert, A. Börger, K. D. Becker, *J. Phys. Chem. B* **2005**, *109*, 23274.
[36] X. Li, P. L. Yue, C. Kutal, *New J. Chem.* **2003**, *27*, 1264.
[37] A. Yermakov, D. Boukhvalov, M. Uimin, V. Mesilov, A. Minin, V. Galakhov, A. Korolyov, A. Volegov, E. Rosenfeld, A. Gubkin, L. Molochnikov, *J. Phys.: Conf. Ser.* **2019**, *1389*, 012026.
[38] X. Wei, J. Chen, Q. Xie, S. Zhang, L. Ge, X. Qiao, *Environ. Sci. Technol.* **2013**, *47*, 4284.
[39] L. Y. Ozer, H. Apostoleris, F. Ravaux, S. I. Shylin, F. Mamedov, A. Lindblad, F. O. L. Johansson, M. Chiesa, S. Jacinto, G. Palmisano, *ChemCatChem* **2018**, *10*, 2949.
[40] M. Sarafraz, M. M. Amini, M. Adiban, A. Eslami, *Mater. Sci. Semicond. Process.* **2020**, *120*, 9.
[41] X. Wang, L. Mayrhofer, M. Hoefer, S. Estrade, L. Lopez-Conesa, H. Zhou, Y. Lin, F. Peiró, Z. Fan, H. Shen, L. Schaefer, M. Moseler, G. Braeuer, A. Waag, *Adv. Energy Mater.* **2019**, *9*, 1900725.
[42] Z. Li, S. Wang, J. Wu, W. Zhou, *Renewable Sustainable Energy Rev.* **2022**, *156*, 111980.
[43] L. N. Costa, F. X. Nobre, A. O. Lobo, J. M. E. de Matos, *Environ. Nanotechnol. Monit. Manage.* **2021**, *16*, 100466.
[44] P. Kubelka, F. Munk, *Z. Tech. Phys.* **1931**, *12*, 593.
[45] P. Makuła, M. Pacia, W. Macyk, *J. Phys. Chem. Lett.* **2018**, *9*, 6814.
[46] S. Stoll, A. Schweiger, *J. Magn. Reson.* **2006**, *178*, 42.

Paper-II

L. Liccardo, P. Moras, P. M. Sheverdyaeva, A. Vomiero, A. Caballero, G. Colón, E. Moretti, Surface Defect Engineered Nano-Cu/TiO_2 Photocatalysts for Hydrogen Production. *Adv. Sustainable Syst.* 2023, 2300418. https://doi.org/10.1002/adsu.202300418

ADVANCED SUSTAINABLE SYSTEMS
www.advsustainsys.com

Surface Defect Engineered Nano-Cu/TiO_2 Photocatalysts for Hydrogen Production

Letizia Liccardo, Paolo Moras, Polina M. Sheverdyaeva, Alberto Vomiero, Alfonso Caballero, Gerardo Colón, and Elisa Moretti**

Surface defects engineered nano-Cu/TiO_2 photocatalysts are synthesized through an easy and cost-effective microwave-assisted hydrothermal synthesis, mixing commercial P25 titania (TiO_2) and oxalic acid (Ox), followed by 2.0 wt% Cu co-catalyst (labeled as $Cu_{2.0}$) loading through in situ photodeposition during reaction. The hydrothermal treatment does not affect the catalyst crystalline structure, morphology, nor the surface area. However, depending on the Ox/TiO_2 molar ratio used an influence on the optical properties and on the reactivity of the system is detected. The presence of surface defects leads to intraband states formation between valence band and conduction band of bare titania, inducing an important enhancement in the photoactivity. Thus, $Cu_{2.0}$/gOx/P25 200 (where g is the weight of Ox and 200 the temperature in Celsius degrees used during the synthesis) have been successfully tested as efficient photocatalysts for hydrogen production through methanol (MeOH) reforming under UV light in a MeOH/ H_2O solution (10% v/v) by fluxing the system with N_2, showing an increased reactivity compared to the bare $Cu_{2.0}$/P25 system.

1. Introduction

The global energy crisis caused by the latest events is having far-reaching implications and natural gas is center stage. The average cost of electricity is greatly increasing and high prices for both fossil fuels and natural gas are the main cause.[1] In a possible scenario, energy demand will rise dramatically, thus people may not be able to afford modern electricity, reverting to the use of traditional biomass and by soaring greenhouse gas emissions into atmosphere. Oil and coal are only a poor and short-term option, and the crisis may be seen as a boost for low-emission alternatives.[2]

As a result, the clean-energy economy is emerging and hydrogen, thanks to its potential as a clean and energy vector, is considered an ideal candidate, playing a crucial role within this transition process. Furthermore, hydrogen can be produced from a variety of processes and feedstocks, including renewable resources such as biomass or water by using renewable energy sources such as solar light.[3] Sunlight is the most abundant renewable source, and it can provide energy to our earth, which is significantly larger than the daily total global energy consumption. Researchers have been focused on H_2 production through solar water splitting methods.[4] However, the efficiency values for their practical use are still too low.[5] In this frame, H_2 production from alcohol photocatalytic reforming reaction is one of the most suitable alternatives in the field of heterogenous photocatalysis.[5] In general, well-designed semiconductor photocatalysts with tailored properties are needed. The main drawbacks that hamper the development at a large-scale concern indeed the catalyst performance. As a matter of fact, back-reactions, the fast photogenerated charge-carriers recombination or the deactivation of the catalyst due to poor stability, are the main issues to overcome their practical exploitation.[6,7]

Thanks to its unique properties and versatility, titania has always been considered an ideal candidate for photocatalytic application such as H_2 production from alcohol photo reforming. However, its wide bandgap (3.0–3.2 eV) that hinders the use of full solar light spectrum, combined with all the aforementioned deficiencies are limiting its practical use.[3,8] Furthermore, large specific surface area, high crystallinity and anatase phase are known to increase photocatalytic activity. Intense investigations

L. Liccardo, A. Vomiero, E. Moretti
Department of Molecular Sciences and Nanosystems
Ca' Foscari University of Venice
Via Torino 155, Venezia Mestre 30172, Italy
E-mail: elisam@unive.it

P. Moras, P. M. Sheverdyaeva
Istituto di Struttura della Materia-CNR (ISM-CNR)
SS 14, Km 163.5, Trieste 34149, Italy

A. Vomiero
Division of Materials Science
Department of Engineering Sciences and Mathematics
Luleå University of Technology
Luleå 97187, Sweden

A. Caballero, G. Colón
Instituto de Ciencia de Materiales de Sevilla
Centro Mixto Universidad de Sevilla-CSIC
Américo Vespucio 49, Sevilla 41092, Spain
E-mail: gcolon@icmse.csic.es

The ORCID identification number(s) for the author(s) of this article can be found under https://doi.org/10.1002/adsu.202300418

DOI: 10.1002/adsu.202300418

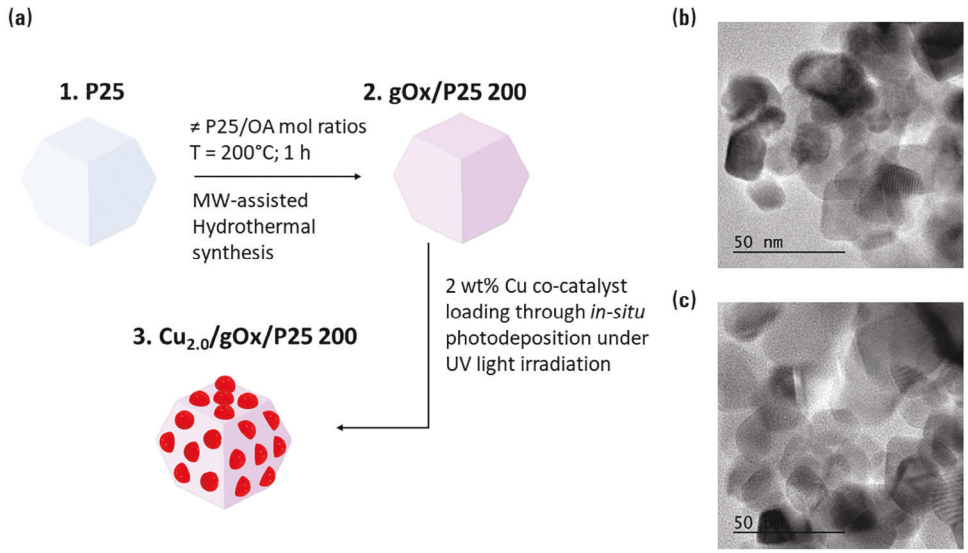

Figure 1. a) Synthesis scheme. TEM images of b) bare P25 and c) 2.5Ox/P25 200.

are still ongoing on different aspects of photocatalytic activity of TiO_2, which can be exploited to improve its performances, including doping and co-doping,[9] nanostructuring,[10] defect engineering,[11,12] reactor configuration,[13] heterostructuring,[14] among the others.

According to the reported literature, among several types of photocatalysts, commercial titania P25 from Evonik is often taken as target material since it shows excellent performance.[3] In fact, P25 is composed of a phase combination ratio between anatase and rutile and an average crystallite size of ≈20 nm, having all the features required to show good photoactivity, that can be further enhanced.[15,16] In general, a good strategy to increase TiO_2 efficiency is the tuning of its optical and electronic properties, by metal co-catalyst loading and simultaneously working on chemical surface composition.[8,15,17]

It is well known that the use of a metal co-catalyst can hinder the fast charge-carriers recombination but, in addition to this traditional strategy, surface defects engineering has been suggested as a novel approach to improve the overall photocatalytic efficiency. In fact, surface defects can induce modifications on the charge distribution around Ti and O, enhancing the separation of the photocarriers, promoting the sacrificial agent adsorption, and extending the light absorption range.[18]

In the present work, surface defect engineered nano-Cu/TiO_2 ($Cu_{2.0}$/gOx/P25 200) photocatalysts have been synthesized through an easy and cost-effective microwave (mw)-assisted hydrothermal synthesis, mixing commercial P25 and oxalic acid (Ox), followed by nominal 2.0 wt% metal co-catalyst (Cu) loading through chemical reduction deposition procedure (see **Figure 1a**). In detail, it is possible to obtain surface defects engineered commercial P25 nanoparticles combined with the use of Cu co-catalyst to improve the electron-hole separation and broaden the absorbance ability, thanks to the presence of mid-gap states below the TiO_2 conduction band, and the photocatalytic activity, thanks to high surface-to-volume ratio, stability of the crystalline structure and finally, enhancement of charge-carriers separation.

2. Results and Discussion

Surface defects engineered nano-TiO_2 photocatalysts were synthesized through an easy mw-assisted hydrothermal synthesis, mixing commercial P25 titania and Ox in different molar ratios (Ox/P25). Samples were labeled as gOx/P25 200, where *g* is the weight of oxalic acid and 200 the temperature (in Celsius degrees) used during the synthesis (Figure 1a step 1 and 2). Subsequently, nominal 2 wt% of Cu (labeled as $Cu_{2.0}$) co-catalyst was loaded through an in situ photodeposition when the photocatalytic tests under UV light irradiation (using a 365 nm UV LED array equipped in the photoreactor) were performed (Figure 1a step 3). In this first section, we report and deeply investigate gOx/P25200 samples, to better understand how the mw-treatment in combination with the oxalic acid can induce surface modifications.

2.1. Morphological and Structural Characterization

The crystal structure of the prepared materials was characterized by X-ray diffraction (XRD) and micro-Raman analysis. **Figure 2** shows the XRD patterns for gOx/P25200 samples, compared with commercial P25, taken as a reference, and the JCPDS cards 21–1276 (rutile) and 21–172 (anatase). As it can be noticed, all the gOx/P25200 samples displayed the typical pattern of commercial P25, including both rutile and anatase phases, which is more evident from the intense peaks located at 2θ 25.3°, 37.7°, 48.0°, 53.9°, and 55.02° corresponding to the (101), (004), (200), (105), and (211) reflections. The addition of oxalic acid during the hydrothermal treatment at 200 °C does not affect the overall crystal structure of commercial P25 which remains stable, as confirmed also by Raman analysis. In fact, as widely reported in literature, the six main Raman active modes for anatase TiO_2 (A_{1g} + $2B_{1g}$ + 3Eg symmetries) are commonly detected at 143, 196, 398, 519 (superimposed with 515 cm^{-1} band), 639 cm^{-1}, corresponding to E_g, E_g, B_{1g}, A_{1g}, B_{1g}, and E_g vibrational modes.[15,19] Moreover, as expected, rutile TiO_2 Raman active modes can only be foreseen

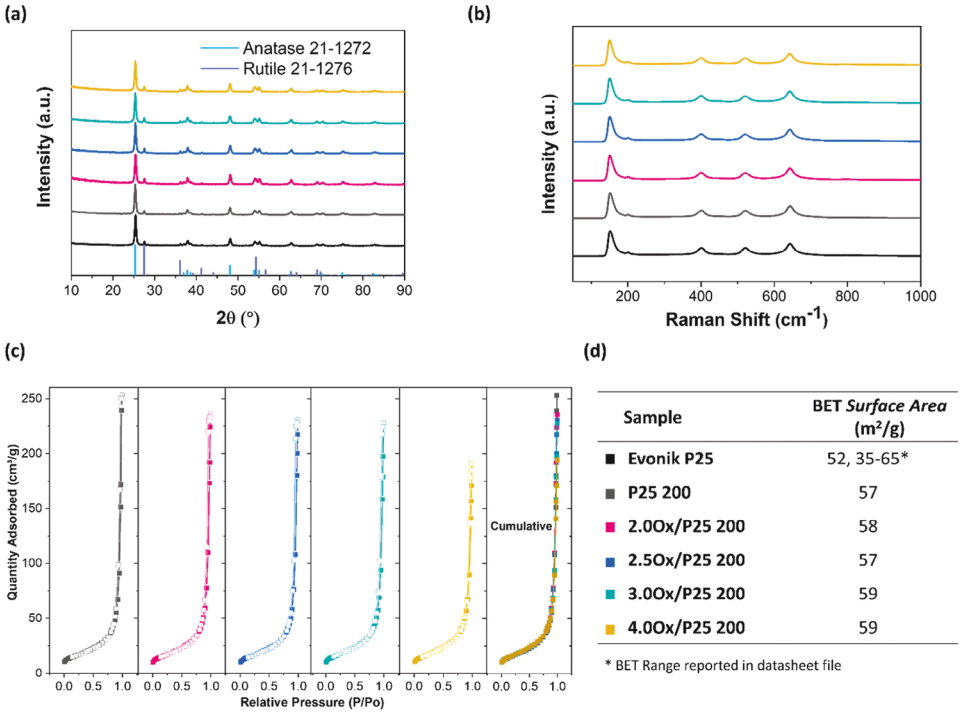

Figure 2. a) XRD patterns; b) Raman spectra; c) N_2 adsorption-desorption isotherms for P25 200 and gOx/P25 200 samples; d) BET surface area values for all the samples including the Evonik P25 reference. All the curves in (a–c) follow the color palette reported in (d).

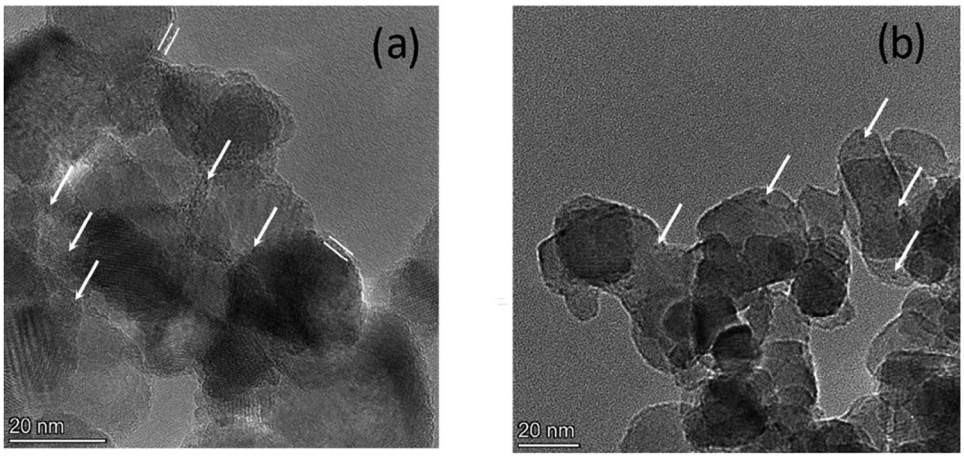

Figure 3. HRTEM images for a) $Cu_{2.0}$/3.0Ox/P25 200 and b) $Cu_{2.0}$/P25 200. In both the panels, the white arrows indicate Cu clusters.

at 140 (B_{1g}), 235 (multiphoton process), 445 (E_g), 609 (A_{1g}), and 825 cm^{-1} (B_{2g}) (Figure 2b).[20] gOx/P25200 samples showed the typical P25 Raman peaks, confirming no apparent changes in the crystal structure. From TEM micrographs (Figure 1b,c) and BET analysis (Figure 2c,d), we can observe that neither the shape nor the morphology and the textural properties of commercial P25 are influenced by the addition of Ox and subsequent hydrothermal treatment, suggesting only the presence of surface modifications. As evidenced in the table of Figure 2d, no relevant differences on the surface areas calculated from the N_2 adsorption-desorption isotherms are detected. In fact, Evonik P25 shows a measured surface area of 52 $m^2 \cdot g^{-1}$ in the range between 35 and 65 $m^2 \cdot g^{-1}$ (values reported in the data sheet file, as expected), which is similar to that of 4Ox/P25 sample (59 $m^2 \cdot g^{-1}$), treated with the highest amount of Ox during the mw-assisted synthesis.

In **Figure 3** we show the HRTEM images for $Cu_{2.0}$/P25 200 and $Cu_{2.0}$/3.0Ox/P25 200 catalysts. The first important issue we can highlight refers to the surface rugosity observed for oxalic acid treated sample (Figure 3a). It is evident that hydrothermal acid treatment leads to the formation of a well-defined amorphous shell of about 2–3 nm. This shell indicates the loss of crystallinity at surface level. Indeed, it is possible to see that anatase planes are

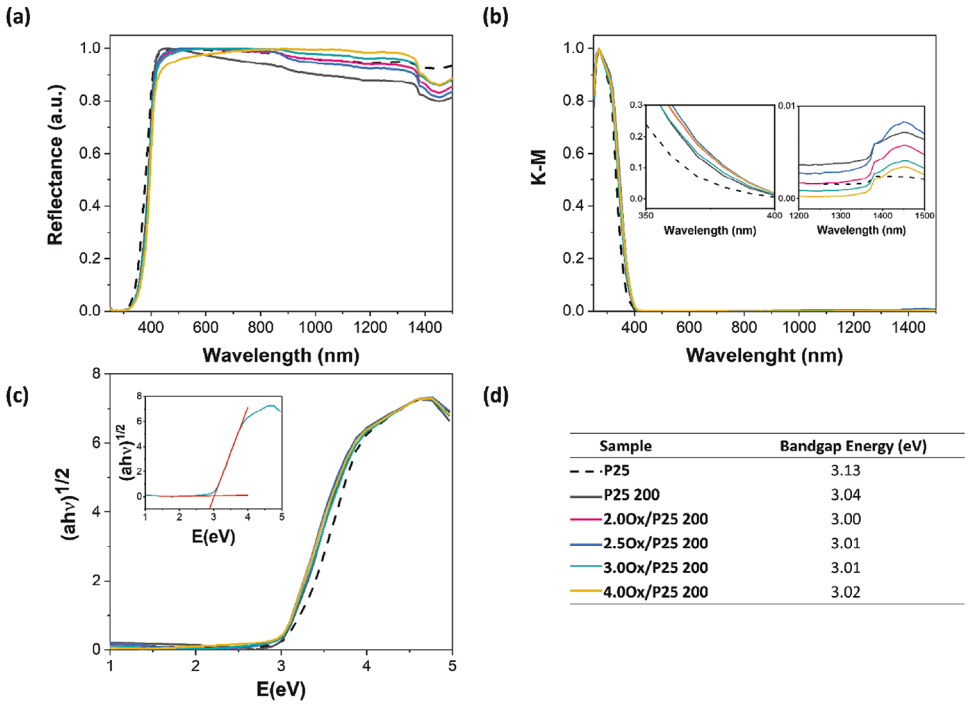

Sample	Bandgap Energy (eV)
P25	3.13
P25 200	3.04
2.0Ox/P25 200	3.00
2.5Ox/P25 200	3.01
3.0Ox/P25 200	3.01
4.0Ox/P25 200	3.02

Figure 4. a) DRUV-vis-NIR spectra; b) Kubelka–Munk functions with inset-graphs focusing on the band changes in UV and NIR region; c) Tauc plots and d) Bandgap energies comparison for all the samples, including Evonik P25 reference.

lost at the surface. This fact is not observed for TiO_2 hydrothermally treated with water, for which particles show flat borders (Figure 3b). Secondly, it is possible to see the effectiveness of copper photodeposition over both TiO_2 support (white arrows in the two panels of Figure 3). However, Cu clusters are more difficult to distinguish on $Cu_{2.0}$/3.0Ox/P25 200 since the cluster size is much smaller (1–2 nm vs 5–6 nm for $Cu_{2.0}$/3.0Ox/P25 200 and $Cu_{2.0}$/P25 200, respectively).

2.2. Optical Properties

All the diffuse reflectance UV–visible–near-infrared (DRUV-vis-NIR) spectra in **Figure** 4a are characterized by the main absorption feature related to the typical optical bandgap of the titania (≈3.1 eV), which induces a strong absorption edge ≈370 nm and is associated to the O^{2-} (2p) → Ti^{4+} (3d) transition. As previously reported, the structure and the morphology of gOx/P25 200 samples are not influenced by the addition of Ox, suggesting only the presence of surface modifications. In the DRUV-vis-NIR analysis, a very small but evident red-shift of the main band toward higher wavelength compared to the bare P25 reference has been detected. The introduction of Ox in combination with the hydrothermal treatment at 200 °C enables an increasing absorbance ability in the region between 350 and 400 nm compared to the bare P25 reference (Figure 4b). This may be ascribed to the presence of surface defects such as Ti^{3+} sites or oxygen vacancies, which result in the introduction of a continuous energy band directly below the conduction band (CB) edge of TiO_2.[18] This is also confirmed by a slight lowering of the bandgap energy values (≈0.1 eV), calculated through the Tauc plot by using the intercept method (Figure 4c,d).[21] Light absorption in the vis–NIR region can be improved by the presence of disordered surface layer or surface defects (i.e., oxygen vacancies).[22–24] Thus, NIR region has also been investigated (Figure 4a,b). Evident changes in all spectra compared to bare P25 can be detected. A wide band centered at 1450 nm and an increase in absorbance capacity from 850 nm occurred for some samples. The onset of the absorption feature at 1450 nm can be attributed to adsorption of water molecules onto the surface of the treated samples P25 200 and gOx/P25 200 with respect to the reference sample P25. In this case, both Ox and the treatment temperature seem to induce some surface modifications by changing the composition of functional groups exposed on the photocatalysts surface. In addition, a higher water adsorption may be ascribed to higher surface content of oxygen vacancies which tend to bind water.[8] This is also confirmed by XPS analysis (see section below).

Since emission processes in semiconductors are strictly related to photogenerated charge carriers recombination,[25] photoluminescence (PL) emission spectra for all gOX/P25 200 samples (including P25 reference) were collected in the range 380–600 nm by using an excitation wavelength of 350 nm (**Figure 5**). One of the most significant drawbacks of TiO_2 is its fast charge carriers recombination. The higher the recombination of free carriers, the higher the PL intensity and, as expected, the highest emission intensity was recorded for bare P25 (dashed black line in Figure 4). It is worth recalling that non-radiative recombination pathways may also occur lowering the overall PL intensity. However, considering similar non-radiative recombination channels for all the samples, the presence of surface defects or adsorbed water molecules seems to decrease the radiative recombination rate resulting in lower emission intensities for all the

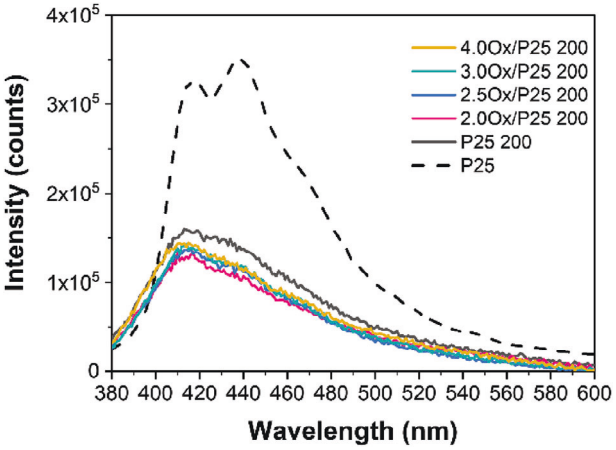

Figure 5. Photoluminescence spectra for all gOX/P25 200 samples, including Evonik P25 reference.

treated samples. Surface defects such as oxygen vacancies or Ti^{3+} act as trapping centers for the photo-excited electrons,[26] providing active sites for the electron transfer processes. Furthermore, the presence of OH groups or water molecules onto the metal oxide surface promotes the trapping phenomena by decreasing electron-hole pairs radiative recombination as well.[27] Consequently, the overall charge-carriers separation efficiency of the photocatalyst is enhanced.

2.3. XPS Analysis

Core level XPS data were acquired for the P25, P25 200 and gOx/P25 200 samples at $h\nu = 750$ eV (**Figure 6**). The O1s spectra were fitted with four components. From the low to the high binding energy side these components correspond to O^{2-} of stoichiometric TiO_2 (530.20 –530.40 eV), OH groups adsorbed on TiO_2 (531.60 –532.20 eV), O (532.65 –532.95 eV), and OH (534.05 –534.3 eV) groups bound to C,[28] which is a surface contaminant. The last component is also associated with the presence of H_2O [29] and displays the most notable increase along the sequence of spectra. This trend could be the fingerprint of an increasing density of surface oxygen vacancies, which tend to bind efficiently H_2O. The Ti2p spectra could be fitted with one doublet attributed to Ti^{4+}, while there is no evidence of defective Ti^{3+}. The O/Ti atomic ratio for the different materials can be derived from the area of the O^{2-} peak and the Ti^{4+} doublet normalized to the respective photoemission cross sections at $h\nu = 750$ eV (0.24 and 0.7[30]). It is evaluated to be 2.09 ± 0.09 for all samples, i.e., very close to the expected ratio 2. **Table 1** reports the Ti/O atomic ratios for all the samples. Moreover, as amount of oxalic acid increased the deconvoluted contributions at energies above 531 eV increases, denoting a higher hydroxylation of the surface leading to a progressively higher O/Ti.

The valence band spectra acquired at $h\nu = 468$ eV do not display sizable differences in the O2p-derived states (4 –9 eV binding energy). Within the gap region (zoom), O vacancy-related feature at 1.25 eV is observed to increase in intensity along the sequence of the P25, P25 200 and 2.0Ox/P25 200 samples. For the other three samples this feature broadens significantly and gives rise

Table 1. O/Ti ratio in the P25, P25 200 and gOx/P25 200 samples.

Sample	O/Ti ratio
P25	2.10
P25 200	2.05
2.0Ox/P25 200	2.02
2.5Ox/P25 200	2.12
3.0Ox/P25 200	2.17
4.0Ox/P25 200	2.12

to two peaks centered at 1.45 and 0.30 eV. This behavior can be associated with surface modifications induced by the treatments with oxalic acid, which give rise to the shell observed in Figure 3a. Although the present dataset does not allow to describe the microscopic origin of the new in-gap states, we observe that their location is compatible with defect states close to the bottom of the conduction band of TiO_2.

The XPS data were also acquired for the $Cu_{2.0}$/P25 and $Cu_{2.0}$/3.0Ox/P25 200 samples (**Figure 7**). In both cases, the binding energy of the Cu3p peaks ($Cu3p_{3/2}$ at 75.40 eV) and the absence of correlation features on the high binding energy side, which characterize CuO,[31] indicate the formation of Cu_2O on the surface of the Cu co-catalyst.[32] The O1s spectra differ from the corresponding O1s spectra before the addition of Cu (Figure 6) mainly in the relative weight of the peak at 530.40 eV, which derives from the overlapping O^{2-} components of TiO_2 and Cu_2O. The Ti2p spectra are very similar to those observed in Figure 6. The broad valence band feature at ≈4.00 eV is ascribed to the Cu3d states of the Cu_2O surface oxide. The photoemission signal from Cu4sp states, which overlaps to the bandgap region of the P25 and 3.0Ox/P25 200 substrates, does not allow to identify the presence of defect states in the proximity of the Fermi level.

2.4. Photocatalytic H_2 Production

The photocatalytic activity of gOx/P25200 samples was evaluated for the H_2 production through methanol reforming under UV light, at room temperature and P_{atm} by using a continuous flow reactor (Apria Systems). The H_2 production rates and the yield evolution over time referred to methanol photoreforming reaction are reported in **Figure 8**. Furthermore, in Figure 8d the band scheme for electron-hole separation of $Cu_{2.0}$/gOx/P25 200 catalysts has been proposed according to literature[26,27,33] and our deep investigation. As already mentioned, the nominal loading of 2.0 wt% (see Experimental Section for further details) of Cu as co-catalyst has been obtained through the in situ photoreduction at the beginning of the photocatalytic test. Thus, copper nanoparticles (Cu NPs) were formed after exciton creation by means of UV light irradiation, giving rise to oxidation and reduction reactions. During the photocatalytic reaction, it is expected that surface defects would play a crucial role. Thus, we may infer that they could act as trapping states for electrons enhancing the separation of photogenerated charge carriers and consequently, the reduction reactions rates, useful not only for the formation of Cu NPs on the surface of gOx/P25 200 catalysts, but also for the H_2 production. Hence, the first step occurring during the photocat-

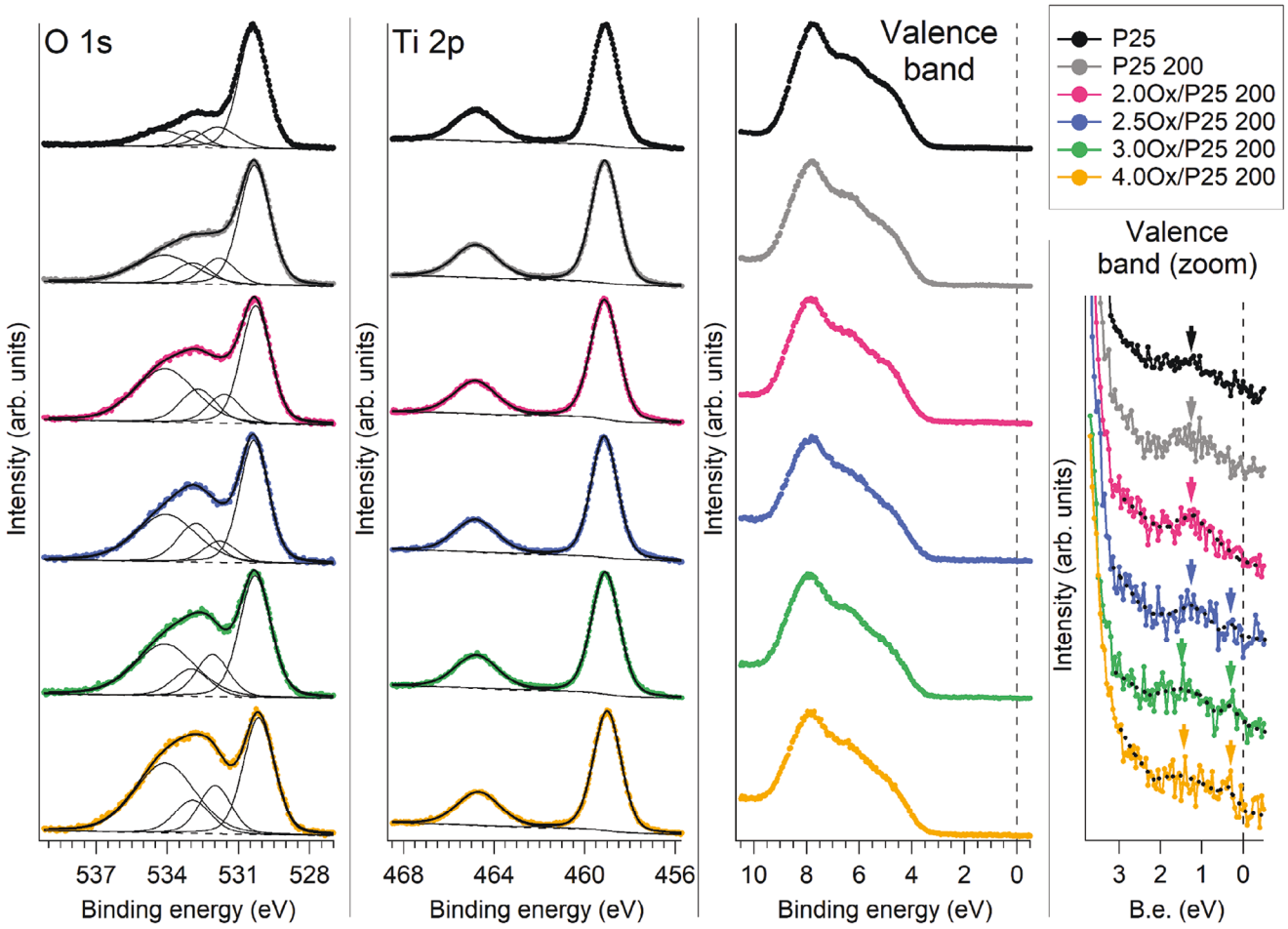

Figure 6. O1s, Ti2p and valence band spectra of the P25, P25 200 and gOx/P25 200 samples. The zoomed valence band spectra indicate the presence of defect states (arrows) in the gap of all samples. Dotted lines are guides to the eye for the identification of the defect-related peaks.

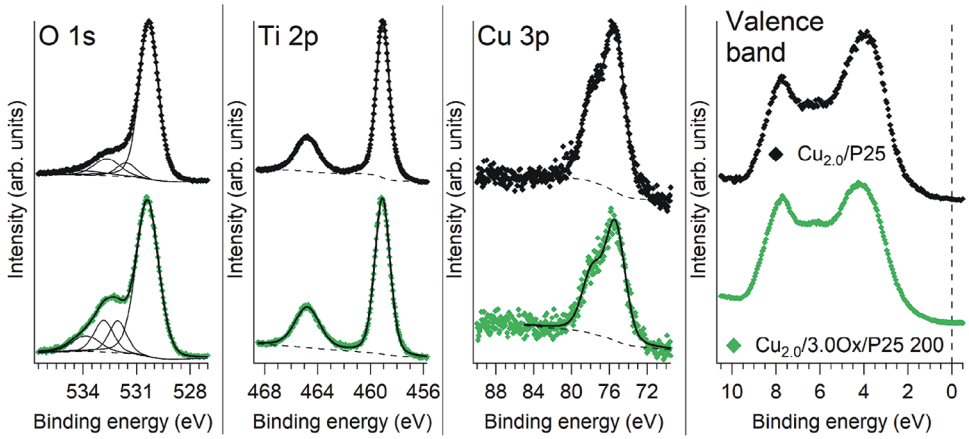

Figure 7. O1s, Ti2p, Cu3p ($h\nu = 750$ eV) and valence band ($h\nu = 469$ eV) spectra of the $Cu_{2.0}$/P25 (*top*) and $Cu_{2.0}$/3.0Ox/P25 200 (*bottom*) samples.

alytic H_2 production is the Cu NPs deposition, also confirmed by a 15-min delay on the H_2 production (see H_2 production rate curves in Figure 8a). The mw-treatment leads to a significant increase in photoreactivity when the loading of Ox during the synthesis is >2.0 g and <4.0 g. In fact, after 6 h of light irradiation, the optimized $Cu_{2.0}$/3Ox/P25200 sample exhibited outstanding photocatalytic H_2 production rates of 6.8 mmol·h^{-1}·g^{-1}, which is two times higher than that of pristine $Cu_{2.0}$/P25 system. Moreover, long-time reaction time for this catalyst shows a rather stable behavior (**Figure 9**). When the Ox loading is below 2.5 g or >3.0 g the

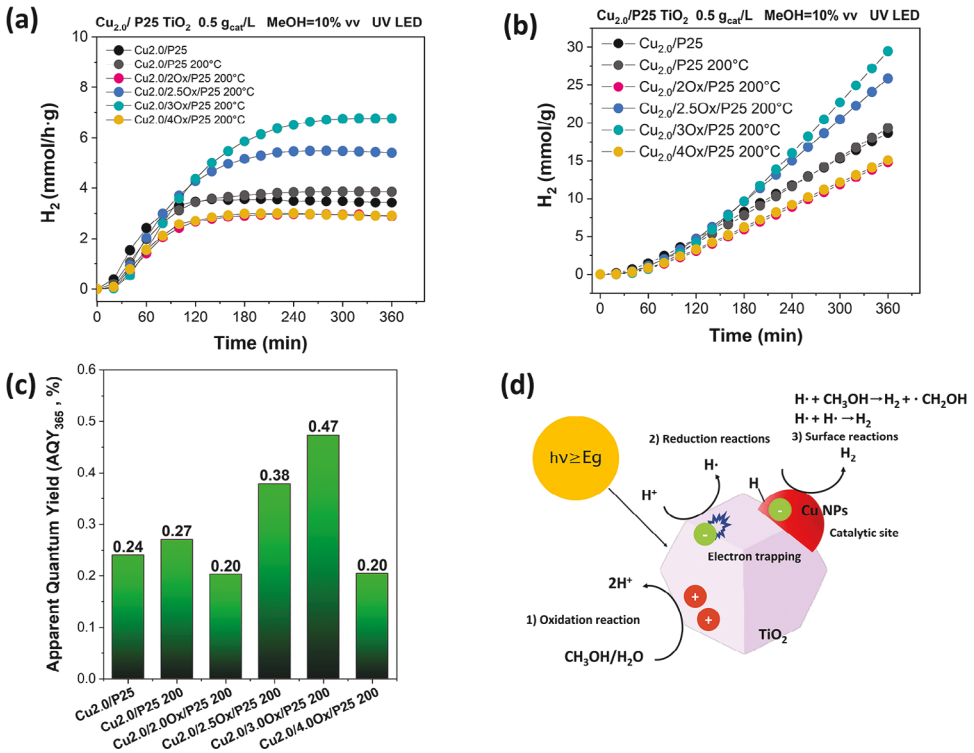

Figure 8. a) H_2 production rates; b) H_2 rates; c) calculated AQYs for $Cu_{2.0}$/P25 $Cu_{2.0}$/P25 200 and $Cu_{2.0}$/gOx/P25 200 photocatalysts; d) Scheme diagram of $Cu_{2.0}$/gOx/P25 200 system.

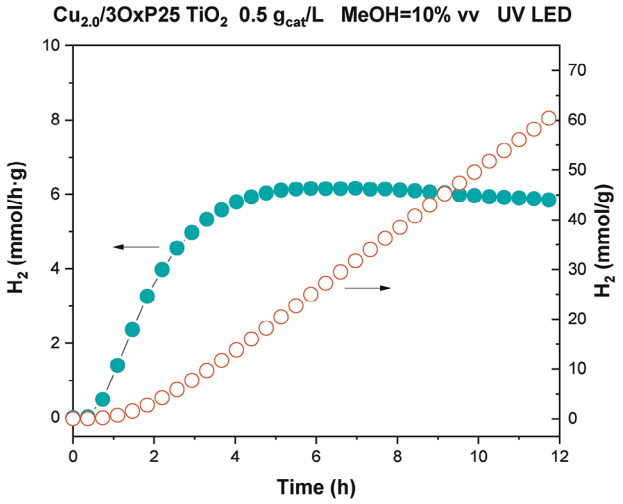

Figure 9. H_2 production rate and yield for $Cu_{2.0}$/3Ox/P25 200 photocatalysts system.

efficiency of the system decreases. This behavior is also marked by the H_2 yields at 6 h of experiment expressed in mmol•g^{-1} and the calculated AQY (Figure 8b,c). $Cu_{2.0}$/3Ox/P25200 is the best performing sample reaching an H_2 yield and an AQY of 29.5 mmol•g^{-1} and 0.47%, respectively, far exceeding $Cu_{2.0}$/P25. Furthermore, after 6 h of experiment the H_2 production reaction reached a steady-state (see the dwell in Figure 8a). Hence, the absence of deactivation during this studied reaction time pointed out the stability of catalyst surface defects.

It is worth mentioning that there are several studies in literature regarding the use of alcohol photoreforming to produce H_2 and each of them is reporting different conditions to optimize the production with their own catalyst/co-catalyst system. For instance, irradiation source, solution composition (water/alcohol ratio) and carrier gas flow are crucial parameters to tune H_2 production rates.[6,7] However, we tried to select some TiO_2/co-catalyst systems to provide a comparison with our samples to highlight their performances by choosing examples tested under similar conditions. Thus, a comparative table is reported (**Table 2**) listing the synthetic method used, the H_2 production rates and apparent quantum yield (AQY) of selected systems concerning the use of TiO_2 in combination with several co-catalysts for the H_2 production through methanol reforming.

As can be observed, the performances of our photocatalytic system are good compared to the listed examples. Furthermore, there is a good compromise between the obtained H_2 production rates, and the synthetic method used in this work. In fact, mw-assisted hydrothermal method followed by the in situ photodeposition can be an innovative way to design a novel and efficient photocatalyst for a future large-scale production.

3. Conclusion

In this work, we have reported an innovative synthesis to obtain a highly active photocatalyst based on the use of surface-defects engineering of TiO_2 in combination with Cu co-catalyst

Table 2. H_2 production rates and apparent quantum yield (AQY) for various TiO_2/co-catalyst systems, tested under similar conditions used in this work (methanol photoreforming reaction under UV light).

System	Co-cat.	Synthetic method	Solution	Irradiation Source	H_2 [mmol g^{-1}•h^{-1}]	AQY [%]	Ref.
1 wt% Pt/TiO_2	Pt	Hydrothermal synthesis in alkaline conditions followed by calcination at 500 °C	25 mL of a 6.7 vol% aqueous methanol solution	LED (λ = 365 nm, 0.438 μmol·s^{-1} of irradiance)	3.6[a)]	∽0.46	[34]
1 wt% NiO/TiO_2	NiO	sol–gel process combined with surfactant-assisted template followed by calcination at 500 °C	200 mL of a 10 vol% aqueous methanol solution	UV 300 W Mercury Lamp	0.8	-	[35]
1.5 wt% NiO/ Anatase TiO_2	NiO	sol–gel process combined with surfactant-assisted template followed by calcination at 500 °C	200 mL of a 10 vol% aqueous methanol solution	UV 300 W Mercury Lamp	0.6	-	[35]
0.4 wt% Au/P25	Au	6 h photodeposition under UV light	75 mL of a 25 vol% aqueous methanol solution	Solarium Philips HB175 lamp (365 nm)	0.4	4.14	[36]
1.5 wt% Au/rutile TiO_2	Au	Hydrothermal synthesis followed by deposition-precipitation with urea method	10 vol% aqueous methanol solution	Spectroline model SB-100P/F lamp (100 W, 365 nm)	0.9	-	[37]
0.5 wt% Au/P25	Au	deposition-precipitation with urea method	200 mL of aqueous methanol solution (1:1 molar ratio)	UV-PC Mercury lamp (2.2 mW·cm^{-2}, 254 nm)	1.9	-	[38]
3 wt% Ru/ TiO_2	Ru	Micro-emulsion method followed by deposition via sonication	50 mL of a 3/7 v/v methanol solution	500 W Xe lamp equipped with a cut-off filter (UV: 280–400 nm)	4.6	-	[39]
1 wt% Nd/ Anatase-brookite TiO_2	Nd	sol–gel method followed by pressurized hot fluids	100 mL of ≈50 vol% aqueous methanol solution	UV 8 W Mercury Lamp (365 nm)	0.7[a)]	-	[40]
6 wt% Bi_2S_3/TiO_2	Bi_2S_3	Sol–gel combined with solvothermal method	200 mL of aqueous methanol solution (1:1 mol ratio)	Mercury Lamp (2.2 mW cm^{-2}, 254 nm)	2.5[a)]	-	[41]
5 wt% Ga_2O_3/TiO_2	Ga_2O_3	Sol–gel and hydrolysis method	200 mL of aqueous methanol (50/50 v/v) solution	Mercury lamp (2.2 mW·cm^{-2}, 254 nm)	0.25[a)]	-	[42]
1 wt% CuO/F- TiO_2	CuO	Sol–gel method followed by impregnation	200 mL of aqueous methanol solution (1:1 v/v)	Mercury lamp (4.4 mW·cm^{-2}, 254 nm)	1.83[a)]	-	[43]
$Cu_{2.0}$/3Ox/P25 200 (optimum)		mw-hydrothermal treatment followed by in situ photodeposition	200 mL of a 10 vol% aqueous methanol solution	365 nm UV LED array	6.8	0.47	This work

[a)] Approximated values from published experimental data.

loaded through in situ photodeposition method. The obtained $Cu_{2.0}$/gOx/P25 200 photocatalysts have shown significant improvement in the photocatalytic H_2 production through methanol reforming reaction with the best-performing sample ($Cu_{2.0}$/3Ox/P25 200) exhibiting outstanding photocatalytic H_2 production rates under UV irradiation of 6.8 mmol·h^{-1}·g^{-1}, two times higher than that of pristine $Cu_{2.0}$/P25 system, as confirmed also by the calculated AQY. Thanks to the use of XPS and optical characterizations, we stated that such a marked increase in the performances of this system is related both to the presence of surface defects, in detail oxygen vacancies, and the use of Cu co-catalyst. In fact, surface defects engineered commercial P25 nanoparticles combined with Cu co-catalyst enable to improve electron-hole separation, broaden the absorbance ability, thanks to the presence of mid-gap states below the TiO_2 conduction band and consequently, increase the overall photocatalytic activity. In conclusion, tailoring the surface properties of commercial P25 might be a good strategy to overcome the fast charge carriers recombination limit of TiO_2 -based photocatalyst leading way for the development of new technologies in the field of energy applications at a large scale.

4. Experimental Section

Materials: The following commercial reagents, without any further purification, were used in all the experimental phases: deionized water (H_2O); commercial TiO_2 (Evonik AEROXIDE TiO_2 P25); oxalic acid (Ox, $H_2C_2O_4$, Sigma–Aldrich 99.0%); copper (II)-nitrate trihydrate ($Cu(NO_3)_2$·$3H_2O$, Merck ≥ 99.0%); methanol (MeOH, Merck ≥ 99.5%).

Photocatalyst Preparation: Surface defects P25 photocatalysts were synthesized by microwave-assisted hydrothermal reaction, mixing commercial P25 and oxalic acid. In a typical synthesis procedure, an aqueous dispersion of P25 was prepared under magnetic stirring. Oxalic acid was added with fixed mole ratios (n/n) between Ox and P25 of 3.7, 4.5, 5.4, and 7.2, respectively. After 30 min stirring, the dispersion was transferred into a 100 mL Teflon-lined microwave reactor and heated at 200 °C and 600 W for 1 h. After cooling to room temperature, the precipitate was separated from the reaction mixture by filtration and washed several times with distilled water. Finally, the obtained specimen was dried in oven at 80 °C overnight. Samples were labeled as gOx/P25200 where *g* refers to the grams of oxalic acid and 200 to the temperature used (i.e., 2Ox/P25 200). To better understand the role of oxalic acid, and the influence of the temperature on bare P25, the same procedure without the addition of Ox was followed, thus obtaining sample for comparison labeled as P25 200. The co-catalyst was loaded on gOx/P25200 surface samples through in situ photoreduction during the first step of the photocatalytic reaction. By this procedure, Cu was well dispersed over the TiO_2 surface showing a particle size of ca. 2–4 nm.[44] In detail, 2 wt% of Cu^{2+} with respect to the catalyst (using a solution of $Cu(NO_3)_2$·$3H_2O$ 0.01 M) was directly added to the MeOH/H_2O solution used for the photocatalytic H_2 production under UV irradiation. Samples were labeled as $Cu_{2.0}$/gOx/P25 200. The deposited Cu loading was determined through the use of a Microwave Plasma-Atomic Emission Spectrometer (Agilent MP-AES 4210) for $Cu_{2.0}$/P25, $Cu_{2.0}$/P25 200, and $Cu_{2.0}$/3Ox/P25 200. Data were acquired after five readings and the mean value was 1.8 wt% for all the samples.

Characterization Techniques: The transmission electron microscopy (TEM) images were obtained by using a FEI S/TEM Talos F200S in the HRTEM mode. The samples were directly dropped on a gold grid.

X-ray diffraction (XRD) patterns were obtained using a Siemens D-501 diffractometer with a Ni filter and a graphite monochromator. The X-ray source was Cu Kα radiation.

For sample identification, diffraction patterns were matched to the JCPDS database.

Micro-Raman spectra were collected using a LabRAM Jobin Yvon spectrometer equipped with a microscope. Laser radiation (λ = 532 nm) was used as an excitation source at 5 mW. All measurements were recorded under the same conditions (2 s of integration time and 30 accumulations) using a 100× magnification objective and a 125 mm pinhole.

Brauner–Emmett–Teller (BET) surface area studies were carried out by N_2 physisorption at −196 °C using a Micromeritics 2000 instrument.

UV–vis–NIR diffuse reflectance (DRUV–vis–NIR) spectra were collected with a Perkin Elmer Lambda 1050+ UV–vis–NIR spectrophotometer, equipped with an integrating sphere, for wavelengths ranging from 200 to 1200 nm. The bandgap (E_g) was determined using the Kubelka–Munk approach (Equation (1)).[21]

$$F(R_\infty) = \frac{(1-R_\infty)^2}{2R_\infty} = \frac{K}{S} \quad (1)$$

Here, $F(R_\infty)$ is the Kubelka–Munk function, R_∞ is the diffuse reflectance, K is the absorption coefficient, and S is the scattering coefficient. Then by exploiting the Tauc method,[45] the bandgap for TiO_2 semiconductors can be expressed using the following equation Equation (2):

$$(F(R_\infty)\,h\nu)^{\frac{1}{2}} = B\left(h\nu - E_g\right) \quad (2)$$

Here, h is the Planck's constant, ν is the frequency of the light and B is a constant. By plotting $F(R_\infty)$ versus the energy expressed in eV, and by finding the *x*-axis intersection point of the linear fit of the Tauc plot, it is possible to estimate the bandgap of a material.

Photoluminescence (PL) measurements were performed in air at room temperature using a FluoroLog 3–21 system (Horiba Jobin-Yvon) equipped with a 450 W xenon arc lamp as excitation source, whose wavelength was selected by a double Czerny–Turner monochromator and signal detection stage including an iHR300 single grating monochromator coupled to a Hamamatsu photomultiplier tube (model R928P for visible range; model R5509-73 N_2-cooled for NIR range). Excitation wavelength was set at 350 nm and PL spectra recorded over a range of 380–600 nm. The XPS measurements were carried out at the VUV-Photoemission beamline of the synchrotron Elettra (Trieste, Italy) using photons of 750 and 469 eV for the core level and valence band analysis, respectively. The spectra were acquired at room temperature with a Scienta R4000 electron spectrometer.

Photocatalytic H_2 Production Tests: The photocatalytic activity of the samples was evaluated for the H_2 evolution reaction from methanol photoreforming. Photocatalytic H_2 production tests were carried out in a liquid-phase flow reactor system supplied by Apria Systems. The photocatalyst was suspended in a MeOH/ H_2O solution (10% v/v) by fluxing the system with N_2(g) at 50 mL·min^{-1} for 60 min before starting the reaction. To start the test, the gas flow was adjusted to 6 mL·min^{-1} and the lamp (365 nm UV LED array) switched on. Such low gas flow (6 mL·min^{-1}) was set just to reach very exigent conditions that allow us to see any small differences between the studied catalyst. A gas chromatographer equipped with a thermal conductivity detector (Agilent 7890B GC) was used to analyze the effluent gases and quantify the H_2 production. Equation (3) was used to estimate the apparent quantum yield (AQY) for the H_2 evolution reaction:[46]

$$AQY = \frac{2 \cdot n_{H_2}}{n_p}\left[\frac{mol \cdot s^{-1}}{mol \cdot s^{-1}}\right] \cdot 100 \quad (3)$$

where n_{H2} is the H_2 molecules number and n_p is the number of incident photons reaching the photocatalyst. n_p was calculated from the ratio between the total incident energy and the energy of one photon. In the experimental setup, the total incident energy was calculated considering the 365 nm incident light used and the power density of the incident light (2100 W·m^{-2}).

Acknowledgements

Elettra Sincrotrone Trieste was acknowledged for providing access to its synchrotron radiation facilities and for financial support under the SUI international project. G.C. acknowledges the financial support from the EU FEDER and Junta de Andalucía under I+D+i Project P20-00156 and the Ministerio de Ciencia e Innovación/FEDER through PLEC202-007906 and TED2021-130173B-C43 projects. Finally, The authors acknowledge Prof. Enrico Trave from Ca'Foscari University of Venice for his support during PL measurements. A.V. acknowledges the Kempe Foundations, the Knut och Alice Wallenberg Foundation, and the European Union – NextGenerationEU – through MUR (National Recovery and Resilience Plan (NRRP) – Mission 4 Component 2, Investment N. ECS00000043 – CUP N. H43C22000540006 (iNEST) and Mission 4 Component 2 Investment 1.3 – CUP D43C22003090001 (NEST)). P.M. and P.M.S. acknowledge EUROFEL-ROADMAP ESFRI of the Italian Ministry of University and Research.

Conflict of Interest

The authors declare no conflict of interest.

Data Availability Statement

The data that support the findings of this study are available from the corresponding author upon reasonable request.

Keywords

H_2 production, methanol photoreforming, photocatalysis, surface defects, TiO_2

Received: September 8, 2023
Revised: November 20, 2023
Published online:

[1] International Energy Agency, International Energy Agency (IEA) World Energy Outlook **2022**, *2022*.
[2] World Meteorological Organization (WMO), WMO Global Annual to Decadal Climate Update, Geneva, **2023**.
[3] A. Kubacka, M. Fernández-García, G. Colón, *Chem. Rev.* **2012**, *112*, 1555.
[4] L. Liccardo, E. Lushaj, L. Dal Compare, E. Moretti, A. Vomiero, *Small Sci.* **2022**, *2*, 2100104.
[5] G. Colón, *Appl. Catal. A Gen.* **2016**, *518*, 48.
[6] M. I. Maldonado, A. López-Martín, G. Colón, J. Peral, J. I. Martínez-Costa, S. Malato, *Appl. Catal. B Environ.* **2018**, *229*, 15.
[7] A. Ruiz-Aguirre, J. G. Villachica-Llamosas, M. I. Polo-López, A. Cabrera-Reina, G. Colón, J. Peral, S. Malato, *Energy* **2022**, *260*, 125199.
[8] L. Liccardo, M. Bordin, P. M. Sheverdyaeva, M. Belli, P. Moras, A. Vomiero, E. Moretti, *Adv. Funct. Mater.* **2023**, *33*, 2370138.
[9] R. Hossain, M. A. Uddin, M. A. Khan, *J. Phys. Chem. C* **2023**, *127*, 10897.
[10] C. J. Querebillo, *Nanomaterials* **2023**, *13*, 982.
[11] L. Liao, M. Wang, Z. Li, X. Wang, W. Zhou, *Nanomaterials* **2023**, *13*, 468.
[12] Y. Zhang, J. Yan, *Chem. Eng. J.* **2023**, *472*, 144831.
[13] R. B. Domínguez-Espíndola, D. M. Arias, C. Rodríguez-González, P. J. Sebastian, *Appl. Therm. Eng.* **2022**, *216*, 119009.
[14] L. Biswal, R. Mohanty, S. Nayak, K. Parida, *J. Environ. Chem. Eng.* **2022**, *10*, 107211.
[15] H. Lu, B. Zhao, R. Pan, J. Yao, J. Qiu, L. Luo, Y. Liu, *RSC Adv.* **2014**, *4*, 1128.
[16] L. Mino, G. Spoto, S. Bordiga, A. Zecchina, *J. Phys. Chem. C* **2012**, *116*, 17008.
[17] K. C. Christoforidis, P. Fornasiero, *ChemCatChem* **2019**, *11*, 368.
[18] G. Colón, M. C. Hidalgo, G. Munuera, I. Ferino, M. G. Cutrufello, J. A. Navío, *Appl. Catal. B Environ.* **2006**, *63*, 45.
[19] S. Wang, L. Yi, J. E. Halpert, X. Lai, Y. Liu, H. Cao, R. Yu, D. Wang, Y. Li, *Small* **2012**, *8*, 265.
[20] M. González-Tejero, J. G. Villachica-Llamosas, A. Ruiz-Aguirre, G. Colón, *ACS Appl. Energy Mater.* **2023**, *6*, 4007.
[21] P. Kubelka, F. Munk, *Z. Tech. Phys.* **1931**, *12*, 593.
[22] Y. Wang, J. Cai, M. Wu, H. Zhang, M. Meng, Y. Tian, T. Ding, J. Gong, Z. Jiang, X. Li, *ACS Appl. Mater. Interfaces* **2016**, *8*, 23006.
[23] T. Xia, Y. Zhang, J. Murowchick, X. Chen, *Catal. Today* **2014**, *225*, 2.
[24] X. Chen, L. Liu, P. Y. Yu, S. S. Mao, *Science* **2011**, *331*, 746.
[25] J. Ma, T. J. Miao, J. Tang, *Chem. Soc. Rev.* **2022**, *51*, 5777.
[26] L. Yan, C. Jing, *J. Phys. Chem. Lett.* **2020**, *11*, 9485.
[27] E. Han, K. Vijayarangamuthu, J.-S. Youn, Y.-K. Park, S.-C. Jung, K.-J. Jeon, *Catal. Today* **2018**, *303*, 305.
[28] B. Gupta, N. Kumar, K. Panda, V. Kanan, S. Joshi, I. Visoly-Fisher, *Scientific Reports* **2017**, *7*, 45030.
[29] I. Luciu, R. Bartali, N. Laidani, *J. Phys. D. Appl. Phys.* **2012**, *45*, 345302.
[30] J. J. Yeh, *Atomic Calculation of Photoionization Cross-Section and Asymmetry Parameters*, Gordon and Breach Science Publishers, Langhorne, PE, USA **1993**.
[31] I. Khalakhan, M. Vorokhta, X. Xie, L. Piliai, I. Matolínová, *J. Electron Spectros. Relat. Phenomena* **2021**, *246*, 147027.
[32] T. Robert, M. Bartel, G. Offergeld, *Surf. Sci.* **1972**, *33*, 123.
[33] F. Platero, A. López-Martín, A. Caballero, G. Colón, *ChemCatChem* **2021**, *13*, 3878.
[34] Y.-H. Chung, K. Han, C.-Y. Lin, D. O'neill, G. Mul, B. Mei, C.-M. Yang, *Catal. Today* **2020**, *356*, 95.
[35] T. Sreethawong, Y. Suzuki, S. Yoshikawa, *Int. J. Hydrogen Energy* **2005**, *30*, 1053.
[36] J. A. Ortega Méndez, C. R. López, E. Pulido Melián, O. González Díaz, J. M. Doña Rodríguez, D. Fernández Hevia, M. Macías, *Appl. Catal. B Environ.* **2014**, *147*, 439.
[37] W.-T. Chen, A. Chan, Z. H. N. Al-Azri, A. G. Dosado, M. A. Nadeem, D. Sun-Waterhouse, H. Idriss, G. I. N. Waterhouse, *J. Catal.* **2015**, *329*, 499.
[38] S. Oros-Ruiz, R. Zanella, R. López, A. Hernández-Gordillo, R. Gómez, *J. Hazard. Mater.* **2013**, *263*, 2.
[39] W. Ouyang, M. J. Muñoz-Batista, A. Kubacka, R. Luque, M. Fernández-García, *Appl. Catal. B Environ.* **2018**, *238*, 434.
[40] K. Kočí, I. Troppová, M. Reli, L. Matějová, M. Edelmannová, H. Drobná, L. Dubnová, A. Rokicińska, P. Kuśtrowski, L. Čapek, *Front. Chem.* **2018**, *6*, 44.
[41] C. García-Mendoza, S. Oros-Ruiz, A. Hernández-Gordillo, R. López, G. Jácome-Acatitla, H. A. Calderón, R. Gómez, *J. Chem. Technol. Biotechnol.* **2016**, *91*, 2198.
[42] M. Navarrete, S. Cipagauta-Díaz, R. Gómez, *J. Chem. Technol. Biotechnol.* **2019**, *94*, 3457.
[43] C. Castañeda, F. Tzompantzi, A. Rodríguez-Rodríguez, M. Sánchez-Dominguez, R. Gómez, *J. Chem. Technol. Biotechnol.* **2018**, *93*, 1113.
[44] F. Platero, A. López-Martín, A. Caballero, T. C. Rojas, M. Nolan, G. Colón, *ACS Appl. Nano Mater.* **2021**, *4*, 3204.
[45] P. Makula, M. Pacia, W. Macyk, *J. Phys. Chem. Lett.* **2018**, *9*, 6814.
[46] M. Qureshi, K. Takanabe, *Chem. Mater.* **2017**, *29*, 158.

Paper-III

N. Spigariol,[1] **L. Liccardo**,[1] E. Lushaj, E. Rodríguez-Castellón, I. B. Martin, F. Polo, A. Vomiero, E. Cattaruzza, E. Moretti, Titania nanorods array homojunction with sub-stoichiometric TiO_2 for enhanced methylene blue photodegradation. *Catalysis Today* 2023, 419, 114134.

[1] These authors contributed equally to this work.

Catalysis Today 419 (2023) 114134

Contents lists available at ScienceDirect

Catalysis Today

journal homepage: www.elsevier.com/locate/cattod

Titania nanorods array homojunction with sub-stoichiometric TiO_2 for enhanced methylene blue photodegradation

Nicolò Spigariol [a,1], Letizia Liccardo [a,1], Edlind Lushaj [a], Enrique Rodríguez-Castellón [b], Isabel Barroso Martin [b], Federico Polo [a], Alberto Vomiero [a,c,*], Elti Cattaruzza [a], Elisa Moretti [a,**]

[a] Department of Molecular Sciences and Nanosystems, Ca' Foscari University of Venice, Via Torino 155, 30172 Venezia, Mestre, Italy
[b] Department of Inorganic Chemistry, Cristallography and Mineralogy (Unidad Asociada al ICP_CSIC), Faculty of Sciences, University of Malaga, Campus de teatinos, 29071 Malaga, Spain
[c] Division of Materials Science, Department of Engineering Sciences and Mathematics, Luleå University of Technology, 97187 Luleå, Sweden

ARTICLE INFO

Keywords:
Photocatalysis
TiO_2/TiO_{2-x}-scheme homojunction
Nanorods
Wastewater treatment

ABSTRACT

TiO_2 thin films are known to promote photodegradation of dyes and pollutants in water solution via heterogeneous photocatalysis. This ability is guided by the photoexcitation through photons having energies above the band gap. To improve photocatalytic activity, nanostructures with high surface area can be applied, which can ease molecular adsorption/desorption mechanisms, enhance electronic transfer properties and lower excitation energy. For this purpose, square cross-section TiO_2 vertically aligned nanorod (TNR) array configuration has been chosen as a semiconductor substrate. On top of it, a thin layer of sub-stoichiometric TiO_{2-x} has been deposited, aiming at inducing a vacancy doped homojunction between two different oxygen rich/deficient TiO_2 layers, possibly leading to lower band gap and enhanced photochemical activity. In principle, promotion of electron and holes separation and suppression of charge recombination could occur. Vertically aligned TNRs have been deposited through a hydrothermal growth in acidic conditions on a pre-seeded glass conducting substrate, optimizing the seeding process through spin coating. Sub-stoichiometric TiO_{2-x} layer (50 nm nominal thickness) has been deposited on top of TNRs via radiofrequency magnetron sputtering at three different stoichiometries, tuning the oxygen partial pressure in sputtering argon atmosphere at 10 %, 15 % and 20 %, respectively. Photocatalytic activity has been investigated in the photodegradation of an aqueous solution of methylene blue, both under UV and simulated solar light irradiation at room temperature and atmospheric pressure, resulting in the degradation of methylene blue target molecule up to 99 % under UV and 85 % under simulated solar irradiation after 6 h. These promising achievements unlock new environmental applications for enhanced dye degradation industrial processes.

1. Introduction

Nowadays, the introduction and spread of numerous pollutants in water sources coming from industrial manufacturing processes made water contamination one of the most pressing issues. Textile industry, among others, is one of the major responsible for releasing a large quantity of dyes coming from the incomplete fixation of fabrics able to resist to oxidizing and reducing agents [1–3]. According to the US EPA (United States Environmental Protection Agency), during a typical dyeing process about 40 L of clean water are required per kilogram of fabrics. Consequently, ecosystems and human health are negatively affected [4,5], especially if such wastewaters are directly discharged without a suitable treatment process. In this regard, photocatalytic advanced oxidation processes (AOPs) have been gaining attention to accelerate oxidation and degradation of a wide range of organic pollutants in wastewater [6]. As predicted by G. Ciamician in his visionary article in 1912 [7], photochemistry is now becoming a popular topic because it is considered a sustainable way to perform chemical reactions and degrade pollutants exploiting solar energy. Combining this strategy with the ability of semiconductor materials to interact with a suitable

* Corresponding author at: Department of Molecular Sciences and Nanosystems, Ca' Foscari University of Venice, Via Torino 155, 30172 Venezia, Mestre, Italy.
** Corresponding author.
E-mail addresses: alberto.vomiero@ltu.se (A. Vomiero), elisa.moretti@unive.it (E. Moretti).
[1] These authors contributed equally to this work.

https://doi.org/10.1016/j.cattod.2023.114134
Received 19 December 2022; Received in revised form 20 March 2023; Accepted 24 March 2023
Available online 25 March 2023

wavelength, electron-hole pairs able to degrade molecules via a radical mechanism are produced [8,9]. Many semiconductors have been investigated and tested as promising photocatalysts but, among them, titania (TiO_2) is still the most widely used [10]. In fact, this material shows excellent chemical properties, being at the same time cheap, non-toxic, and stable. Furthermore, thanks to its ease of synthesis, it is possible to tune crystallinity, polymorph composition, morphology, surface area and particle size. There are several chemical and physical methods that can be exploited to synthesize TiO_2 nanoparticles (NPs) in the form of powders or thin films. Physical vapor deposition (PVD) methods, such as radiofrequency (RF) magnetron sputtering, are widely used to obtain thin films with controlled thickness, desired composition, high purity, and strong adhesion to the substrate [11,12]. The use of thin films, instead of powders, displays many advantages, among which the possibility to synthesize these films on a substrate, making them easily recoverable. Additionally, combining different morphologies appears to be one of the most appealing strategies to increase the overall performances of the photocatalyst [13]. In fact, the higher the surface area, the higher the possibility to have an increased number of active sites at the surface. Rutile nanorods (NRs) grown on the surface of a fluorine-doped tin oxide glass (FTO) have been extensively studied and recently considered effective in the field of heterogeneous catalysis. A possible strategy to easily recover the catalyst from the system after the treatment process involves the combination of the large surface area of the rod-like shape with the non-dispersed bulk feature. Moreover, NRs configuration can be suitable for the photodegradation of organic pollutants under UV light. In this regard, several studies have been reported in literature, stating the effectiveness of rod configuration especially for the delay on the charge carriers' recombination and the availability of active sites exposed at the surface. In detail, the delaying on the charge-carriers recombination may be ascribed to quantum confinement due to size effect (nanorods radius smaller than the exciton Bohr radius), as well as surface and bulk trapping effect [14,15]. However, if not properly designed, pure TNRs may have several drawbacks, such as wide band gap (from 3.0 eV of rutile up to 3.2 eV of anatase) and high rate of charge recombination. To improve the overall photocatalytic performances of this material, different strategies have been proposed. Several authors reported that a vacancy doped homojunction induced in the TiO_2 array could efficiently enhance the properties of UV-Visible driven photocatalytic processes of the material [16,17]. Based on these considerations, the controlled introduction of a thin film of sub-stoichiometric TiO_{2-x} over the surface of TiO_2 NR array may be an interesting approach to influence the oxygen vacancies parameter. TiO_{2-x} thin layer can be easily created by a RF sputtering deposition by inducing a larger deficiency of oxygen (lowering the partial pressure of oxygen in the working gas), leading to the formation of a homojunction between the NR structure and the sub-stoichiometric TiO_{2-x}. Therefore, the combination of pure and sub-stoichiometric titania may lead to several advantages: the composite system could show changes in its electronic structure, broadening its absorbance ability, and enhancing its photocatalytic properties compared to the bare material. For instance, the vacancy doped TiO_{2-x} surface layer is reported to interact with the TiO_2 NR promoting the separation between electrons and holes simultaneously suppressing recombination [17,18]. Furthermore, TiO_{2-x} shows a narrower band gap in comparison to stoichiometric titanium dioxide, typically about 1.5 eV, and tunable according to the synthetic method, thus leading to an increase in the visible light absorption [19,20]. In this work, the role of TiO_{2-x} titania thin films deposited via RF magnetron sputtering was investigated, comparing the photocatalytic performances of pure and sputtered TiO_2 NR samples. Homojunctions were prepared tuning two parameters: the number of cycles for the creation of the seed layer to induce the growth of TNRs and the O_2 partial pressure of the vacuum chamber during sputtering deposition. The films were tested in a photodegradation reaction in water solution under UV and solar light irradiation at room temperature (RT) and P atm, taking methylene blue (MB) as a dye probe, correlating the photocatalytic activity and the physicochemical and optical properties of the samples.

2. Experimental

2.1. Materials

Titanium (IV) butoxide (TBOT), absolute ethanol (EtOH), acetic acid (HAac), hydrochloric acid (37 % v/v), sodium hydroxide and methylene blue (MB) were all analytical grade and purchased by Sigma Aldrich without further purification. Fluorine tin oxide (FTO) glasses were purchased by Pilkington.

2.2. FTO substrates preparation

FTO glasses were ultrasonically cleaned for 5 min three times, each in a different solvent: absolute ethanol, deionized water, and acetone, respectively. Cleaned samples were then dried in a stream of nitrogen and then stored at room temperature.

2.3. TiO_2 nanorods synthesis

Titania Nanorods (TNR) were synthesized through hydrothermal growth method. Two different solutions, a seed layer solution (A) and a NR growth solution (B), were used during the process. Solution A was prepared mixing 10^{-3} mol of titanium(IV) butoxide in a solution of absolute ethanol and acetic acid in molar ratio 1:5 under stirring for 2 h before being left aging 24 h at RT. Seed solution was then deposited on the conductive side of a FTO glass by spin coating at the rate of 500 rpm for 5 s and 3000 rpm for 30 s. The FTO glass was then heated at 120 °C for 10 min in air flow. Samples were labelled as single layer (SL) and double layer (DL) when this procedure had been repeated one or two times respectively. Finally, the samples were annealed in a furnace at 450 °C for 1 h in air flow. Solution B, containing titanium butoxide 0.03 M, was prepared by adding $1.2 \bullet 10^{-3}$ mol of titanium butoxide to a solution of hydrochloric acid and deionized water (1:1 v/v). The as obtained solution B was stirred for 5 min until the solution was colorless transparent. The FTO substrates were placed on a Teflon support inside a Teflon-line of a stainless-steel autoclave (40 mL). Solution B was transferred in the Teflon-line and the hydrothermal growth was carried out at 150 °C for 4 h. Lastly, the samples were washed with deionized water and dried at 60 °C for 2 h.

2.4. TiO_2 thin films deposition

The desired TiO_2/TiO_{2-x} homojunctions were obtained by physical vapor deposition (PVD). TiO_{2-x} nanostructures were synthesized by reactive sputtering deposition on TiO_2 NR (TNR) surface in a custom-made RF (radiofrequency) magnetron sputtering deposition apparatus. Depositions were performed starting from a target of pure metallic titanium by using a 13.56 MHz RF source and three reactive atmospheres $Ar+O_2$: 90 % + 10 %, 85 % + 15 % and 80 % + 20 %. The total pressure was $50 \bullet 10^{-4}$ mbar in dynamic vacuum conditions and the sample holder was rotated at 5 rpm during deposition to improve homogeneity of the film composition and thickness. The RF power to the 2 in. diameter titanium target was fixed at 250 W. During the deposition, temperature was lower than 60 °C to avoid induced phase transition. The deposition duration was around 1 h according to the desired film thickness of titanium between 50 and 60 nm (as obtained by a stylus profilometer, with relative uncertainty around 20 %), depending on the reactive atmosphere used. Samples were referred to as: XTNRY, where X stands for SL or DL and Y for 10 %, 15 %, 20 % of O_2 in Ar. For instance, sample SLTNR10 is made using a single layer of seed solution and it has been sputtered under a 10 % O_2 in Ar atmosphere (See Table 1).

Table 1
Sample label, layer type, working gas composition and deposition time of the synthesized photocatalysts.

Sample label	Seed layer type	Working composition ($Ar + O_2$, %)[a]	Gas deposition time (s)
SLTNR	Single	-	-
DLTNR	Double	-	-
SLTNR10	Single	90 + 10	3600
DLTNR10	Double	90 + 10	3600
SLTNR15	Single	85 + 15	4000
DLTNR15	Double	85 + 15	4000
SLTNR20	Single	80 + 20	4685
DLTNR20	Double	80 + 20	4685

[a] Total pressure = $50 \bullet 10^{-4}$ mbar.

2.5. Characterization

The morphology of bare and sputtered TNR was characterized using a field-emission scanning electron microscope (FEG-SEM, Zeiss Sigma 174 Cz). Morphology was further characterized using a Bruker Dimension ICON AFM in tapping operation mode with a Bruker SCM-PIT-V2 probe having a Platinum-Iridium coated electrically conductive tip (spring constant ~ 0.3 N/m, nominal tip radius ~ 25 nm). Crystal structure was examined by X-ray diffraction (XRD) using an X-ray diffractometer (Philips PW1050/37) with Cu K_α radiation ($\lambda = 1.5418$ Å). Diffuse reflectance UV-Visible absorption spectra (DRUV-Vis) were investigated to compare the light-harvesting ability of bare and modified samples. The DRUV-Vis spectra of the samples were collected with a Cary100 UV-Vis spectrophotometer using and integrating sphere accessory and $BaSO_4$ as a reflectance standard during the measurements. The surface of the materials was studied by X-ray photoelectron spectroscopy (XPS). The high-resolution C 1s, O 1s, Ti 2p and N 1s core level spectra were registered using a Physical Electronics PHI 5700 spectrometer with non-monochromatic Al-K_α radiation (1486.6 eV), recorded in the constant pass energy mode at 29.35 eV with a 720 μm diameter analysis area. Adventitious carbon (C 1s at 284.8 eV) was used as a reference. We are well aware that this signal usually falls in a very large binding energy range (284.0–285.6 eV, as reported in literature), thus making difficult a consistent energy calibration of the binding energy scale [21,22]; however, the present choice gives for our samples reliable BE values for all the detected XPS bands. A Shirley-type background was subtracted from the signals and the deconvolution curves were fitted using Gaussian–Lorentzian model in Multipak 9.0 software. The materials were also studied after etching with Ar^+ at 1 keV for 1 min.

2.6. Photocatalytic degradation experiments

To evaluate the photocatalytic activity of the synthesized materials under both UV and visible light irradiation, MB degradation was selected as a test reaction. All the photocatalytic tests were carried out in a glass reactor containing 50 mL of 6×10^{-6} M MB aqueous solution with constant stirring at 30 °C and placing the glass samples on a Teflon support. The solution containing the photocatalyst was kept in dark for 30 min to reach MB adsorption/desorption equilibrium. The photocatalytic tests under UV light were carried out using a 125 W high pressure mercury lamp, operating at wavelengths between 180 and 420 nm with a peak at 366 nm and the sputtered glass samples were placed right underneath the lamp's filament at a distance from the glass surface of 10 cm. To explore the possibility of solar-driven photocatalysis a solar simulation has been performed using a M-LS Rev B solar simulator from ABET technologies with a 100 Watts xenon lamp. Standard cell is set to measure a 130 mA current when exposed to 1 Sun of solar irradiance. Calibration revealed the required distance to be around 12.5 cm between the sample surface and the light source. Afterward, the glasses were exposed to the light irradiation under ambient conditions and aliquots of 0.7 mL of the aqueous solution were collected from the reactor at fixed intervals up to 6 h. A Cary100 UV-Vis spectrometer was used for the determination of the MB concentration, after calibration. The degradation processes were monitored following the absorbance at the maximum of the UV-Vis spectrum of the target molecule (664 nm). Since its photodegradation pathway is well known, the possible formation of byproducts was monitored acquiring the overall UV–Vis spectrum of the solutions recovered at different times during the degradation experiments [23].

The rate constant was calculated according to the following Eq. (1):

$$\ln \frac{C}{C_0} = -kt \quad (1)$$

where C is the concentration after time t, C_0 represents the initial concentration and k is the pseudo-first order rate constant (min^{-1}), calculated as (2):

$$k = 2.303 \times slope \quad (2)$$

To evaluate the stability and reusability of the photocatalysts, a 3-cycle recycling test was performed. The sample was washed with deionized water and dried overnight after each photocatalytic cycle for the recycling test. To explore the effect of surface activity in acidic or basic conditions two photocatalytic tests were carried out by adjusting the pH at 4.0 and 9.0 both with sample SLTNR20.

3. Results and discussion

3.1. Structural and morphological characterization

According to single or double seed-layer (SL or DL) deposition, two different series of samples were produced with three different sputtering atmospheres: 10 %, 15 % and 20 % oxygen in argon, respectively (See Table 1, Section 2).

In Fig. 1(a–d), SEM images of the samples are reported showing the morphology of the TNRs before and after the sputtering deposition. In Figs. 1a and 1b it can be noticed the presence of nanostructured vertically aligned TNRs for both the SL and DL, which are closely packed and uniformly covering the surface of the FTO, proving the effectiveness of the seed layer procedure. It must be pointed out that a not uniform seed deposition can create the so-called dried-soil pattern, which leads to the presence of voids and cracks on the array. All rods appeared with a square cross section geometry with a rather uniform average size. Two different calculation methods were applied to better estimate the average size: software analysis and intercept method [24] (see Supplementary material). The latter method is typically applied to determine the grain size dimension in alloys and polycrystalline materials. However, since TNR are not perfectly packed but very close together, this approach is supposed to give a reasonable rough estimate for the average diameter. The results are shown in Tables S1 and S2. Values of (78 ± 4) nm for SL and (68 ± 5) nm for DL can be compared with SEM micrographs measurements confirming the intercept method is a suitable alternative to software imaging. Thanks to the cross-section imaging analysis, the average TNR layer thickness was estimated around 310 ± 63 nm for SLTNR and 350 ± 84 nm for DLTNR. Fig. 1c–d shows the SEM images of the post sputtered samples, revealing the presence of newly grown nanorods on the pristine TNR surface. The as-obtained TiO_{2-x} rods are thinner and they homogeneously cover the NR surface, thus indicating the effectiveness of the sputtering deposition procedure.

In addition to SEM, AFM topography images of SLTNR and SLTNR15 nanorod arrays (Figs. 2a and 2b, respectively) acquired in tapping mode show an overall uniform coverage. Moreover, it can be observed the presence of much thinner nanorods in the sputtered sample, suggesting a second growth onto the pre-existing nanostructures. These observations are in good agreement with the SEM measurements (Figs. 1c and 1d).

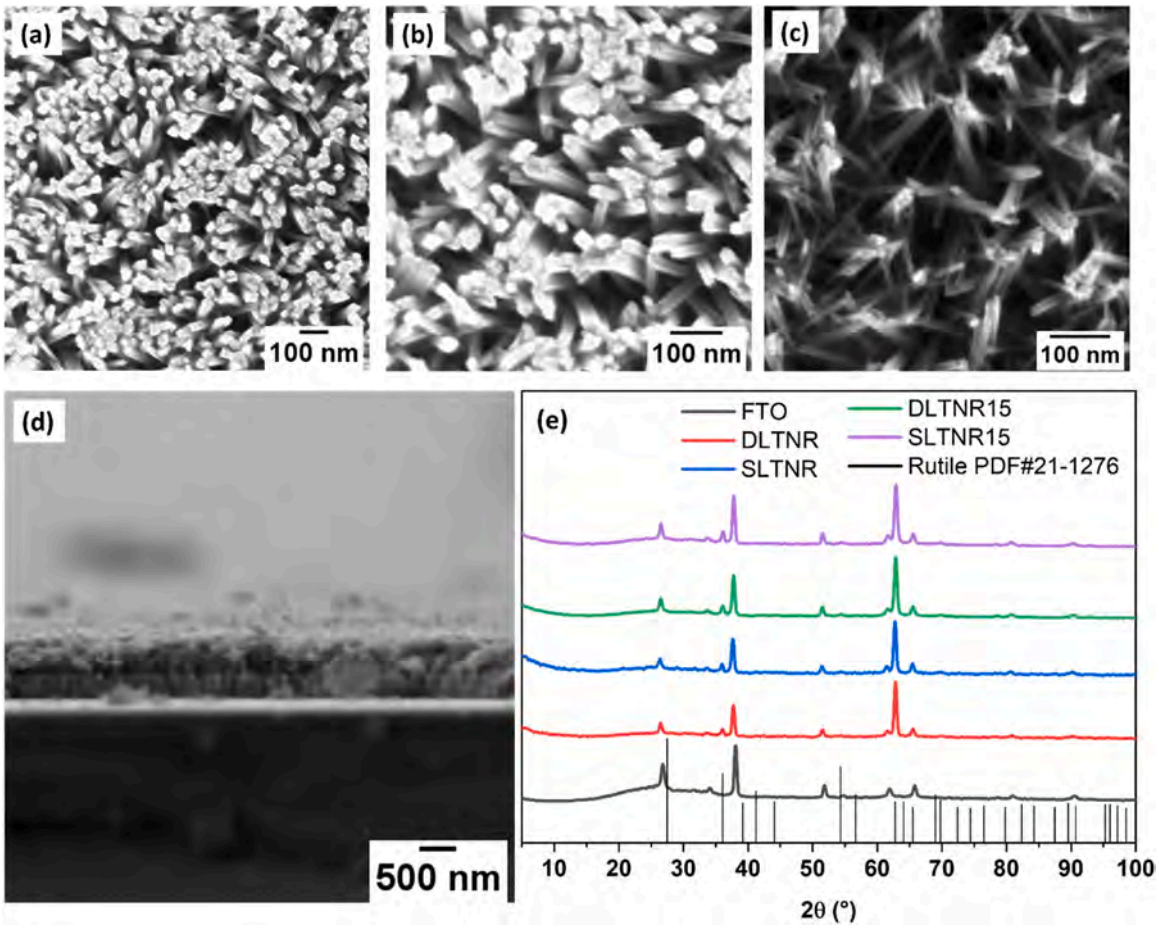

Fig. 1. (a–d) SEM images of bare (a) SLTNR and (b) DLTNR at different magnifications and after the sputtering deposition (d) from top and (e) cross-section view (e) XRD diffractogram comparing pristine FTO glass and both stages of seed (SLTNR, DLTNR) and sputtered layers (SLTNR15 and DLTNR15).

This was further confirmed by the line profiles of the SLTNR and SLTNR15 (Supplementary material, Fig. S3a and S3b) that allowed to estimate the lateral size of the nanostructures. Nanorods with a lateral dimension ranging from about 75–87 nm were detected in the SLTNR sample, while the sputtered sample (SLTNR15) showed a more uniform surface, presenting features with a smaller diameter (about 17–25 nm).

Moreover, the surface roughness parameter of a material highlights the differences depending on the irregularity of the profiles. For vertical profiles such as the nanorods reported in this study, the surface roughness is evaluated from amplitude parameters, among which the root mean square (rms) roughness (Rq) is included. Rq is a measure of the standard deviation of the Z height [25] and its extrapolated value for SLTNR and SLTNR15 was 19.6 nm and 2.2 nm, respectively. A higher value of Rq for SLTNR can be explained by the fact that the nanostructures are not perfectly packed, as previously observed from SEM analyses (Fig. 1). The decrease in roughness highlighted by AFM results indicates that the introduction of sub-stoichiometric TiO_{2-x} induces a secondary growth of much thinner nanorods on top of the starting TiO_2 nanostructures.

Fig. 1e shows the XRD patterns for all the samples of TNR grown on FTO glasses before and after the sputtering process. SLTNR and DLTNR samples show a peak at 2θ of 36° identified with (101) peak of rutile crystalline phase of TiO_2 nanorods and 2θ of 64° identified as the (002) peak accounting for the vertically aligned structure of the rods growing perpendicularly to the surface of the FTO along the [001] direction [26]. Consequently, it can be affirmed that for all the samples there is a clear preferential orientation of the rutile phase, which calls for a single crystal growth perpendicular to the FTO substrate. It should be considered that several factors are playing a crucial role in the TNR growth, one in particular is the amount of the titanium precursor in the seed and hydrothermal growth solution. Rutile nanorods crystallinity is enhanced as the quantity of titanium butoxide is increased. Samples SLTNR15 and DLTNR10 contained 10 % more titanium precursor than the other samples.

3.2. XPS analysis

The surface chemical composition of the materials (in atomic concentration %) is shown in Table 2. This table also includes the composition after etching 1 min with Ar^+. The studied materials present a high concentration of carbon that is almost totally removed after etching. Samples DLTNR20 and SLTNR20 also present Si.

All the samples exhibit a high content of carbon on the surface. The high-resolution C 1*s* core level spectra (Fig. 3-left panel and Table 2) show different functional groups on the surface. All the spectra can be decomposed in four contributions at about 284.8, 286.2, 287.5 and 288.7 eV. The main contribution at 284.8 eV comes from the presence of -C—C- and -C═C- bonds mainly from adventitious carbon. The second contribution at 286.1–286.3 eV is assigned to C—O and C—N bonds. The third and fourth contributions are very weak and appear at 287.5–287.6 eV and 288.7–288.8 eV and are assigned to residual C═O and carboxylate groups, respectively [27,28]. The relative intensities of these contributions are slightly modified with the different treatments. Upon Ar^+ etching, the surface content of carbon is dramatically reduced, indicating that most of the surface carbon comes from adventitious contamination.

O 1*s* core level spectra (not reported) can be decomposed in three contributions. The main contribution at 529.8–529.9 eV is assigned to

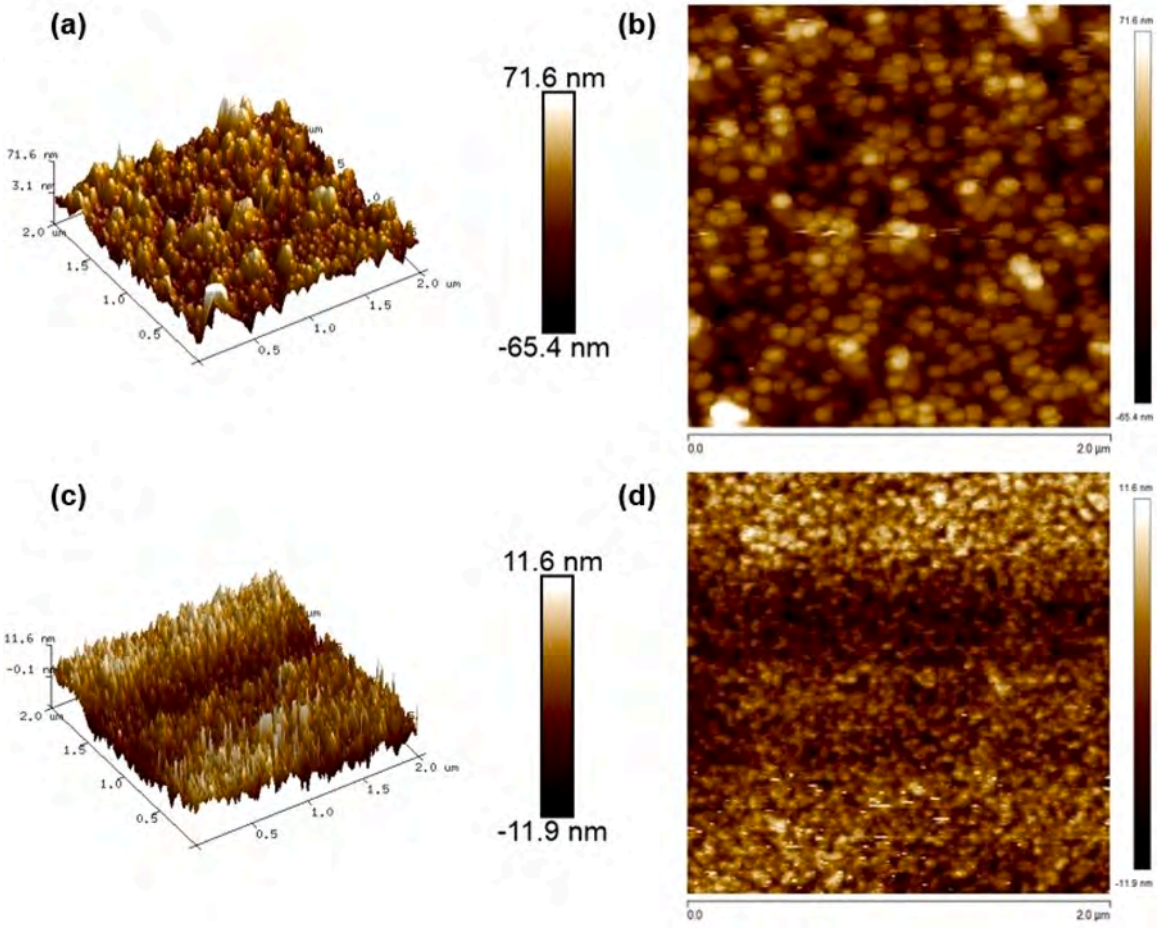

Fig. 2. AFM 3D morphologies of (a) SLTNR and (c) SLTNR15 samples. AFM 2D images of (b) SLTNR and (d) SLTNR15 nanorod arrays.

Table 2
Surface chemical composition (in atomic concentration %) determined by XPS.

Sample	C	O	N	Ti	Si
DLTNR10	44.7	42.0	-	13.3	-
SLTNR10	48.3	37.6	2.5	11.6	-
DLTNR15	44.8	40.3	1.3	13.6	-
DLTNR20	45.1	38.2	1.2	11.5	4.0
SLTNR20	47.3	36.9	1.6	9.9	4.3
DLTNR10[a]	10.9	61.7	-	27.4	-
SLTNR10[a]	12.3	60.1	1.0	26.6	-
DLTNR15[a]	11.2	60.7	0.8	27.3	-
DLTNR20[a]	9.2	61.6	0.8	30.0	1.4
SLTNR20[a]	10.5	59.4	1.1	26.9	2.1

[a] After etching 1 min Ar*.

lattice oxygen of titania [29]. The second contribution at 531.5–531.8 eV is assigned to surface oxygen mainly as Ti-OH groups and carboxylate. The relative intensity of this contribution is higher for SL samples than for DL samples. The third contribution at higher binding energy is assigned to C-O bonds and water.

The high-resolution Ti 2*p* core level spectra in the different samples (Fig. 3 – central panel) are very similar, with Ti $2p_{3/2}$ binding energies falling at 458.4–458.6 eV, typical of titania [29]. The Ti $2p_{3/2}$ signal is always symmetric and Ti(IV) species are the main ones. However, after a mild etching with Ar^+ plasma, the presence of sub-stoichiometric titania is observed too, as shown by the lower BE 2*p* doublet overlapping the Ti (IV) signals (Fig. 3-right panel).

In the five samples, the mean distance between these two different 2*p* signals is around 1.5 eV. We suppose that the first few nm of our sub-stoichiometric titania coatings completely oxidized as a consequence of the interaction with the environmental oxygen. The mild sputtering needed for removing the surface contamination allowed to detect the as-deposited sub-stoichiometric titania. Considering a rough comparison between the intensity of the two different Ti 2*p* signals, the sub-stoichiometric titania should have a O/Ti ratio ranging between 1.8 and 1.9.

An explanation of the presence of nitrogen in some samples may be ascribed to contamination induced by an incorrect handling of the sample. Upon Ar^+ etching the nitrogen content decreases, confirming its presence at the sample surface only.

Samples DLTNR20 and SLTNR20 show the presence of Si, probably coming from the leaching of the glass substrate under hydrothermal conditions. Aforementioned Si is present as Si(IV) and the oxygen combined with Si appears as a part of the contribution at high binding energy in the O 1*s* core level spectra. No traces of F and Sn from FTO were detected on the surface of all studied materials.

3.3. Optical studies

To investigate the optical properties of the prepared junctions, the Uv-Vis absorption spectra were recorded, and the results are shown in Fig. 4. TNR sample is showing the typical TiO_2 strong absorption in the UV region with a band-edge slightly shifted toward the visible region with respect to the pristine FTO glass absorption. Thanks to the homo-junction formation, the absorption edge is showing a considerable redshift with an extension of the overall absorption toward higher wavelengths up to ∽ 800 nm. It is worth noting that samples appeared red-shifted with decreasing concentration of oxygen in deposition

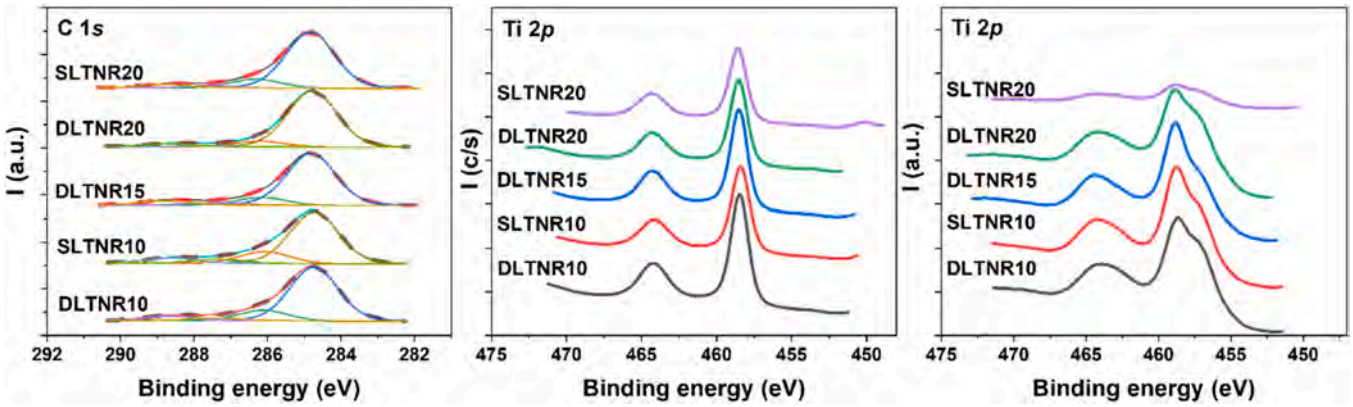

Fig. 3. High resolution XPS bands: C 1s (on the left), Ti 2p before (on the center) and after (on the right) mild Ar^+ sputtering for removing surface contamination.

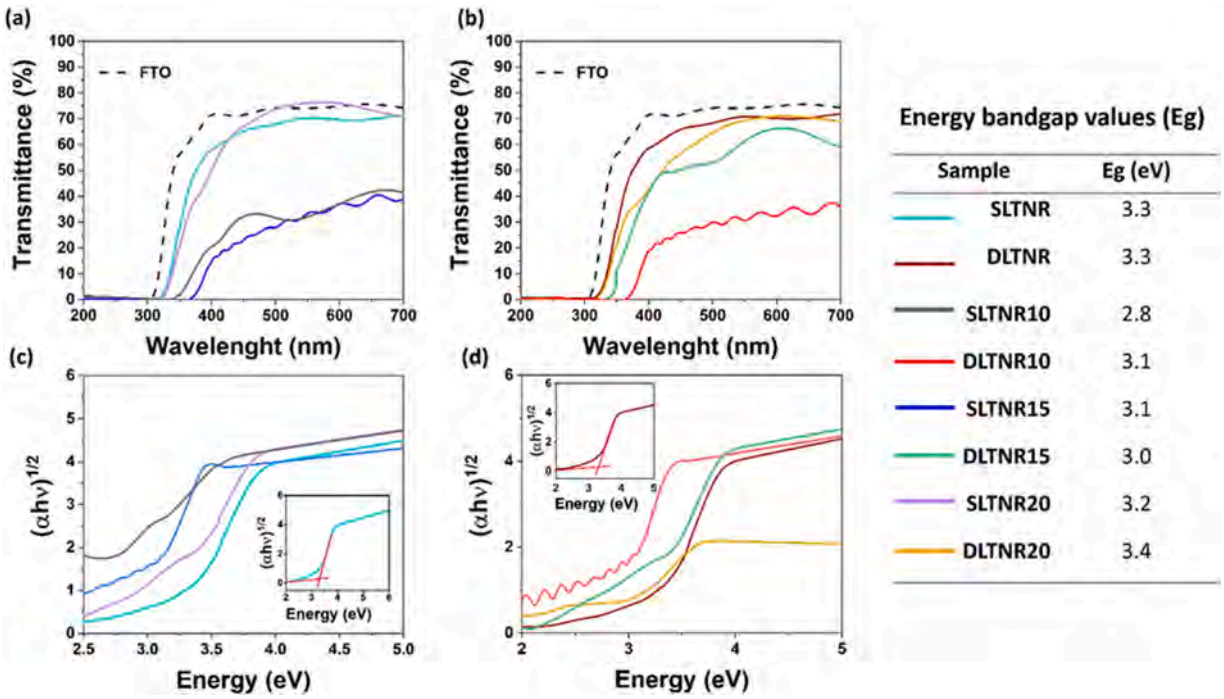

Fig. 4. : Transmittance UV-Vis spectra (top) and Tauc plots (bottom) referring to (a, c) SLTNRX series and (b, d) DLTNRX series. The energy band gap values are listed in the inset table.

working-gas (from 30 % to 10 %), hence with titanium dioxide being more sub-stoichiometric, as expected. Oscillations above 400 nm may be associated with interference effects rising from internal reflections. The improved spectral response can be attributed to the homojunction formation between TiO_2 and TiO_{2-x} [16]. To better understand the junction mechanism, the band gap of the samples was extrapolated from Tauc plots using the baseline approach method for indirect band gap (Fig. 4) [30]. The band gap energies are presented in the Fig. 4. As it can be noticed, band gap energies exhibit a direct correlation with increasing stoichiometry in deposited layer TiO_{2-x} composition: the lowest value is measured in SLTNR10 sputtered sample (2.8 eV), while the highest is measured in SLTNR20 (3.4 eV). In addition to the redshift of the absorption onset, optical spectra showed an increased absorption in the full visible spectral range after the deposition of the sputtered layer. As expected, the absorption is stronger in samples with larger oxygen sub-stoichiometry, as clearly visible in Fig. 4. This suggests a potential enhancement in the catalytic properties towards the photo-degradation of MB under simulated solar illumination.

3.4. Photocatalytic activity

Methylene Blue (MB), a heterocyclic aromatic compound and a well-known pollutant dye, was taken as the photocatalytic probe molecule. MB photodegradation pathway is well known and deeply investigated through liquid chromatography-mass spectroscopy and gas chromatography-mass spectroscopy analyses, under UV light and in the presence of TiO_2 based materials. It is based on the conversion of the organic dye into harmless compounds such as CO_2, nitrate, ammonium, and sulphate ions [23]. During the photocatalytic tests, the absorbance values have been measured following the 664 nm peak evolution, which is the maximum value of MB typical absorption band. To test the photo activity of the sputtered samples, they were tested under both UV and simulated solar light irradiation, and UV-Visible spectra were recorded and monitored in the range 300–800 nm at different photoreaction times (after 5, 10, 20, 40, 60, 90, 120, 180, 240, 300 and 360 min), also investigating the possible presence of Leuco Methylene Blue (LMB) in solution. LMB is a colorless reduced form of MB, which can be produced during the experiment and can be rapidly reduced back to MB. It is stable

in a vacuum or under inert atmosphere and as the MB, it exhibits a characteristic and strong absorbance band at 520 nm [31]. Fig. 5a and b show the MB UV-Vis absorption spectra in dark mode and under both UV light and solar simulated irradiation for the samples SLTNR15 and DLTNR15, taken as examples. The decrease in the absorption at 664 nm can be ascribed to the degradation of benzene rings and heteropoly aromatic linkages. The LMB typical band was not detected, hence the reduced colorless form of MB was not present in the reaction environment neither under UV nor under simulated solar light and the sample solution bleaching was exclusively due to the MB degradation.

In Fig. 5c-f the photocatalytic performances of the NRs series are presented under both UV and simulated solar light irradiation. While the corresponding degradation efficiencies, the pseudo-first order kinetic constant values and uncertainty $k \pm \delta_k$ (10^{-3} min^{-1}), calculated using the data from the non-stationary regime during the light phase, are listed in Table 3 (further details on the fitting profiles are reported in Fig. S4). As can be noticed from C/C_0 profiles reported in Fig. 5, there is an abrupt slope variation for SLTNR15 after 40 min under UV irradiation. Less notably, the same behavior is observed in sample SLTNR20.

By analyzing photodegradation kinetics (Table S4), we assume that the sudden change in slope is influenced by the absorption phenomena occurring during the photolysis of MB. As a matter of fact, previous studies reported in literature, highlight pseudo-first and pseudo-second order kinetics associated with absorption phenomena, similar to what has been observed during our study [32]. Further investigations will be led to shed light on the actual mechanism and/or concurring processes.

The adsorption phenomenon of the MB taking place on the samples' surfaces during the dark interval equilibration time (30 min without light irradiation) can be also noticed from the C/C_0 plots.

The bare FTO glass substrate displays the highest capability of adsorbing MB molecules on its surface, significantly reducing its concentration up to 40 %. This can be ascribed to the fact that the pH of the MB solution is higher than the FTO point of zero charge (PZC) [33,34]. Instead, a correlation could be inferred between the decrease in the MB concentration (from 2 % to 17 %) and the increase in the O_2% in Ar. This means that the presence of less sub-stoichiometric TiO_{2-x}, having a higher number of surface exposed hydroxyl groups, leads to a higher number of interactions with MB's exposed functional groups. Under UV light, all photocatalysts show a very interesting catalytic performance, with a significant decrease in the MB concentration ranging from 30 % up to 99 %. As shown in Fig. 5c–f, both non-deposited SL and DL exhibit a certain degree of photocatalytic activity, revealing a behavior similar to all the other samples. The SLTNR15 is the most photoactive one, showing a kinetic constant for MB degradation around $9 \bullet 10^{-3}$ and a dye photodegradation ability of 99 % after 360 min. From XRD analysis and SEM images it can be stated that sample SLTNR15 possesses desired vertically aligned morphology and similar band gap energy value as sample DLTNR15 (having identical stoichiometry). However, from degradation profiles it is evident that SLTN15 exhibits strikingly different photocatalytic activity. This could stem from a combination between the rationally designed structure and the sub-stoichiometric sputtering deposition with 15% O_2 atmosphere, leading to an overall enhancement of the photocatalytic efficiency.

Careful comparison between single and double layer photodegradation profiles could open to the consideration that all SL samples performance is overall superior to DL. Since the goal of this work designing TiO_2/TiO_{2-x} nanostructures were to enhance photocatalytic efficiency under solar light irradiation, XTNRY were tested under the same operating conditions also using standard simulated solar light

Table 3
Degradation efficiency (% Dr) and k values for all the samples both under UV and Simulated Solar Light (SS) irradiation.

Sample	UV % Dr	SS % Dr	$k_{UV} \pm \delta_{kuv}$ (10^{-3} min^{-1})	$k_{ss} \pm \delta_{kss}$ (10^{-3} min^{-1})
SLTNR	36	73	-	-
DLTNR	43	78	-	-
SLTNR10	32	70	1.6 ± 0.2	4.9 ± 0.4
DLTNR10	53	65	8 ± 1	4.2 ± 0.6
SLTNR15	99	86	9 ± 1	6.8 ± 0.5
DLTNR15	44	70	2.8 ± 0.4	3.5 ± 0.5
SLTNR20	66	65	4.9 ± 0.5	6.3 ± 0.5
DLTNR20	53	70	2.4 ± 0.3	3.0 ± 0.4

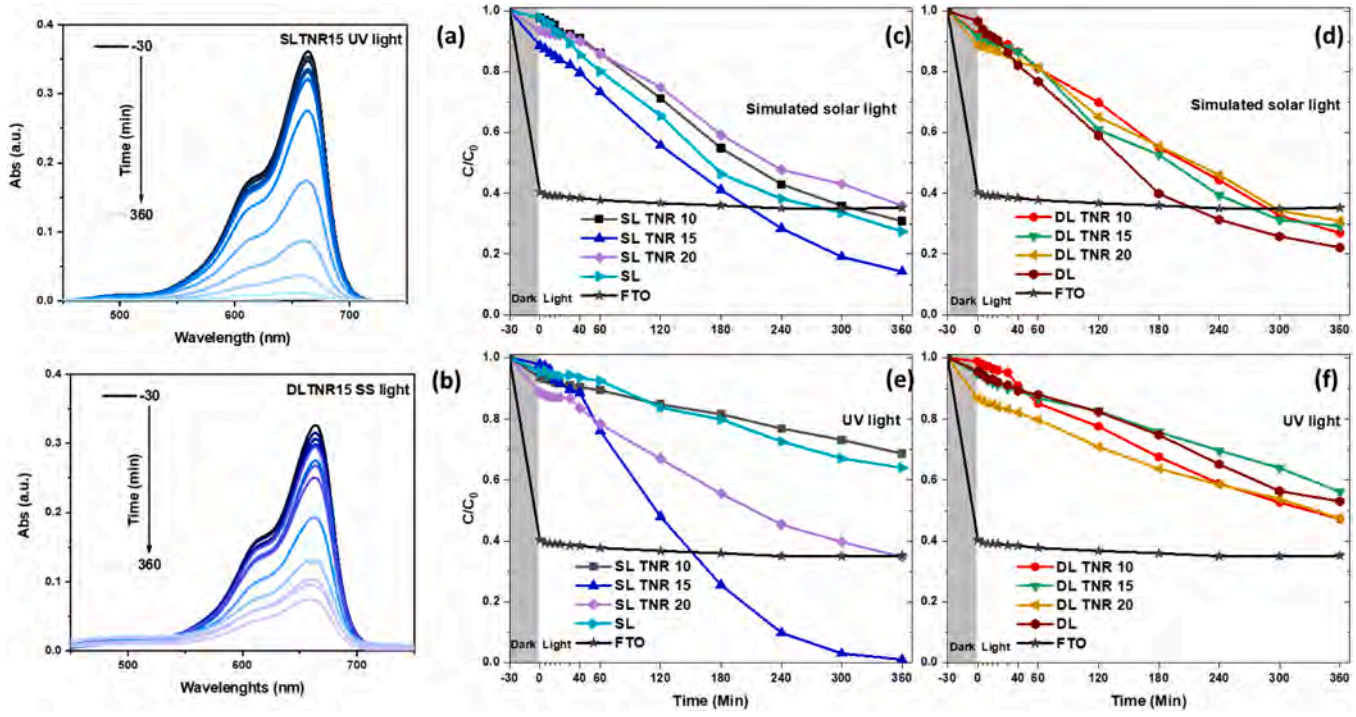

Fig. 5. Methylene blue (a,b) absorption spectra for SLTNR15 under UV and DLTNR15 under simulated solar (SS) light. Photodegradation curves of the investigated samples under (c, d) simulated solar light and (e, f) UV light irradiation at room temperature and atmospheric pressure.

irradiation. In general, every sample is showing an enhanced efficiency towards MB degradation under simulated solar light, with no exceptions (Table 3). The catalytic behavior of these systems is in accordance with their optical characterization: the band edge absorption redshift may be responsible for the overall increase in the photocatalytic efficiency. Even in this case, the best performing sample is SLTNR15, reaching a MB degradation of 86 % with a k value around $7 \bullet 10^{-3}$, thus confirming previous statements.

Since the recyclability of a catalyst is very important for its practical use, stability and reusability tests were carried out on sample SLTNR15 under UV light irradiation with the previous operating conditions. As shown in Fig. 6a, after three recycling processes, the SLTNR15 sample was not only still active towards MB dye degradation under UV light, suggesting a very good physico-chemical stability, but it also showed an improved photodegradation efficiency. This result could suggest a long-term application of the proposed catalyst in water treatment.

Since wastewaters sources can be found in a great range of pH, we exposed the synthesized catalyst to acidic and basic conditions and carried photodegradation process under UV light irradiation with the purpose of understanding the role of pH on the surface of the catalyst. Two different photocatalysis were carried at pH 4.0 and 9.0 both with sample SLTNR20 (Fig. 6b). Being MB a positively charged dye, its adsorption on the catalyst surface strongly depends on the charge of the catalyst surface itself. Point of zero charge values reported for TiO_2 are ranging from 5.0 and 6.2 [33–38], while the MB solution pH has been measured to be 6.2. TiO_2 surface is very sensitive to the presence of H^+ ions in the solution, since it is rich in terminal hydroxyl groups. Therefore, the surface catalyst is positively charged when the solution pH is below the PZC, conversely hydroxyl groups are deprotonated leaving the surface negatively charged when above the PZC. As it can be noticed from Fig. 6b, there are two opposite trends at pH 4.0 and 9.0, respectively. In acidic conditions, the positively charged surface of the catalyst attracts a higher number of oxidizing species. The latter can interact with positively charged MB molecules, which can be degraded almost by 100 after 360 min, without any adsorption phenomena onto the catalyst surface. On the contrary, in alkaline conditions the hydroxyl groups exposed on the catalyst surface are deprotonated. In this case, the adsorption phenomena easily occur, because of the electrostatic interactions. Hence, the strong decrease of the C/C_0 curve at pH 9.0 is not related to the photodegradation process.

Photodegradation processes under acidic and basic conditions were also carried out for the pristine FTO. The efficiency of SLTNR15 sample in both acidic and basic conditions compared with a bare FTO substrate was then investigated. Although FTO conductive layer promoted the formation of electron/hole pairs being active for the photodegradation of MB (Fig. S5), photolysis of MB under acid/alkaline conditions with SLTNR15 reached higher degradation efficiency (100 % degradation after 40 min and 98 % after 240 min under pH 4 and 9, respectively), thus proving the effectiveness of the TiO_2/ TiO_{2-x} system.

4. Conclusions

TiO_2 thin films are widely used in the field of heterogeneous photocatalysis to promote the degradation of organic pollutants in wastewater. To improve surface-to-volume ratio, ease adsorption/desorption mechanisms, avoid fast charge recombination processes and lower the wide TiO_2 band gap, a homojunction between two different oxygen rich/deficient TiO_2 layers has been proposed. According to SEM analyses, TiO_2 vertically aligned nanorods grown on the conductive side of a FTO glass were obtained through hydrothermal treatment in acidic conditions by optimizing the seeding process via spin coating. The average diameter was estimated to be of (78 ± 4) nm for SL and (68 ± 5) nm for DL, revealing that the number of seed layer deposition influenced the diameter growth generated by a large number of nucleation sites. By RF magnetron sputtering deposition, a homogeneous layer of thin TiO_{2-x} nanorods was then generated to form three different homojunctions by tuning the oxygen partial pressure in sputtering argon atmosphere at 10 %, 15 % and 20 %, respectively, inducing a substoichiometry in the structure that is reported by other authors to be consistent with oxygen vacancies. It should be mentioned that a distortion in the TiO_2 structure cannot be ruled out as a possibility, as suggested by XPS results. Both TiO_2 nanorods and TiO_{2-x} layer showed the same crystalline phase (rutile) as confirmed by XRD pattern. AFM studies confirmed what was previously observed by SEM. Rather uniform nanorod arrays were obtained, with nanostructures having an average lateral dimension of 80 nm (SLTNR sample) and of about 20 nm for the sputtered sample (SLTNR15). Moreover, AFM highlighted a decrease in the surface roughness due to the introduction of substoichiometric titania thin film, as expected. Photocatalytic activity has been investigated by monitoring the photodegradation of methylene blue (MB), chosen as target water contaminant, both under UV and simulated solar light irradiation at room temperature and atmospheric pressure. A MB degradation up to 99 % and 85 % under UV and simulated solar irradiation, respectively, was achieved for the best performing sample (SLTNR15) laying the groundwork for new environmental applications to enhance dye degradation industrial processes.

CRediT authorship contribution statement

Nicolò Spigariol: Conceptualization, Methodology, Formal analysis, Investigation, Data curation, Writing – original draft. **Letizia Liccardo:**

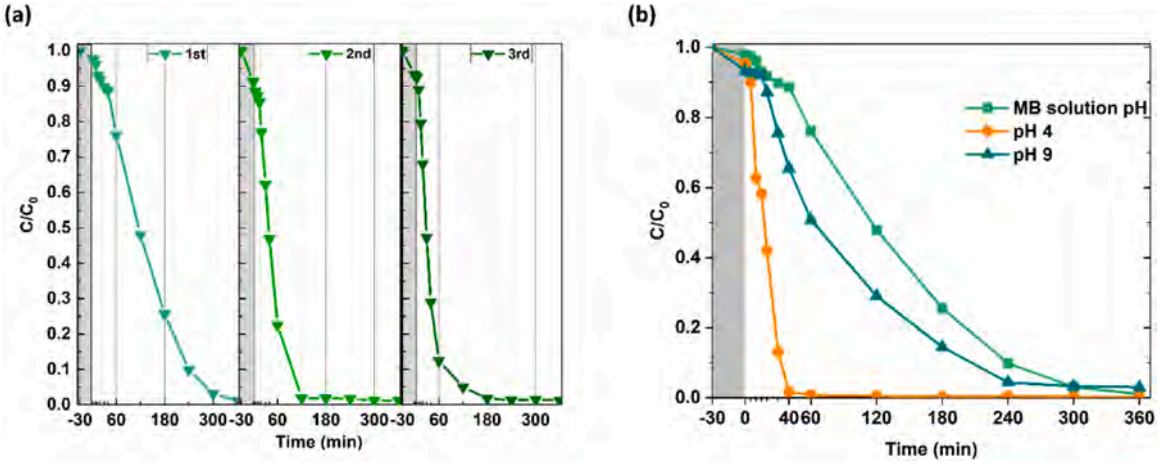

Fig. 6. (a) Reusability test for sample SLTNR15 performed under UV irradiation (b) Photocatalytic activity behavior in acidic and basic conditions.

Conceptualization, Methodology, Formal analysis, Investigation, Data curation, Writing – original draft, Writing – review & editing. **Edlind Lushaj:** Methodology, Formal analysis, Investigation, Data curation, Writing – review & editing. **Enrique Castellon:** Formal analysis, Methodology, Investigation, Resources, Data curation, Funding acquisition. **Isabel Barroso Martin:** Methodology, Formal analysis, Investigation, Data curation. **Federico Polo:** Investigation, Resources, Supervision, Funding acquisition, Writing – review & editing. **Alberto Vomiero:** Conceptualization, Resources, Supervision, Funding acquisition, Writing – review & editing. **Elti Cattaruzza:** Conceptualization, Investigation, Resources, Supervision, Funding acquisition, Writing – review & editing. **Elisa Moretti:** Conceptualization, Investigation, Resources, Supervision, Funding acquisition, Writing – review & editing.

Declaration of Competing Interest

The authors declare that they have no known competing financial interests or personal relationships that could have appeared to influence the work reported in this paper.

Data Availability

Data will be made available on request.

Acknowledgments

A.V. acknowledges financial support from the Kempe Foundation, the Knut och Alice Wallenberg Foundation (Grant no. KAW 2016.346), and the ÅFORSK Foundation. A.V. acknowledges Ca' Foscari University of Venice for SPIN2019 project. The authors acknowledge Mr. Tiziano Finotto from the Department of Molecular Sciences and Nanosystems, Ca' Foscari University of Venice, Italy, for his support on the XRD measurement. I.B.M. and E.R.C thank to Ministerio de Ciencia e Innovación of Spain, Grants PID2021-126235OB-C32 and TED2021-130756B-C31, and FEDER funds.

Appendix A. Supporting information

Supplementary data associated with this article can be found in the online version at doi:10.1016/j.cattod.2023.114134.

References

[1] T.O. Ajiboye, O.A. Oyewo, D.C. Onwudiwe, Simultaneous removal of organics and heavy metals from industrial wastewater: a review, Chemosphere 262 (2021), 128379, https://doi.org/10.1016/j.chemosphere.2020.128379.
[2] S. Anandan, V. Kumar Ponnusamy, M. Ashokkumar, A review on hybrid techniques for the degradation of organic pollutants in aqueous environment, Ultrason. Sonochem. 67 (2020), 105130, https://doi.org/10.1016/j.ultsonch.2020.105130.
[3] S. Varjani, P. Rakholiya, T. Shindhal, A.V. Shah, H.H. Ngo, Trends in dye industry effluent treatment and recovery of value-added products, J. Water Process Eng. 39 (2021), 101734, https://doi.org/10.1016/j.jwpe.2020.101734.
[4] C.R. Holkar, A.J. Jadhav, D.V. Pinjari, N.M. Mahamuni, A.B. Pandit, A critical review on textile wastewater treatments: possible approaches, J. Environ. Manag. 182 (2016) 351–366, https://doi.org/10.1016/j.jenvman.2016.07.090.
[5] C. Alberoni, I. Barroso-Martin, A. Infantes-Molina, E. Rodriguez-Castellon, A. Talon, H. Zhao, S. You, A. Vomiero, E. Moretti, Ceria doping boosts methylene blue photodegradation in titania nanostructures, Mater. Chem. Front. 5 (2021) 4138–4152, https://doi.org/10.1039/d1qm00068c.
[6] M. Telkhozhayeva, B. Hirsch, R. Konar, E. Teblum, R. Lavi, M. Weitman, B. Malik, E. Moretti, G.D. Nessim, 2D TiS_2 flakes for tetracycline hydrochloride photodegradation under solar light, Appl. Catal. B Environ. 318 (2022), 121872, https://doi.org/10.1016/j.apcatb.2022.121872.
[7] G. Ciamician, The photochemistry of the future, Science 36 (1912) 385–394, https://doi.org/10.1126/science.36.926.385.
[8] D. Ma, H. Yi, C. Lai, X. Liu, X. Huo, Z. An, L. Li, Y. Fu, B. Li, M. Zhang, L. Qin, S. Liu, L. Yang, Critical review of advanced oxidation processes in organic wastewater treatment, Chemosphere 275 (2021), 130104, https://doi.org/10.1016/j.chemosphere.2021.130104.
[9] P. Naliwajko, J. Strunk, Photocatalysis – the heterogeneous catalysis perspective, Heterog. Photocatal. (2021) 101–126, https://doi.org/10.1002/9783527815296.ch5.
[10] M.R. Al-Mamun, S. Kader, M.S. Islam, M.Z.H. Khan, Photocatalytic activity improvement and application of UV-TiO_2 photocatalysis in textile wastewater treatment: a review, J. Environ. Chem. Eng. 7 (2019), 103248, https://doi.org/10.1016/j.jece.2019.103248.
[11] M.T. Noman, M.A. Ashraf, A. Ali, Synthesis and applications of nano-TiO_2: a review, Environ. Sci. Pollut. Res. 26 (2019) 3262–3291, https://doi.org/10.1007/s11356-018-3884-z.
[12] E. Moretti, E. Cattaruzza, C. Flora, A. Talon, E. Casini, A. Vomiero, Photocatalytic performance of Cu-doped titania thin films under UV light irradiation, Appl. Surf. Sci. 553 (2021), 149535, https://doi.org/10.1016/j.apsusc.2021.149535.
[13] L. Liccardo, E. Lushaj, L. Dal Compare, E. Moretti, A. Vomiero, Nanoscale ZnO/α-Fe_2O_3 heterostructures: toward efficient and low-cost photoanodes for water splitting, Small Sci. 2 (2022) 2100104, https://doi.org/10.1002/smsc.202100104.
[14] J. Liu, L. Zhu, S. Xiang, H. Wang, H. Liu, W. Li, H. Chen, Cs-doped TiO_2 nanorod array enhances electron injection and transport in carbon-based $CsPbI_3$ perovskite solar cells, ACS Sustain. Chem. Eng. 7 (2019) 16927–16932, https://doi.org/10.1021/acssuschemeng.9b04772.
[15] Q. Guo, C. Zhou, Z. Ma, X. Yang, Fundamentals of TiO_2 photocatalysis: concepts, mechanisms, and challenges, Adv. Mater. 31 (2019) 1901997, https://doi.org/10.1002/adma.201901997.
[16] L. Pan, S. Wang, J. Xie, L. Wang, X. Zhang, J.J. Zou, Constructing TiO_2 p-n homojunction for photoelectrochemical and photocatalytic hydrogen generation, Nano Energy 28 (2016) 296–303, https://doi.org/10.1016/j.nanoen.2016.08.054.
[17] M. Iraj, F.D. Nayeri, E. Asl-Soleimani, K. Narimani, Controlled growth of vertically aligned TiO_2 nanorod arrays using the improved hydrothermal method and their application to dye-sensitized solar cells, J. Alloy. Compd. 659 (2016) 44–50, https://doi.org/10.1016/j.jallcom.2015.11.004.
[18] Z. Miao, G. Wang, L. Li, C. Wang, X. Zhang, Fabrication of black TiO_2/TiO_2 homojunction for enhanced photocatalytic degradation, J. Mater. Sci. 54 (2019) 14320–14329, https://doi.org/10.1007/s10853-019-03900-2.
[19] Z. Li, S. Wang, J. Wu, W. Zhou, Recent progress in defective TiO_2 photocatalysts for energy and environmental applications, Renew. Sustain. Energy Rev. 156 (2022), 111980, https://doi.org/10.1016/j.rser.2021.111980.
[20] X. Wang, L. Mayrhofer, M. Hoefer, S. Estrade, L. Lopez-Conesa, H. Zhou, Y. Lin, F. Peiró, Z. Fan, H. Shen, L. Schaefer, M. Moseler, G. Braeuer, A. Waag, Facile and efficient atomic hydrogenation enabled black TiO_2 with enhanced photoelectrochemical activity via a favorably low-energy-barrier pathway, Adv. Energy Mater. 9 (2019) 1900725, https://doi.org/10.1002/aenm.201900725.
[21] G. Greczynski, L. Hultman, *X-ray photoelectron spectroscopy*: towards reliable binding energy referencing, Prog. Mater. Sci. 107 (2020), 100591, https://doi.org/10.1016/j.pmatsci.2019.100591.
[22] G. Greczynski, L. Hultman, The same chemical state of carbon gives rise to two peaks in X-ray photoelectron spectroscopy, Sci. Rep. 11 (2021) 11195, https://doi.org/10.1038/s41598-021-90780-9.
[23] A. Houas, H. Lachheb, M. Ksibi, E. Elaloui, C. Guillard, J.M. Herrmann, Photocatalytic degradation pathway of methylene blue in water, Appl. Catal. B Environ. 31 (2001) 145–157, https://doi.org/10.1016/S0926-3373(00)00276-9.
[24] J. Shao, W. Sheng, M. Wang, S. Li, J. Chen, Y. Zhang, S. Cao, In situ synthesis of carbon-doped TiO_2 single-crystal nanorods with a remarkably photocatalytic efficiency, Appl. Catal. B Environ. 209 (2017) 311–319, https://doi.org/10.1016/j.apcatb.2017.03.008.
[25] S. Kaya, O. Ozturk, L. Arda, Roughness and bearing analysis of ZnO nanorods, Ceram. Int. 46 (2020) 15183–15196, https://doi.org/10.1016/j.ceramint.2020.03.055.
[26] J. Yang, J. Du, X. Li, Y. Liu, C. Jiang, W. Qi, K. Zhang, C. Gong, R. Li, M. Luo, H. Peng, Highly hydrophilic TiO_2 nanotubes network by alkaline hydrothermal method for photocatalysis degradation of methyl orange, Nanomaterials 9 (2019) 526, https://doi.org/10.3390/nano9040526.
[27] D. Rodríguez-Padrón, M. Algarra, L.A.C. Tarelho, J. Frade, A. Franco, G. De Miguel, J. Jiménez, E. Rodríguez-Castellón, R. Luque, Catalyzed microwave-assisted preparation of carbon quantum dots from lignocellulosic residues, ACS Sustain. Chem. Eng. 6 (2018) 7200–7205, https://doi.org/10.1021/acssuschemeng.7b03848.
[28] D. Polidoro, A. Perosa, E. Rodríguez-Castellón, P. Canton, L. Castoldi, D. Rodríguez-Padrón, M. Selva, Metal-free N-doped carbons for solvent-less CO_2 fixation reactions: a shrimp shell valorization opportunity, ACS Sustain. Chem. Eng. 10 (2022) 13835–13848, https://doi.org/10.1021/acssuschemeng.2c04443.
[29] E. Rodríguez-Aguado, A. Infantes-Molina, A. Talon, L. Storaro, L. León-Reina, E. Rodríguez-Castellón, E. Moretti, Au nanoparticles supported on nanorod-like TiO_2 as catalysts in the CO-PROX reaction under dark and light irradiation: effect of acidic and alkaline synthesis conditions, Int. J. Hydrog. Energy 44 (2019) 923–936, https://doi.org/10.1016/j.ijhydene.2018.11.050.
[30] P. Makuła, M. Pacia, W. Macyk, How to correctly determine the band gap energy of modified semiconductor photocatalysts based on UV-vis spectra, J. Phys. Chem. Lett. 9 (2018) 6814–6817, https://doi.org/10.1021/acs.jpclett.8b02892.
[31] M. Basu, A.K. Sinha, M. Pradhan, S. Sarkar, A. Pal, C. Mondal, T. Pal, Methylene blue-Cu_2O reaction made easy in acidic medium, J. Phys. Chem. C 116 (2012) 25741–25747, https://doi.org/10.1021/jp308095h.
[32] E.D. Revellame, D.L. Fortela, W. Sharp, R. Hernandez, M.E. Zappi, Adsorption kinetic modelling using pseudo-first order and pseudo-second order rate laws: a review, Clean. Eng. Technol. 1 (2020), 100032 https://doi.org/10.1016/j.clet.2020.100032.
[33] S. Haq, W. Rehman, M. Waseem, Adsorption efficiency of anatase TiO_2 nanoparticles against cadmium ions, J. Inorg. Organomet. Polym. Mater. 29 (2019) 651–658, https://doi.org/10.1007/s10904-018-1038-x.

[34] L. Tan, Z. Liu, C. Zhou, L. Ding, Combined factors influencing the surface charge and aggregation behaviors of TiO_2 nanoparticles in the presence of humic acid and UV irradiation, J. Nanopart. Res. 23 (2021) 191, https://doi.org/10.1007/s11051-021-05315-0.

[35] Q. Xiang, X. Ma, D. Zhang, H. Zhou, Y. Liao, H. Zhang, S. Xu, I. Levchenko, K. Bazaka, Interfacial modification of titanium dioxide to enhance photocatalytic efficiency towards H_2 production, J. Colloid Interface Sci. 556 (2019) 376–385, https://doi.org/10.1016/j.jcis.2019.08.033.

[36] M. Zeng, Influence of TiO_2 surface properties on water pollution treatment and photocatalytic activity, Bull. Korean Chem. Soc. 34 (2013) 953–956, https://doi.org/10.5012/bkcs.2013.34.3.953.

[37] C. Navas-Cárdenas, N. Benito, E.E. Wolf, F. Gracia, Tuning activity of $Pt/FeO_x/TiO_2$ catalysts synthesized through selective-electrostatic adsorption for hydrogen purification by prox reaction, Int. J. Hydrog. Energy 47 (2022) 20867–20880, https://doi.org/10.1016/J.IJHYDENE.2022.04.192.

[38] F. Azeez, E. Al-Hetlani, M. Arafa, Y. Abdelmonem, A.A. Nazeer, M.O. Amin, M. Madkour, The effect of surface charge on photocatalytic degradation of methylene blue dye using chargeable titania nanoparticles, Sci. Rep. 8 (2018) 7104, https://doi.org/10.1038/s41598-018-25673-5.

Other publications

Journal articles

E. Lushaj, M. Bordin, K. Akbar, **L. Liccardo**, I. Barroso-Martín, E. Rodríguez-Castellón, A. Vomiero, E. Moretti, F. Polo, Highly Efficient Solar-Light-Driven Photodegradation of Metronidazole by Nickel Hexacyanoferrate Nanocubes Showing Enhanced Catalytic Performances. *Small Methods* **2024**, 2301541. https://doi.org/10.1002/smtd.202301541

L. Liccardo, E. Lushaj, L. Dal Compare, E. Moretti, A. Vomiero, Nanoscale ZnO/α-Fe_2O_3 Heterostructures: Toward Efficient and Low-Cost Photoanodes for Water Splitting. *Small Sci.* **2022**, 2 (3), 2100104. https://doi.org/10.1002/smsc.202100104

Y. Han, **L. Liccardo**, E. Moretti, H. Zhao, A. Vomiero, Synthesis, Optical Properties and Applications of Red/near-Infrared Carbon Dots. *J. Mater. Chem. C* **2022**, 10(33), 11827–11847. https://doi.org/10.1039/D2TC02044K

J. Wang, **L. Liccardo**, H. Habibimarkani, E. Wierzbicka, T. Schultz, N. Koch, E. Moretti, N. Pinna, Precise control of TiO_2 overlayer on hematite nanorod arrays by ALD for the photoelectrochemical water splitting. *Sustain. Energy Fuels.* 2024, Submitted and under review.

B. Shani, **L. Liccardo**, M. Bordin, I. Barroso-Martín, A. Infantes-Molina, E. Rodríguez-Castellón, A. Vomiero, E. Moretti, CeO_2-TiO_2 nano-octahedra as active photocatalysts for ciprofloxacin photodegradation under solar light. *Adv. Sustain. Syst.* 2024, Submitted and under review.

Book Chapter

G. Liu, **L. Liccardo**, E. Moretti, H. Zhao, A. Vomiero, Quantum Dots in Photoelectrochemical Hydrogen Production, in Photoelectrochemical Engineering for Solar Harvesting: Chemistry, Materials, Devices Ed., S. Kazim, M. N. Tahir, S. Ahmad, S. Mathur, *Elsevier* **2024**.

Scientific Contributions

Oral communications

1. Liccardo, L.; Moras, P.; Sheverdyaeva, P. M.; Vomiero, A.; Caballero, A.; Colón, G.; Moretti, E. *Engineering the surface on nano-Cu/TiO_2 toward efficient H_2 photo-production*, ISIPM-11 & FLM2023, 11th International Symposium on Inorganic Phosphate Materials International Workshop on Forward-Looking Materials, oral communication (November 22-24th, 2023 in Venice)

2. Liccardo, L.; Vomiero, A.; Colón, G.; Moretti, E. *Surface defects engineered Nano-Cu/TiO_2 photocatalysts for hydrogen production*, GIC2023-XXIII National Congress on Catalysis, oral communication (participation with grant, June 14-16th, 2023, Genova)

3. Liccardo, L.; Bordin, M.; Moras, P.; Vomiero, A.; Moretti, E. *Shades of grey TiO_2 Hollow Spheres as efficient photocatalysts for the degradation of ciprofloxacin in wastewater*, GIC2022- XXII National Congress on Catalysis, oral communication (participation with grant, September 11-14th, 2022, Riccione)

4. Liccardo, L.; Bordin, M.; Moras, P.; Vomiero, A.; Moretti, E. *Colored TiO_2 Hollow Spheres as efficient photocatalyst for the degradation of ciprofloxacin in wastewater*, SYNC2022 - First Symposium for YouNg Chemists: Innovation and Sustainability Conference, oral communication (June 20-23rd, 2022, Rome)

5. Liccardo, L.; Moretti, E. *Facciamo luce sul tema degli inquinanti: fotocatalizzatori per la degradazione di contaminanti organici in acque reflue* IDL2022- Giornata Internazionale della Luce a Ca' Foscari "La luce attraverso la materia: nuove tecnologie per la scienza e lo sviluppo sostenibile", oral communication as invited speaker (May 23rd, 2022, Venice)

6. Liccardo, L.; Vomiero, A.; Moretti, E. *Nanostructured homo and heterojunctions for the photocatalytic degradation of wastewater pollutants: new outlook for our future,* CIRCC (Consorzio Interuniversitario Reattività Chimica e Catalisi) XVII PhD Day, oral communication (April 29-30st, 2021, Venice)

7. Liccardo, L.; Vomiero, A.; Moretti, E. *CeO_x/TiO_2 Hollow Spheres as efficient photocatalyst for the degradation of organic pollutants in*

wastewater, 27° Congresso Nazionale della Società Chimica Italiana, SCI, oral communication (participation with grant, September 14-23rd, 2021 held online)

8. Polo, F.; Lushaj, E.; Bordin, M.; Liccardo, L. *Highly Performing Solar-Light-Driven Photodegradation of Metronidazole by Nickel Hexacyanoferrate Nanocubes,* Materials Science and Technology (MS&T) 2023, oral communication (October 1-4th, 2023, Columbus, OH, USA)

Poster communications

9. Liccardo, L.; Colón, G.; Vomiero, A.; Moretti, E. *Surface defects engineering on Nano-Cu/TiO_2 for efficient hydrogen production*, 49° Congresso Nazionale di Chimica Inorganica, SCI – INORG2023, poster presentation (participation with grant and best poster prize, September 12-15th, 2023, Perugia)

10. Wang, J.; Liccardo, L.; Habibimarkani, H.; Moretti, E.; Pinna, N. Jiao Wang, *Impact of ALD-TiO_2 overlayer on hematite nanorod arrays for the photoelectrochemical water splitting* ALD2022 – 22nd International conference on atomic layer deposition, poster presentation (June 26-29th, 2022, Ghent, Belgium)

11. E. Moretti, L. Liccardo, M. Bordin, P. Moras, A. Vomiero, *Colored TiO_2 hollow spheres as efficient photocatalysts for drugs degradation in wastewater,* XLVIII Congresso Nazionale di Chimica Inorganica, poster presentation, (September 6-9th, Pisa 2022)

Acknowledgements

These past three years were one of the most important and unforgettable moments of my life. Anyway, I am convinced that it is impossible to achieve great results without being surrounded by extraordinary people. Thus, this section is to express my deepest and sincere gratitude to whoever I have met and supported me during my path. First, I would like to express my immense gratitude to my Supervisor Prof. Elisa Moretti and to Prof. Alberto Vomiero, who first welcomed me with full confidence in their research group. Thank you, Prof. Moretti, for your constant and invaluable help, time, and confidence in me. Your unique kindness and support have been instrumental for my academic journey and personal growth. Thank you, Prof. Vomiero, for your continuous support and all-round advice. Thank you sincerely for all the respect and regard you two have for me. Thank you both for being the best mentors I could have ever wished for. I would like to thank all the Nano4Gea members for the wonderful working environment. Thank you Kassa and Tofik for the nice talks and advice. A special thanks to my closest colleagues and friends, Nicolò, Matteo, Edlind and Sandro. I would like to express my gratitude to Dr. Cecilia Cerretani for her assistance and suggestions on the first part of this thesis. Cecilia, your mentorship, and friendship have been instrumental in my academic and personal journey. I was truly lucky to have met you. I also would like to acknowledge the great support received from my collaborators, Prof. Elti Cattaruzza, Prof. Federico Polo, Dr. Paolo Moras, Dr. Polina Sheverdyaeva, Prof. Marta Maria Natile, Dr. Matteo Belli, Dr. Shujie You, Dr. Jiao Wang, Dr. Isabel Barroso Martin, and Dr. Gerardo Colón. A special thanks to Prof. Nicola Pinna and Prof. Alfonso Caballero who hosted me during my periods abroad.

Finally, while these few lines may not be enough, I would like to genuinely thank my family and Walter for having steadily believed in me. Thank you for letting and making me always become the wannabe-me with your deep and endless love.